Lithium Ion Conducting Inorganic Solid Electrolytes and All Solid-State Lithium Batteries

by

Laidong Zhou

A thesis
presented to the University of Waterloo
in fulfillment of the
thesis requirement for the degree of
Doctor of Philosophy
in
Chemistry (Nanotechnology)

Waterloo, Ontario, Canada, 2021

Examining Committee Membership

The following served on the Examining Committee for this thesis. The decision of the Examining Committee is by majority vote.

External Examiner	M. Stanley Whittingham Professor Dept. of Chemistry, Binghamton University
Supervisor	Linda F. Nazar Professor Dept. of Chemistry, University of Waterloo
Internal Member	Holger Kleinke Professor Dept. of Chemistry, University of Waterloo
Internal-external Member	Michael Pope Associate Professor Dept. of Chemical Engineering, University of Waterloo
Other Members	Vivek Maheshwari Associate Professor Dept. of Chemistry, University of Waterloo

AUTHOR'S DECLARATION

I hereby declare that I am the sole author of this thesis. This is a true copy of the thesis, including any required final revisions, as accepted by my examiners.

I understand that my thesis may be made electronically available to the public.

Abstract

As the world transitions away from fossil energy to green and renewable energy, electrochemical energy storage techniques, especially rechargeable batteries, increasingly become a vital component for this transition. High energy density lithium-ion batteries are currently the most popular candidates. Conventional lithium-ion batteries exploit flammable liquid electrolytes and carbon anodes that suffer from low energy density and safety risks. To meet the requirements for high energy density and high safety, rechargeable batteries based on the 'beyond lithium ion' technologies have been widely investigated. Among them, all solid-state lithium batteries that use a solid electrolyte in place of a liquid electrolyte - and ideally a Li metal anode - can eliminate safety concerns and provide higher energy density. Particularly, solid electrolytes are the vital component which can realize the potential of ASSBs. This thesis presents a thorough investigation on discovering new Li fast ion conductors (> 1 $mS.cm^{-1}$) and understanding the fundamental structure-property relationships in ionic conductors and developing high energy density and long-lasting all solid-state lithium batteries and understanding the critical requirements for all solid-state lithium batteries operations.

Chapter 3 presents an entropically stabilized lithium fast ion conductor, $Li_{3+x}Si_xP_{1-x}S_4$, with high ionic conductivity above 1 $mS.cm^{-1}$. Using a combination of single crystal X-ray and powder neutron diffraction, the maximum entropy method, and impedance spectroscopy to explore the influence of aliovalent substitution in the thermodynamically unstable β-Li_3PS_4 lattice. Aliovalent substitution induces structural splitting of the localized Li sites, effectively stabilizing bulk β-Li_3PS_4 structure at room temperature and delocalizing lithium-ion density.

The inherent entropic Li site disorder induced a frustrated energy landscape for Li ion diffusion, which leads to the highest ionic conductivity of 1.22 $mS.cm^{-1}$ for the optimal material, $Li_{3.25}Si_{0.25}P_{0.75}S_4$, represents three orders of magnitude increase of ionic conductivity compared to bulk β-Li_3PS_4 and one order of magnitude higher than the nanoporous form. The significantly enhanced Li ion conduction and lowered activation barrier with increasing Li site disorder induced by aliovalent tuning represent an important strategy toward the design of new fast ion conductors.

Chapter 4 presents the first family of thioantimonate argyrodite lithium superionic conductors, $Li_{6+x}M_xSb_{1-x}S_5I$ (M = Si, Ge, Sn). Exploration of the series using a combination of single crystal X-ray and synchrotron/neutron powder diffraction, combined with impedance spectroscopy, reveals that substitution induces negligible S^{2-}/I^- anion site disorder, but more importantly Li^+ cation site disorder. The additional, delocalized Li ion density sits in new high energy lattice sites that serve as intermediate interstitial positions for Li ion diffusion. The corresponding coulombic repulsion force between Li ions, due to close distance ~ 1 Å, activate concerted ion migration, leading to a low activation energy of 0.25 eV. Superionic conductivity up to 24 $mS.cm^{-1}$ is achieved - among one of the highest values reported to date. The new argyrodite SEs also demonstrate good compatibility with Li metal, sustaining over 1000 h of Li stripping/plating at current densities up to 0.6 $mA.cm^{-2}$. The significantly enhanced Li ion conduction and lowered activation energy barrier with increasing Li cation site disorder reveals an important strategy toward the development of new superionic conductors (> 10 $mS.cm^{-1}$).

Chapter 5 presents a new chloride fast ion conductor, $Li_2Sc_{2/3}Cl_4$ with a disordered spinel structure, which exhibits an ionic conductivity of 1.5 $mS.cm^{-1}$ and a low activation

energy barrier 0.34 eV for Li ion diffusion. This material represents the first spinel-type chloride fast ion conductor. Powder neutron diffraction reveals a significantly disordered Li ion distribution over available tetrahedral and octahedral sites within the lattice, which forms an infinitely 3D connected Li ion diffusion pathway comprised of face-sharing octahedra and tetrahedra. Due to the intrinsic high oxidative stability of chloride materials, all solid-state batteries employing this new chloride solid electrolyte and typically high voltage cathodes ($LiCoO_2$, $LiNi_{0.6}Mn_{0.2}Co_{0.2}O_2$ (NMC622) or high-Ni $LiNi_{0.85}Mn_{0.05}Co_{0.1}O_2$ (NMC85)) - without any coating - exhibit excellent electrochemical performance up to 4.6 V in terms of capacity retention and cycle life.

Chapter 6 presents a new lithium mixed-metal chlorospinel, $Li_2In_xSc_{0.666-x}Cl_4$ ($0 < x \leq 0.666$), with high ionic conductivity (up to 2.0 $mS.cm^{-1}$) owing to a very disordered Li ion distribution and all solid-state batteries with exceptional electrochemical performance. All solid-state batteries using $LiCoO_2$, NMC622, or NMC85 as cathode materials exhibit superior rate capability, extremely high discharge and areal capacities (> 4 $mAh.cm^{-2}$, ~ 190 $mAh.g^{-1}$), very high Coulombic efficiency close to 100%, and long-term cyclability - more than 3000 cycles - with 80 % capacity retention at room temperature (up to 4.8 V vs Li^+/Li), surpassing the reported literature values for state-of-the-art all solid-state batteries. The excellent electrochemical performance originates from the superior interfacial stability between chloride solid electrolytes and un-coated high voltage cathode materials as revealed by impedance analysis and time-of-flight secondary ion mass spectrometry. This work provides valuable insight into the design and development of ASSBs and may serve as an important point of reference.

Acknowledgements

I would like to express my greatest gratitude to my supervisor Dr. Linda F. Nazar for her guidance, support, and the freedom she gave me during my doctoral study. I have been enjoying my research life originated from my interest and curiosity. The scientific arguments between us lead to great scientific discussions in the past few years. I have gained great experience in critical and independent thinking and planning. Her dedication to science greatly influences me.

I would like to thank my Ph.D. committee members Dr. Holger Kleinke, Dr. Michael Pope, and Dr. Vivek Maheshwari for their time and suggestions about my research. I would also like to thank Dr. M. Stanley Whittingham for being my external examiner and his time to participate in my thesis defense. It is my great honor to have Prof. Whittingham as my external examiner.

I would like to thank all the Research collaborators: Dr. Juergen Janek; Dr. Tongtong Zuo; Dr. Abdeljalil Assoud; Dr. Ashfia Huq and Dr. Qiang Zhang, for their help and the great collaboration. I would like to thank Dr. Joel Reid for the synchrotron X-ray powder diffraction data collection.

I would also like to extend my gratitude to Dr. Guang He; Dr. Xiaoqi Sun and Dr. Quan Pang for their help to get my projects started when I just joined the group. Also, many thanks to Dr. Xiao Liang; Huang He; Xiaoqi and Quan for bringing me out of the lab to enjoy the life in Canada. Furthermore, thanks to Abhinandan Shyamsunder; Chun Yuen Kwok; Chang Li;

Dr. Zhizhen Zhang; Shiqi Xu; Fabien; Kavish; SeYoung and all the previous and current group members for all the great moments.

I would also like to thank all my friends for their support and making my life so delightful and enjoyable throughout my Ph.D. study.

Finally, I would like to thank my parents for bringing me up and supporting me under all conditions.

Table of Contents

List of Figures

List of Tables

List of Abbreviations

ASSBs	All solid-state Li batteries
BSE	Backscattered electrons
BVSE	Bond Valence Site Energy
CAM	Cathode active material
CEI	Cathode-electrolyte interface
CLS	Canadian light source
CPE	Constant phase element
DFT MD	Density functional theory molecular dynamics simulations
EDX	Energy Dispersive X-ray Spectroscopy
EIS	Electrochemical Impedance Spectroscopy
GB	Grain boundary
LIBs	Li-ion batteries
LSV	Linear sweep voltammetry
MAS NMR	Magic-angle spinning nuclear magnetic resonance
MEM	Maximum entropy method
PEEK	Polyether ether ketone
PND	Powder neutron diffraction
SEs	Solid electrolytes
SEI	Solid electrolyte interphase
SEM	Scanning Electron Microscopy
ToF-ND	Time-of-flight neutron diffraction
ToF-SIMS	Time-of-flight secondary ion mass spectrometry
XRD	X-ray diffraction

Chapter 1. Introduction

1.1 Energy Storage

Our increasing global population and the alarming consequences of heavily utilizing fossil fuels, such as global warming and air pollution caused by their massive production of CO_2, SO_2 gas, have led to an ever-increasing demand for sustainable energy in the last decade. Alternative energy generation technologies, such as solar and wind are renewable energies and environmentally clean. However, these are only intermittently available and depend on time, weather, seasons, and locations. To fully utilize these intermittent energy sources drives research for low cost, environmentally friendly and high-performance energy storage technologies.[1, 2] Rechargeable batteries are currently the most popular candidates. Among all the rechargeable battery systems, Li-ion batteries (LIBs) have dominated the commercial battery market.[3, 4] The current start-of-the-art LIBs are widely used for portable devices such as cell phones and laptops.

1.2 Rechargeable Li-ion Batteries and Li Metal Batteries

A typical LIB consists of two electrodes - positive and negative electrodes (cathode and anode) - which are separated by the electrolyte. An electrolyte permeable and insulating porous separator is needed for liquid electrolyte cells to avoid direct contact between two electrodes. Driven by the difference in the chemical potentials of the two electrodes, electrochemical reduction and oxidation occur at each electrode separately. By applying external power, the process reverses in rechargeable batteries. Thus, energy can be reversibly released and stored in rechargeable batteries. For LIBs using a graphite anode and a lithium metal oxide cathode, as shown in **Figure 1.1**.[4] Li ion de/intercalation mechanism[5] takes place

at both electrodes. During charging, the cell is charged with an external power supply, the electrons were forced to move out from cathode to anode through the outer circuit. The loss of electrons in $LiCoO_2$ leads to the oxidation of Co^{3+} to Co^{4+} and Li ion deintercalated from the structure to balance the charge, following **Equation 1.1**. Then, the Li ions migrate to the graphite anode through the electrolyte, intercalate into the graphite and recombine with electrons, following **Equation 1.2**. Due to the higher chemical potential of the cathode than the anode, the reverse process (discharging) takes place spontaneously, following **Equations 1.3** and **1.4**.

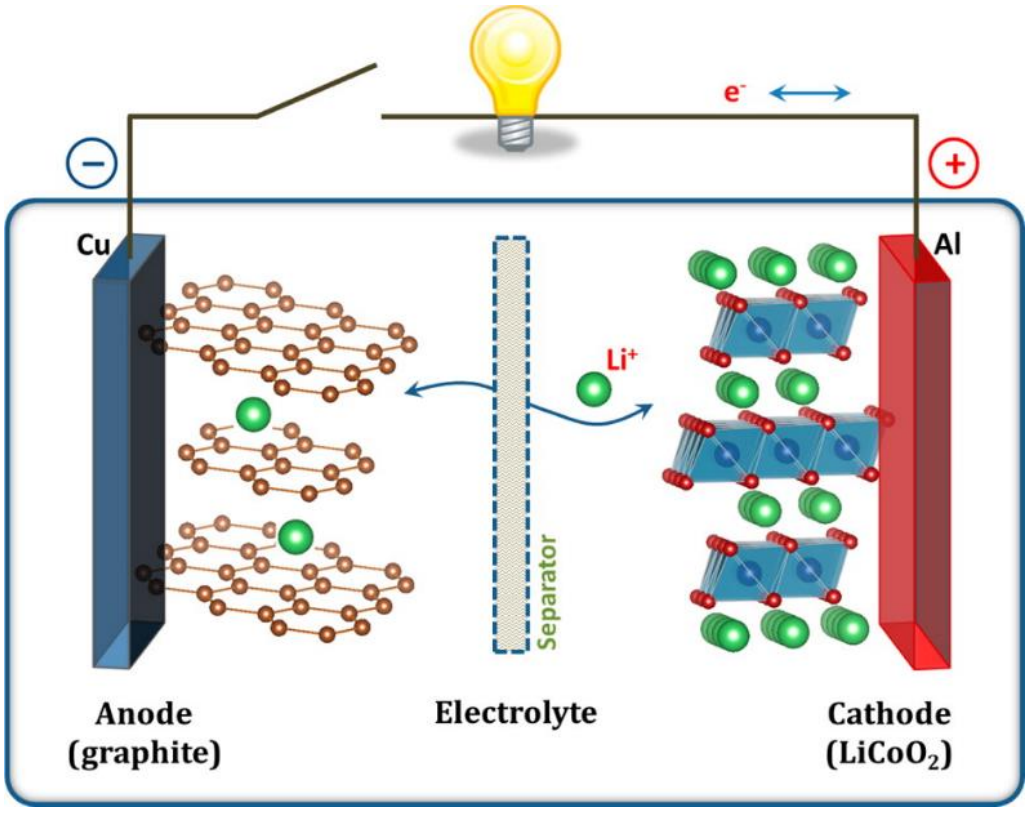

Figure 1.1 Schematic illustration of a conventional lithium-ion battery consists of a graphite anode, layered $LiCoO_2$ cathode, and a porous separator immersed in a liquid electrolyte, respectively. The electrolyte contains lithium salts dissolved in organic solvents. Adapted from Ref. 4. Copyright 2013 American Chemical Society.

During Charging:

Positive electrode (Cathode): $LiCoO_2 - x\ Li^+ - x\ e^- \rightarrow Li_{1-x}CoO_2$ **Equation 1.1**

Negative electrode (Anode): $C_6 + x\ Li^+ + x\ e^- \rightarrow Li_xC_6$ **Equation 1.2**

During Discharging:

Positive electrode (Cathode): $Li_{1-x}CoO_2 + x\ Li^+ + x\ e^- \rightarrow LiCoO_2$ **Equation 1.3**

Negative electrode (Anode): $Li_xC_6 - x\ Li^+ - x\ e^- \rightarrow C_6$ **Equation 1.4**

$LiCoO_2$ can only sustain half Li ion be taken out to maintain structural stability, which provides a specific capacity of 137 $mAh.g^{-1}$. Deeper charging (remove more than half Li ions) will lead to oxygen evolution from the crystal lattice, which leads to fast capacity fade.[6] Due to this structural instability during deeper charging and the high price, limited resource and high toxicity of cobalt, developing alternative cathode active materials (CAMs) has attracted great interests. Substitution Co with other transition metals has led to one of the most extensively investigated CAM family $LiNi_{1-x-y}Mn_xCo_yO_2$ (NMC) over the last 10 years.[7] In this cathode material class, electrochemical-inactive Mn maintains 4^+ oxidation state to stabilize the structure and Co can decrease the cation site mixing that results from the similar ionic radii between Li^+ and Ni^{2+}. High-Ni NMC cathodes offer high discharge capacity (~ 200 $mAh.g^{-1}$), relying on $Ni^{2+/4+}$ and $Co^{3+/4+}$ redox couples, which provide higher energy density compared to $LiCoO_2$.

As LIBs are approaching the theoretical capacity of cathode/anode materials, especially graphite anode, Li metal batteries offer the promise for next-generation high energy density electrochemical energy storage systems. Li metal anode exhibits the highest specific capacity (3840 $mAh.g^{-1}$) which is an order of magnitude higher than graphite and the lowest reduction

potential (-3.04 V versus standard hydrogen electrode) among all metal anodes.[8, 9] However, Li metal anodes suffer from its dendrite-like electrodeposition behavior, instead of film-like plating, as shown in **Figure 1.2**.[10] Furthermore, organic liquid electrolytes are thermodynamically unstable towards the reduction by Li metal, which leads to the growth of a high resistance solid electrolyte interphase (SEI) and consume of liquid electrolyte. During continuous cycling, the growth of Li dendrites leads to a high surface area of fresh Li which endlessly reacts with liquid electrolyte and consumes Li and liquid electrolyte, and finally cell failure. Upon further long-term cycling, Li dendrites can penetrate through the separator layer which will lead to cell short circuit. The cell short circuit accompanies by the thermal runway and combining with the intrinsic flammable nature of organic solvents can lead to explosion, as summarized in **Figure 1.2**.

With the rapid growth of electric vehicles and grid energy storage demands, high energy density, and high safety batteries are urgently needed. Safety is particularly important for electric vehicles. Among the various technologies, including Li-S battery, Metal-O_2 battery,

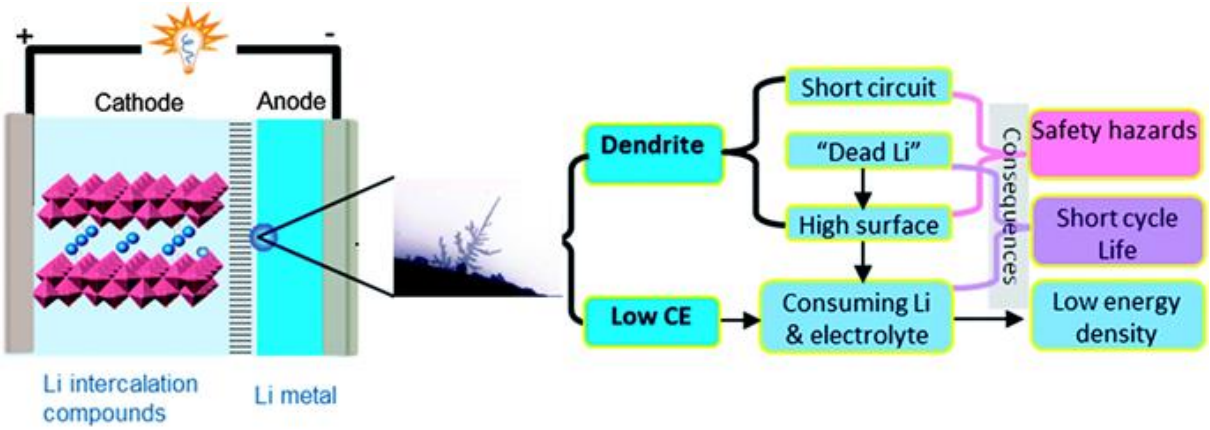

Figure 1.2 Schematic diagram of Li metal batteries and the typical Li dendrite morphology and the corresponding problems related to Li dendrite growth and low Coulombic efficiency. Reproduced with permission from Ref. 8. Copyright 2014 Royal Society of Chemistry. Reproduced with permission from Ref. 10. Copyright 2013 Elsevier.

Na-ion battery, multivalence (Zn, Mg, Ca) battery, *et al*, all solid-state Li batteries (ASSBs) offers the greatest promise. As a result, LIBs are starting to undergo an evolution from conventional LIBs to ASSBs. The development, current status, and the problems facing today ASSBs will be discussed in detail in the following sections.

1.3 All Solid-State Li Batteries

1.3.1 Overview of All Solid-State Batteries

Based on the types of solid electrolytes (SEs) used, ASSBs can be divided into two types: ASSBs with polymer SEs or polymer-ceramic composite SEs and ASSBs with inorganic SEs. The poor interfacial contact between active materials-SEs and the chemo-mechanical expansion/constriction of Li cathode materials[11] can lead to high internal cell resistance. Thus, a small amount of liquid electrolyte is usually added in between the electrolyte/electrode interface to improve the cell performance, which is then regarded as quasi or hybrid ASSBs. This thesis focuses on inorganic SEs and ASSBs with inorganic SEs, thus the following discussions also focus on the development of inorganic SEs and ASSBs with inorganic SEs only.

ASSBs that use a SE in place of a liquid electrolyte - and ideally a Li metal anode - can eliminate safety concerns and provide higher energy density, as shown in **Figure 1.3**.[12-14] Typically, ASSBs consist of a thin layer of SE as separator and cathode and anode composites which is a homogeneous mixture of active material, SE powder and electronic conductive material (such as carbon, if necessary). To further improve the energy density, Li metal anode or other high specific capacity material (such as silicon anode) is required. Furthermore, the

bipolar ASSBs packing architecture offers substantial benefits regarding battery performance and fabrication cost, as shown in **Figure 1.4**.[15] The bipolar cell stacking allows multiple cells connected in series without external wiring and can lower the cell pack volume, weight, and cost, which further improve the cell energy density.

Ionically conductive inorganic SEs (> 1 $mS.cm^{-1}$) are the key component in ASSBs which removes the safety concerns inherent with flammable organic liquid electrolytes in conventional LIBs. Inorganic SEs also provide excellent thermal stability and conductivities over a wider temperature range, which enables battery operation in a broad range of conditions (for example, -10 to 100 °C) where conventional liquid electrolytes will freeze, boil or decompose.[16] To realize the potential of ASSBs, a range of new SE materials have been developed and investigated.[17, 18]

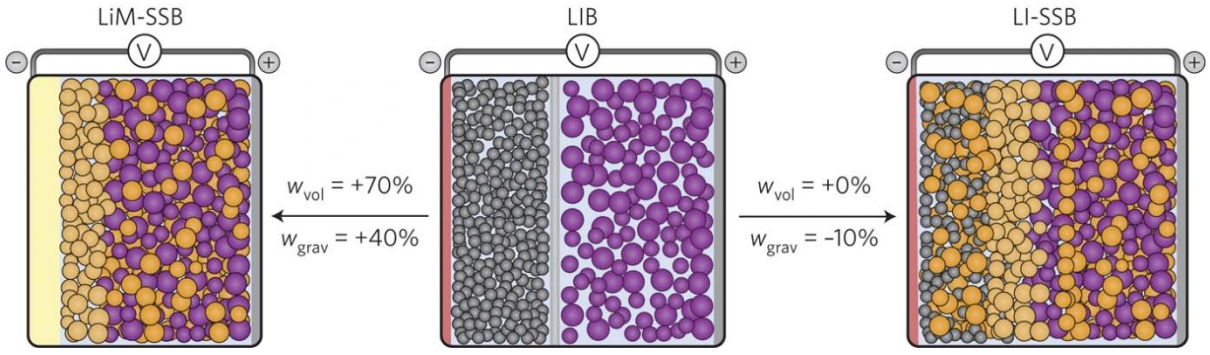

Figure 1.3 Schematic diagrams of typical battery architectures for conventional Li-ion battery (middle), all solid-state Li-ion battery (right), and all solid-state Li metal battery (left). The W_{vol} and W_{grav} represent volumetric and gravimetric energy densities, respectively. Only with Li metal anode (rather than graphite) and a thin solid electrolyte layer, the energy density of ASSBs can be significantly increased. Reproduced with permission from Ref. 12. Copyright 2016 Nature Publishing Group.

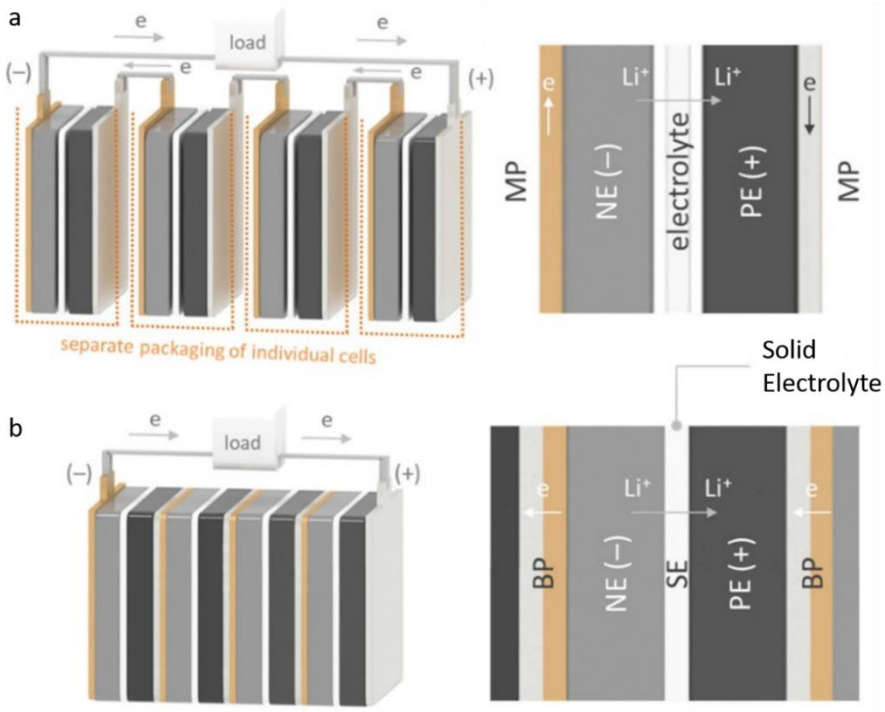

Figure 1.4 Schematic diagrams of (a) monopolar (MP) design of current LIBs with liquid electrolytes and (b) bipolar (BP) design of ASSBs with solid electrolytes. Reproduced with permission from Ref. 15. Copyright 2019 Chemistry Europe.

1.3.2 Categorization of Various Inorganic Solid Electrolytes

SEs should meet several critical criteria: high Li ion conductivity, low electronic conductivity, good chemical and electrochemical stability against Li metal and cathode/anode active materials. Concerning practical application, they should also be cost-effective, low toxic, and environmentally friendly. Heretofore various inorganic SEs have been discovered and investigated, which including oxides, phosphates, thiophosphates (sulfides), halides, *et al.*[13, 17, 19] The representative examples for oxides and phosphate SEs: LISICON-type $Li_{14}Zn(GeO_4)_4$ (LZGO), perovskite-type $Li_{3x}La_{2/3-x}TiO_3$ (LLTO), NASICON-type $Li_{1.07}Al_{0.69}Ti_{1.46}(PO_4)_3$ (LATP) and $Li_{1.5}Al_{0.5}Ge_{1.5}(PO_4)_3$ (LAGP), and garnet-type $Li_5La_3Zr_2O_{12}$ (LLZO); sulfide SEs: glassy sulfides, thio-LISICON-type binary/trinary sulfides,

LGPS-type: $Li_{10}MP_2S_{12}$ (M = Ge, Sn) and argyrodite-type Li_6PS_5X (X=Cl, Br, I); chloride SEs: binary/trinary LiCl-M_xCl_y and derivatives. The properties of each type of SEs are compared in the following sections.

1.3.2.1 Oxide and Phosphate Solid Electrolytes

Oxide and phosphate SEs are typically ceramics, which are rigid, brittle, and exhibit relatively good stability in air. Based on their structures, they can be divided into four representative categories: LISICON, Perovskite, NASICON, and Garnet.

LISICON

The LISICON structure $Li_{14}Zn(GeO_4)_4$ was discovered far back 1978 by Hong and exhibits a really low ionic conductivity 1 x 10^{-7} S.cm^{-1}.[20] Furthermore, it is also highly reactive towards CO_2 and can be easily reduced by Li metal,[21] thus it is not suitable to be used as SEs, but the derivatives: thio-LISICON which exhibits significantly higher Li ion conductivity and will be discussed in the following section.

Perovskite

Perovskite structure SEs with general formula ABO_3 with the structure of $CaTiO_3$.The atomic A site is occupied by divalent alkali cation (Ba^{2+}, Ca^{2+}, Sr^{2+}, *et al*) and the atomic B site is occupied by tetravalent transition metal cation (Ti^{4+}). By replacing the divalent cation at A site with trivalent rare earth element La^{3+} and monovalent alkali metal cation Li^+, perovskite $Li_{0.5}La_{0.5}TiO_3$ were first reported by Brous *et al*.[22] By controlling the Li substitution content, $Li_{3x}La_{2/3-x}TiO_3$, a high bulk ionic conductivity ~ 1 mS.cm^{-1} (total ionic conductivity: 2 x 10^{-5} S.cm^{-1}) can be achieved at room temperature.[23] The crystal structure of $Li_{3x}La_{2/3-x}TiO_3$ mainly

depends on the composition (x) and synthesis conditions, cubic, tetragonal and orthorhombic have been previously reported.[24] When synthesizing at 1350 ^{o}C and then quenching to room temperature, the product exhibits cubic structure; while when slowly cooling to room temperature, tetragonal or orthorhombic structure can be obtained.[24] The Li ion conductivity of perovskites depends on the concentration of Li ions and vacancies at A site, as Li ions diffuse from A site to neighboring A site through a diffusion bottleneck channel surrounded by four oxygen atoms. Due to the Coulombic attraction force between O^{2-} and Li^{+}, the oxygen bottleneck channel acts as a potential barrier for Li ion diffusion.[25] With co-existence of La^{3+} and Li^{+} in the A site, which leads to vacancy in A site, thus Li ions diffuse through A sites by vacancy mechanism. By controlling the Li ion and vacancy contents through different cation doping, a high Li ion conductivity ~ 1 mS.cm^{-1} has been achieved.[26] However, due to the presence of transition metal cation, such as Ti^{4+}, it can be easily reduced by Li metal and form an insulating interface.[27]

NASICON

NASICON compounds have the general formula $AM_2(PO_4)_3$, where A site is occupied by Li^{+} or other cations such as Na^{+} and K^{+} and the M site is occupied by Ge^{4+}, Ti^{4+} or Zr^{4+}. Among a variety of compositions, two representative materials $Li_{1.07}Al_{0.69}Ti_{1.46}(PO_4)_3$ (LATP) and $Li_{1.5}Al_{0.5}Ge_{1.5}(PO_4)_3$ (LAGP) exhibit the highest ionic conductivity 1.3 mS.cm^{-1} and 0.4 mS.cm^{-1}, respectively.[28, 29] They are also not stable with Li metal, due to the reduction of transition metal cations by Li metal. However, NASICON-type SEs are suitable for high voltage ASSBs application, due to their high ionic conductivity and good chemical stability towards air and moisture, and wide oxidative potential window. Extensive studies on

LATP/LAGP coated CAMs to improve the high voltage electrochemical performance in both liquid cells and ASSBs have been conducted.[30-34] However, due to the mechanical rigidity of NASICON materials, high temperature sintering is required to improve grain boundary contact between NASICON particles to achieve high total ionic conductivity and improve contact between SE-CAMs to lower interfacial resistance. High temperature sintering can also lead to side reactions between NASICON SE and CAM.[34] Both hinder their practical application in ASSBs.

Garnet

Garnet structured SEs with general formula $Li_7La_3M_2O_{12}$ (M = Zr, Hf, Sn, *et al*) have been intensively studied and regarded as one of the best SEs, due to its intrinsic stability with Li metal, wide electrochemical window, and good ionic conductivity.[35, 36] The representative material cubic $Li_7La_3Zr_2O_{12}$ exhibit a reasonably high ionic conductivity 0.3 $mS.cm^{-1}$.[37] Based on the Li content, garnet SEs can be classified into four categories, including Li3 series: $Li_3M_3Te_2O_{12}$ (M = Y, Pr, Nd, *et al*)[38]; Li5 series: $Li_5La_3M_2O_{12}$ (M = Nb, Ta, *et al*)[39, 40]; Li6 series: $Li_6ALa_2M_2O_{12}$ (A = Ca, Sr, Ba, etc., and M = Ta, *et al*)[41]; and Li7 series: $Li_7La_3M_2O_{12}$ (M = Zr, Sn, Hf, *et al*)[37]. The ionic conductivity of garnet SEs increases with increasing Li content.[42] Among them, the Li7 phases and its derivatives, $Li_{7-x}La_3Zr_{2-x}M_xO_{12}$ (M = Ta, *et al*),

exhibit the highest ionic conductivity ~ 1 $mS.cm^{-1}$.[43-46] Same as other oxide SEs, the mechanical rigidity of materials and high synthesis temperature hinder its practical application.

1.3.2.2 Sulfide Solid Electrolytes

Since the discovery of superionic conductor $Li_{10}GeP_2S_{12}$,[47] sulfide SEs have been extensively studied over the last decade. Due to the lower electronegativity of S^{2-} compared to O^{2-}, the S^{2-}-Li^+ bond is weaker compared to O^{2-}-Li^+ bond. And the large ionic radius of S^{2-} leads to a larger bottleneck channel for Li ion diffusion. Thus, sulfide SEs have been shown to exhibit particularly high ionic conductivity > 10 $mS.cm^{-1}$ that even surpasses that of conventional organic liquid electrolytes. Accompanied by a ductile nature,[48] which makes them relatively easy to process and realize intimate interfacial contact with cathode and anode active materials - a requirement for ASSB operation. Thus, sulfide SEs have been a particular focus of recent research. However, most sulfide SEs are extremely moisture sensitive, which hydrolysis to form toxic H_2S once exposed to moisture. Therefore, the preparation and storage of sulfide SEs require an inert atmosphere, which significantly increases the processing and storage cost. Sulfide SEs can be divided into several representative categories: glassy sulfides, thio-LISICON-type binary/trinary sulfides, LGPS-type: $Li_{10}MP_2S_{12}$ (M = Ge, Sn), and argyrodite-type Li_6PS_5X (X=Cl, Br, I).

Glassy Sulfide Solid Electrolytes

Glassy sulfide SEs have been studied before any crystalline and glass-ceramic sulfide SE materials which generally exhibit relatively high ionic conductivity in the range of 10^{-4} - 10^{-3} $S.cm^{-1}$. Examples include: Li_2S-P_2S_5-LiI;[49] x Li_2S-(1-x) SiS_2 (x< 0.6);[50] Li_2S-M (M = SiS_2,

GeS_2, P_2S_5, B_2S_3, As_2S_3);[51] Li_2S-SiS_2-Li_3N;[52] Li_2S-SiS_2-LiI;[53] Li_2S-B_2S_3-LiI;[54] and *et al*. However, the synthesis either requires high energy ball milling or high temperature quenching under inert atmosphere, which is prohibitively costly and not practical.

Thio-LISICON and LGPS

Thio-LISICON SEs are one of the first high ionic conductive crystalline sulfide SEs.[55] The materials based on Li_3PS_4 are particularly appealing. The most thermodynamically stable form of Li_3PS_4 is the γ-phase, with a reported low ionic conductivity of 0.0003 $mS.cm^{-1}$ at room temperature.[56] Above 195 °C, it converts to the more highly conductive β-phase.[56] As β-Li_3PS_4 is not stable at room temperature, the conductivity of β-Li_3PS_4 at 25 °C was determined by extrapolation of the Arrhenius plot from elevated temperature, and is only 0.0009 $mS.cm^{-1}$.[57] Several groups have attempted to stabilize the β-Li_3PS_4 structure at room temperature. Liu *et al* reported a solution synthesis of nanoporous β-Li_3PS_4 (0.16 $mS.cm^{-1}$ at room temperature).[57] The high-temperature β-Li_3PS_4 appears to be stabilized at room temperature in the nanoporous form by the inclusion of tetrahydrofuran in the material arising from the synthetic procedure. As far back as 2002, Kanno *et al* reported on substitution of P^{5+} with Ge^{4+} to form $Li_{3+x}Ge_xP_{1-x}S_4$, where the composition $Li_{3.25}Ge_{0.25}P_{0.75}S_4$ showed the highest ionic conductivity (2.2 $mS.cm^{-1}$).[55] Kawamoto *et al* reported thio-LISICON $Li_{3+x}Si_xP_{1-x}S_4$ with maximum ionic conductivity of 0.64 $mS.cm^{-1}$ at x = 0.4.[58] These seminal work led to the discovery of the superionic 'LGPS-type' phases exemplified by $Li_{10}GeP_2S_{12}$.[47] However, both $Li_{3+x}Ge_xP_{1-x}S_4$ and LGPS suffer from poor cathodic stability in contact with a highly reducing

Li metal due to the presence of Ge^{4+}.[59] Since then, a lot of LGPS derivatives were reported with the highest ionic conductivity 25 $mS.cm^{-1}$ for $Li_{9.54}Si_{1.74}P_{1.44}S_{11.7}Cl_{0.3}$.[60-63]

Argyrodite Solid Electrolytes

Li-argyrodite SEs are currently the dominantly used SEs for ASSB fabrication.[64] Li-argyrodite SEs have a general formula $Li_{7+x-y}M^{V}_{1-x}M^{IV}_{x}Ch_{6-y}X_{y}$ (M^{V} = P, Sb; M^{IV} = Si, Ge, Sn; Ch = O, S, Se; X = Cl, Br, I, BH_4; $0 \leq x \leq 1$; $0 \leq y \leq 2$)[65-77] and are particularly appealing owing to their high Li ion conductivity (up to 24 $mS.cm^{-1}$)[65] and scalable solution-assisted synthetic approaches[78], which are both vital for commercial applications.

The argyrodite structure originates from the mineral Ag_8GeS_6 (orthorhombic, S. G.: *Pna*2_1). The Li-argyrodites exhibit two structural polymorphs with phase transition temperature depending on the chemical composition.[79] Compounds that crystallize in the low-temperature orthorhombic structure, such as Li_7PS_6 (S. G.: *Pna*2_1), show very low Li ion conductivity at room temperature, while high ionic conductivities have only been achieved in the high-temperature cubic phase (S.G.: $F\bar{4}3m$). The cubic structure can be stabilized at room temperature by replacement of one or more sulfide anions with halide anion, resulting in Li_6PS_5X (X = Cl, Br, I).[68] Depending on the composition of Li_6PS_5X, a certain degree of S^{2-}/X^{-} anion site disorder has been observed.[66] Caused by a much larger ionic size difference between I^{-} and S^{2-} in Li_6PS_5I, both remain on their two unique crystallographic sites, while for X = Br^{-} and Cl^{-}, a significant site disorder is observed.[66] Anion-ordered Li_6PS_5I exhibits very

low Li ion conductivity, while anion-disordered Li_6PS_5Br and Li_6PS_5Cl exhibit high Li ion conductivity.

1.3.2.3 Chloride Sold Electrolytes

Chloride SEs gained little attention, unlike oxide and sulfide SEs. Until 2018, there is no chloride SE has been reported with high ionic conductivity > 1 $mS.cm^{-1}$. Asano *et al* reported poorly crystalline Li_3YCl_6 and Li_3YBr_6 synthesized by high energy ball milling which exhibit relatively high ionic conductivity 0.51 and 0.72 $mS.cm^{-1}$, respectively.[80] Due to the intrinsic high oxidative potential and ductile nature, ASSBs with uncoated $LiCoO_2$ exhibit stable cycling up to 4.22 V vs Li^+/Li.[80] Subsequently, several chloride SEs were developed, including poorly crystalline Li_3ErCl_6 (0.31 $mS.cm^{-1}$);[81] Li_3InCl_6 (1.49 $mS.cm^{-1}$);[82] and $Li_{3-x}M_{1-x}Zr_xCl_6$ (M = Y, Er, up to 1.4 mS cm^{-1})[83]. These lithium metal chlorides are also not stable with Li metal, due to the presence of metal cation such as (In^{3+}).[84]

1.3.3 Ion Diffusion Mechanism and Fast Ion Conduction Design Mechanism

Better understanding of the ion diffusion mechanism in fast ion conductors is essential to guide the development of new materials. The conventional ion diffusion mechanism in inorganic solid electrolytes is based on classic diffusion model: ion diffusion as the hopping of an individual ion from one lattice site to another adjacent site, which is termed as direct-hopping. However, in fast ion conductors, fast ion conduction is achieved with multiple ions migrate at the same time, rather than single ion diffusion. Thus, mobile ions interaction needs to be considered. In accord, another conduction mechanism – concerted mechanism[85] – is proposed, where multiple ions migrate together. Mobile ion occupying high energy sites can migrate downhill towards low energy occupied site with low energy barrier and the

corresponding coulombic interactions between two mobile ions will help lower the activation energy barrier for mobile ion occupying low energy site to move uphill towards another unoccupied high energy sites. This concerted ion migration mechanism explains the origin of fast ion conduction in doped LLZO, NASICON and argyrodite materials at certain compositions with increased ion concentration.

In general, some structural requirements should be satisfied to ensure fast in conduction in inorganic materials. Firstly, as ion migration occurs locally with thermally activated jumps and the jumps need to be connected through the diffusion pathway to allow long range diffusion. The diffusion pathways need to be consisted of well-connected face-sharing polyhedras with suitable bottleneck size, as narrow bottleneck will restrict mobility and too large bottleneck will also impair diffusion. In fast ion conductors, mobile ions possess high diffusivity and rapidly migrate within the lattice, which in turns suggests that they are well-distributed over the diffusion pathways. From a crystallographic point of view, this means that mobile ions partially occupy the available sites within the pathway and adopt good connectivity that sustains fast diffusion. However, whether mobile ion site disorder drives high conductivity, or the latter leads to a disordered mobile ion sublattice remains unclear. It is obvious that to achieve high conductivity, a disordered mobile ion sublattice is required. Secondly, a balanced vacancy and interstitial concentration is required. As with low defect concentration, a defect formation step is necessary for ion diffusion which significantly increases the overall activation energy. Thirdly, the anion sub-lattice arrangements are also important for ion diffusion. Ceder's group has proposed that body-centered cubic-like anion framework allows Li ions migrate within interconnected tetrahedral sites with a low activation

energy barrier.[86] Fourthly, high-polarizability anion is advantageous for fast ion mobility.[66, 87] High polarizability of anion sublattice leads to softer bonds which will lower activation energy barrier of the mobile ions.

1.3.4 Comparison of Different Type Inorganic Solid Electrolytes

Even though a high ionic conductivity is a key property for SE materials, other factors, including wide electrochemical stability window, good chemical and electrochemical compatibility with electrode active materials (cathode and anode), excellent thermal and air/moisture stability, good mechanical properties, simple synthesis process, easy integration, environmental friendliness, and low cost are all important for practical applications such as for electrical mobilities.

Oxide SEs exhibit relatively high ionic conductivity ~ 1 $mS.cm^{-1}$ and high oxidative potential, but not stable with Li metal, except garnet. Due to their mechanical rigidness, high temperature sintering or hot-pressing is required to improve grain boundary contact to achieve high total ionic conductivity. To achieve good contact between oxide SEs-CAMs or direct coating oxide SE onto CAM particles also requires high temperature sintering which will induce side reaction between oxide SEs and CAMs.

Sulfide SEs exhibit much higher ionic conductivity (> 10 $mS.cm^{-1}$) which exceeds that of liquid electrolytes. Some sulfide SEs can also form a quasi-stable SEI with Li metal and sustain relatively high current density Li stripping/plating.[88, 89] However, sulfide SEs feature a low oxidative potential (< 2.5 V vs Li^+/Li) as shown in **Figure 1.5**,[90-92] which is not compatible with typical high voltage CAMs such as $LiCoO_2$ and $LiNi_{1-x-y}Mn_xCo_yO_2$. Utilization of sulfide

SEs with high voltage CAMs leads to decomposition of sulfide SEs to form Li ion and electron blocking interfaces that cause increasing interfacial resistance and total cell resistance, thus fast cell capacity fading.[93, 94] Overall, due to their high ionic conductivity and quasi-stable SEI formation with Li metal, sulfide SEs are suitable for the separator layer in ASSBs.

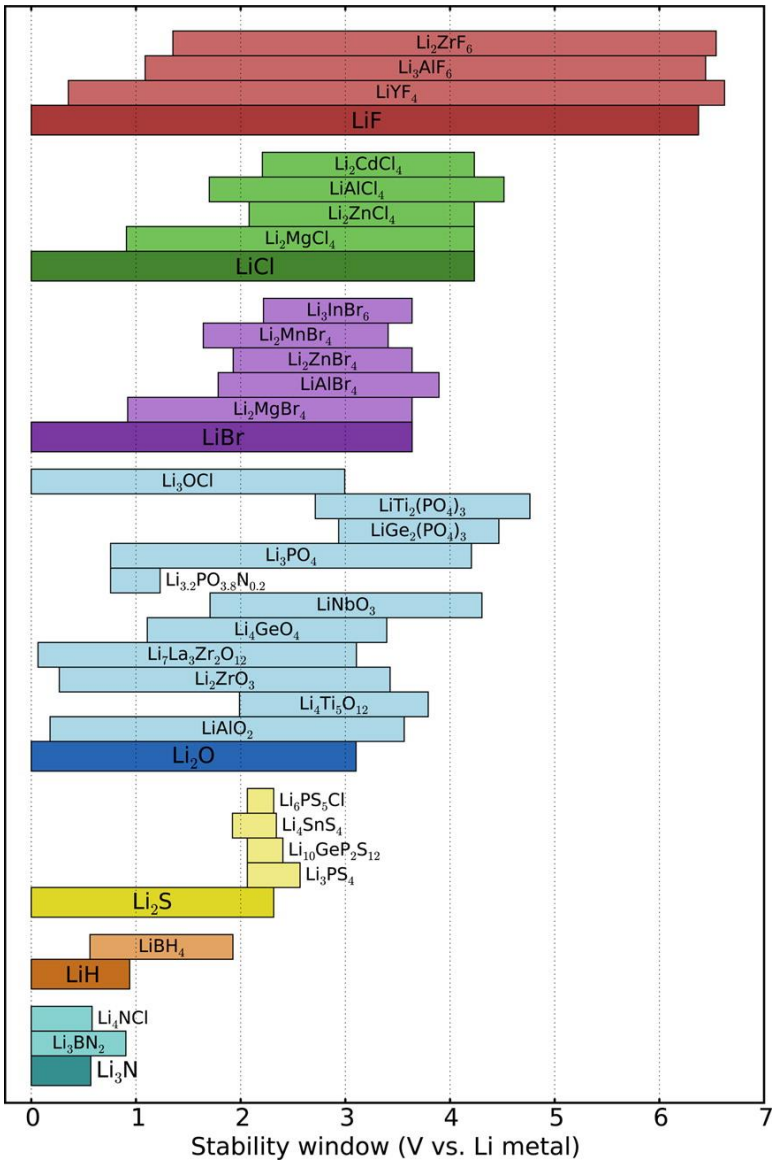

Figure 1.5 The calculated electrochemical stability window of various SE materials. Reproduced with permission from Ref. [92]. Copyright 2015 American Chemical Society.

Chloride SEs exhibit reasonable high Li ion conductivity (10^{-4} - 10^{-3} $S.cm^{-1}$) and high oxidative stability window. Furthermore, the ductile nature of the chloride materials allows good interfacial contact between chloride SEs-CAMs by simply grinding which is essential for ASSB performance. Thus, chloride SEs are suitable for cathode composite.

Heretofore, single SE material which meets all essential requirements for ASSBs has not been developed. Thus, it is necessary to take advantages of each material, a bilayer architecture with sulfide SEs as the separator and chloride SEs for the cathode is ideal for current high voltage ASSBs. Furthermore, a better understanding of Li ion conducting mechanism in inorganic SEs is essential for the discovery of new SE materials which potentially can meet all requirements for ASSBs.

1.3.5 Challenges in All Solid-State Batteries

Besides the above-mentioned issues on lack of SE materials and understanding of ion diffusion in SEs, other challenges including interfacial reactions, limit electrochemical window, contact (mechanical) issues (crack or pulverization), instability towards moisture and CO_2, Li dendrite growth need to be conquered for achieving better ASSB performance and final target of commercialization, as shown in **Figure 1.6**. These challenges are discussed in detail in the following sections.

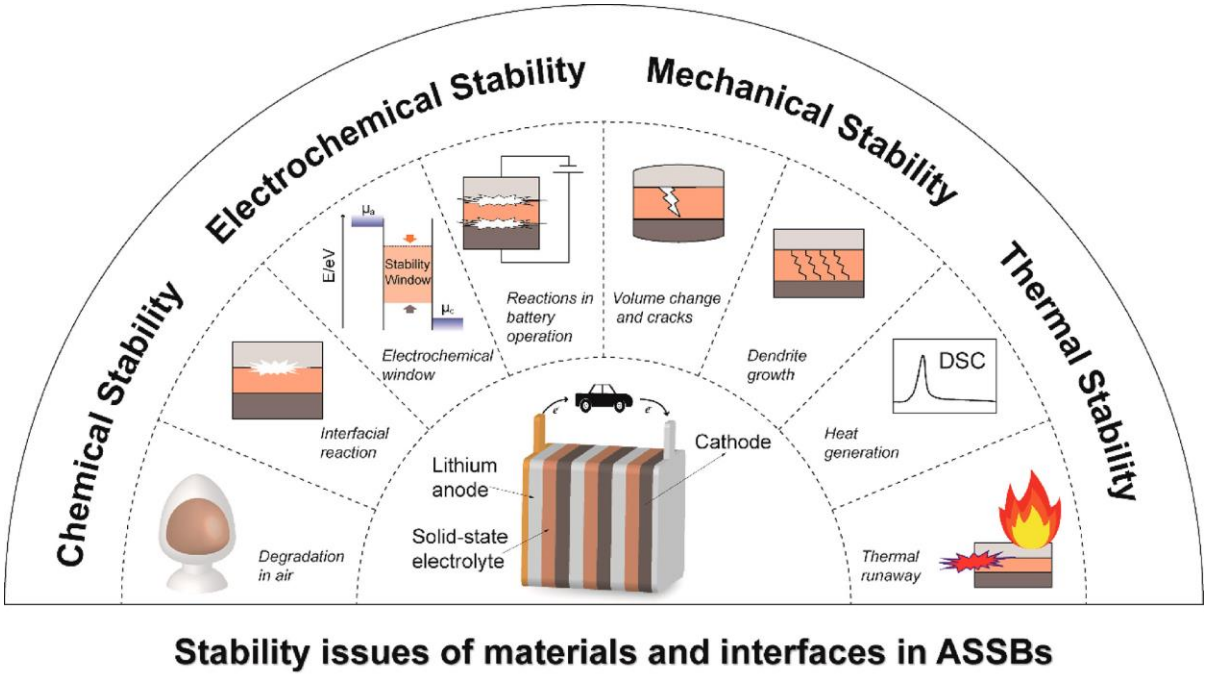

Figure 1.6 Schematic illustration of challenges in ASSBs. Reproduced with permission from Ref. 19. Copyright 2021 American Chemical Society.

Cathode / Solid Electrolyte Interface

The first interface is the cathode/SE interface due to chemical/electrochemical reaction between SEs and high voltage CAMs, especially for sulfide SE materials, due to their low oxidative potential. The spontaneous reactions lead to the formation of transition metal oxide, sulfide, phosphate, sulfate, and other undesirable products on the cathode/SE interface which results in increasing cell internal resistance.[94] The electrochemical decomposition of sulfide SE at high voltage results from the transfer of electrons from sulfide SE to CAMs (or carbon additives), as sulfide SE materials exhibit extremely low ionic conductivity. Thus, the obvious approach to prevent this is to adopt an electronic insulating and Li ion conductive coating layer on CAM particles. Such protective coating materials including $LiNbO_3$, $Li_4Ti_5O_{12}$, $LiTaO_3$, Li_2ZrO_3, Li_3BO_3-Li_2CO_3 have been shown to reduce the interfacial resistance growth.[95-98]

However, these coating materials generally exhibit low ionic conductivity < 10^{-6} S.cm^{-1}, which significantly reduce the cell performance at high current density. Furthermore, forming a thin homogeneous coating layer on the CAM surface is hard to achieve. Typical cathode composite consists of only SE and CAM without the addition of other electronic conducting material such as carbon, as the addition of carbon also leads to the SE decomposition at high potential. Thus, the electronic insulating coating on CAM particles will block the electronic conducting pathway through the contact between CAM particles within the cathode composite. Although, during the initial mixing of CAM and SE, a certain degree of the coating will break which lead to some electronic conducting pathway between CAM particles. The limit electronic conducting and Li ion conducting pathway significantly limit the cell performance especially for high loading cells and high-rate performance. For oxide SEs, even though oxide SEs exhibit high oxidative stability which is compatible with typical high voltage cathode materials. Due to its intrinsic mechanical rigidness nature of oxide materials, simple mixed CAM and oxide SE exhibits poor contact. High temperature sintering to improve the contact will induce side reactions between CAMs and oxide SEs. Furthermore, typical cathode materials suffer from volume change during cycling, which will unavoidably lead to contact loss between SE and cathode material during cycling. Upon continuously cycling, the volume expansion and contraction can cause pulverization of cathode composite which leads to cell failure.

Anode / Solid Electrolyte Interface

As above-mentioned, almost all SE materials are not stable with Li metal, besides garnet LLZO. Oxide and chloride SE materials contain metal cation which can be easily reduced by Li metal. Sulfide SE materials are also not stable with Li metal, but form a quasi-

stable interface, such as for Li_6PS_5Cl, which consists of Li_2S, LiCl, Li_3P.[88] Although garnet is stable with Li metal, garnet LLZO is not stable with moisture and CO_2, which forms Li_2CO_3 and LiOH on the surface. As a result, LLZO is not wetting well by Li metal. Poor physical contact also leads to high interfacial resistance.[99] A lot of work has been done focusing on improving the interfacial stability and lowering the interfacial resistance between garnet and Li metal.

The low Coulombic efficiency and volumetric expansion due to Li dendrite growth is another major challenge for ASSBs. Inorganic SEs with high elastic moduli have been believed to suppress Li dendrite growth. However, multiple groups have reported Li dendrite formation caused short circuits at even low current density.[100-103] Depends on the surface defects such as crack and current density, plated Li infiltrates the cracks and penetrates through grain boundary for polycrystalline material or cracks caused by Li plating which leads to short circuit.[102, 103] Recent work shows Li plating results in the formation of propagating cracks, then Li infiltration.[104] And they also show Li stripping leads to void formation at the interface and accumulate on cycling. During plating, the increased local current density at the interface leads to dendrite formation, short circuits, and cell failure.[89] The critical current density for void formation is pressure dependent, higher pressure leads to higher critical current density.

However, due to the soft nature of lithium metal, higher pressure can directly lead to Li penetration through SE layer.[105]

Thin Solid Electrolyte Separator Layer

Most of the current reported bulk type ceramic ASSBs use simply cold pressed thick SE layers ~ 1 mm as separator which significantly lower the energy density of ASSBs. To increase the energy density of ASSBs, a thin layer of SE (10-20 μm) is necessary.[106-108] The previously reported SE thin layers are typically a composite of inorganic SE, polymer, and maybe Li salt in liquid electrolyte for flexibility.[109-113] However, such a thin SE layer cannot sustain high current density Li stripping/plating due to dendrite formation. Further understanding on the defect generation process during Li stripping/plating with a thin SE layer is needed or a protected Li metal anode is necessary to be compatible with such thin film SEs to suppress Li dendrite formation and growth. Finding an environmental-friendly thin film processing method with proper inorganic SE and polymer and potentially Li salt with liquid electrolyte to suppress Li dendrite is another major challenge facing the commercialization of ASSBs.

Mechanical Failure

The volume change from CAMs and Li metal anode during cycling will unavoidably lead to contact loss between SE/CAM and void formation at the anode interface. One obvious method to suppress this problem is to apply high pressure during cell cycling. However, high pressure can lead to Li penetration and thus cell short circuit. Thus, it is also essential to explore

new CAMs which exhibit minor volume change during Li extraction and insertion and other high specific capacity anode materials which can sustain high pressure.

1.4 Summary

ASSBs utilizing Li metal anode have the potential to enable improved cell performance, safety, potentially lower cost compared to conventional LIBs, which are critical for electric vehicle applications. In spite of these inimitable advantages, there is still a long way for the practical application of ASSBs. The above-mentioned challenging facing ASSBs includes the sluggish Li ion diffusion in SEs and active material / SE interfaces; continuously interface growth at cathode and anode interface; limit electrochemical window; contact issues; instability at ambient condition.

SEs with ultra-high ionic conductivity (*i.e.* superionic conductors, > 10 $mS.cm^{-1}$ at room temperature) are the key component of ASSBs necessary to achieve fast charging-discharging and high energy densities.[114] Such high ionic conductivity is needed to enable thick electrode configurations with high CAM loading, allowing for good percolation and ionic transport in composite electrodes.[114, 115] Thus, it is essential to focus on the discovery and design of new SE materials which fulfill the requirements for ASSBs. Single material fulfills all the requirements is hard but developing materials for each part of ASSBs including cathode composite, separator layer, and anode is possible. With the discovery of new SE materials, it is also important to gain a better understanding of the Li ion diffusion mechanism in inorganic SEs to provide guidance for the future development of new SE materials. Understanding the interface growth at cathode and anode interface is also essential to improve cell performance, especially for high current density and high loading cells. The continuous Li ion blocking

interface formation caused by the limit chemical and electrochemical stability can lead to significantly increased cell internal resistance, thus fast discharge capacity fading. Either finding SE materials which are chemical and electrochemical stable towards electrode materials or a thin cathode coating and artificial SEI on Li metal is essential for improving cell performance.

The mechanical problem caused by the volume change of CAMs and Li metal requires further exploration of cathode active materials which exhibit minor volume change during Li extraction/insertion, new anode architecture which can sustain Li volume change, and potentially other high-capacity anode materials such as silicon. Since silicon possesses high rigidness, ASSBs combining Si anode with typical cathode materials which suffer from volume changes can suppress the mechanical failure by applying high pressure during cycling.

1.5 Scope of the Thesis

This thesis presents a thorough investigation on the synthesis, characterization, electrochemical performance of novel Li fast ion conductors and understanding the fundamental structure - ionic transport relationships in ionic conductors, and developing high energy density and long-lasting ASSBs, and understanding the critical requirements for ASSBs operations.

Chapter 1 gives a general introduction and overview of pertinent research that has been conducted in the past decades on Li ion conductors and ASSBs. Parts of this chapter have been published as: L. Zhou, N. Minafra, W. G. Zeier, L. F. Nazar, Innovative approaches to Li- Argyrodite solid electrolytes for all-solid-state lithium batteries. *Acc. Chem. Res.*, **2021**,

54, 2717-2728, Copyright © 2021 American Chemical Society, reproduced with permission from American Chemical Society.

Chapter 2 describes the research experimental methods and characterization techniques that are employed in this thesis. Parts of this chapter have been published as my master thesis: L. Zhou, Synthesis and Characterization of New Solid-State Li-Superionic Conductors. *UWSpace*, **2017**, http://hdl.handle.net/10012/12617, reproduced with permission from UWSpace.

Chapter 3 reports a family of lithium fast ion conductors, $Li_{3+x}Si_xP_{1-x}S_4$, that exhibit an entropically stabilized structure type in a solid solution regime ($0.15 < x < 0.33$) with high ionic conductivity above 1 $mS.cm^{-1}$. Exploration of the influence of aliovalent substitution in the thermodynamically unstable β-Li_3PS_4 lattice using a combination of single crystal X-ray and powder neutron diffraction, the maximum entropy method, and impedance spectroscopy reveals that substitution induces structural splitting of the localized Li sites, effectively stabilizing bulk β-Li_3PS_4 structure at room temperature and delocalizing Li ion density. The optimal material, $Li_{3.25}Si_{0.25}P_{0.75}S_4$, exhibits inherent entropic Li site disorder and a frustrated energy landscape, resulting in a high ionic conductivity of 1.22 $mS.cm^{-1}$ that represents three orders of magnitude increase compared to bulk β-Li_3PS_4 and one order of magnitude higher than the nanoporous β-Li_3PS_4. The enhanced Li ion conduction and lowered activation barrier with increasing Li site disorder as a result of aliovalent 'tuning' reveal an important strategy toward the design of fast ion conductors that are vital as SEs. The work has been published as: L. Zhou, A. Assoud, A. Shyamsunder, A. Huq, Q. Zhang, P. Hartmann, J. Kulisch, L. F. Nazar, An entropically stabilized fast-ion conductor: $Li_{3.25}[Si_{0.25}P_{0.75}]S_4$. *Chem. Mater.*, **2019**, 31,

7801-7811, Copyright © 2019 American Chemical Society, reproduced with permission from American Chemical Society.

Chapter 4 shows a new family of argyrodite lithium superionic conductors, as solid solutions $Li_{6+x}M_xSb_{1-x}S_5I$ (M = Si, Ge, Sn), that exhibit superionic conductivity. These represent the first thioantimonate argyrodites to date. Exploration of the series using a combination of single crystal X-ray and synchrotron/neutron powder diffraction, combined with impedance spectroscopy, reveals that an optimal degree of substitution (x), and substituent induces slight S^{2-}/I^- anion site disorder - but more importantly drives Li cation site disorder. The additional, delocalized Li ion density located in the new high energy lattice sites serves as intermediate interstitial positions for Li ion diffusion and activates concerted ion migration, leading to a low activation energy of 0.25 eV. Excellent room temperature ionic conductivity of 24 $mS.cm^{-1}$ is achieved among the highest values reported to date. This enables prototype ASSBs that exhibit promising properties. Furthermore, even at -78 °C, a suitable bulk ionic conductivity of the SE is retained (0.25 $mS.cm^{-1}$). Selected thioantimonate iodides also demonstrate good compatibility with Li metal, sustaining over 1000 h of Li stripping/plating at current densities up to 0.6 $mA.cm^{-2}$. The significantly enhanced Li ion conduction and lowered activation energy barrier with increasing Li site disorder represents an important strategy toward the development of superionic conductors. The work has been published as: L. Zhou, A. Assoud, Q. Zhang, X. Wu, L. F. Nazar, New family of argyrodite thioantimonate lithium superionic conductors. *J. Am. Chem. Soc.*, **2019**, 141, 19002-19013,

Chapter 5 shows a new chloride Li fast ion conductor, $Li_2Sc_{2/3}Cl_4$, that crystallizes in a disordered spinel structure, and exhibits an ionic conductivity of 1.5 $mS.cm^{-1}$ with a low activation energy barrier of 0.34 eV for Li ion diffusion. Structural elucidation *via* powder neutron diffraction reveals a significantly disordered Li ion distribution over available tetrahedral and octahedral sites within the lattice, forming an infinitely 3D connected Li ion diffusion pathway comprised of face-sharing octahedra and tetrahedra. Due to the high oxidative stability of $Li_2Sc_{2/3}Cl_4$, ASSBs employing $Li_2Sc_{2/3}Cl_4$ and high voltage cathodes ($LiCoO_2$, NMC622, or NMC85) without any coating - exhibit excellent electrochemical performance up to 4.6 V in terms of capacity retention and cycle life. The work has been published as: L. Zhou, C. Y. Kwok, A. Shyamsunder, Q. Zhang, X. Wu, L. F. Nazar, A new halospinel superionic conductor for high voltage all solid state lithium batteries. *Energy Environ. Sci.*, **2020**, 13, 2056-2063,

Chapter 6 presents a new family of soft lithium mixed-metal chlorospinel, $Li_2In_xSc_{0.666-x}Cl_4$ ($0 < x \leq 0.666$), with high ionic conductivity (up to 2.0 $mS.cm^{-1}$) owing to a very disordered Li ion distribution and ASSBs with exceptional electrochemical performance. They exhibit excellent interfacial stability against un-coated high voltage cathode materials (up to 4.8 V vs Li^+/Li). As a result, catholyte-engineered ASSBs utilizing NMC622 or NMC85 as cathode materials exhibit superior rate capability and long-term cycling (up to 4.8 V vs Li^+/Li) compared to state-of-the-art ASSBs. The NMC85 ASSB exhibits an exceptionally long

life - > 3000 cycles - with 80 % capacity retention at room temperature, and high cathode loadings provide stable capacity retention of > 4 $mAh.cm^{-2}$ (~ 190 $mAh.g^{-1}$). The work is current under review: L. Zhou, C. Y. Kwok, S. Kim, A. Assoud, Q. Zhang, L. F. Nazar, High-areal capacity, long cycle-life 4 V ceramic all solid-state Li batteries. *Nat. Energy* **2021**, in press.

The final chapter summarizes the work of the entire thesis and proposes potential further directions of the Li ion conducting SEs and ASSBs.

Chapter 2. Methods and Techniques

2.1 Solid Electrolyte Synthesis

SEs in this thesis are synthesized through the traditional solid state synthesis method. Solid state synthesis consists of two steps: mixing of precursors and then pressing into pellets, followed by heat treatment. At high temperatures, the thermal energy drives atoms to rearrange themselves to form the most thermodynamically stable products. Since simple hand grounding only provides limited contact between different precursors, thus the number of nucleation sites for final products is low. As a result, solid state synthesis usually requires a long time sintering to achieve phase-pure final products. Since both sulfide and chloride materials in this thesis are moisture sensitive, the mixed precursor pellets are sealed in quartz tubes under vacuum to avoid any reaction with moisture. For sulfide materials, a glassy carbon crucible is used to avoid reactions between sulfides and quartz tubes at high temperatures. All processing steps are conducted in Argon glovebox with low oxygen and moisture level (< 0.5 ppm).

2.2 Diffraction Techniques

2.2.1 Lab and Synchrotron Powder X-ray Diffraction

Powder X-ray diffraction is the most commonly used technique to identify phase composition and analyze crystal structure. X-ray with wavelength 0.01 - 10 nm can be diffracted by the repeated atom planes, as it is in the same range as the atomic distance in a crystal. Bragg's law is used to explain the appearance of a unique diffraction pattern which identifies a specific structure, as shown in **Equation 2.1**:

$$n\lambda = 2d \cdot \sin\Theta \qquad \textbf{Equation 2.1}$$

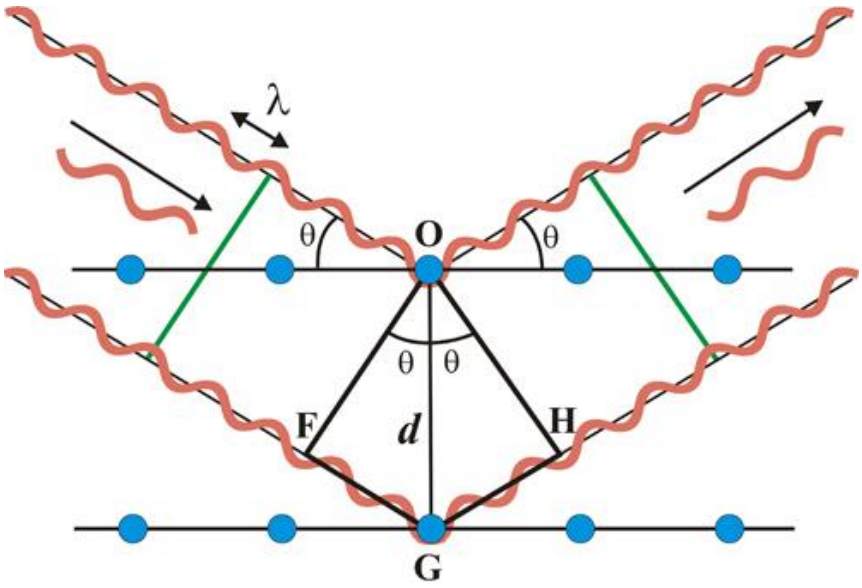

Figure 2.1 Schematic of Bragg's law, Reproduced from Ref. [116]. CC BY-NC 4.0.

where Θ is the angle between the incident X-ray beam and the respective imaginary parallel planes, λ is the X-ray wavelength, and *d* represents the distance between crystallographic planes, as shown in **Figure 2.1**. The basic idea is that X-ray beams scattered from successive planes in the crystal will travel distance differing by exactly one wavelength (for the case of *n*=1). At the angle Θ, X-rays scattered from successive planes will interact constructively when they eventually reach the X-ray detector. As powder sample contains millions of single crystals that are oriented differently, diffraction beams are going towards all the directions obeying Bragg's law which results in the diffraction pattern. As X-ay is scattered by electron clouds around the atoms, the intensity of the diffraction beam directly correlates to the number and position of electrons. The intensity of the peaks is related to the structure factor (*F*) *via* the following **Equation 2.2**:

$$I = A \cdot F^2 \qquad \textbf{Equation 2.2}$$

Where *A* includes other factors such as polarization, absorption, and temperature. Thus, the XRD pattern can be used to evaluate the crystal structure information.

Lab XRD patterns in this thesis were collected using a PANalytical Empyrean with PIXcel^{3D} detector operating at 45 kV and 40 mA with Cu K*a* (λ = 1.5405 Å) radiation. Air sensitive samples were applied on a silicon zero background holder and a protective Kapton film was sealed with vacuum grease on the top to allow X-ray penetration, while avoiding exposure to air and moisture during measurement. For overnight scans, the powder samples were packed into glass capillary tubes (0.3 or 0.5 mm diameter) sealed under Argon atmosphere with an acetylene oxygen torch. In this thesis, the Bragg-Brentano geometry (**Figure 2.2a**) was used for the short scans, long scans were conducted in Debye-Scherrer geometry (**Figure 2.2b**).

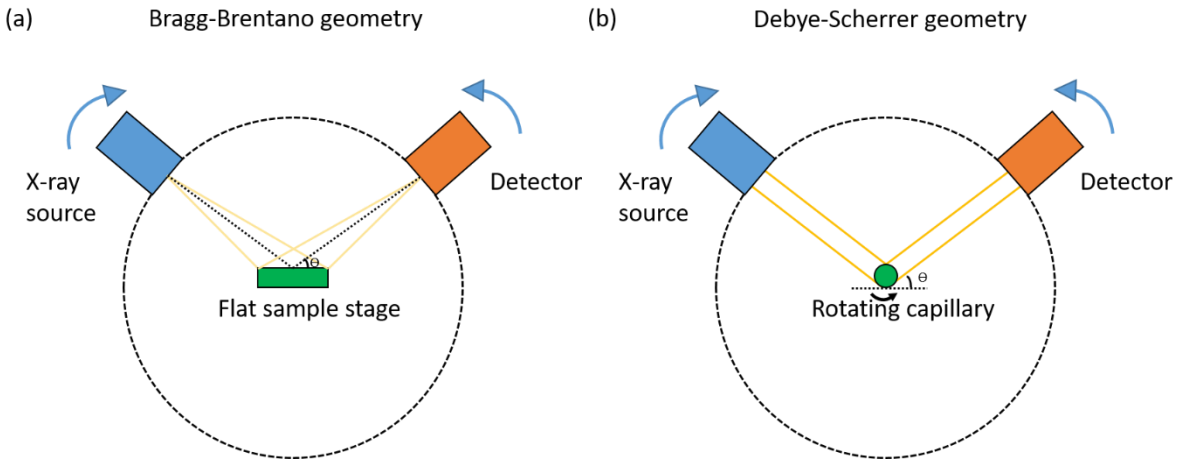

Figure 2.2 Schematic diagram of (a) Bragg-Brentano and (b) Debye-Scherrer geometries.

Synchrotron X-ray is produced from forcing high energy accelerated electrons to travel in a curved path by a magnetic field. This results in a more intensity, tunable energy

(wavelength) X-ray compared to laboratory X-ray which was generated by the photoelectron effect of a metal target hit by electrons. Thus, synchrotron XRD offers a better resolution, signal-to-noise ratio, and a more well-defined peak shape. Synchrotron XRD patterns in this thesis were collected on the Canadian Macromolecular Crystallography Facility beamline at the Canadian Light Source. The samples were sealed in 0.5 mm glass capillaries under Argon atmosphere and data were collected at a wavelength of an energy 18 keV (0.68916 Å). Refinement of the XRD patterns was performed by using the software of GSAS II[117].

2.2.2 Time-of-Flight Power Neutron Diffraction

As the beam of neutrons also has the wave character, it can be diffracted by atomic planes in crystals, following Bragg's Law. Since X-ray is scattered by the electron clouds around the atoms, it is not sensitive to light atoms, such as Li. Unlike X-ray, neutron interacts with the nucleus instead of electrons. The contribution to the diffracted intensity and scattering length of neutron diffraction varies from isotope to isotope, rather than linearly with the atomic number for X-ray. Typically light atoms contribute strongly to the diffracted intensity. Thus, neutron powder diffraction is essential to accurately determine the site and occupancy of light atoms, such as Li in this thesis.

Instead of fixing λ and changing Θ in XRD or constant wavelength neutron diffraction, various wavelengths neutron with fixed diffraction beam angle is applied to sample in time-of-flight neutron diffraction (TOF-ND). By fixing the initial and final position of neutrons and measuring the time that the neutron is detected, the time (t) of neutrons travel a fixed path length (L) gives its velocity (v = L / t). Based on the de Broglie equation ($\lambda = h / mv$) where h is Planck's constant and m is the mass of neutron, combining with Bragg's law gives:

$$\lambda = ht / mL = 2d \cdot \sin\Theta \qquad \textbf{Equation 2.3}$$

Thus, *d* spacing is proportional to time. The resolution and signal-to-noise ratio of ToF-ND can be optimized by changing the scattering angle.

The ToF-ND patterns in this thesis were carried in POWGEN beamline at Oak Ridge National Laboratory. Refinement of the ToF-ND patterns was performed by using the software of TOPAS6.

2.2.3 Single Crystal X-Ray Diffraction

Since the neutron beamtime is often unavailable or requires a long waiting time before proposals get approved, single crystal X-ray diffraction is initially used to solve crystal structures in this thesis. Unlike powder XRD which is a bulk characterization technique provides additional information about the samples, such as crystallinity, single crystal X-ray diffraction just provides crystal structure and is the most common way to precise resolve crystal structure.

The single crystal diffraction in this thesis was carried out using Bruker APEX II diffractometer equipped with a SMART APEX II CCD, utilizing graphite-monochromated Mo-Kα radiation (0.71073 Å). The crystal was protected by Paratone-N oil and a liquid nitrogen flow using an OXFORD Cryostream controller 700 at the desired temperature (< 300 K) to ensure no reaction of the materials with moisture occurred. The data were collected by scanning ω in a few groups of frames at different ϕ and an exposure time per frame. The data were corrected for Lorentz and polarization effects. Absorption correction was carried out using the empirical multi-scan method SADABS part of Bruker suite. Cell_now software was

used to check for potential twinning and indexing the unit cell reflections with I/sigma below 5 to check for a possible supercell. The structure was solved by direct method to locate the atom positions. These positions were then anisotropically refined using the least-squares method incorporated in the SHELXTL package. The program Tidy was used to standardize the atomic positions.

2.3 Scanning Electron Microscopy and Energy Dispersive X-ray Spectroscopy

Scanning Electron Microscopy (SEM) is used to visualize the micro/nanostructural morphology and the distribution of elements on the surface of a solid sample. In a typical SEM, a focused primary electron beam with an energy ranging from 0.2 keV to 40 keV hits the specimen surface, thus generating secondary electrons, backscattered electrons, transmitted electrons, and characteristic X-rays (fluorescence), as shown in **Figure 2.3**. They are detected by specialized detectors. Due to the repeated random scattering and absorption of primary electrons, their interaction with sample atoms only occurs within a certain depth which forms a teardrop shape (**Figure 2.3a**). A few interactions would take place together. Loosely bond electrons are ejected by collisions with incoming electrons and form secondary electrons. Their energies are typically low, so they only occur near the surface of the specimen (~ 10 nm depth) and the deeper ones are absorbed on their way out. Meanwhile, the incident electrons are elastically scattered by the specimen, which are called backscattered electrons (BSE). Heavier elements scatter more strongly than lighter ones. Thus, the BSE provides information about the atomic number and phase difference. With much larger energies than secondary electrons, deeper BSE (1~3μm depth) can also be detected. However, the spatial resolution of the BSE images is worse, due to the teardrop shape of the interaction volume. When a secondary

electron is generated, a shell electron with relatively low binding energy is excited and leaves an empty electron site behind. Consequently, one electron from the outer shell will jump into the low energy empty site with the excessive energy released by emitting X-ray. The energy of the X-ray depends on the orbital energies involved and thus that is used for identifying elements for energy dispersive X-ray spectroscopy (EDX).

SEM images and EDX measurement in this thesis were carried out on a Zeiss Ultra Plus field emission SEM equipped with an EDX detector.

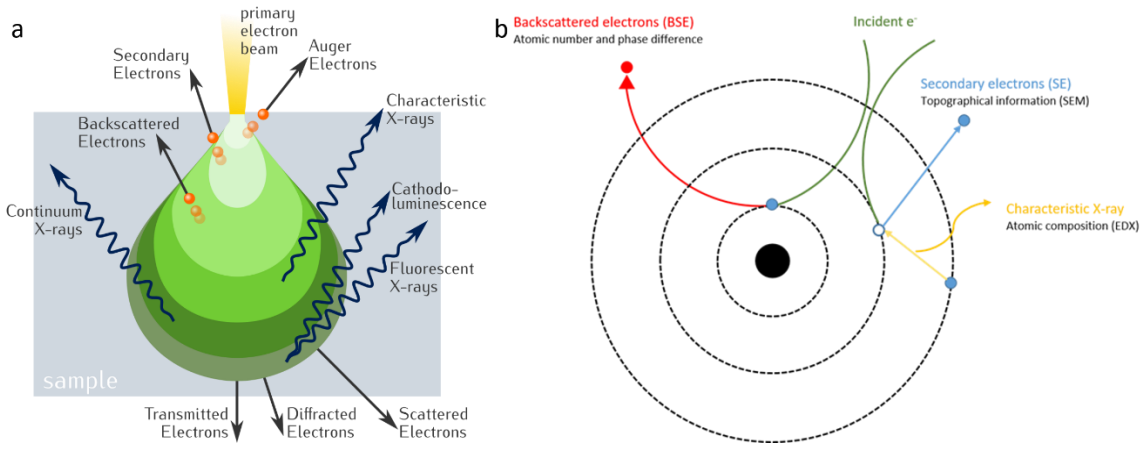

Figure 2.3 Schematic diagram of (a) teardrop shape of the interaction volume in SEM, Reproduced from Ref. [118]. CC BY-SA 4.0. and (b) different types of interaction between the incident electron beam and specimen.

2.4 Electrochemical Techniques

2.4.1 Electrochemical Impedance Spectroscopy

Impedance is a measurement of the circuit characteristic to impede the flow of electrons through the circuit. Electrochemical impedance measurements are normally conducted by applying an AC potential to an electrochemical cell and measuring the responding current through the cell over a wide frequency range. Assume that a sinusoidal potential excitation is applied, the response to this potential is an AC current which can be analyzed as a sinusoid at

the same frequency but shifted in phase. The excitation potential is usually small to ensure the cell's response is pseudo-linear. The expression of the impedance Z(ω) is presented in **Equation 2.3**.

$$Z(\omega) = E / I = Z_0 \exp(j\,\phi) = Z_0(\cos\phi + j \sin\phi) \qquad \textbf{Equation 2.3}$$

Where ω represents the radial frequency, ϕ is the shift in phase, $j = \sqrt{1}$, and Z_0 is the amplitude of the impedance.

The expression of Z(ω) is composed of a real ($Z_0\cos\phi$) and an imaginary part ($Z_0\sin\phi$). Among various ways to present the data, the Nyquist plot is commonly used in the battery field by plotting the real part on X-axis and the imaginary part on Y-axis. The Nyquist plot usually consists of single or multiple semicircles at high frequencies (charge transfer process), followed by an inclined line at low frequencies (diffusion limit).

For the impedance measurements on a SE, three semicircles correspond to resistance and capacitance of the bulk, the grain boundary resistance of the electrolyte, and the electrolyte/current collector interface will appear on the high frequencies and normally they form a single semicircle at room temperature. The total impedance of the SE is the sum of the abovementioned three semicircles resistance. And the straight line at low frequencies corresponds to diffusion limit at electrode/SE interfaces. For SEs with high ionic conductivity, the semicircle is normally not well defined or not observed in the measurements, the resistance value can be extrapolation of the linear part to the X-axis. The corresponding ionic conductivity can be obtained following **Equation 2.4**:

$$\sigma = d / \pi r^2 R \qquad \text{Equation } \textbf{2.4}$$

where d is the thickness of the SE pellet and r is the radius of the SE pellet, R is the resistance from EIS measurement. The ionic conductivity and temperature are related by the Arrhenius equation:

$$\sigma = A \exp(-E_a / RT) \qquad \textbf{Equation 2.5}$$

where A is the pre-exponential factor, E_a is the activation energy for ion diffusion, R is the ideal gas constant and T is the temperature in Kelvin. Plotting ln (σT) *vs* 1/T gives the activation energy for Li ion diffusion. Thus, EIS measurements on SEs are conducted over the temperature range 25 ^{o}C to 60 ^{o}C to derive activation energy.

The impedance measurements on ASSBs at different states of charge/discharge or different cycles can be conducted to monitor interfacial resistance growth during cell cycling. Semicircles observed can be attributed to bulk ionic conductivity of SE/electrode materials, cathode/SE, and anode/SE interfaces.

In this thesis, EIS measurements were performed on VMP3 potentiostat/galvanostat station with EIS capabilities (Bio-Logic Science Instruments). For SE EIS measurements, typically, 100 - 300 mg of the SE powder was placed between two Ti rods and pressed into a 10 mm diameter pellet by a hydraulic press at 3 tons for 3 min in an Argon glovebox. EIS experiments were performed with 100 mV constant voltage within a frequency range of 1 MHz - 100 mHz. For activation energy measurements, 100 - 300 mg of the SE powder was placed between two Ti rods and pressed into a 10 mm diameter pellet by a hydraulic press at 3 tons for 3 min in a custom-made Swagelok cell, and the pellet was placed between two indium foils in order to maintain a good interface as the temperature varies or the cell was placed in a special

cage which maintains the high applied pressure. The impedance was measured from 35 MHz - 100 mHz at temperatures ranging from 30 to 60 °C. Low temperature EIS measurements were conducted at -78 °C by placing the cell in a cooling bath (dry ice + acetone) for about half an hour or until the temperature fully stabilized, and impedance measurements were then conducted from 35 MHz to 100 mHz with 100 mV constant voltage using the MTZ-35 impedance analyzer (Bio-Logic Science Instruments).

2.4.2 Linear Sweep Voltammetry

Linear sweep voltammetry (LSV) is a potentiodynamic technique where the potential is swept at a constant scan rate. The potential is swept only in one direction in order to study one reaction. It is used in this thesis to study the oxidative potential window of SEs. LSV was performed with a two-electrode cell setup consisting of a working electrode and Li-In alloy as the counter and reference electrode. The cathode is a mixture of SE and carbon (Super P). Since SE is electronic insulating, carbon is added to improve the electronic percolation within the cathode composite. The experiments were conducted with VMP3 potentiostat/galvanostat station (Bio-Logic Science Instruments).

2.4.3 Galvanostatic Charge/Discharge

Galvanostatic cycling is a typical electrochemical cycling method where a constant current is applied to a cell until a certain amount of charge has been passed or reaching a cut-off voltage. Typically, negative current forces discharge a cell and positive current forces charge a cell.

Galvanostatic cycling is usually used to study the specific capacity, rate capability, capacity retention, and cycle life of an electrode active material. By applying a constant current, the electrode (active materials) is oxidized/reduced with cation de/insertion. The corresponding voltage response could be either a linear increase/decrease with respect to capacity, which corresponds to a solid solution de/insertion mechanism, or a flat plateau which results from a two-phase reaction. Approaching the capacity limit will lead to a dramatically faster voltage increase/decrease. The current applied for cycling is defined by "C-rate". The "C" is related to the specific capacity (Q) of the materials which is related to the molar mass (M_w) of the compound and can be calculated from:

$$Q = nF / 3.6M_w \quad (mAh/g) \qquad \textbf{Equation 2.6}$$

where F is the Faraday's constant, n is the number of electrons transferred. 1C rate means charging and discharging the cell in one hour, respectively. C/x rate means charging and discharging the cell in x hours, respectively.

The electrochemical cycling in this thesis was carried out with two electrodes configuration. The cell consists of a cathode (cathode active material mixed with SE) and an anode (typically Li-In alloy) which is separated by a layer of SE. The measurements were carried out using VMP3 potentiostat/galvanostat station (Bio-Logic Science Instruments) at a specific C-rate and proper voltage window.

Chapter 3. An Entropically Stabilized Fast Ion Conductor: $Li_{3.25}Si_{0.25}P_{0.75}S_4$

3.1 Introduction

Among the above-mentioned thiophosphates (**Section 1.3.2.2**), Li_3PS_4 and its derivatives are one of the first reported sulfide SEs with high ionic conductivity. Stabilization of the high-temperature conductive β-Li_3PS_4 structure at room temperature attracts great attention. The efforts were devoted to the substitution of various elements in the Li_3PS_4 structure, to achieve high room temperature conductivity. As far back as 2002, Kanno *et al* reported on partial replacement of P^{5+} with Ge^{4+} to form $Li_{3+x}Ge_xP_{1-x}S_4$, where the composition at $Li_{3.25}Ge_{0.25}P_{0.75}S_4$, showed the highest ionic conductivity (σ = 2.2 mS.cm^{-1}).[55] Kawamoto *et al* reported thio-LISICON $Li_{3+x}Si_xP_{1-x}S_4$ with maximum ionic conductivity of 0.64 mS.cm^{-1} at x = 0.4.[58] In both papers, the crystal structures of the Ge and Si substituted phases were indexed to a superlattice of the corresponding parent monoclinic Li_4SiS_4 phase and orthorhombic Li_4GeS_4 phase, although no structural data were reported. An 'orthorhombic modification' of $Li_{3+x}Si_xP_{1-x}S_4$ was also alluded by Lotsch *et al*, but no details were provided on lattice parameters, structure, or conductivity.[60]

Herein, we report on a family of orthorhombic $Li_{3+x}Si_xP_{1-x}S_4$ compositions. Using a combination of direct method structure solution allowed by single crystal X-ray diffraction, combined with powder neutron diffraction and the maximum entropy method (MEM) that reveals pathways for lithium transport, we identify the fundamental structural changes created by the incorporation of Si and Li into the lattice. Effectively, this stabilizes the β-Li_3PS_4 structure at room temperature, but one in which importantly significant Li site disorder is induced. We correlate this to the changes in Li site energy and the Li ion diffusion energy

landscape. With increasing (Li^+ + Si^{4+}) content (x) in $Li_{3+x}Si_xP_{1-x}S_4$ over a limited compositional range ($0.25 \leq x \leq 0.50$), the three independent sites that Li occupies each are split in two, positioned about 1 Å apart. The Li ion disorder over these split sites leads to a frustrated energy landscape and partial vacancies, as Li ions can occupy either site, but not simultaneously. The Li site disorder is experimentally correlated to a decrease in activation energy for Li ion transport. The highest room temperature conductivity of 1.22 $mS.cm^{-1}$ is achieved for $Li_{3.25}Si_{0.25}P_{0.75}S_4$, which represents an order of magnitude increase compared to the nanoporous β-Li_3PS_4, and three orders higher than the extrapolated value of the bulk β-Li_3PS_4. With higher (Li^+ + Si^{4+}) content, the Li site splitting partly disappears, accompanied by a decrease in conductivity. Owing to its extensive site disorder, it is an example of an entropically stabilized chalcogenide, akin to entropically stabilized oxides.[119] This work proves that deliberately inducing disorder in materials to generate frustrated energy landscapes in SEs is a fruitful strategy to enhance ionic conductivity.

Dr. Abdeljalil Assoud performed the single crystal X-ray diffraction and structural resolution. Abhinandan Shyamsunder performed the MAS NMR measurements. Dr. Ashfia Huq and Qiang Zhang performed the powder neutron diffraction measurements.

3.2 Experimental Approaches

3.2.1 Material Synthesis

Li_2S (99.98%, Sigma-Aldrich), P_2S_5 (99%, Sigma-Aldrich), Si (99%, Sigma-Aldrich), and sulfur (99.5%, Sigma-Aldrich) were mixed together in a mortar at the targeted ratio, and 5 wt % excess sulfur was added to fully oxidize the Si. The mixture was pelletized and placed

in a glassy-carbon crucible in a sealed quartz tube under vacuum. The sample was heated to 750 °C, slowly cooled to 725 °C over the period of 18 h, and then cooled to room temperature with a ramp rate of 5 °C.min^{-1}. The final product was gently separated to find single crystals suitable for single crystal X-ray diffraction. The remaining crystals, or those from subsequent synthesis preparation, were crushed into a polycrystalline powder for powder X-ray diffraction to check their purity and also for neutron diffraction, NMR, and impedance spectroscopy analysis.

3.2.2 Single Crystal Diffraction and Structure Resolution

Several colorless plate-shaped single crystals of $Li_{3.15}Si_{0.15}P_{0.85}S_4$, $Li_{3.25}Si_{0.25}P_{0.75}S_4$, $Li_{3.33}Si_{0.33}P_{0.67}S_4$, $Li_{3.5}Si_{0.5}P_{0.5}S_4$, $Li_{3.67}Si_{0.67}P_{0.33}S_4$, and $Li_{3.8}Si_{0.8}P_{0.2}S_4$ with dimensions of approximately 0.150 × 0.080 × 0.020 mm^3 were scanned to determine their quality. Multiple data sets were collected for each composition and gave exactly the same results. The data were collected at 280 or 180 K by scanning ω and φ of 0.3° or 0.5° in a couple of groups of frames at different ω and φ and an exposure time of 30 or 60 s per frame. The structure was solved using direct methods to locate the positions of P/Si1, S1, S2, and S3 atoms. First, these 4 positions were anisotropically refined using the least-squares method incorporated in the SHELXTL package, and then the Li positions were located in the remaining electron density in the Fourier map, which revealed Li-S bonds very similar in nature to those found in binary and ternary Li sulfides. Subsequently, the Li site occupancies were freely and anisotropically refined. Since it is difficult to distinguish between P and Si using X-ray scattering and the powder data revealed phase-pure samples, the P/Si ratio was fixed to the target stoichiometry.

3.2.3 Neutron Diffraction

The ToF powder neutron diffraction pattern of $Li_{3.25}Si_{0.25}P_{0.75}S_4$ was measured at 300 and 180 K, and a single bank wave with center wavelengths of 2.665 Å was used. With the structure factors obtained from Rietveld refinements, the nuclear densities were analyzed by the Maximum Entropy Method (MEM). Since only lithium possesses a negative scattering length in $Li_{3.25}Si_{0.25}P_{0.75}S_4$ (b_{Li} = -1.9 fm), the nuclear density map is limited to the negative part only. Reconstruction of the three-dimensional (3D) nuclear density map using the MEM was performed using Dysnomia software[120] which visualizes the Li nuclear density and provides Li-ion diffusion pathways in $Li_{3.25}Si_{0.25}P_{0.75}S_4$.

3.2.4 Nuclear Magnetic Resonance Spectroscopy: Solid State MAS ^{29}Si and ^{31}P

Samples were filled in a 4 mm zirconia rotor inside the glovebox with a loading of approximately 80 mg. ^{31}P MAS NMR measurements were obtained at 11.7 T and 295 K on a Bruker Avance 500 MHz spectrometer operating at 202 MHz at spinning rates of both 5 kHz and 6 kHz to determine the spinning side bands. The spectra were referenced using an external sample of solid ammonium dihydrogen phosphate which has an isotropic ^{31}P chemical shift of δ = +0.81 ppm. ^{29}Si MAS NMR measurements were obtained using the same instrument operating at 100 MHz at a spinning rate of 6 kHz. The spectra were referenced to tetramethyl silane (δ = 0 ppm).

3.2.5 Bond Valence Site Energy (BVSE) Calculations

BVSE calculations were performed with the SoftBV program,[121] using the single crystal structural model as input and the SoftBV bond valence parameter set[122] developed by S. Adams. In this approach, Li-ion site energies are calculated for a dense grid of points with

a resolution of 0.1 Å covering the crystal structure using the transferable Morse-type softBV force field. Li-ion diffusion pathways are identified with the regions of low bond valence site energy. BVSE maps with isosurface levels 0.54 eV over global minimum are shown which provide an indication of Li-ion diffusion pathways. The reported nanoporous β-Li_3PS_4 structure determined from powder neutron diffraction was used as the input structure for the BVSE calculations.[123]

3.3 Structural Characterization: $Li_{3.25}Si_{0.25}P_{0.75}S_4$

3.3.1 Single Crystal X-Ray Diffraction

The structure of orthorhombic $Li_{3.25}Si_{0.25}P_{0.75}S_4$ determined from single crystal XRD measurements is depicted in **Figure 3.1 a, c**, and the crystallographic details are summarized in **Table 3.1** and **Tables A3**. The unit cell was indexed in the orthorhombic space group *Pnma* with a = 13.158(2) Å, b = 8.029(1) Å, and c = 6.129(1) Å. The framework is related to that reported for 'single crystal β-Li_3PS_4' (**Figure 3.1b, d**; *Pnma*; a = 13.066(3) Å, b = 8.015(2) Å, and c = 6.101(2) Å, see **Table 3.2** for comparison);[124] however, we note that the latter structure was very likely stabilized with a low fraction of Si substitution via reaction with the quartz tube at 950 °C, because the pure β-phase is certainly not stable at the ambient temperature where the crystallographic study was conducted.[124]

The important difference on substitution of 0.25 ($Li^+ + Si^{4+}$) for P^{5+} is that the three Li positions in β-Li_3PS_4 [tetrahedral Li(1) on the 8*d* site); octahedral Li(2) on the 4*b* site; and tetrahedral Li(3) on the 4*c* site] are each split into two Li sites in $Li_{3.25}Si_{0.25}P_{0.75}S_4$ that are each separated by about 1 Å (see **Figure 3.1a**). These split sites cannot be simultaneously occupied

within each pair due to proximity. All attempts to refine the structure with a large anisotropic thermal parameter (as used to model positional disorder in ion conductive γ-phases such as $Li_{3.5}Ge_{0.5}V_{0.5}O_4$[125] and related Li ion defect clustered interstitial solid solutions[126]) on any of the sites did not result in a converged solution; therefore, a two-site model was necessary. That further confirms these are true 'split sites' that are equivalent to a highly smeared-out Li ion distribution. Inspection of the $Li_{3.25}Si_{0.25}P_{0.75}S_4$ framework, **Table 3.1** and **3.2** and **Figure 3.2**, reveals that the octahedral Li(2) on the 4*b* site in β-Li_3PS_4 shifts slightly to form octahedral Li(2) on an 8*d* site in the Si-substituted material. Because this position (the original 4*b* site) lies on an inversion center, the new site (8*d* site) is split into two positions 1.02 Å apart with equal fractional occupation due to symmetry (**Figure 3.2a**). These highly delocalized octahedral sites are connected to each other via edge sharing to form a one-dimensional LiS_6

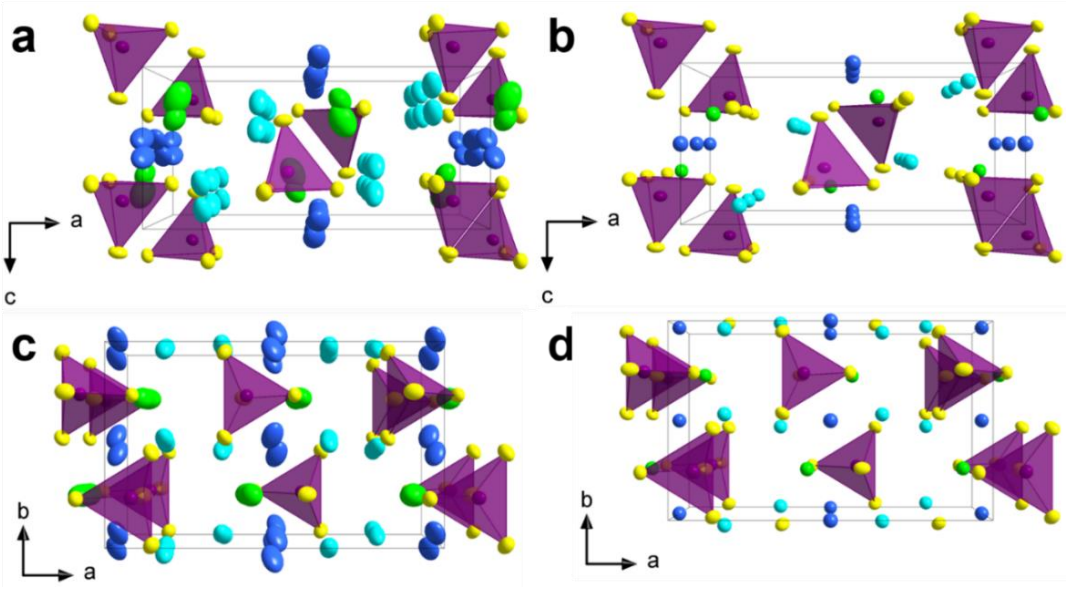

Figure 3.1 (a) Structure of orthorhombic $Li_{3.25}Si_{0.25}P_{0.75}S_4$ from single crystal data and (b) structure of β-Li_3PS_4 along [010]; view along [001] of (c) $Li_{3.25}Si_{0.25}P_{0.75}S_4$ and (d) β-Li_3PS_4; [P/Si]S_4 (violet) tetrahedra, Li(8*d*)-1A/B (turquoise), Li(8*d*)-2 (blue) in $Li_{3.25}Si_{0.25}P_{0.75}S_4$ / Li(4*b*)-2 (blue) in β-Li_3PS_4, Li(4*c*)-3A/B (green), and S (yellow).

Table 3.1 Atomic coordinates, occupation factors, and equivalent isotropic displacement parameters of orthorhombic $Li_{3.25}Si_{0.25}P_{0.75}S_4$ obtained from single crystal X-ray diffraction at 280 K, refined composition $Li_{3.274(20)}Si_{0.25}P_{0.75}S_4$.

Atom	Wyck. site	*x*	*y*	*z*	Occ.	U_{eq} (Å^2)
Li1A	8*d*	0.3299(2)	0.0305(4)	0.3846(5)	0.912(6)	0.0402(8)
Li1B	8*d*	0.334(2)	0.012(4)	0.218(6)	0.088(6)	0.0402(8)
Li2	8*d*	0.0061(5)	0.0447(8)	0.5572(9)	0.457(10)	0.046(2)
Li3A	4*c*	-0.079(3)	0.25	-0.178(18)	0.20(5)	0.07(2)
Li3B	4*c*	-0.071(3)	0.25	-0.312(13)	0.16(5)	0.047(15)
P1	4*c*	0.08729(3)	0.25	0.15622(6)	0.75	0.01522(11)
Si1	4*c*	0.08729(3)	0.25	0.15622 (6)	0.25	0.01522(11)
S1	8*d*	0.15281(2)	0.03571(4)	0.27631(5)	1	0.02359(10)
S2	4*c*	-0.0619(1)	0.25	0.2684(1)	1	0.01986(11)
S3	4*c*	0.10084(4)	0.25	-0.17765(7)	1	0.02334(12)

Table 3.2 Comparison of the atomic coordinates, occupation factors, and isotropic displacement parameters of β-$Li_{2.96(12)}PS_4$ from single crystal X-ray diffraction reported in Ref [124].

Atom	Wyck. site	*x*	*y*	*z*	Occ.	U_{eq} (Å^2)
Li1	8*d*	0.332(2)	0.033(5)	0.386(5)	1	0.0709
Li2	4*b*	0	0	0.5	0.68(12)	0.1013
Li3	4*c*	-0.074(11)	0.25	-0.306(29)	0.28(12)	0.0532
P1	4*c*	0.0874(4)	0.25	0.1576(8)	1	0.0286
S1	8*d*	0.1532(3)	0.0367(5)	0.2784(6)	1	0.0344
S2	4*c*	-0.0624(4)	0.25	0.2674(9)	1	0.0300
S3	4*c*	0.1012(5)	0.25	-0.1758(8)	1	0.0360

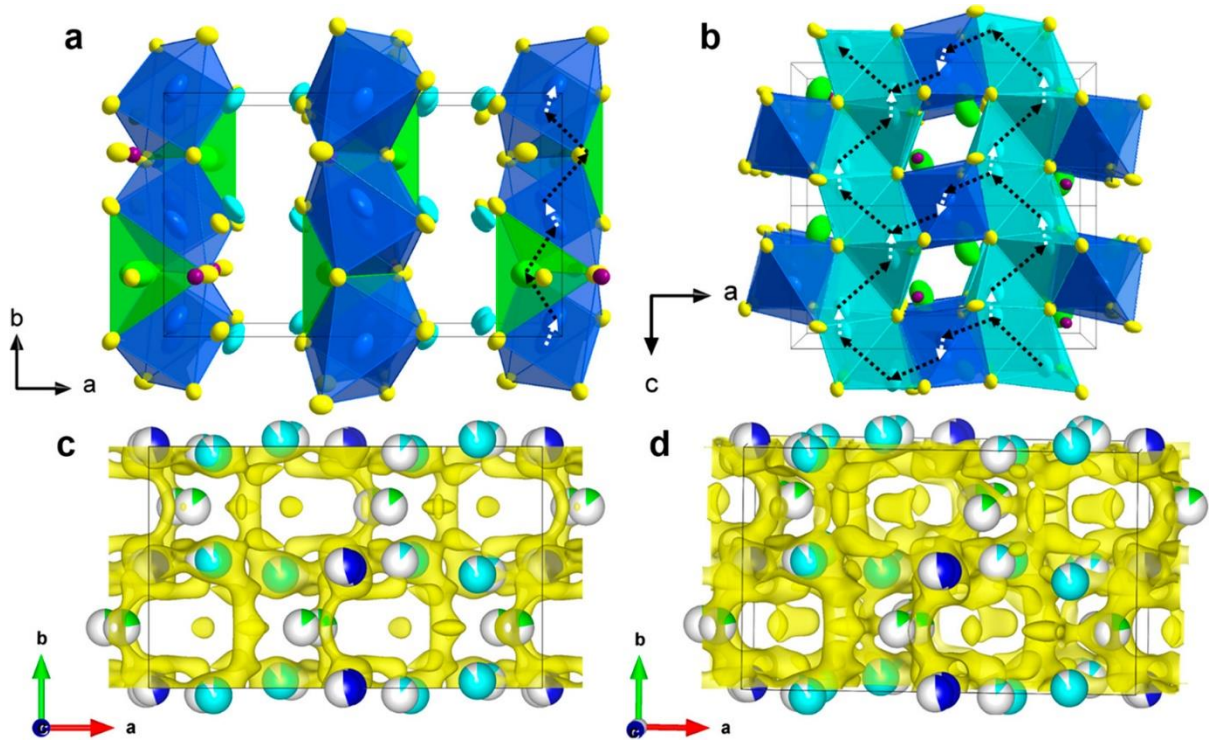

Figure 3.2 Structure of $Li_{3.25}Si_{0.25}P_{0.75}S_4$: (a) view along [001] showing the connectivity along the *b*-axis; (b) view along [010] showing the potential Li-ion diffusion channels along the *c*-axis formed by Li1A/B bipyramids and within the *a*, *c*-plane, formed by octahedral Li(2) connected with the Li1A/B bipyramids; and negative nuclear density distribution (of Li ions) in $Li_{3.25}Si_{0.25}P_{0.75}S_4$ at 300 K, calculated using the maximum entropy method (MEM) along [001] (c) at the iso-surface level of -0.035 fm.Å^{-3} and (d) at the iso-surface level of -0.025 fm.Å^{-3} between $-0.1 < a < 1.1$, Li1-8*d* (turquoise), Li2-8*d* (blue), Li3-4*c* (green).

chain. The Li(3) tetrahedra split into Li3A and Li3B sites 0.83 Å apart, each with fractional occupancy of around 20%, and the Li3B sites share opposite faces with the LiS_6 octahedra along this chain. This site population generates potential channels for Li ion diffusion along the [010] direction (**Figure 3.2a**). The Li(1) tetrahedra-split into Li1A and Li1B sites 1.03 Å apart-share a common face, effectively forming a bipyramidal moiety. These bipyramids form a one-dimensional chain along the [001] direction (**Figure 3.2b**), which creates a potentially additional Li diffusion pathway along the *c*-axis. In addition, in the $Li_{3.25}Si_{0.25}P_{0.75}S_4$ phase, the

c-axis diffusion pathway formed by edge sharing bipyramidal moieties are connected by an octahedral Li(2) by sharing a common face which forms an *a*, *c*-plane diffusion pathway. The importance of these pathways to Li ion mobility is confirmed using MEM (next section).

3.3.2 Neutron Diffraction

Figure 3.3 shows the powder neutron diffraction (PND) pattern of polycrystalline $Li_{3.25}Si_{0.25}P_{0.75}S_4$ at 300 K (**Figure 3.3a**) confirming the formation of a single-phase composition with no visible impurities. Rietveld refinement of the neutron time-of-flight data, which allows the location of the Li ions owing to their significant and negative neutron scattering length, provided results (see **Table A6**) that show disorder of the Li over each of the three site pairs in excellent agreement with the single crystal data described above. Low temperature (180 K) PND and single crystal XRD measurements were also conducted on

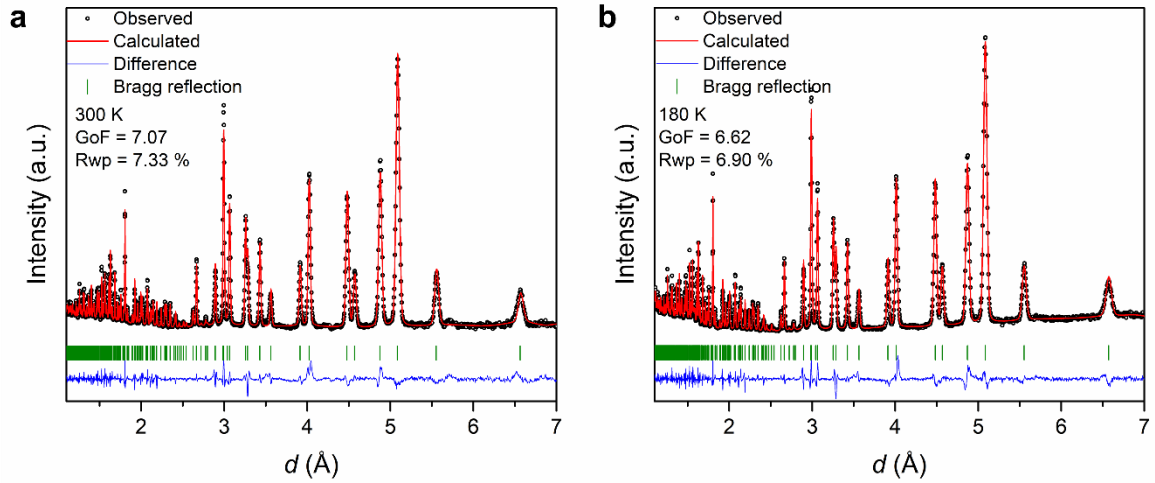

Figure 3.3 Time-of-flight neutron diffraction patterns and the corresponding Rietveld refinement fits of $Li_{3.25}Si_{0.25}P_{0.75}S_4$ at (a) 300 K and (b) 180 K. Experimental data are shown in black circles; the red line denotes the calculated pattern; the difference profile is shown in blue; and the calculated positions of the Bragg reflections are shown as green vertical ticks. Rwp and GoF are the weighted profile R-factor and goodness of fit, respectively.

$Li_{3.25}Si_{0.25}P_{0.75}S_4$ (**Figure 3.3b**). These data sets, summarized in **Tables A4-5**, and **A7**, were in excellent accord with the data at 300 K and show that the same degree of Li site disorder remains at 180 K. Extracted structure factors from the neutron diffraction pattern generated the negative nuclear density maps that revealed pathways for Li-ion transport (see below).

3.4 Ionic Conductivity in $Li_{3.25}Si_{0.25}P_{0.75}S_4$ and Pathways for Transport

Temperature-dependent impedance spectroscopy measurements were performed to determine the ionic conductivity of $Li_{3.25}Si_{0.25}P_{0.75}S_4$ and the activation energy for Li ion transport (**Figure 3.4** and **Table 3.3**). The corresponding impedance responses (illustrated as Nyquist plots) from which the data were obtained are shown in **Figure 3.5a-g**. Low temperature (-78 °C) EIS measurements were also conducted in order to distinguish bulk conductivity and grain boundary conductivity (**Figure 3.5h**). Only one semicircle is present, indicating that bulk and grain boundary conductivity could not be separated, which is due to the soft nature of sulfide materials, even with high Si content (the results of the fit with an equivalent circuit are summarized in **Table 3.4**). The total Li ion conductivity of 1.22 $mS.cm^{-1}$ (labeled in red in **Figure 3.4a**) is about 10 fold higher than nanoporous β-Li_3PS_4 synthesized by a wet-chemical method (0.16 $mS.cm^{-1}$).[57] It is also more than a factor of 10^3 higher than bulk β-Li_3PS_4 (8.93×10^{-4} $mS.cm^{-1}$). In accord, $Li_{3.25}Si_{0.25}P_{0.75}S_4$ shows an Arrhenius behavior that was fit to an activation energy, E_a = 0.34 eV (**Figure 3.4b**), which is much lower than that of bulk β-Li_3PS_4 (E_a = 0.47 eV)[56] and slightly lower than that in nanoporous β-Li_3PS_4 (E_a = 0.36 eV).[57]

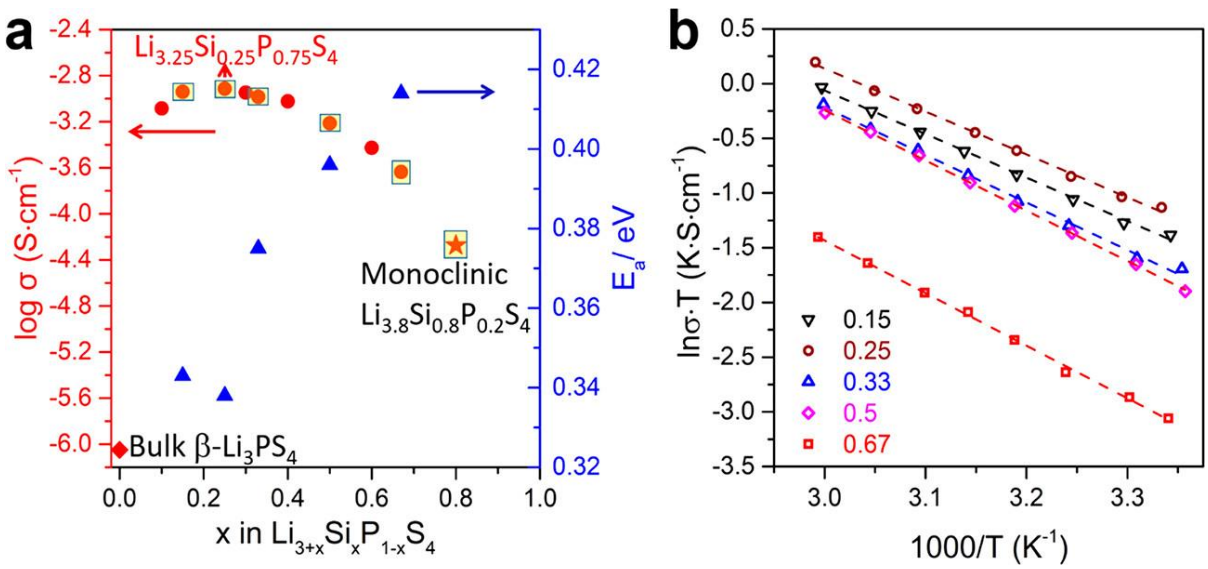

Figure 3.4 (a) Ion conductivity (red dots) at RT and activation energy (blue triangles) of $Li_{3+x}Si_xP_{1-x}S_4$ as a function of Si content (x); squares around the data points indicate compositions for which the structure has been solved by single crystal diffraction. (b) Arrhenius plots of $Li_{3+x}Si_xP_{1-x}S_4$ (x = 0.15, 0.25, 0.33, 0.5, 0.67).

To understand how the possible Li ion diffusion pathways in $Li_{3.25}Si_{0.25}P_{0.75}S_4$ could lead to a high conductivity and low activation energy, the Li ion nuclear density distribution was visualized based on the MEM in conjunction with Rietveld analysis of powder neutron diffraction data, which is depicted as 3D distributions of (negative) Li nuclear densities. The MEM maps are presented in **Figure 3.2**, underneath the depiction of the structure in the polyhedral motif for comparison. Well-connected Li ion diffusion pathways that lie both along the *b*-axis (**Figure 3.2c**) and in the *a*,*c*-plane (perspective view, **Figure 3.2d**) form a highly connected 3D diffusion pathway. In contrast, similar MEM analysis based on PND data of nanoporous β-Li_3PS_4 reveals only Li pathways in the *a*,*c*-plane but no connectivity along the *b*-axis.[127] These findings are further supported by the bond valence site energy (BVSE) maps,[121] as discussed below.

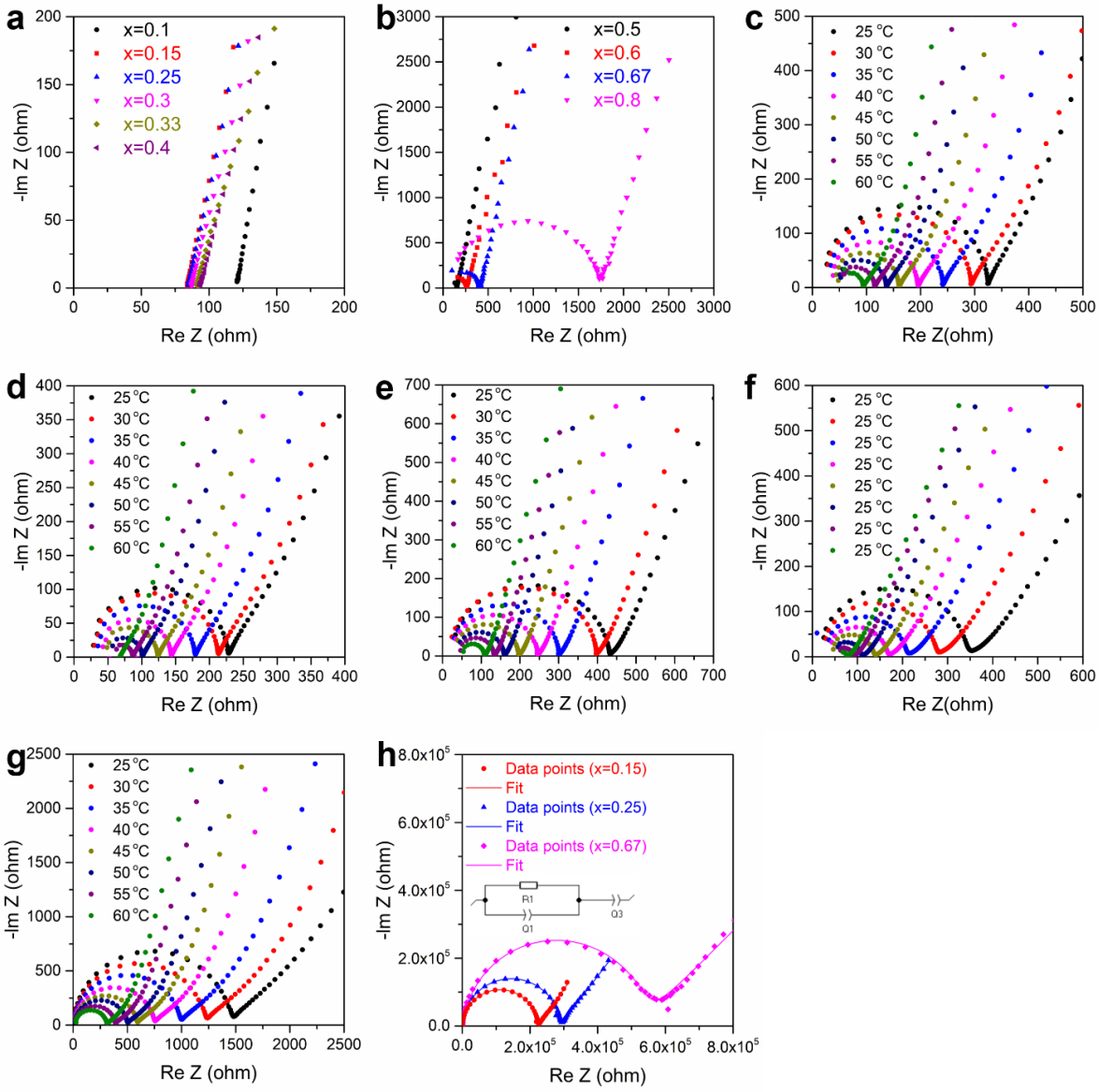

Figure 3.5 Nyquist plots of $Li_{3+x}Si_xP_{1-x}S_4$ phases at room temperature (a) $0.1 \leq x \leq 0.4$ and (b) $0.5 \leq x \leq 0.8$; Nyquist plots at each temperature used to determine activation energies: (c) $Li_{3.15}Si_{0.15}P_{0.85}S_4$, (d) $Li_{3.25}Si_{0.25}P_{0.75}S_4$, (e) $Li_{3.33}Si_{0.33}P_{0.67}S_4$, (f) $Li_{3.5}Si_{0.5}P_{0.5}S_4$and (g) $Li_{3.67}Si_{0.67}P_{0.33}S_4$; (h) Nyquist plots at -78 ^oC of $Li_{3.15}Si_{0.15}P_{0.85}S_4$, $Li_{3.25}Si_{0.25}P_{0.75}S_4$ and $Li_{3.67}Si_{0.67}P_{0.33}S_4$, along with corresponding equivalent circuit fits.

Table 3.3 Ionic conductivity of $Li_{3+x}Si_xP_{1-x}S_4$ as a function of Si content (x) at room temperature.

Composition	Ionic conductivity ($mS.cm^{-1}$)
$Li_{3.15}Si_{0.15}P_{0.85}S_4$	1.15
$Li_{3.25}Si_{0.25}P_{0.75}S_4$	1.22
$Li_{3.3}Si_{0.3}P_{0.7}S_4$	1.13
$Li_{3.33}Si_{0.33}P_{0.67}S_4$	1.04
$Li_{3.4}Si_{0.4}P_{0.6}S_4$	0.947
$Li_{3.5}Si_{0.5}P_{0.5}S_4$	0.612
$Li_{3.6}Si_{0.6}P_{0.4}S_4$	0.374
$Li_{3.67}Si_{0.67}P_{0.33}S_4$	0.231

Table 3.4 Parameters of the fit for the impedance data of $Li_{3+x}Si_xP_{1-x}S_4$ (x= 0.15, 0.25, 0.67) at -78 ^oC; fitting parameters errors are shown in brackets.

Element	$Li_{3.15}Si_{0.15}P_{0.85}S_4$	$Li_{3.25}Si_{0.25}P_{0.75}S_4$	$Li_{3.67}Si_{0.67}P_{0.33}S_4$
Resistance (R1) /ohm	$2.878(5) \times 10^5$	$2.230(2) \times 10^5$	$5.23(3) \times 10^5$
CPE (Q1) /$S \cdot s^{-\alpha}$	$3.69(6) \times 10^{-10}$	$3.98(3) \times 10^{-10}$	$5.2(2) \times 10^{-10}$
CPE Alpha ($\alpha 1$)	0.978(2)	0.9719(8)	0.952(4)
CPE (Q2) /$S \cdot s^{-\alpha}$	$5.44(5) \times 10^{-6}$	$8.58(5) \times 10^{-6}$	$8.85(5) \times 10^{-7}$
CPE Alpha ($\alpha 2$)	0.584(6)	0.606(3)	0.503(4)

3.5 Correlating Structure and Li Ion Transport in the Series $Li_{3+x}Si_xP_{1-x}S_4$

The targeted synthesis of $Li_{3+x}Si_xP_{1-x}S_4$ phases in the composition range of $0.1 \leq x \leq 0.67$ provided phase pure solid solutions as polycrystalline powders, as proven by X-ray diffraction (**Figure 3.6a**). All the phases were indexed in the same space group, *Pnma*. We note that in the composition range $0.4 \leq x \leq 0.475$ under slightly different heat-treatment conditions, the tetragonal 'LGPS'-type structure of $Li_{3+x}Si_xP_{1-x}S_4$ can also crystallize,[128] in

addition to the monoclinic superlattice $Li_{3+x}Si_xP_{1-x}S_4$[58] that exhibits a different PXRD pattern. However, by adjusting heat treatment and cooling parameters, these side products can be completely avoided. When the Si content reaches 0.8, the symmetry of $Li_{3.8}Si_{0.8}P_{0.2}S_4$ switches to monoclinic (**Figure 3.6a**) which is similar to the parent monoclinic phase Li_4SiS_4[58] (see crystallographic details summarized in **Tables A14-15** from single crystal diffraction). The clear difference of the XRD patterns (**Figure 3.6a**) between the orthorhombic and the monoclinic phases is the peak at 2θ ~16° (black arrow, (101) reflection) in the former which shifts to ~14.5° (blue arrow, (100) reflection) in the monoclinic phase. X-ray single crystal solutions of the structures were also achieved for other selected compositions aside from the

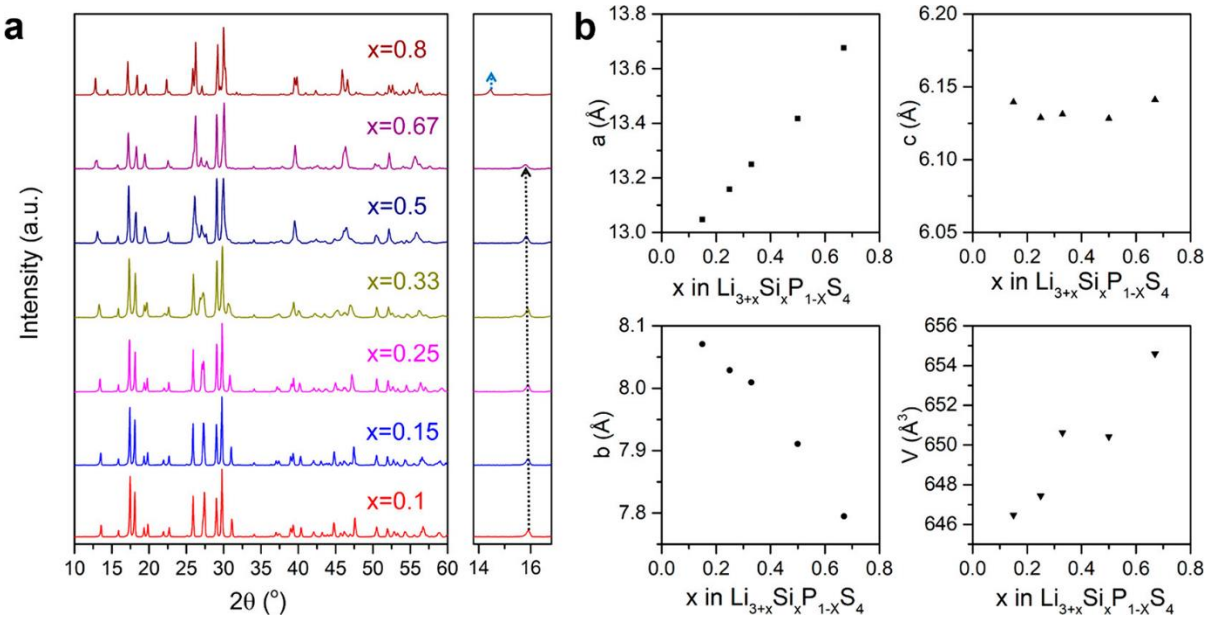

Figure 3.6 (a) Selected X-ray diffraction patterns of as-synthesized $Li_{3+x}Si_xP_{1-x}S_4$ with x = 0.1, 0.15, 0.25, 0.33, 0.5 0.67, 0.8; the black arrow indicates the (101) reflection in orthorhombic $Li_{3+x}Si_xP_{1-x}S_4$ (x = 0.1, 0.15, 0.25, 0.33, 0.5 0.67) and the blue arrow indicates the (100) reflection in monoclinic $Li_{3.8}Si_{0.8}P_{0.2}S_4$. (b) Lattice parameters and unit cell volume change of orthorhombic $Li_{3+x}Si_xP_{1-x}S_4$ phases with Si content from single crystal structure solutions at 280 K.

$Li_{3.25}Si_{0.25}P_{0.75}S_4$ framework, namely, x = 0.15, 0.33, 0.5, and 0.67 (see **Tables A1-2** and **A8-13** for details, and crystallographic information). Together, this series provides a systematic way of investigating the effect of composition/structure on Li ion conductivity. For all of the $Li_{3+x}Si_xP_{1-x}S_4$ phases (including $Li_{3.25}Si_{0.25}P_{0.75}S_4$ described above), due to the similar X-ray/neutron scattering factors of Si and P, in the X-ray single crystal and neutron powder refinements, the Si/P ratios were fixed to the experimental targeted values as no impurity phases were visible in the XRD patterns. To prove the successful substitution of P for Si in the lattice, ^{29}Si and ^{31}P MAS NMR studies of $Li_{3+x}Si_xP_{1-x}S_4$ (x = 0.25, 0.33, 0.67) were performed, shown in **Figure 3.7**. We observed peaks corresponding to SiS_4^{4-} ($\delta \sim 5$ ppm) and PS_4^{3-} ($\delta \sim 86.5$ ppm) moieties; typical chemical shifts in accord with prior reports.[129, 130]

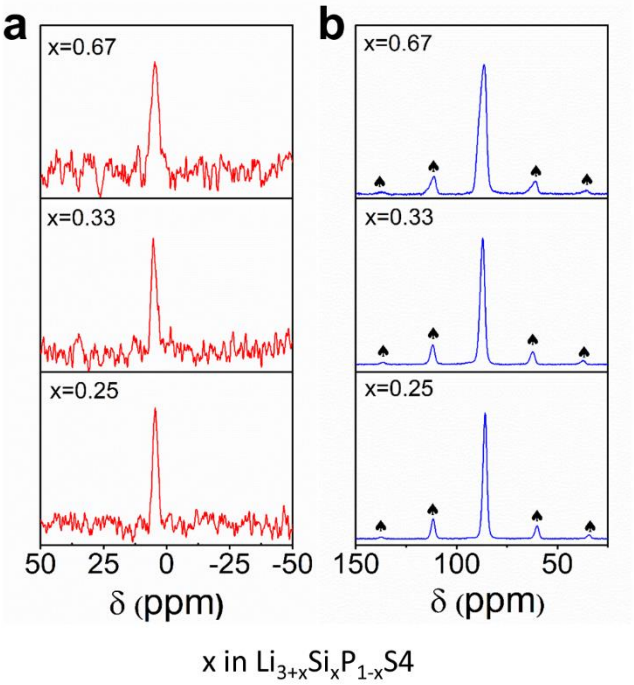

Figure 3.7 (a) ^{29}Si MAS NMR (b) ^{31}P MAS NMR of $Li_{3+x}Si_xP_{1-x}S_4$ (x=0.25, 0.33, 0.67), spades indicate spinning side bands.

The lattice parameters and unit cell volume changes based on single crystal data for $Li_{3+x}Si_xP_{1-x}S_4$ with different Si fractions are shown in **Figure 3.6b**. With increasing Si, the *a* lattice parameter increases, whereas the *b* parameter decreases and the *c* parameter shows a small variation. Overall, the cell volume thus enlarges almost linearly with increasing Si content in accord with solid solution behavior, because of the introduction of the larger Si^{4+} on the P^{5+} site. The variable temperature conductivity data and Arrhenius plots of compositions $Li_{3+x}Si_xP_{1-x}S_4$ as a function of x are presented in **Figures 3.4** and **3.5**. The conductivity is not strongly dependent on x within $0.15 \leq x \leq 0.33$, but outside of this regime, the conductivity drops off markedly (**Figure 3.4a**). The activation energy also increases with greater Si content (a trend that is correlated with a decrease in ionic conductivity) from 0.34 eV (x = 0.25) to 0.38 eV (x = 0.33) and 0.40 eV (x = 0.5), reaching 0.41 eV for x = 0.67 (**Figure 3.4b**).

3.6 Effect of Entropic Disorder

Aliovalent substitution in $Li_{3+x}Si_xP_{1-x}S_4$ has a large influence on ionic transport due to characteristic and distinct changes in the structure. For example, at low Si fractions, the single crystal structure of $Li_{3.15}Si_{0.15}P_{0.85}S_4$ reveals different Li environments compared to x = 0.25; namely, only partial site splitting is observed (**Figure 3.8a-c**). The octahedral Li(2) ions shift from 4*b* sites to 8*d* sites which are split into two positions due to symmetry, as in x = 0.25. The tetrahedral Li(1) site, however, does not split and attains 97.6% occupancy (**Figure 3.8b**), similar to β-Li_3PS_4. Li(3) shifts from its original tetrahedral sites to disordered trigonal bipyramidal sites that now exhibit large anisotropic thermal displacement parameters (as opposed to a true split site) and still shares opposite faces with octahedral Li(2) to form a potential Li-ion diffusion channel shown in **Figure 3.8c**. The structure of this relatively highly

conductive composition, $Li_{3.15}Si_{0.15}P_{0.85}S_4$, can thus be regarded as a transition between β-Li_3PS_4 and $Li_{3.25}Si_{0.25}P_{0.75}S_4$, where all three Li sites are split into two.

With increasing Si^{4+}/P^{5+} ratio, more Li is stuffed into the structure to balance the charge. The single crystal solution of $Li_{3.67}Si_{0.67}P_{0.33}S_4$ is shown in **Figure 3.8d**, and the details are summarized in **Tables A12-13**. The split Li2 sites move closer within the octahedra with increasing Si content as shown in **Figure 3.9**, and at x = 0.67, the octahedral Li2 now occupies the original 4*b* site, albeit with a large atomic displacement parameter. This is explained by the

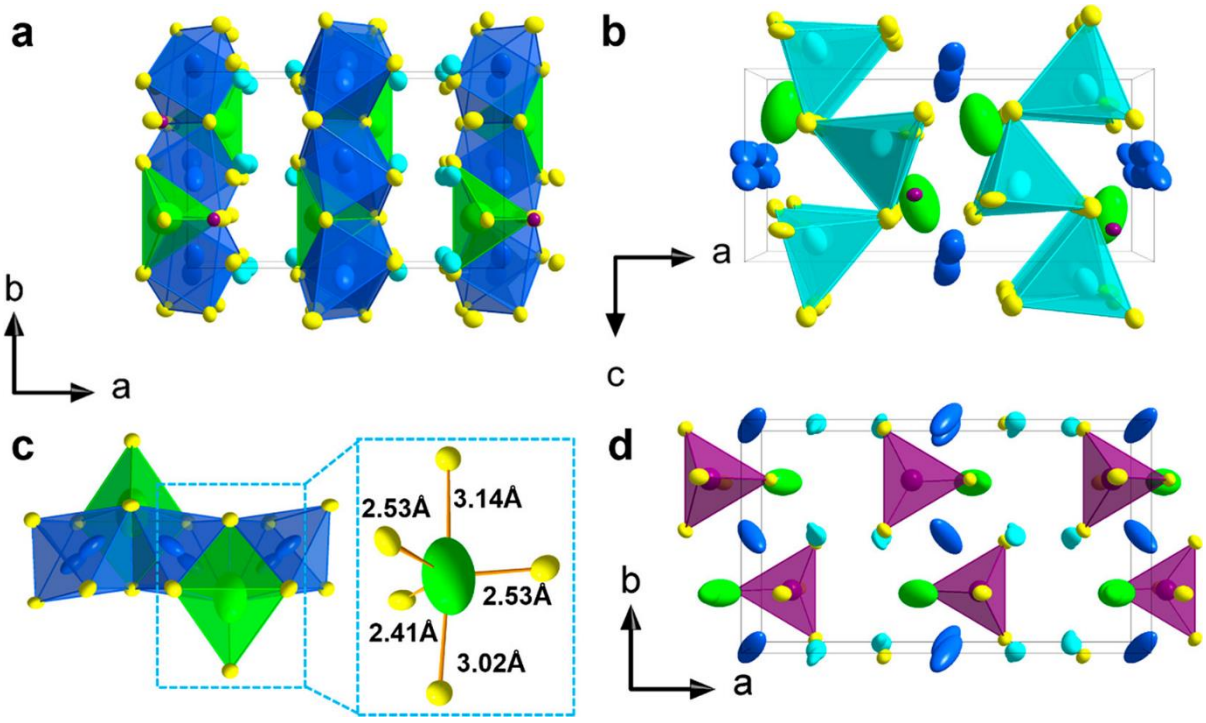

Figure 3.8 View along (a) [001] and (b) [010] of $Li_{3.15}Si_{0.15}P_{0.85}S_4$ showing the zigzag Li-ion conduction channels along the b-axis and the isolated Li(8d)S_4-1 tetrahedra along the *c*-axis; (c) zigzag Li-ion diffusion along the *b*-axis with the octahedral Li(2) and disordered trigonal bipyramids Li(3); and (d) view along [001] of $Li_{3.67}Si_{0.67}P_{0.33}S_4$ showing the nonsplit Li2 site with a large thermal displacement parameter: Li(8*d*)S_4-1 (turquoise) tetrahedra, Li(8*d*)S_6-2 (blue) octahedra, Li(4*c*)S_5-3 (green) trigonal bipyramids, P/Si (violet spheres), and S (yellow spheres).

fact that the Li2 octahedra share common faces with the surrounding Li1 and Li3 tetrahedra (inset in **Figure 3.9**). The additional Li content with increasing x is accommodated on the (still split) Li3 sites, and the total occupancy of the Li1 sites is always ≥90%. We propose that this significantly increases the Coulombic repulsion between the Li ions in the Li2 site and the Li1,3 sites, thereby changing the site energy of Li2 and making the split site less favorable. The increased occupancy in the Li3 split sites also greatly reduces their vacancy populations. The combination of these two factors lowers the ionic conductivity to 0.23 $mS.cm^{-1}$ and increases the activation energy to 0.41 eV.

BVSE maps in the SoftBV program[121, 122] developed by S. Adams were used to analyze the energetics of probable ion diffusion pathways in the lattice. It provides an estimate of the changes in the energy landscape for Li-ion diffusion induced by Li site splitting. Split Li sites indicate the existence of many local minima which serve to frustrate the overall energy

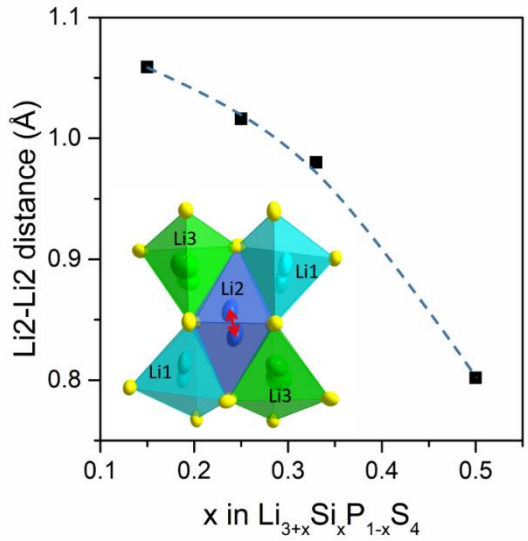

Figure 3.9 Li2-Li2 distance (red arrow) changes with different Si content (x) in $Li_{3+x}Si_xP_{1-x}S_4$; the inset shows the Li2 octahedra is surrounded by Li1 and Li3 tetrahedra.

landscape and should lead to lower activation energy barriers for Li ion diffusion.[131] This supposition is confirmed by examining the BVSE calculations for the x = 0, 0.25, and 0.67 compositions shown in **Figure 3.10**. The average activation energy barrier for $Li_{3.25}Si_{0.25}P_{0.75}S_4$ in the Li2-Li3 pathway along the *b*-axis is lower than for nanoporous β-Li_3PS_4 as a result of the change in the energy landscape resulting from the splitting of the Li2 and Li3 sites (**Figure 3.10a**). We suggest this accounts for the Li-ion diffusion along the *b*-axis determined by the MEM analysis of the negative nuclear densities. Whereas in β-Li_3PS_4, only quasi 2D *a,c*-plane Li-ion diffusion is observed.[127] In x = 0.67 where the Li2 site is not split, the activation energy barrier along the *b*-axis is higher. Especially noteworthy is that the diffusion pathway for the x = 0.25 and 0.67 compositions along the *c*-axis (which passes through the split Li1A and Li1B sites that connect interstitial sites (i1, i3)) exhibits a relatively low activation energy ~0.2 eV (**Figure 3.10b**). This value is much lower than that of β-Li_3PS_4 (~0.3 eV) due to significantly increased Li1 and i1, i3 site energies and likely compensates for the increased energy barrier in the *a,c*-plane as x increases (**Figure 3.10c**). In short, the BVSE calculations indicate the lowest overall activation energy pathways are for x = 0.25 and suggest that Li ion diffusion takes place both along the *b*-axis and in the *a,c*-plane. Furthermore, recent *ab initio* modeling[85] has pointed out that mobile Li ions occupying high-energy sites can activate concerted migration with a reduced migration energy barrier. As indicated in **Figure 3.10a**, the Li3 split site energy is significantly higher than that of the split Li2 and thus occupation of the high energy split Li3 site may activate concerted ion migration to further lower the activation energy.

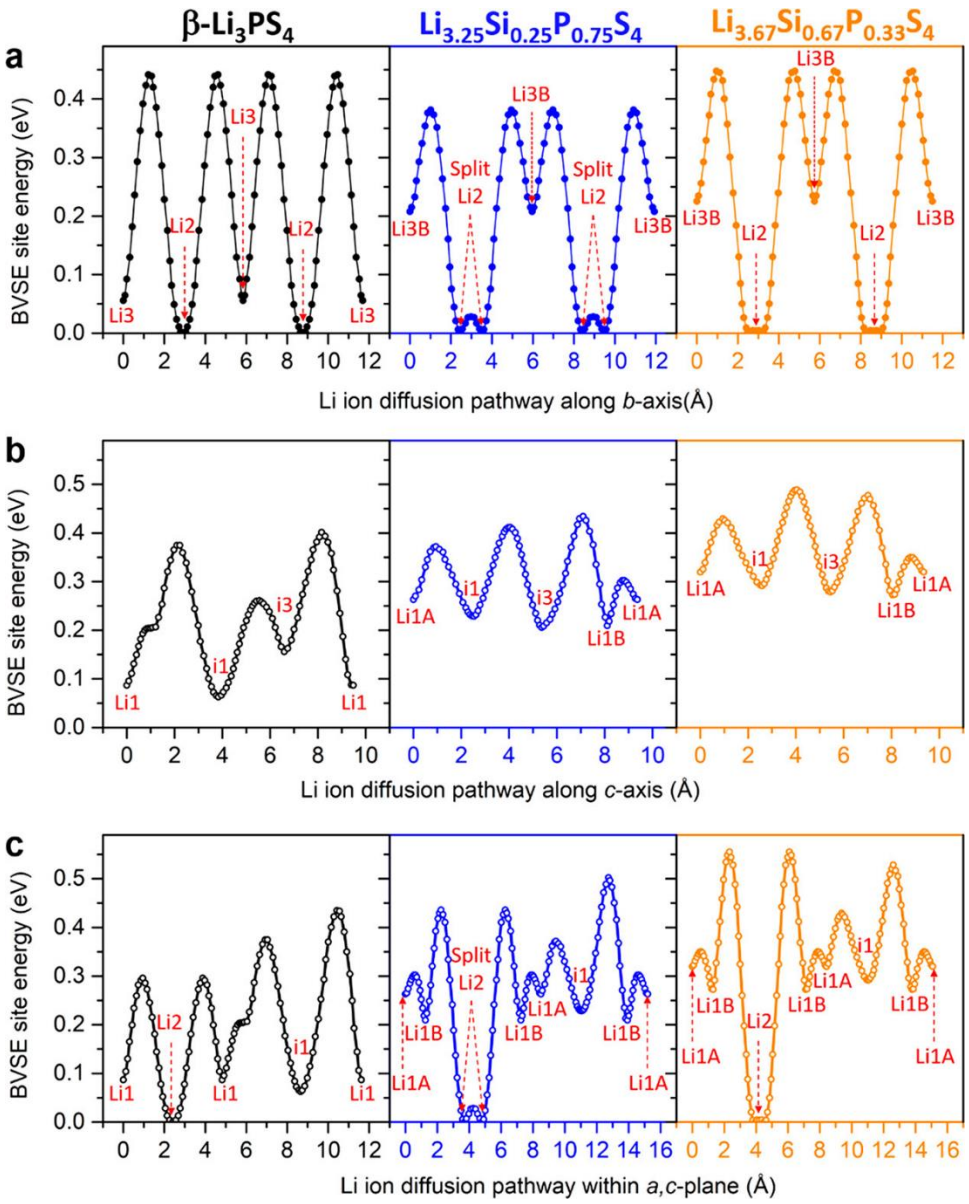

Figure 3.10 BVSE models of migration barriers along the (a) *b*-axis and (b) *c*-axis and (c) within the *a*,*c*-plane for β-Li_3PS_4 (black) with no split sites, $Li_{3.25}Si_{0.25}P_{0.75}S_4$ (blue) with three split sites, and $Li_{3.67}Si_{0.67}P_{0.33}S_4$ (orange) with two split sites. Note that the site energies are referenced to zero for the Li2 site as the lowest energy in each case which is a relative, not absolute value; it does not imply the lowest energies are the same in each calculation.

We note that excess volume and attendant geometric frustration have been invoked in increasing the fluoride ion conductivity in $Ba_{1-x}Ca_xF_2$.[132] Moreover, the correlated disorder has been linked to clear crystallographic signatures[133] which are present in our case. The connection between the Li site disorder and the increasing ion conductivity and decreasing activation energy barrier shows that substitution-induced Li site disorder has a major influence on the Li ion diffusion in $Li_{3+x}Si_xP_{1-x}S_4$, which may apply more generally to other solid electrolytes of this nature. We also note that molecular dynamics simulations of β-Li_3PS_4 suggest maximal ionic conductivity is coincident with the highest configurational entropy. These calculations show that 'melting' (*i.e.* complete disorder) of the Li sublattice at 600 K in β-Li_3PS_4 occurs as more Li sites become available due to an increase in intrinsic vacancies.[134] This report suggests that the melted Li sublattice leads to a liquid-like ionic diffusivity, and the sublattice melt-induced Li disorder can possibly be stabilized by quenching. Our studies confirm experimental verification of the onset of such disorder that is stabilized by substitution instead of quenching.

3.7 Conclusions

In summary, we have synthesized a fast-ion conductor, orthorhombic $Li_{3+x}Si_xP_{1-x}S_4$, with an entropically stabilized structure in a limited solid solution range ($0.15 \leq x \leq 0.33$) that results in high ionic conductivities above 1 $mS.cm^{-1}$, and where the highest ionic conductivity of 1.22 $mS.cm^{-1}$ is exhibited for the composition $Li_{3.25}Si_{0.25}P_{0.75}S_4$. This represents an increase by 3 orders of magnitude compared to bulk β-Li_3PS_4. The ionic conductivities can likely be further improved by reducing grain boundary resistance by hot pressing as reported elsewhere.[67, 135] The orthorhombic phase is a promising sulfide SE for ASSBs as the ductile

and flexible nature of thiophosphates makes them more easily processed and densified, compared to oxide SEs. This work shows aliovalent substitution can lead to structural changes and Li site disorder which can induce a flatter potential energy landscape and lower the activation energy for mobile Li ions. These observations highlight the importance of a detailed and reliable structure analysis enabled by single crystal diffraction combined with powder neutron diffraction to gain a better understanding of the structure-property relations in these solid-state ion conductors. These findings can help to guide further enhancements in ionic conductivity, new materials discovery, and the understanding of Li ion transport in SEs.

Chapter 4. A New Family of Argyrodite Thioantimonate Lithium Superionic Conductors

4.1 Introduction

Most ASSBs reported in the literature can only be cycled at low current density with low active material loading, as they are limited by moderate ionic conductivity of the SEs and/or poor contact between the SEs and active materials. Ultra-highly conductive (>10 $mS.cm^{-1}$) and relatively soft SEs offer the possibility to achieve high energy densities with improved rate capabilities, which are enabled by utilizing thick electrode configurations and a high active material loading.[115]

Until now, only a limited number of SEs have been reported with conductivity approaching 10 $mS.cm^{-1}$; namely $Li_{10}GeP_2S_{12}$ and related phases with substitution of the Ge for Si and Sn,[47, 136, 137] $Li_7P_3S_{11}$,[135] and Ge-substituted Li-argryodite[67]. Most of these materials exhibit high ionic conductivity (>10 $mS.cm^{-1}$) for pellets sintered at elevated temperatures, but much lower ionic conductivity for 'cold-pressed' pellets prepared at ambient temperature due to poorer crystallite contact (**Table 4.1**). While sintered values are more indicative of the inherent bulk ionic conductivity, practical ASSBs require their electrode/electrolyte components to be pressed at ambient temperature to limit reactivity. Classic argyrodites Li_6PS_5X (X=Cl, Br)[68, 138] have attracted considerable interest, due to their good ionic conductivity (up to 4 - 5 $mS.cm^{-1}$ by direct annealing of precursors,[139] or from scalable solution-engineered synthesis[78]). The ionic conductivity of argyrodites is strongly dependent on the S^{2-}/X^- (X=Cl, Br, I) disorder over the 4*a* and 4*c* sites as demonstrated by density functional theory molecular dynamics simulations (DFT MD).[140] Indeed, Cl/Br compositions with mixed halide

occupation on these sites give rise to higher ionic conductivity (up to 4 $mS.cm^{-1}$) than either pure Cl or Br compositions.[78] As Li_6PS_5I exhibits no S^{2-}/I^- disorder due to the large ionic radii difference between S^{2-} and I^-, this arrangement leads to very low ionic conductivity, in the range of 1.3×10^{-3} $mS.cm^{-1}$.[66] Recently, Zeier's group reported Ge-substituted Li_6PS_5I phases.[67] As the Ge content increases from 0 to 0.6, a small degree (*ca.* ~7%) of S^{2-}/I^- site disorder is induced based on powder X-ray and neutron diffraction analysis, which was correlated to a drop in the activation energy and a dramatic increase in ionic conductivity. The composition $Li_{6.6}P_{0.4}Ge_{0.6}S_5I$ exhibits a high ionic conductivity of 5.4 $mS.cm^{-1}$ for the cold pressed material, and triple that for the sintered pellet (see **Table 4.1**). However, whether the induced S^{2-}/I^- disorder is due to a larger unit cell upon Ge^{4+} substitution, which allows for better mixing of the mismatched anions, or owes to the increased Li^+ concentration in the structure was not identified in this report.

Table 4.1 Comparison of ionic conductivities between cold pressed powders and sintered pellets for some recently reported superionic conductors.

Compositions	Cold-pressed powder ($mS.cm^{-1}$)	Ref.	Sintered Pellet ($mS.cm^{-1}$)	Ref.
$Li_7P_3S_{11}$	3.2	[135]	17 (hot-pressing)	[135]
$Li_{10}GeP_2S_{12}$	5-9	[61, 141]	12	47
$Li_{10.35}Sn_{0.27}Si_{1.08}P_{1.65}S_{12}$	3.31	[136]	11	[136]
$Li_{9.54}Si_{1.74}P_{1.44}S_{11.7}Cl_{0.3}$	3-16	[142, 143]	25	[137]
$Li_{6.6}Ge_{0.6}P_{0.4}S_5I$	5.4	67	18.4	67
$Li_{6.7}Si_{0.7}Sb_{0.3}S_5I$	12.6	This work	19	This work
$Li_{6.6}Si_{0.6}Sb_{0.4}S_5I$	14.8	This work	24	This work

Here, we report on a new family of thioantimonate iodide argyrodites $Li_{6+x}M_xSb_{1-x}S_5I$ (M=Si, Ge, Sn), where the highest ionic conductivities above 10 $mS.cm^{-1}$ are exhibited by Si compositions ($0.5 \leq x \leq 0.7$) that constitute low-cost, abundant elements. They are prepared *via* simple, non-ball milled synthesis. Optimum values were obtained for x = 0.6 (14.8 $mS.cm^{-1}$, cold pressed pellet; 24 $mS.cm^{-1}$, sintered pellet, see **Table 4.1**). These materials demonstrate good compatibility with Li metal, sustaining over 1000 hours Li stripping/plating at current densities up to 0.6 $mA.cm^{-2}$, and enable good room temperature cycling performance in prototype ASSBs. Moreover, with the aim to unravel the underlying factors driving the superionic conductivity, a combination of exact structure solution enabled by single crystal X-ray and powder X-ray synchrotron/neutron methods reveal the origin of the fundamental structural changes associated with increased Li^+ content and anion/cation site disorder. Highly delocalized Li ion density in the lattice serves as important interstitial sites for Li ion diffusion and activates concerted ion migration, leading to a lowering of the activation energy from 0.41 eV to 0.25 eV. We find that Li ion disorder and concentration dictate superionic conductivity more so than anion site disorder, although the two factors are not necessarily independent.

Dr. Abdeljalil Assoud performed single crystal X-ray diffraction and structural resolution. Dr. Qiang Zhang performed powder neutron diffraction measurements.

4.2 Experimental Approaches

4.2.1 Material Synthesis

A simple approach based on mixing and heating of the precursors was used. Stoichiometric amounts of Li_2S (99.98%), P_2S_5 (99%), Sb_2S_3 (99.995%), Si (99%), GeS_2 (Kojundo, 99.99%), SnS_2 (Kojundo, >99.9%), S (99.98%) and LiI (99.9%) (the source was

Sigma-Aldrich unless otherwise stated) were mixed together in an agate mortar at the targeted ratio, and 5 wt% excess sulfur was added to fully oxidize Si and Sb_2S_3. The mixtures were pelletized and placed in a glassy carbon crucible in a sealed quartz tube under vacuum. $Li_{6+x}Si_xSb_{1-x}S_5I$ was heated to 550°C ($0.5 \leq x \leq 0.7$) or 500 °C ($0.1 \leq x \leq 0.4$) for 7 days with a ramp rate of 5 °C·min^{-1} (designated as *as-synthesized* materials). To improve purity, the as-synthesized samples were ground, repelletized and heated again to 500 °C for another 7 days at a ramp rate of 5 °C·min^{-1} (designated as *annealed* materials). $Li_6Sb_xP_{1-x}S_5I$ was heated to 550°C ($0.1 \leq x \leq 0.4$) or 500 °C ($0.5 \leq x \leq 1$) for 100 h with a ramp rate 5 °C·min^{-1}. $Li_{6+x}Ge_xSb_{1-x}S_5I$ was heated to 550 °C for 50 h, then cooled down to 450 °C for another 100 h with an ramp rate of 5 °C·min^{-1}. $Li_{6+x}Sn_xSb_{1-x}S_5I$ was heated to 550 °C for 50 h with the same ramp rate. Finally, the final product in each case was gently separated to find single crystals suitable for single crystal diffraction. The remaining crystals, or those from subsequent synthesis preparations, were crushed into polycrystalline powders for X-ray and neutron diffraction and impedance spectroscopy analysis.

4.2.2 Single Crystal Diffraction and Structure Resolution

Several colorless plate-shaped single crystals with dimensions of approximately 0.040 × 0.040 × 0.030 mm^3 were scanned to determine their quality. Multiple data sets were collected and gave exactly the same results. The data were collected at 280 K by scanning ω and ϕ of 0.3° or 0.5° in a few groups of frames at different ω and ϕ and an exposure time of 30 or 60 seconds per frame. The structure was solved using direct methods to locate the positions of Sb/Si/Ge/Sn, S, and I atoms. First, these positions were anisotropically refined using the least squares method incorporated in the SHELXTL package, and then the Li positions were located

in the remaining electron density in the Fourier map, which revealed Li-S bonds very similar in length to those found in binary and ternary Li sulfides. Subsequently, the Li site occupancies were freely and anisotropically refined. No constraints were used during the structure refinements, aside from fixing the Sn/Sb occupancy to the experimental targeted value due to the similar X-ray scattering of Sn and Sb. No constraints were used for Si:Sb or Ge:Sb occupancy refinement. The Li2 (24*g*) site was only identified in $Li_{6.2}Sn_{0.2}Sb_{0.8}S_5I$ and was isotropically refined.

4.2.3 Synchrotron X-ray and Neutron Powder Diffraction

For Rietveld analysis of the $Li_{6+x}Si_xSb_{1-x}S_5I$ series, synchrotron XRD measurements were also carried out on the Macromolecular Crystallography Facility beamline at the Canadian Light Source (CLS). The samples were sealed in 0.5 mm glass capillaries and data was collected at a wavelength of an energy 18 KeV. Refinement took benefit from the significantly different X-ray scattering factors between the component elements and the well-defined peak shapes afforded by synchrotron diffraction. This data was especially essential to resolve the very low degree of S^{2-}/I^- disorder, where the mixed S^{2-}/I^- occupancy on the 4*a* and 4*c* site was refined without occupancy constraints, and the U_{iso} value for S^{2-} and I^- was refined to be equal at the same sites.

The time-of-flight powder neutron diffraction patterns were measured at 300 K or 195 K, and a single bank wave with a center wavelength of 1.5 Å was used.

4.2.4 Electrochemical Measurements

For the fabrication of Li | SE | Li symmetric cells, ~ 100 mg of $Li_{6.7}Si_{0.7}Sb_{0.3}S_5I$ or $Li_{6.4}Ge_{0.4}Sb_{0.6}S_5I$ powder was placed into a PEEK cylinder and cold-pressed at 3 tons for 1

min (10 mm diameter). On both sides of the SE pellet, Li foil (99.9%, Sigma-Aldrich, 0.38 mm thickness) with a diameter of 10 mm was attached. The cell was subjected to constant uniaxial pressure using the screw of a stainless-steel framework with 4 Nm torque. Galvanostatic cycling of the symmetric cell for $Li_{6.7}Si_{0.7}Sb_{0.3}S_5I$ was carried out at a current density and capacity of a) 0.3 $mA.cm^{-2}$ and 0.3 $mAh.cm^{-2}$; b) 0.6 $mA.cm^{-2}$ and 0.6 $mAh.cm^{-2}$; and for $Li_{6.4}Ge_{0.4}Sb_{0.6}S_5I$, a lower current density and capacity of c) 0.1 $mA.cm^{-2}$ and 0.1 $mAh.cm^{-2}$; and d) 0.3 $mA.cm^{-2}$ and 0.3 $mAh.cm^{-2}$.

ASSBs employing the $Li_{6.7}Si_{0.7}Sb_{0.3}S_5I$ SE in combination with a TiS_2 (or $LiCoO_2$) cathode and a Li-In alloy anode were assembled in an argon glovebox. First, ~ 80 mg of SE powder was placed into a PEEK cylinder and cold pressed at 3 tons for 1 min (10 mm diameter). The composite cathode mixtures were prepared by mixing TiS_2 or $LiCoO_2$ and the SE in an agate mortar at a weight ratio of 50:50 for TiS_2, and 70:30 for $LiCoO_2$. On one side of the SE pellet, ~ 8 - 10 mg composite cathode mixture (37.4 mg for the high loading TiS_2 cell) was spread and pressed at 3 tons for 3 min. On the other side of the pellet, a thin indium foil (10 mm diameter, Alfa Aesar, 99.99%, 0.125 mm thickness) was attached and ~ 1 mg Li powder (FMC Lithium, ~ 2 mg for the high loading cell) was spread over the Indium foil, and pressed at 1.5 tons for 1 min. The cell was placed into a stainless-steel casing with a constant applied pressure of ~ 1.5 tons. Galvanostatic cycling of the cell was carried out in the voltage range of 2.3 V - 3.7 V *vs* LiIn for the $LiCoO_2$ cell and 0.9 V - 2.4 V *vs* LiIn for the TiS_2 cell.

4.3 Structural evolution in the series $Li_{6+x}M_xSb_{1-x}S_5I$ (M = Si, Sn, Ge)

X-ray diffraction shows that the targeted synthesis of $Li_{6+x}Si_xSb_{1-x}S_5I$ ($0.1 \leq x \leq 0.7$) phases provide almost phase-pure polycrystalline powders in this solid solution range (**Figure**

4.1a). All the phases were indexed in the same cubic space group, $F\bar{4}3m$, that is adopted by most other argyrodites. Higher Si^{4+} content (x > 0.7) leads to increasing amounts of impurities, indicative of the solubility limit (**Figure 4.2a**). All solid solution phases exhibit very minor fractions of LiI and Li_2S (**Figure 4.1a**). While the tiny Li_2S peak exhibits almost no change, the intensity of the LiI peaks increases with increasing Si^{4+} content, which correlates with I^- deficiency in the high-Si compositions as revealed by single crystal diffraction (see below). The argyrodite peaks shift to smaller *d*-spacing with increasing Si^{4+} content (**Figure 4.1a**), because of the substitution of Sb^{5+} with the smaller Si^{4+} ion. Similar results are observed for Ge^{4+} and Sn^{4+} substituted $Li_{6+x}(Ge/Sn)_xSb_{1-x}S_5I$. **Figure 4.1b** shows that phase pure $Li_{6+x}Ge_xSb_{1-x}S_5I$ ($0.1 \leq x \leq 0.4$) can be prepared, while for Sn substituted compositions, even at low content (x = 0.2), small impurities signal the limit of solubility, as shown in **Figure 4.1b** and **4.2b**.

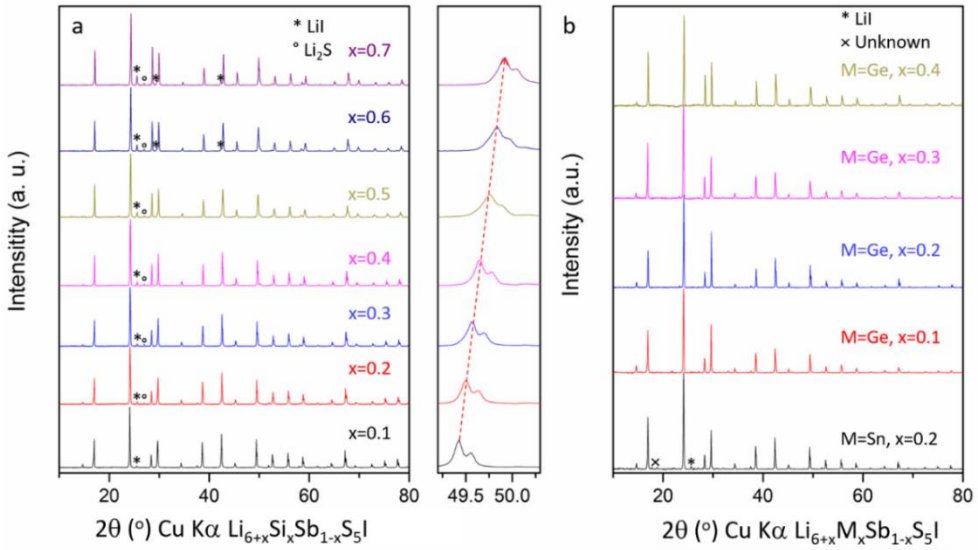

Figure 4.1 X-ray diffraction patterns of as-synthesized (a) $Li_{6+x}Si_xSb_{1-x}S_5I$ ($0.1 \leq x \leq 0.7$) and (b) $Li_{6+x}M_xSb_{1-x}S_5I$ (M = Sn, x= 0.2; M = Ge; $0.1 \leq x \leq 0.4$). All reflections correspond to the respective argyrodite phase except for the trace impurities as marked.

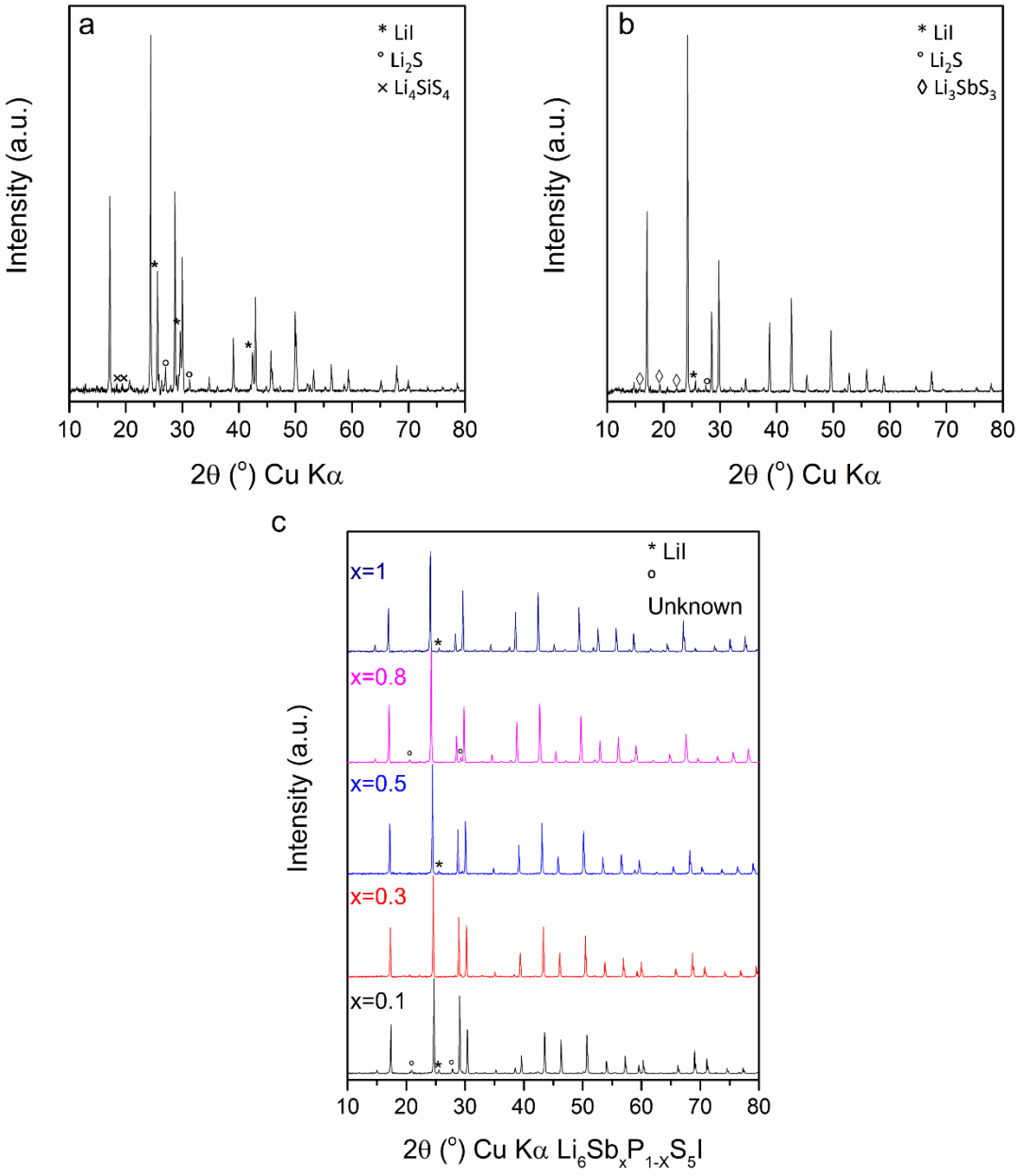

Figure 4.2 X-ray diffraction patterns of as-synthesized (a) $Li_{6.8}Si_{0.8}Sb_{0.2}S_5I$ and (b) $Li_{6.45}Ge_{0.45}Sb_{0.55}S_5I$, with impurities present, indicate the respective solubility limits; (c) X-ray diffraction patterns of as-synthesized $Li_6Sb_xP_{1-x}S_5I$ ($0 \leq x \leq 1$), all reflections correspond to the respective argyrodite phase except the trace impurities as marked.

4.4 Ionic Conductivity and Li ion transport

Temperature-dependent impedance spectroscopy measurements were performed to determine the ionic conductivity of cold-pressed *as-synthesized* $Li_{6+x}M_xSb_{1-x}S_5I$ (M=Si, Sn, Ge) and the activation energy for Li ion transport (**Figure 4.3-4.6**). Arrhenius plots for all samples of $Li_{6+x}M_xSb_{1-x}S_5I$ (M=Si, Sn, Ge) are shown in **Figure 4.3f** and **Figure 4.5i,** and the activation energies are summarized in **Table 4.2**. Due to the high ionic conductivity of many of these phases, bulk and grain boundary contributions cannot be deconvoluted at room temperature. **Figure 4.3e, f** shows the ionic conductivities of cold-pressed *as-synthesized* $Li_{6+x}Si_xSb_{1-x}S_5I$ and the extracted activation energy barriers for Li ion diffusion, as measured by impedance spectroscopy **(Figure 4.4)**. With increasing Si^{4+}+Li^+ content, the ionic conductivity increases dramatically, accompanied by a decrease in the activation energy from 0.41 eV (at x = 0) to about 0.25 eV (**Figure 4.3e**). The highest ionic conductivities were obtained in the range x = 0.6 - 0.7 of 9.4 and 11.2 $mS.cm^{-1}$, respectively; annealing these two materials **(Figure 4.7**) further improved the cold-pressed pellet conductivity to 14.8 (x = 0.6) and 12.6 $mS.cm^{-1}$ (x = 0.7). The ionic conductivity data for the cold-pressed pellets of *as-synthesized* and *annealed* materials is summarized in **Tables 4.2** and **4.3**. The sintered pellets of x = 0.6, 0.7 exhibit an even higher ion conductivity, up to 24 $mS.cm^{-1}$ for $Li_{6.6}Si_{0.6}Sb_{0.4}S_5I$, due to improved grain boundary contact (**Figure 4.8** and **Table 4.4**) as discussed below. For the Sn^{4+} and Ge^{4+} substituted samples $Li_{6+x}(Ge/Sn)_xSb_{1-x}S_5I$, a similar trend (**Figure 4.5**)is observed with increasing x but the corresponding conductivities are lower; the highest value reaches 6.25 $mS.cm^{-1}$ for $Li_{6.4}Ge_{0.4}Sb_{0.6}S_5I$, and 0.12 $mS.cm^{-1}$ for $Li_{6.2}Sn_{0.2}Sb_{0.8}S_5I$ (**Figure 4.6** and **Table 4.2**).

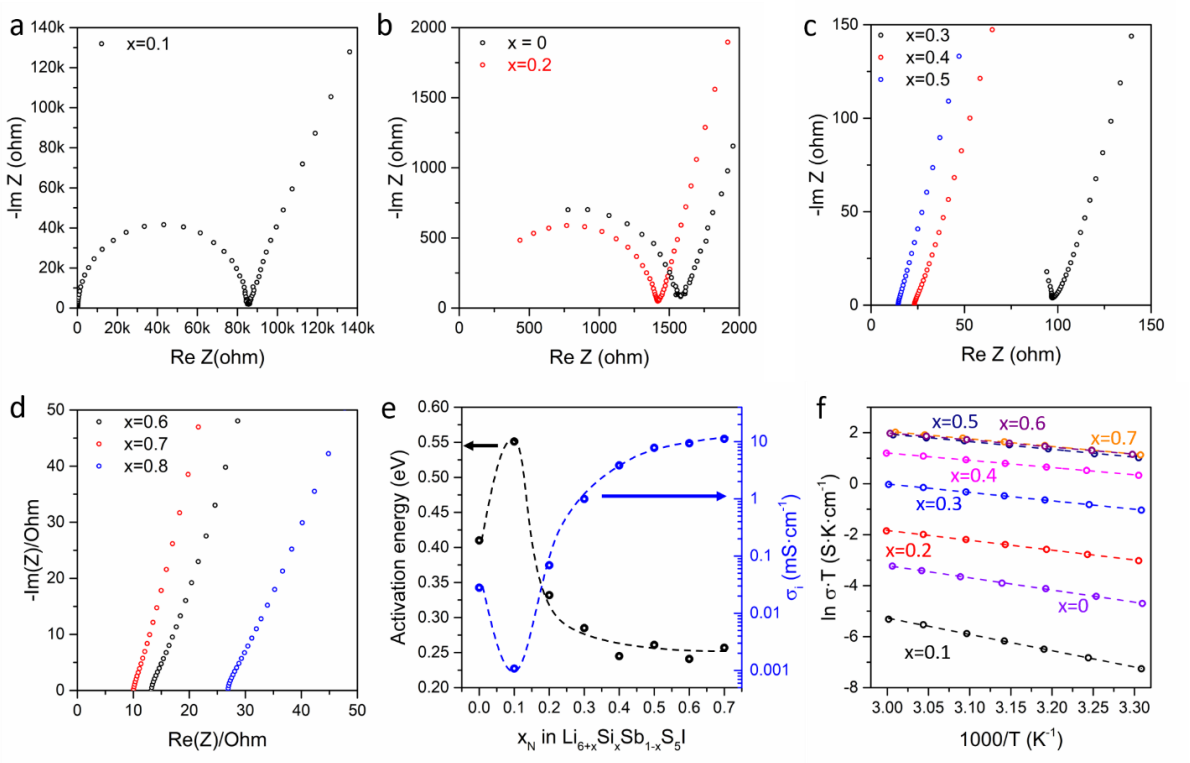

Figure 4.3 Nyquist plots (a) x = 0.1, (b) x= 0, 0.2, (c) x = 0.3, 0.4, 0.5 and (d) x = 0.6, 0.7, 0.8 for all degrees of substitution in the solid solution series $Li_{6+x}Si_xSb_{1-x}S_5I$ at room temperature; (e) activation energy and ionic conductivities of cold pressed as-synthesized $Li_{6+x}Si_xSb_{1-x}S_5I$ as a function of nominal Si^{4+} content (curves show the trend, and are not a fit of the data); (f) Arrhenius plots of the conductivity values for $Li_{6+x}Si_xSb_{1-x}S_5I$ in the temperature range from 30°C to 60°C. The anomalous low conductivity/high E_a value for x = 0.1 may be the result of an amorphous insulating material in the grain boundary.

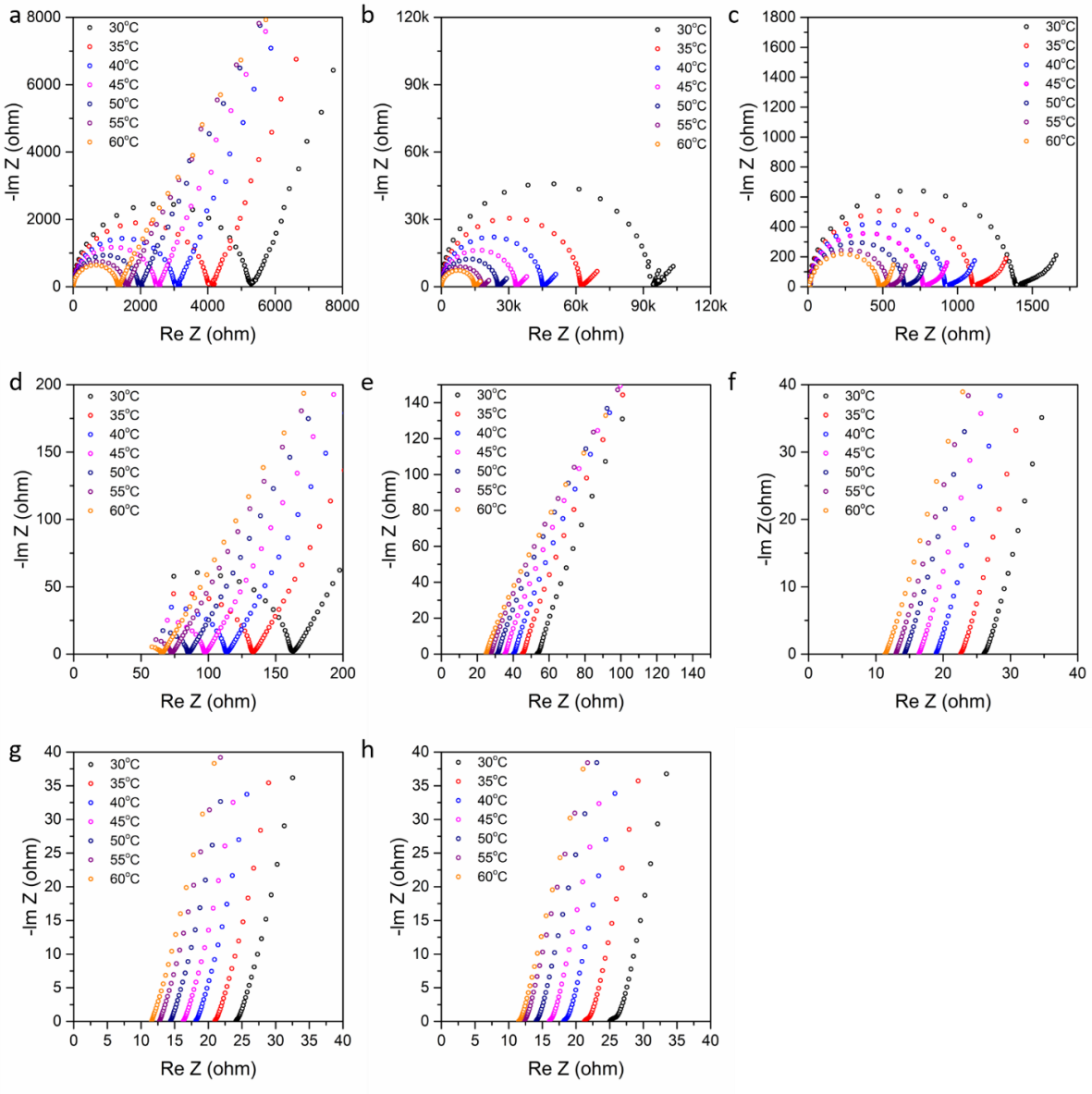

Figure 4.4 Nyquist plots at each temperature used to extract the conductivity values for activation energy measurements of the $Li_{6+x}Si_xSb_{1-x}S_5I$ phases (a) x = 0; (b) x = 0.1; (c) x = 0.2; (d) x = 0.3; (e) x = 0.4; (f) x = 0.5; (g) x = 0.6; (h) x = 0.7.

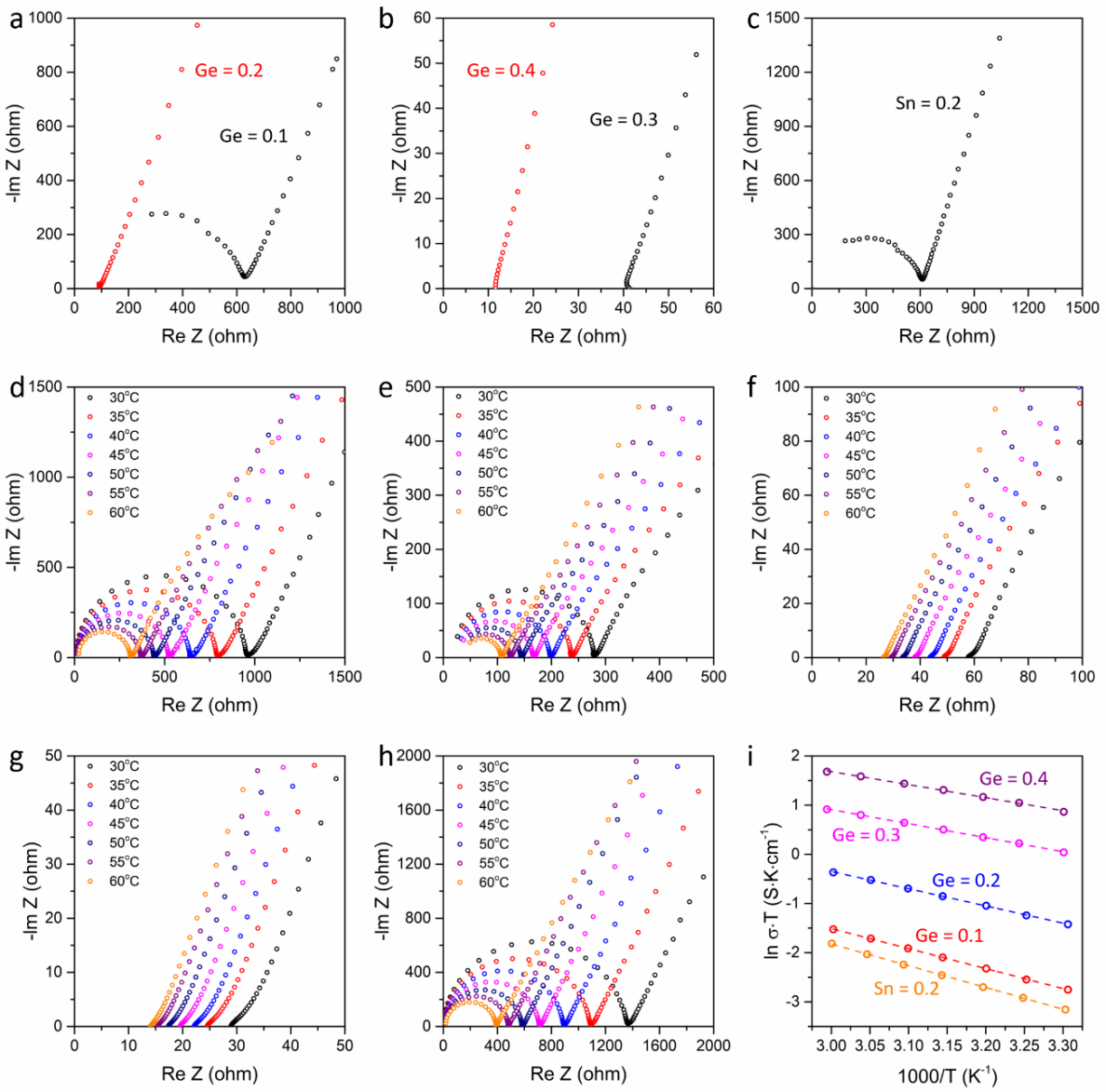

Figure 4.5 Nyquist plots for cold-pressed as-synthesized $Li_{6+x}Ge_xSb_{1-x}S_5I$ (a) x = 0.1, 0.2 and (b) x = 0.3, 0.4 and (c) $Li_{6.2}Sn_{0.2}Sb_{0.8}S_5I$ at room temperature. Nyquist plots at each temperature used to extract the conductivity values for activation energy measurements of (d) $Li_{6.1}Ge_{0.1}Sb_{0.9}S_5I$; (e) $Li_{6.2}Ge_{0.2}Sb_{0.8}S_5I$; (f) $Li_{6.3}Ge_{0.3}Sb_{0.7}S_5I$; (g) $Li_{6.4}Ge_{0.4}Sb_{0.6}S_5I$; (h) $Li_{6.2}Sn_{0.2}Sb_{0.8}S_5I$; and (i) corresponding Arrhenius plots of the conductivity values in the temperature range from 30 ºC to 60 ºC.

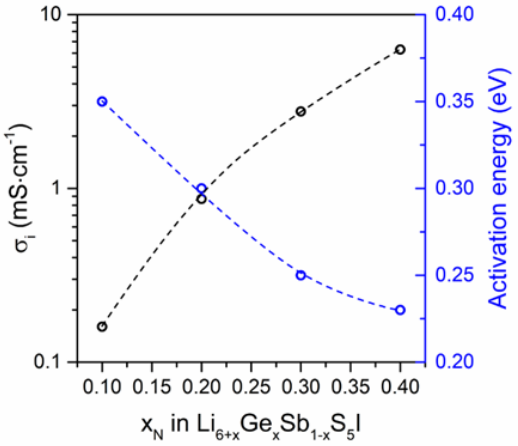

Figure 4.6 Activation energy and ionic conductivities of cold pressed $Li_{6+x}Ge_xSb_{1-x}S_5I$ as a function of nominal Ge^{4+} content (curves show the trend and are not a fit of the data).

Table 4.2 Ionic conductivity of cold-pressed *as-synthesized* (non-annealed) $Li_6Sb_xP_{1-x}S_5I$ and $Li_{6+x}M_xSb_{1-x}S_5I$ (M=Si, Ge, Sn) at room temperature and activation energy for selected compositions. The refined Si: Sb occupancy from synchrotron diffraction is shown in brackets.

Composition	Ionic conductivity ($mS.cm^{-1}$)	Activation energy (eV)
Li_6PS_5I	2.9×10^{-3}	
$Li_6Sb_{0.1}P_{0.9}S_5I$	1.4×10^{-3}	
$Li_6Sb_{0.3}P_{0.7}S_5I$	1.2×10^{-3}	
$Li_6Sb_{0.5}P_{0.5}S_5I$	2.1×10^{-3}	
$Li_6Sb_{0.8}P_{0.2}S_5I$	5.5×10^{-3}	
Li_6SbS_5I	2.8×10^{-2}	0.41
$Li_{6.1}Si_{0.1}Sb_{0.9}S_5I$	1.1×10^{-3}	0.55
$Li_{6.2}Si_{0.2}Sb_{0.8}S_5I$	6.9×10^{-2}	0.33
$Li_{6.3}Si_{0.3}Sb_{0.7}S_5I$	0.93	0.29
$Li_{6.4}Si_{0.4}Sb_{0.6}S_5I$	3.9	0.25
$Li_{6.5}Si_{0.5}Sb_{0.5}S_5I$	7.8	0.26
$Li_{6.6}Si_{0.6}Sb_{0.4}S_5I$	9.4	0.24
$Li_{6.7}Si_{0.7}Sb_{0.3}S_5I$	11.2	0.26
$Li_{6.2}Sn_{0.2}Sb_{0.8}S_5I$	0.12	0.38
$Li_{6.1}Ge_{0.1}Sb_{0.9}S_5I$	0.16	0.35
$Li_{6.2}Ge_{0.2}Sb_{0.8}S_5I$	0.87	0.30
$Li_{6.3}Ge_{0.3}Sb_{0.7}S_5I$	2.77	0.25
$Li_{6.4}Ge_{0.4}Sb_{0.6}S_5I$	6.3	0.23

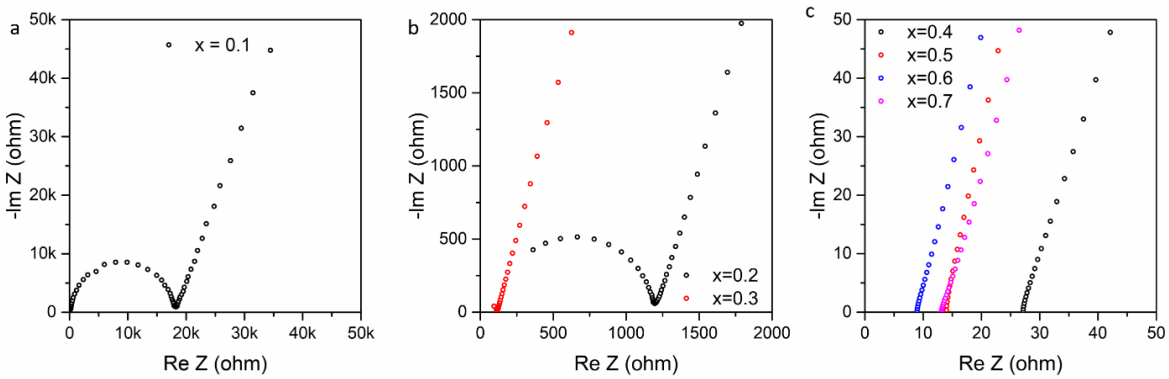

Figure 4.7 Nyquist plots for cold-pressed annealed $Li_{6+x}Si_xSb_{1-x}S_5I$ (a) x = 0.1; (b) x = 0.2, 0.3 and (b) x = 0.4 - 0.7.

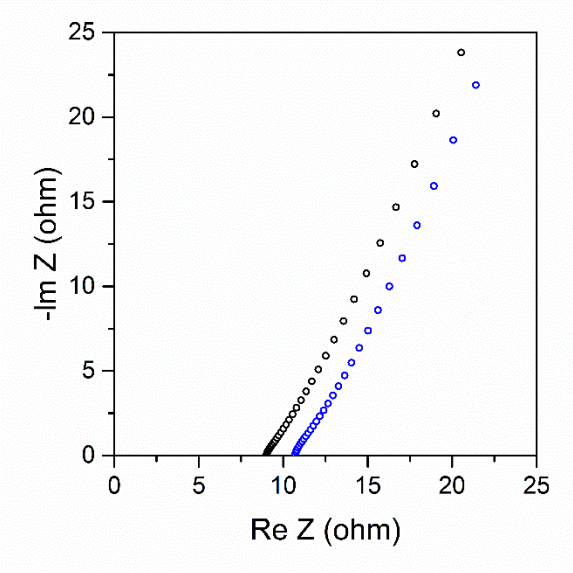

Figure 4.8 Nyquist plots for sintered pellets of $Li_{6.6}Si_{0.6}Sb_{0.4}S_5I$ (black circles) and $Li_{6.7}Si_{0.7}Sb_{0.3}S_5I$ (blue circles) at room temperature.

Table 4.3 Ionic conductivity of *annealed* $Li_{6+x}Si_xSb_{1-x}S_5I$ ($0.1 \leq x \leq 0.7$) (cold pressed pellets) at room temperature.

Composition	Ionic conductivity ($mS.cm^{-1}$)
$Li_{6.1}Si_{0.1}Sb_{0.9}S_5I$	6.7×10^{-3}
$Li_{6.2}Si_{0.2}Sb_{0.8}S_5I$	8.8×10^{-2}
$Li_{6.3}Si_{0.3}Sb_{0.7}S_5I$	1.03
$Li_{6.4}Si_{0.4}Sb_{0.6}S_5I$	4.14
$Li_{6.5}Si_{0.5}Sb_{0.5}S_5I$	9.98
$Li_{6.6}Si_{0.6}Sb_{0.4}S_5I$	14.8
$Li_{6.7}Si_{0.7}Sb_{0.3}S_5I$	12.6

Table 4.4 Ionic conductivity of *annealed* $Li_{6+x}Si_xSb_{1-x}S_5I$ ($x = 0.6, 0.7$) (sintered pellets) at room temperature.

Composition	Ionic conductivity ($mS.cm^{-1}$)
$Li_{6.6}Si_{0.6}Sb_{0.4}S_5I$	24
$Li_{6.7}Si_{0.7}Sb_{0.3}S_5I$	19

To determine the grain boundary resistance, low temperature (195 K) measurements were conducted for selected Si-substituted compositions. **Figure 4.9a** shows Nyquist plots for $Li_{6+x}Si_xSb_{1-x}S_5I$ ($x = 0.4 - 0.7$). They exhibit two slightly depressed semicircles at high and mid frequencies and a clear polarization spike at low frequencies. The spectra were fit with an equivalent circuit consisting of a serial connection of two parallel arrangements of a resistor (R) and a constant phase element (CPE, Q), representing the conductive and capacitive behaviors of the SE, respectively, and an additional CPE component for polarization. For $Li_{6.7}Si_{0.7}Sb_{0.3}S_5I$, the capacitance of the high frequency semicircle is about two orders of magnitude lower than that for mid-frequency semicircle (details of the fits are listed in **Table**

4.5). Thus, the high-frequency semicircle is attributed to bulk (*i.e.*, grain) conductivity and the mid-frequency semicircle is attributed to the grain boundary resistance **(Figure 4.9a)**. At this low temperature of 195 K, significant grain boundary resistance was observed for all materials, as summarized in **Table 4.7**. Because the grain boundary conductivity is about eight-fold lower than the bulk in all cases, it significantly lowers the total ionic conductivity. This explains why sintered pellets exhibit much higher ionic conductivity (see above),[67, 135, 136, 144] which enhances grain boundary contact. Nonetheless, even at 195 K, all these materials still exhibit high bulk ionic conductivity > 0.1 mS.cm^{-1} which is significantly higher than of an organic electrolyte at that temperature (**Figure 4.9a**). For the Ge^{4+} substituted sample $Li_{6.4}Ge_{0.4}Sb_{0.6}S_5I$, relatively high grain boundary resistance was also observed as shown in **Figure 4.9b** and **Table 4.6**.

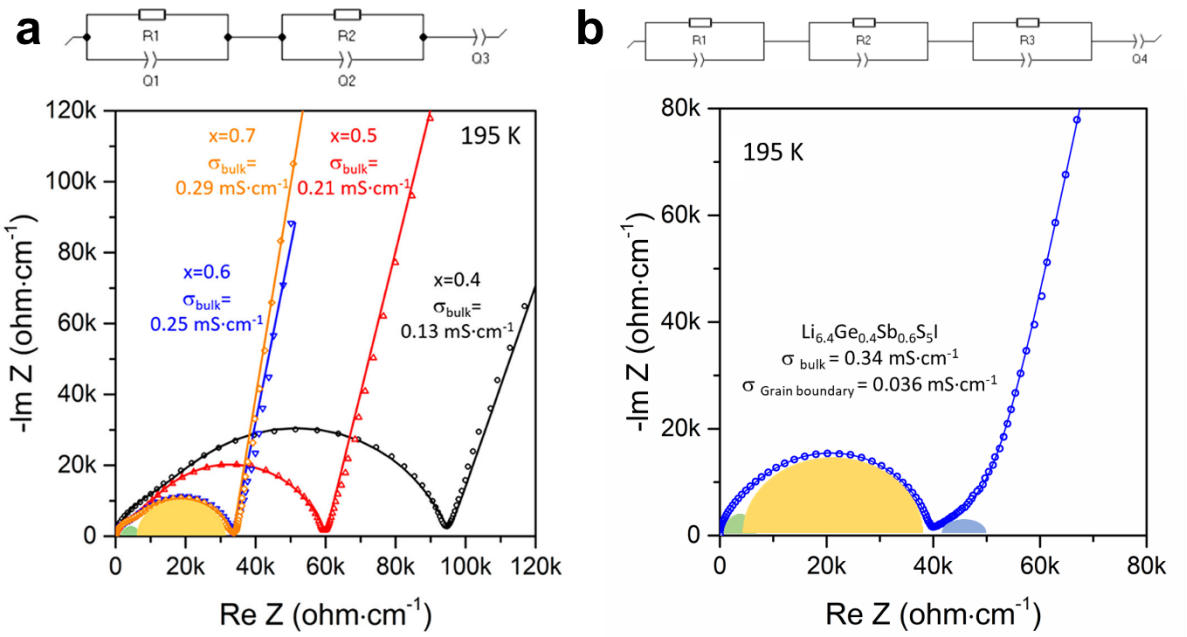

Figure 4.9 Low temperature (195 K) Nyquist plots for (a) $Li_{6+x}Si_xSb_{1-x}S_5I$ (x = 0.4, 0.5, 0.6, 0.7) and (b) $Li_{6.4}Ge_{0.4}Sb_{0.6}S_5I$ show two semicircles, corresponding to bulk and grain boundary contributions. The third semicircle (grey-blue) is ascribed to the contact between the SE pellet and In foil owing to its capacitance value. The data were fit (shown by the line) with the indicated equivalent circuit.

Owing to the high ionic conductivity of the Si-substituted compositions, this family was targeted for single crystal, and powder X-ray synchrotron and neutron diffraction studies in order to correlate structure-property relationships as described below.

Table 4.5 Parameters of the fit for the impedance data of $Li_{6+x}Si_xSb_{1-x}S_5I$ (x= 0.4, 0.5, 0.6, 0.7) at 195 K; fitting parameters errors are shown in brackets.

Element	**$Li_{6.4}Si_{0.4}Sb_{0.6}S_5I$**	**$Li_{6.5}Si_{0.5}Sb_{0.5}S_5I$**	**$Li_{6.6}Si_{0.6}Sb_{0.4}S_5I$**	**$Li_{6.7}Si_{0.7}Sb_{0.3}S_5I$**
Resistance (R1) / ohm	1952.8 (92.5)	1138.3 (26.2)	1016.1 (27.1)	909.19 (38.5)
CPE (Q1) /S·s$^{-\alpha}$	2.0(4) x 10^{-9}	1.0(2) x 10^{-9}	7(1) x 10^{-10}	2.5(6) x 10^{-10}
CPE Alpha (α1)	0.89(2)	0.91(1)	0.93(1)	1.00(2)
Resistance (R2) /ohm	16030 (107)	10066 (33.6)	5588.4 (31)	6050.5 (45)
CPE (Q2) / S·s$^{-\alpha}$	1.42(4) x 10^{-8}	1.12(3) x 10^{-8}	7.5(2) x 10^{-9}	1.12(5) x 10^{-8}
CPE Alpha (α2)	0.782(4)	0.817(3)	0.842(3)	0.798(5)
CPE (Q3)/ S·s$^{-\alpha}$	4.20(2) x 10^{-5}	5.35(2) x 10^{-5}	8.65(3) x 10^{-5}	5.59(2) x 10^{-5}
CPE Alpha (α3)	0.785(3)	0.844(2)	0.873(2)	0.895(2)

Table 4.6 Parameters of the fit for the impedance data of $Li_{6.4}Ge_{0.4}Sb_{0.4}S_5I$ at 195 K; fitting parameters errors are shown in brackets.

Element	**$Li_{6.4}Ge_{0.4}Sb_{0.6}S_5I$**
Resistance (R1) / ohm	660.02 (49.6)
CPE (Q1) / S·s$^{-\alpha}$	1.5(3) x 10^{-9}
CPE Alpha (α1)	0.99(2)
Resistance (R2) /ohm	6332.8 (57.6)
CPE (Q2) / S·s$^{-\alpha}$	3.67(8) x 10^{-9}
CPE Alpha (α2)	0.886(3)
Resistance (R3) /ohm	2394.7 (153)
CPE (Q3) / S·s$^{-\alpha}$	6.7(6) x 10^{-5}
CPE Alpha (α3)	0.55(2)
CPE (Q4)/ S·s$^{-\alpha}$	9.86(6) x 10^{-5}
CPE Alpha (α4)	0.873(5)

Table 4.7 Bulk and grain boundary conductivities of *as-synthesized* $Li_{6+x}Si_xSb_{1-x}S_5I$ (x = 0.4 - 0.7, cold-pressed pellets) at 195 K.

Compositions	Bulk conductivity ($mS.cm^{-1}$)	Grain boundary conductivity ($mS.cm^{-1}$)
$Li_{6.7}Si_{0.7}Sb_{0.3}S_5I$	0.29	0.044
$Li_{6.6}Si_{0.6}Sb_{0.4}S_5I$	0.25	0.045
$Li_{6.5}Si_{0.5}Sb_{0.5}S_5I$	0.21	0.024
$Li_{6.4}Si_{0.4}Sb_{0.}$ 5I	0.13	0.015

4.5 Structural characterization of $Li_{6+x}(Si/Ge/Sn)_xSb_{1-x}S_5I$ and ion diffusion pathways

Li-argyrodite $Li_{6+x}Si_xSb_{1-x}S_5I$ ($0.1 \leq x \leq 0.7$) superionic conductors were synthesized with varying Si^{4+}/Sb^{5+} ratios in order to study the structural changes and assess the effect of increasing Li^+ content on the ionic conductivity. Single crystal diffraction was performed for crystals obtained at selected compositions (x = 0.1, 0.4, 0.5, 0.7) to determine the changes in Li site and S^{2-}/I^- disorder. As small compositional variance from crystal to crystal is always possible, powder synchrotron X-ray diffraction measurements were then conducted for all compositions to evaluate the overall sample purity, the solubility limit of Si^{4+}, and the degree of S^{2-}/I^- disorder. Due to the superionic conductivity of the Si-substituted compositions (*i.e.*, very high Li ion mobility), and hence possible location of some Li on alternative sites in the lattice that cannot be easily refined owing to very low occupation, single crystal diffraction results show slightly lower Li^+ content than experimental targeted values. Neutron powder diffraction measurements (300 K) were carried out to determine the Li^+ position and occupancy changes with different Si^{4+} content on selected compositions (x = 0, 0.3, 0.5, 0.7). In addition, low temperature (195 K) neutron powder diffraction was also conducted on $Li_{6.7}Si_{0.7}Sb_{0.3}S_5I$ to freeze the Li^+ mobility, thus allowing more accurate determination of the Li position and occupation.

The structure of the composition with the highest conductivity, $Li_{6.7}Si_{0.7}Sb_{0.3}S_5I$ (refined composition $Li_{6.77}Si_{0.66}Sb_{0.34}S_{5.01}I_{0.99}$) from the neutron diffraction study (**Figure 4.10d**) is shown in **Figure 4.11a, b, c** and compared to that of the classic phosphorus argyrodite Li_6PS_5I (**Figure 4.11d, e**)[66]. The unit cell of the antimony phases adopts the same cubic space group $F\bar{4}3m$ as Li_6PS_5I (a = 10.1414(1) Å), but with a larger lattice parameter of a = 10.3231(1) Å, and a different Li sublattice (four Li^+ sites) than typical Li-argyrodite materials. Li ions still diffuse via three discrete jumps (doublet, intra and inter cage jumps) as for classic argyrodite Li_6PS_5X (X= Cl, Br, I), as shown in **Figure 4.11e**.[140] The difference is that a new Li3(48*h*) site is identified in $Li_{6.7}Si_{0.7}Sb_{0.3}S_5I$ which resides between the intra-cage jump sites

Table 4.8 Atomic coordinates, occupation factors, and isotropic displacement parameter of representative $Li_{6.7}Si_{0.7}Sb_{0.3}S_5I$ obtained from powder neutron diffraction at 300 K.

a = 10.32309(5) Å, 4.32 wt% Li_2S, 6.43 wt% LiI						
Atom	Wyck. Site	x	y	z	Occ.	U_{iso} (Å^2)
Li1	48*h*	0.290(1)	0.5175(9)	0.790(1)	0.29(2)	0.034(3)
Li2	24*g*	0.021(1)	0.25	0.25	0.34(3)	0.032(5)
Li3	48*h*	0.732(3)	0.067(2)	0.567(2)	0.097(9)	0.08(1)
Li4	4*d*	0.75	0.25	0.25	0.04(1)	0.01(2)
Si1	4*b*	0.5	0.5	0.5	0.655	0.0123(3)
Sb1	4*b*	0.5	0.5	0.5	0.345	0.0123(3)
S1	4*c*	0.25	0.25	0.25	0.983	0.0157(5)
S2	16*e*	0.3771(2)	0.3771(2)	0.6229(2)	1	0.0234(3)
S3	4*a*	0.5	0.5	0	0.026	0.0385(5)
I1	4*a*	0.5	0.5	0	0.974	0.0385(5)
I2	4*c*	0.25	0.25	0.25	0.017	0.0157(4)

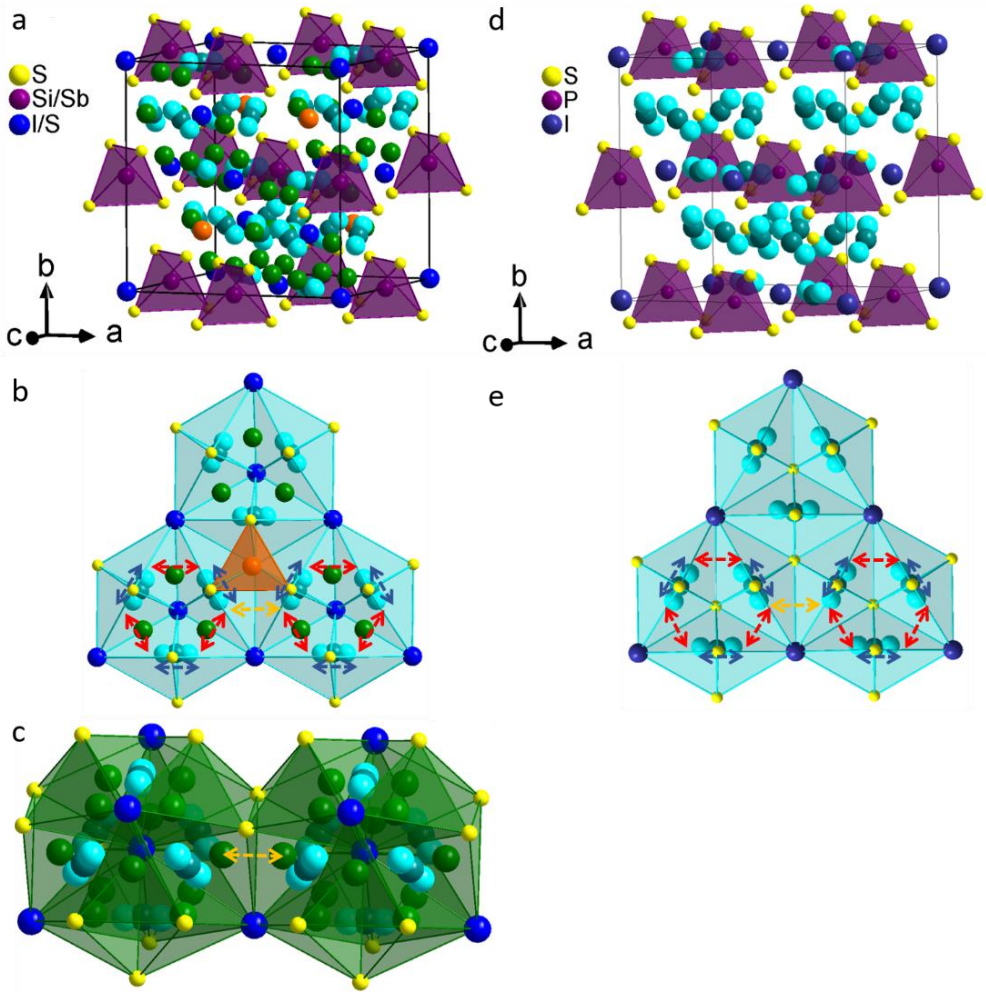

Figure 4.10 (a) Crystal structure of $Li_{6.7}Si_{0.7}Sb_{0.3}S_5I$ from powder neutron diffraction at 300 K, showing the fully occupied S (16e) site and the 2.6 and 1.7% S^{2-}/I^- (4*a*, 4*c*) mixed occupied site. $(Sb/Si)S_4$ tetrahedra are shown in dark violet. Four Li^+ sites exist: Li1(48*h*) - turquoise, Li2(24*g*) - teal, Li3(48*h*) - green, Li4(4*d*) - orange; (b) Li ion diffusion showing the discrete jumps: the doublet jump (Li1(48*h*)-Li1(48*h*) within bipyramids passing through Li2(24*g*), blue arrow), intracage jump (Li1(48*h*)-Li1(48*h*) within cage passing through the Li3(48h) site, red arrow) and intercage jump (Li1(48*h*)-Li1(48*h*) between cages, orange arrow); (c) new intercage jump Li3(48*h*)-Li3(48*h*) between cages is shown by the orange arrow; (d) crystal structure of Li_6PS_5I from ref. 57 is shown for comparison, with a fully ordered S (16*e*, 4*c*) and I (4a) arrangement. PS_4 tetrahedra are depicted in violet. The Li ion forms pseudo-octahedral cages (four/unit cell) with two crystallographically distinct sites, Li1(48*h*) and Li2(24*g*); (d) Li ion diffusion by discrete jumps: doublet jump (Li1(48*h*)-Li1(48*h*) within bipyramids passing through the Li2(24*g*) site, blue arrow); intracage jump (Li1(48*h*)-Li1(48*h*) within the cage, red arrow) and intercage jump (Li1(48*h*)-Li1(48*h*), orange arrow).

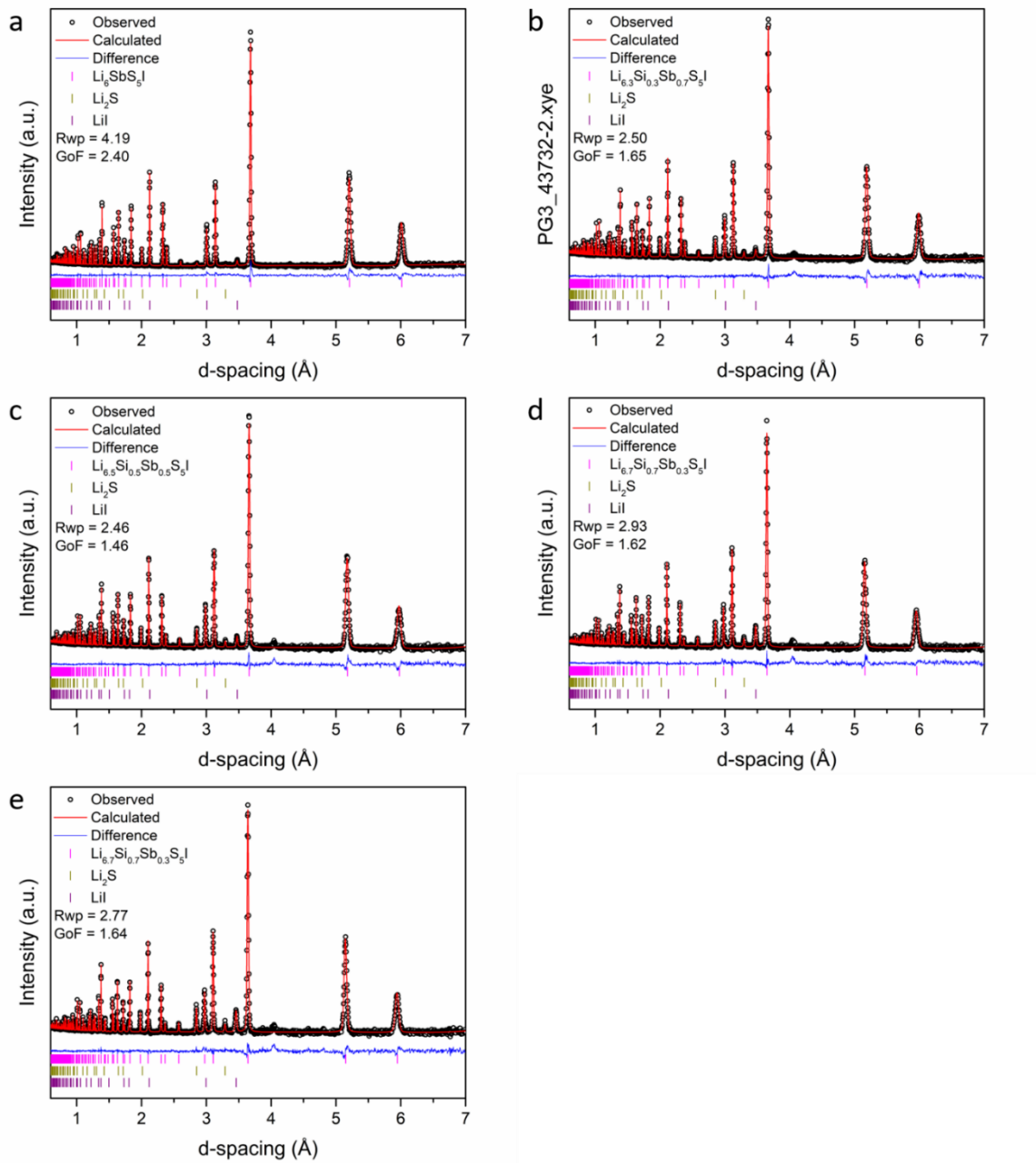

Figure 4.11 Time-of-flight neutron diffraction patterns and the corresponding Rietveld refinement fits of (a) Li_6SbS_5I, (b) $Li_{6.3}Si_{0.3}Sb_{0.7}S_5I$, (c) $Li_{6.5}Si_{0.5}Sb_{0.5}S_5I$, and (d) $Li_{6.7}Si_{0.7}Sb_{0.3}S_5I$ at 300 K and (e) $Li_{6.7}Si_{0.7}Sb_{0.3}S_5I$ at195 K. Experimental data are shown in black circles; the red line denotes the calculated pattern; the difference profile is shown in blue and calculated positions of the Bragg reflections are shown as vertical ticks. R_{wp} and GoF are the weighted profile R-factor and goodness of fit, respectively.

(**Figure 4.11b**). This Li3(48*h*) site also creates a new inter-cage jump pathway (directly through the face shared Li3(48*h*) tetrahedra, as shown in **Figure 4.11c**. The crystallographic details of $Li_{6.7}Si_{0.7}Sb_{0.3}S_5I$ and $Li_{6+x}Si_xSb_{1-x}S_5I$ (x=0, 0.3, 0.5) phases are summarized in **Table 4.8** and **B1-4**. The structure exhibits one crystallographically distinct Sb/Si site for all compositions (x), which is partially occupied by Si (up to 70% in $Li_{6.7}Si_{0.7}Sb_{0.3}S_5I$) and is tetrahedrally coordinated by four S atoms. The refined lattice parameter (**Figure 4.12a**), $(Si_xSb_{1-x})S_4$ tetrahedral volume, and (Si_xSb_{1-x})-S bond distance (**Figure 4.12b**) from single crystal XRD (**Table B13-20**) and synchrotron XRD (**Table B5-12**) all decrease nearly linearly with increasing (Si^{4+} + Li^+) content in $Li_{6+x}Si_xSb_{1-x}S_5I$, indicating the formation of a solid solution in accordance with Vegard's law.

The effect of S^{2-}/I^- site disorder in these materials merit discussion, in light of its proposed role in dictating conductivity in the argyrodites. From single crystal X-ray diffraction results, there is only slight (~1-2) % S^{2-}/I^- site disorder on the 4*a* and 4*c* site for x = 0.1 (**Figure 4.12c**). At higher Li^+/Si^{4+} content (x > 0.1), only site disorder on the 4*a* site can be identified (but not on the 4*c* site) that increases with x to reach 7(1) % for the highly conductive phase (x = 0.7). We note that single crystal diffraction offers superior accuracy in determining the low degree of S^{2-}/I^- site disorder over any powder diffraction techniques. Most importantly, several percent of S^{2-}/I^- site disorder clearly will not lead to a three order of magnitude increase in ionic conductivity compared to the parent phase (x = 0). This is further proved in the Ge and Sn substituted materials. Crystallographic details of $Li_{6+x}Ge_xSb_{1-x}S_5I$ (*x*= 0.2, 0.4) and $Li_{6.2}Sn_{0.2}Sb_{0.8}S_5I$ are summarized in **Table B21-26**) and the S^{2-}/I^- site disorder as a function of *x* and ionic conductivity is shown in **Table 4.9**. For the Ge phase, even though x = 0.2 and 0.4

exhibit essentially the same anion disorder (~ 2.5%) ionic conductivity increases by almost an order of magnitude from 0.87 mS·cm^{-1} for x = 0.2, to 6.3 mS.cm^{-1} for x = 0.4. The Sn phase at x = 0.2 shows a slightly higher disorder but even lower ionic conductivity of 0.12 mS.cm^{-1}. Furthermore, as small compositional variance from crystal to crystal is always possible, powder synchrotron diffraction measurements (**Figure 4.13**) were conducted for annealed

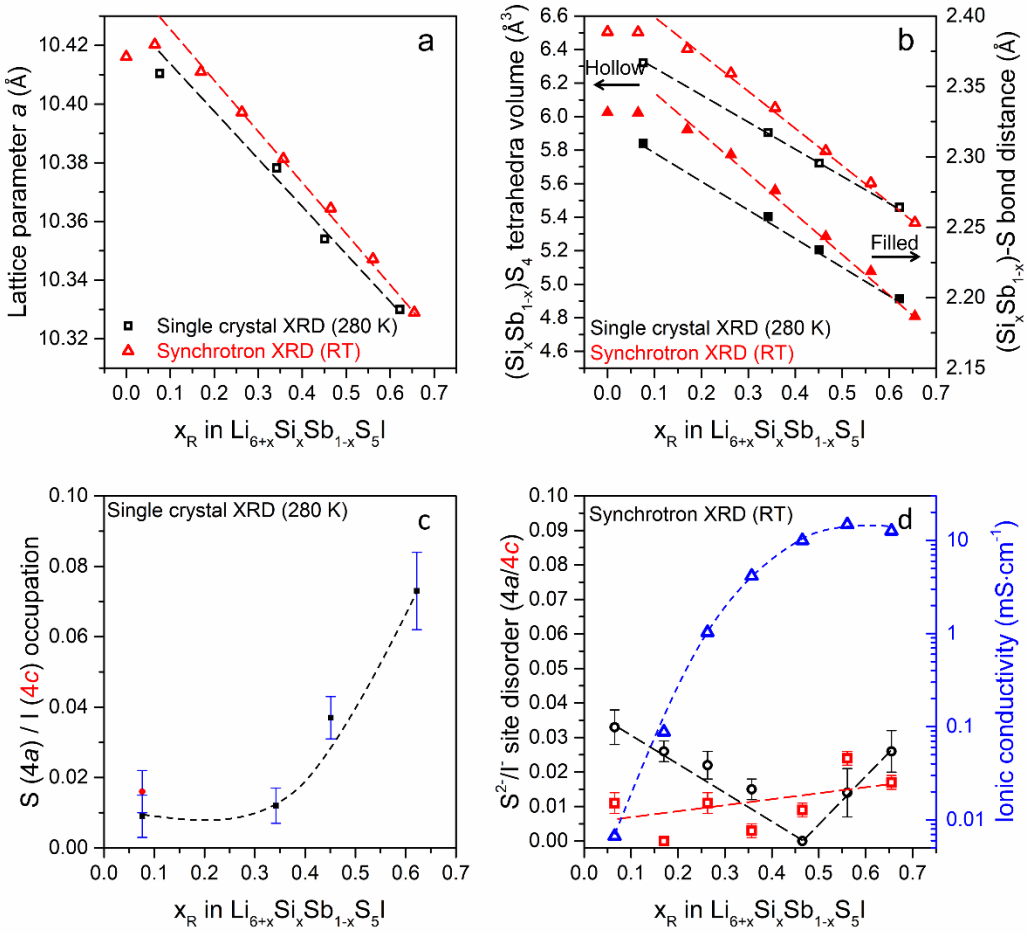

Figure 4.12 (a) lattice parameters, (b) $(Si_xSb_{1-x})S_4$ tetrahedral volume (left, hollow) and (Si_xSb_{1-x})-S bond distance (right, filled) of solid solutions $Li_{6+x}Si_xSb_{1-x}S_5I$ vs refined Si content (x_R) from single crystal XRD at 280 K (black) and synchrotron XRD at room temperature (red) and (c) S^{2-}/I^- disorder vs refined Si content (x_R) from single crystal XRD at 280 K; (d) S^{2-}/I^- site disorder and ionic as a function of refined Si content (x_R) from synchrotron diffraction measurements. Curves show the trend and are not a fit of the data.

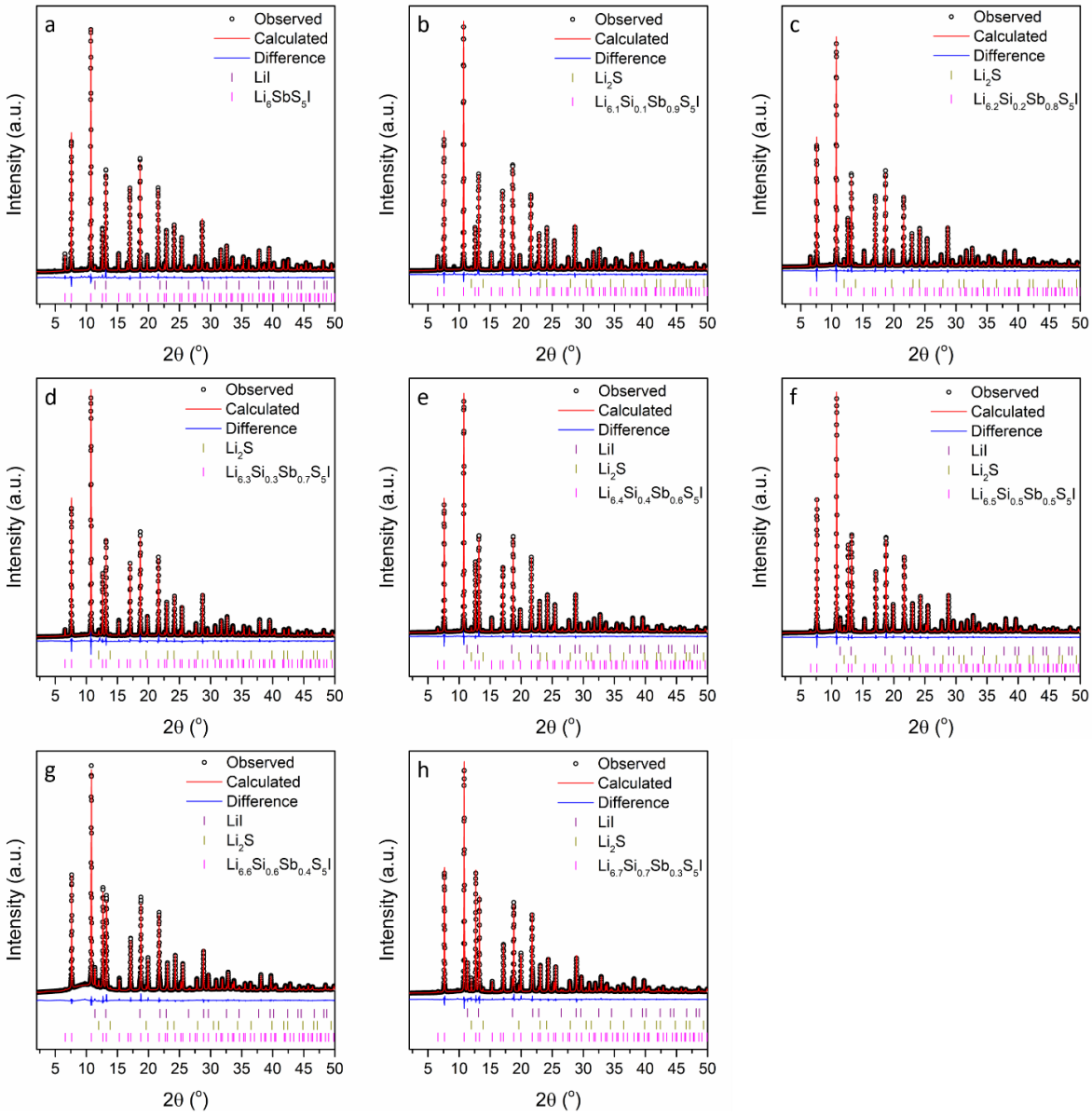

Figure 4.13 Synchrotron diffraction patterns and the corresponding Rietveld refinement fits of (a) Li_6SbS_5I, (b) $Li_{6.1}Si_{0.1}Sb_{0.9}S_5I$, (c) $Li_{6.2}Si_{0.2}Sb_{0.8}S_5I$, (d) $Li_{6.3}Si_{0.3}Sb_{0.7}S_5I$, (e) $Li_{6.4}Si_{0.4}Sb_{0.6}S_5I$, (f) $Li_{6.5}Si_{0.5}Sb_{0.5}S_5I$ and (g) $Li_{6.6}Si_{0.6}Sb_{0.4}S_5I$ and (h) $Li_{6.7}Si_{0.7}Sb_{0.3}S_5I$ at room temperature. Experimental data are shown in black circles; the red line denotes the calculated pattern; the difference profile is shown in blue and calculated positions of the Bragg reflections are shown as vertical ticks.

$Li_{6+x}Si_xSb_{1-x}S_5I$ ($0.1 \leq x \leq 0.7$) compositions. **Figure 4.12d** confirms that upon annealing, there is no obvious correlation between S^{2-}/I^- site disorder and conductivity. Overall, the annealed samples show slightly higher ionic conductivity compared to non-annealed samples but yet all materials exhibit < 3.3 % S^{2-}/I^- site disorder. Thus, the compositions $Li_{6+x}M_xSb_{1-x}S_5I$ (M = Si, Sn, Ge) exhibit very high ionic conductivity with a low degree of S^{2-}/I^- disorder, and the latter is ruled out as a major contributing factor.

Table 4.9 S^{2-}/I^- site disorder from single crystal X-ray diffraction at 280 K and ionic conductivities at room temperature for $Li_{6+x}M_xSb_{1-x}S_5I$ (M=Sn, Ge).

$Li_{6+x}M_xSb_{1-x}S_5I$			
S^{2-}/I^- disorder	M=Sn, x=0.2	M=Ge, x=0.2	M=Ge, x=0.4
4*a* site	1.0(2) %	2.4(6) %	2.6(5) %
4*c* site	4.4(6) %	1.2(7) %	2.2(5) %
Ionic conductivity ($mS.cm^{-1}$)	0.12	0.87	6.3

4.6 Interfacial Stability with Li Metal

The Li plating/stripping behavior and interfacial stability of $Li_{6.7}Si_{0.7}Sb_{0.3}S_5I$ towards a Li metal anode were evaluated in symmetric Li | $Li_{6.7}Si_{0.7}Sb_{0.3}S_5I$ | Li cells. $Li_{6.7}Si_{0.7}Sb_{0.3}S_5I$ exhibited excellent stability with Li metal, exhibiting a steady voltage profile at a current of 0.3 $mA.cm^{-2}$ and capacity of 0.3 $mAh.cm^{-2}$ for 600 hours. At even a higher current of 0.6 $mA.cm^{-2}$ and capacity of 0.6 $mAh.cm^{-2}$, stripping/plating continued up to a total of 1000 hours (**Figure 4.14a**). **Figure 4.14b** shows that the initial cell voltage for the cell cycled at 0.3 $mA.cm^{-2}$ increases slightly from 7.3 mV to 11.3 mV after 600 hours, and then a stable voltage profile at 22.0 mV was observed for another 400 hours at the current density of 0.6 $mA.cm^{-2}$. Nyquist plots of cell impedance are shown in **Figure 4.14c**, directly after contact of the Li metal and SE; after 600 hours cycling at 0.3 $mA.cm^{-2}$; and after an additional 400 hours cycling

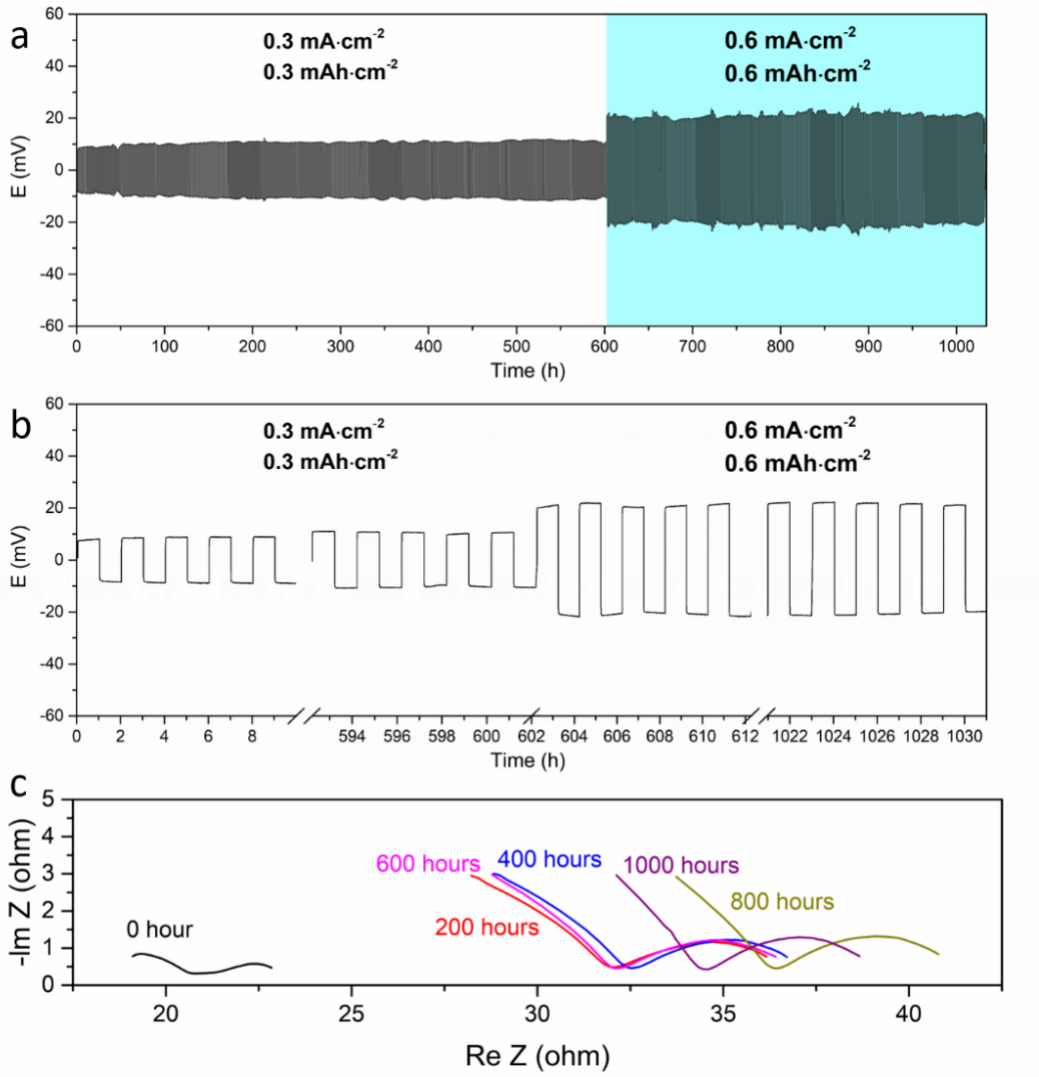

Figure 4.14 (a) the voltage profile of Li^+ plating/stripping in a Li | $Li_{6.7}Si_{0.7}Sb_{0.3}S_5I$ | Li symmetric cell, cycled at different currents and capacities (0.3 $mA.cm^{-2}$ and 0.3 $mAh.cm^{-2}$ for 600 h; 0.6 $mA.cm^{-2}$, 0.6 $mAh.cm^{-2}$ (blue) for another 400 h); (b) enlarged voltage profiles of the Li | $Li_{6.7}Si_{0.7}Sb_{0.3}S_5I$ | Li symmetric cell of the first and last 10 cycles at different current densities; (c) Nyquist plots of the Li | $Li_{6.7}Si_{0.7}Sb_{0.3}S_5I$ | Li symmetric cell: before cycling (0 h, black); cycling at 0.3 $mA.cm^{-2}$ and 0.3 $mAh.cm^{-2}$ for 200 h (red), 400 h (blue) and 600 h (magenta); cycling at 0.6 $mA.cm^{-2}$, 0.6 $mAh.cm^{-2}$ for another 200 h (800 h in total, dark yellow) and 400 h (1000 h in total, purple).

at 0.6 $mA.cm^{-2}$. While the spectra cannot be fit well with an equivalent circuit, it is nonetheless very clear that the total resistivity increases slightly during cycling and then stabilizes at a relatively low value (**Figure 4.14c**). Furthermore, $Li_{6.4}Ge_{0.4}Sb_{0.6}S_5I$ also exhibits relatively

stable Li stripping/plating (albeit at lower current density and capacity) up to 0.3 $mA.cm^{-2}$ and 0.3 $mAh.cm^{-2}$ (**Figure 4.15a**), which is still much more stable compared to other Ge-containing materials such as LGPS or even protected LGPS.[59, 145, 146] At a higher current density of 0.6 $mA.cm^{-2}$ (**Figure 4.15b**), microshorts appear (in contrast to $Li_{6.7}Si_{0.7}Sb_{0.3}S_5I$ at that same current, which exhibits a steady profile). Nyquist plots of cell impedance are shown in **Figure 4.15c**, which shows the total resistivity increases during cycling and then stabilizes. We note that recent work indicates the pressure-dependent critical stripping current can lead to Li voids and dendrite formation, [89] whereas microstructural characteristics of a garnet SE lead to locally differing Li deposition kinetics and morphologies.[147] Further densification, surface polishing of the argyrodite pellet, and control of applied pressure will possibly enable stable Li plating/stripping at even higher current density and capacity. Nevertheless, the stable symmetric cell cycling, steady voltage profile, and stable total resistivity all indicate the formation of a relatively stable interphase between Li metal and $Li_{6.7}Si_{0.7}Sb_{0.3}S_5I$ which is favorable to ultimately develop a long-life Li-metal ASSB.

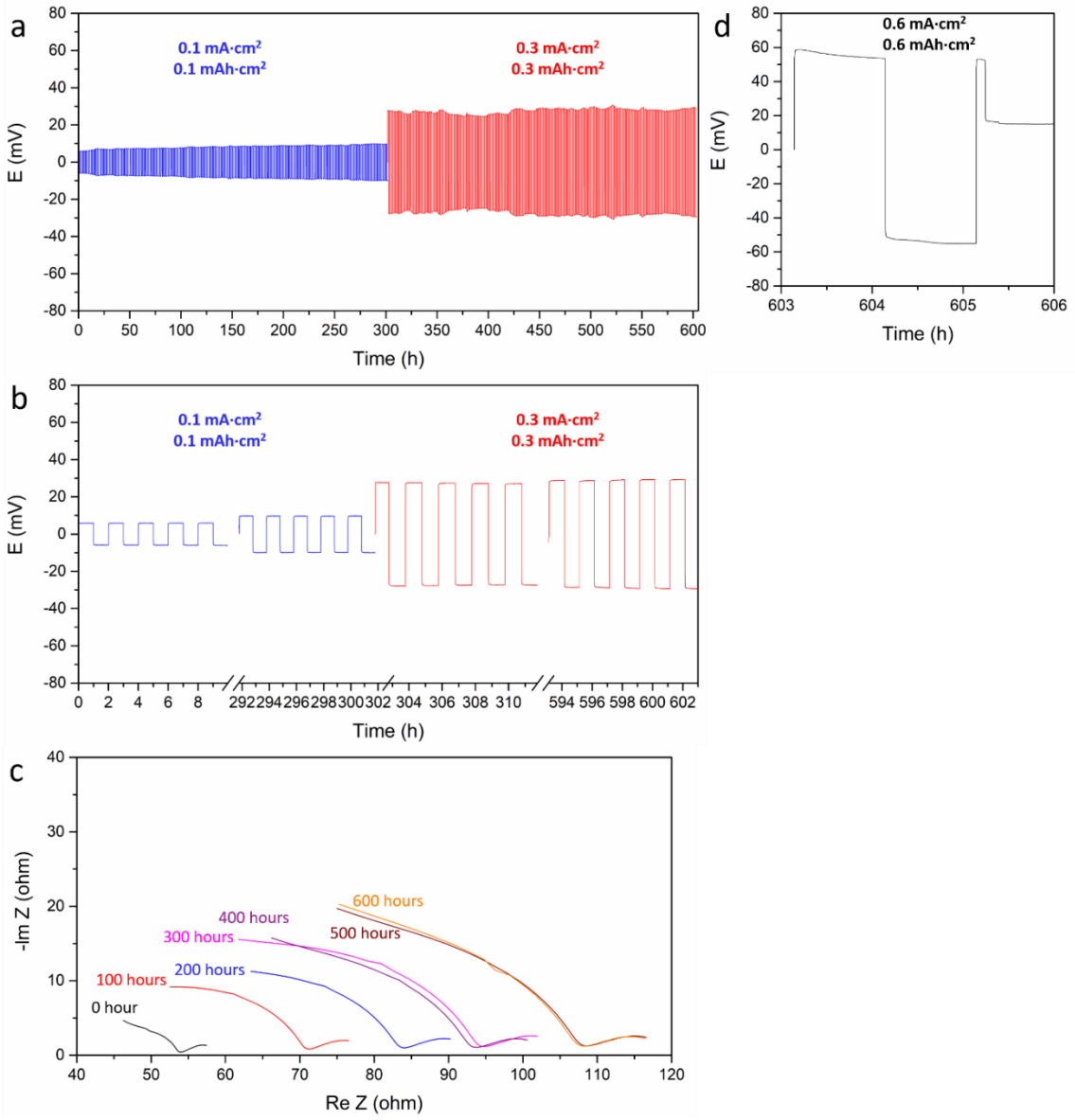

Figure 4.15 (a) the voltage profile of Li^+ plating/stripping in a Li | $Li_{6.4}Ge_{0.4}Sb_{0.6}S_5I$ | Li symmetric cell, cycled at different currents and capacities (0.1 mA.cm^{-2} and 0.1 mAh.cm^{-2} for 300 h; 0.3 mA.cm^{-2}, 0.3 mAh.cm^{-2} for another 300 h); (b) enlarged voltage profiles of the first and last 10 cycles at different current densities; (c) Nyquist plots of the symmetric cell: before cycling (0 h, black); cycling at 0.1 mA.cm^{-2} and 0.1 mAh.cm^{-2} for 100 h (red), 200 h (blue) and 300 h (magenta); cycling at 0.3 mA.cm^{-2}, 0.3 mAh.cm^{-2} for another 100 h (400 h in total, purple), 200 h (500 h in total, wine) and another 300 h (600 h in total, orange); (d) the voltage profile of Li^+ plating/stripping at higher current and capacity (0.6 mA.cm^{-2} and 0.6 mAh.cm^{-2}) which leads to a short circuit after 2 h.

4.7 All Solid-State Batteries Performance

To further evaluate the electrochemical properties of these new superionic conductors, prototype cells were assembled with $Li_{6.7}Si_{0.7}Sb_{0.3}S_5I$, where a Li-In alloy as the negative electrode was paired with TiS_2 or $LiCoO_2$ as the positive. These choices were made in order to more clearly showcase the conductive properties of the SE. Pairing the SE with Li metal and high voltage positive electrodes will be the topic of future work devoted to ASSBs. **Figure 4.16a** shows the 1st, 2nd, 10th, and 20th cycle discharge-charge voltage profiles for the TiS_2 cell cycled at 0.1 C between 0.9 and 2.4 V at room temperature. A highly reversible capacity of 240 $mAh.g^{-1}$ is exhibited, corresponding to the theoretical value for TiS_2. The discharge/charge capacity at different C-rates and the Coulombic efficiencies are displayed in **Figure 16b** (see **Figure 4.16c** for the corresponding voltage profiles). At a practical rate of C/5, the cell still retains almost 100% theoretical capacity after 130 cycles, and delivers ~ 85% capacity (200 $mAh.g^{-1}$) at a C/2 rate. The cell delivers a somewhat lower capacity at 1C (~70% of theoretical capacity), possibly due to the slight oxidation of SE on the 1st charge shown in **Figure 4.16a** (SE oxidation occurs at ~2.1 V vs Li-In). Slow Li-ion diffusion kinetics in the Li-In alloy may also be responsible. Furthermore, a high loading cell (23.8 $mg.cm^{-2}$ TiS_2) also exhibits highly reversible, theoretical capacity (close to 240 $mAh.g^{-1}$) at C/10, as shown in **Figure 4.16d**. The $LiCoO_2$ cell (**Fig. 4.17**) also exhibits relatively stable cycling, though the capacity fades due to an insulating interface build-up between the $LiCoO_2$ and $Li_{6.7}Si_{0.7}Sb_{0.3}S_5I$. This naturally results from oxidation of the SE at the higher voltage of the $LiCoO_2$ positive electrode, since a protective coating layer was not used on the oxide in these

preliminary studies. Overall, the respectable electrochemical performance for the ASSBs using $Li_{6.7}Si_{0.7}Sb_{0.3}S_5I$ highlights its very high room temperature Li ion conductivity.

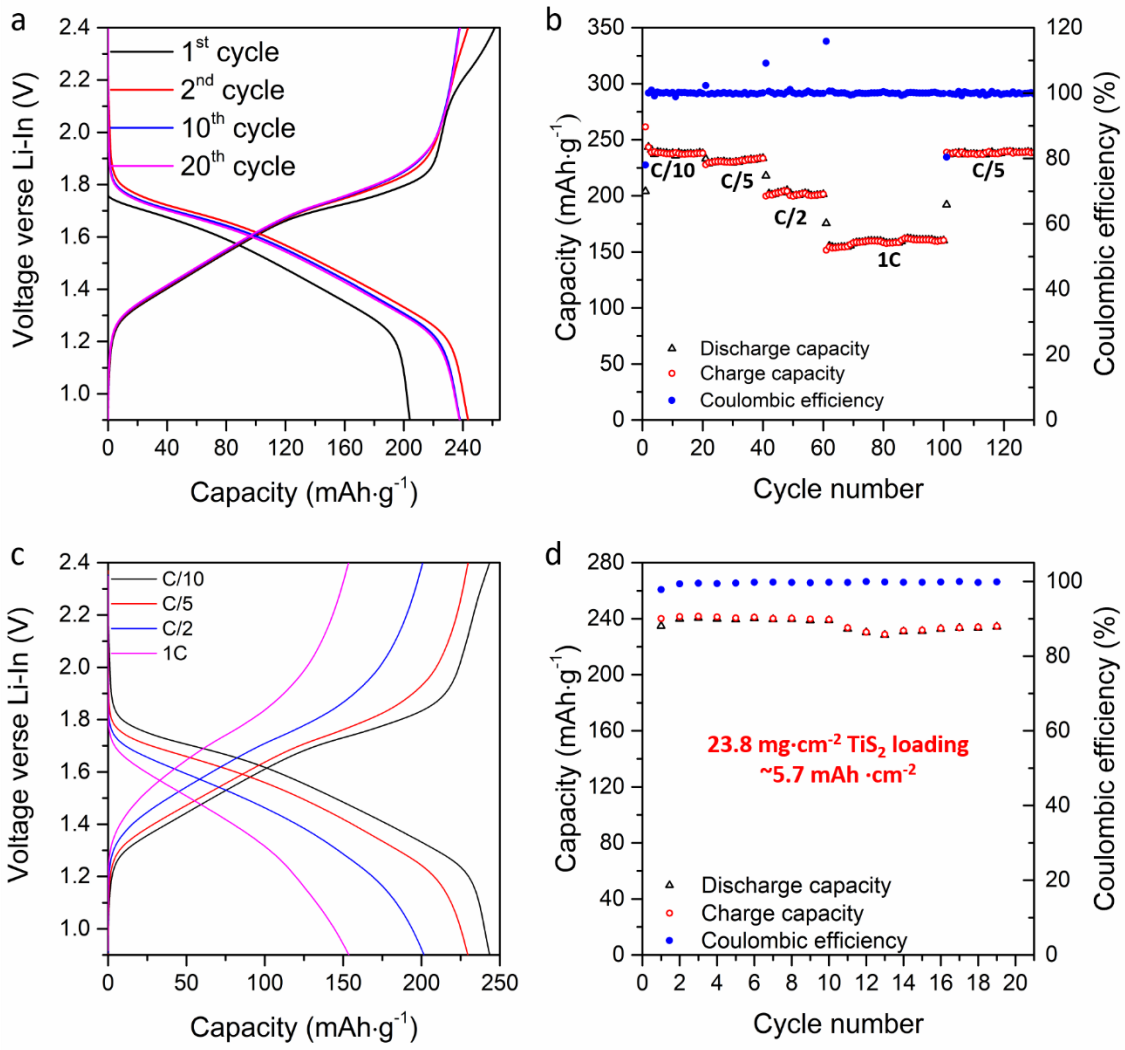

Figure 4.16 Electrochemical performance of TiS_2/Li-In ASSBs using $Li_{6.7}Si_{0.7}Sb_{0.3}S_5I$ as the solid electrolyte at room temperature. (a) 1st, 2nd, 10th, 20th cycle discharge-charge voltage profiles at C/10. (b) discharge-charge capacity and the Coulombic efficiency (CE) as a function of cycle number at different C-rates. (c) 2nd discharge-charge voltage profiles at different C-rates. (d) Discharge-charge capacity and the Coulombic efficiency (CE) of TiS_2/Li-In ASSBs with high TiS_2 loading (23.8 mg.cm^{-2}) as a function of cycle number.

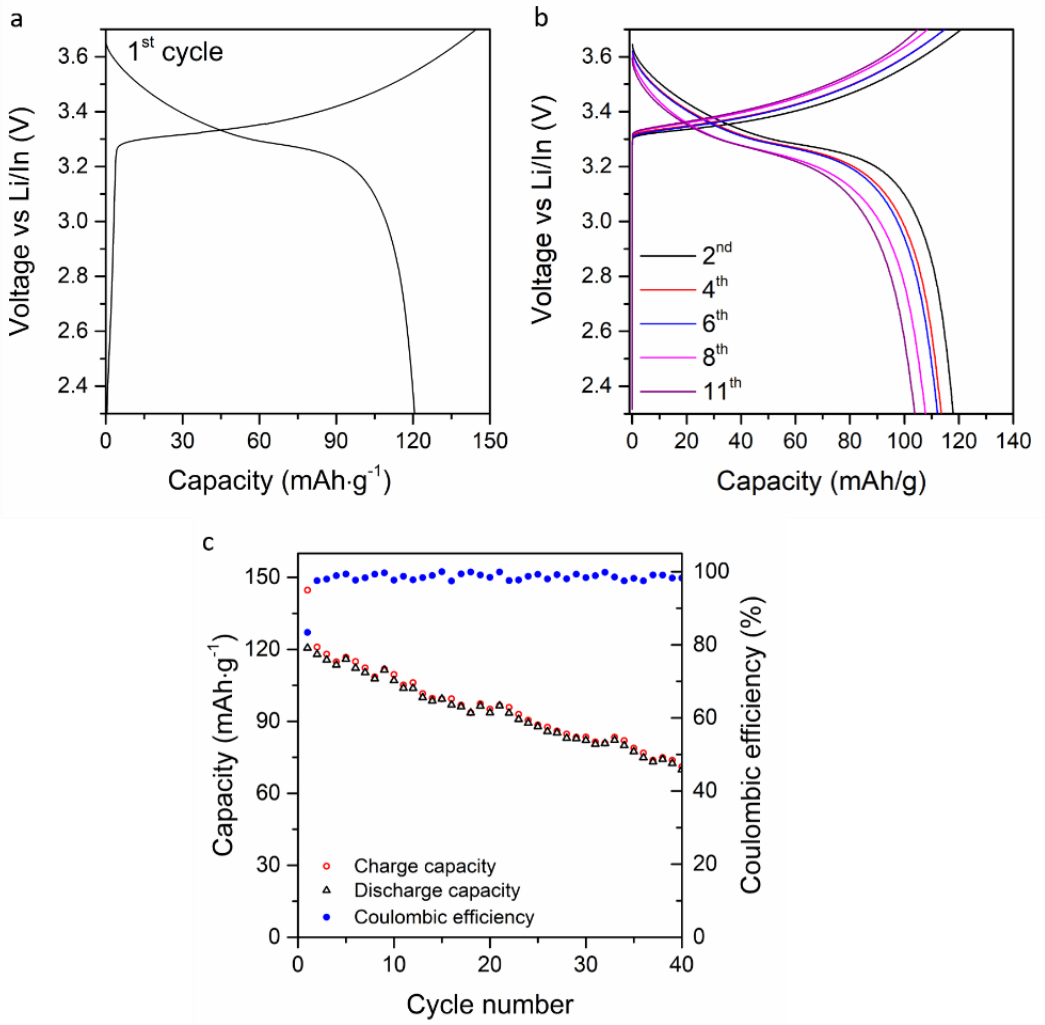

Figure 4.17 (a) 1st and (b) 2nd, 4th, 6th, 8th, and 11th charge-discharge voltage profiles for $LiCoO_2$/Li-In ASSBs employing $Li_{6.7}Si_{0.7}Sb_{0.3}S_5I$ at C/10; the extra capacity before reaching the $LiCoO_2$ plateau on the first charge voltage profile indicates the slight oxidation of the SE; (c) charge-discharge capacity and the corresponding Coulombic efficiency (CE) as a function of cycle number at C/10.

4.8 Origin of the Superionic Conductivity of $Li_{6+x}M_xSb_{1-x}S_5I$ - Concerted Ion Migration

A summary of the results above indicates that the aliovalent substitution of ($Li^+ + M^{4+}$) for Sb^{5+} in $Li_{6+x}M_xSb_{1-x}S_5I$ (M=Si, Sn, Ge) - and hence increased Li^+ concentration and altered distribution - tremendously influences the Li ion conductivity in the argyrodite structure even at low levels of x. A superionic conductivity of 14.8 $mS.cm^{-1}$ (cold-pressed pellet) for the

optimal composition $Li_{6.6}Si_{0.6}Sb_{0.4}S_5I$ is accompanied by a low activation energy barrier for Li ion diffusion of 0.25 eV. Structure solution from powder X-ray synchrotron/neutron and single crystal diffraction shows a slight increase in the S^{2-}/I^- site disorder over the 4*a*/*c* site in the Si phases $Li_{6+x}Si_xSb_{1-x}S_5I$ with increasing x, but this is small even for the x= 0.7 composition (up to 7% for single crystal measurements, and up to 3.3% for synchrotron diffraction measurements on *annealed* samples). As recently experimentally and theoretically suggested,[67, 72, 140] site disorder between sulfide and halide can lead to lower activation barriers. However, such low level S^{2-}/I^- site disorder does not lead to the three-order of magnitude increase in ionic conductivity we observe here. It has also been suggested that the high multiplicity of the Li site can make percolation possible at a low degree of disorder.[67] We note that $Li_{6.6}Si_{0.6}Sb_{0.4}S_5I$ shows tripled ionic conductivity compared to $Li_{6.6}Ge_{0.6}P_{0.4}S_5I$: namely 14.8 $mS.cm^{-1}$ *vs* 5.4 $mS.cm^{-1}$, respectively (measurements being both conducted on cold-pressed materials). The increased ionic conductivity can be ascribed to the different Li ion distribution between these materials (as discussed below).

In the stoichiometric Li_6PnS_5I (Pn = P, Sb) argyrodite structure, Li ions occupy tetrahedral sites: each site shares a common face with one other to form a bipyramid; in turn, each bipyramid shares an edge with another bipyramid and six bipyramids form a cage (**Figure 4.11**, above). In one unit cell, there are 4 cages (24 bipyramids) and each bipyramid is occupied by one Li ion that can only move freely within the bipyramid (equilibrium state). To sustain macroscopic Li ion diffusion, a defect formation step is necessary, and the sum of defect formation and migration energies correspond to a high activation energy as measured by EIS. This is further supported by a DFT MD simulation of Li_6PS_5I[140] which shows inter and intra

cage jumps pass through a much higher activation barrier than that in Li_6PS_5Cl and Li_6PS_5Br as depicted in **Figure 4.18a**, which leads to low ionic conductivity. However, in Li-rich $Li_{6+x}Si_xSb_{1-x}S_5I$, our neutron diffraction analysis (**Figure 4.19**) reveals a different Li^+ sublattice than other typical Li-argyrodites and the previously reported Li-rich $Li_{6.6}Ge_{0.6}P_{0.4}S_5I$[67, 72]. Two new Li sites, along with the original two sites in Li_6SbS_5I, are identified. These sit within the Li cages at the mid-point of the intra-cage jump and between the Li cages at the mid-point of the inter-cage jump with relatively low occupancy (**Figure 4.11b-c, Table 4.8**). They can be regarded as high-energy interstitial sites for Li ion diffusion. The occupancy of the Li3(48*h*) site increases with increasing Li^++Si^{4+} content, and meanwhile creates vacancies on the

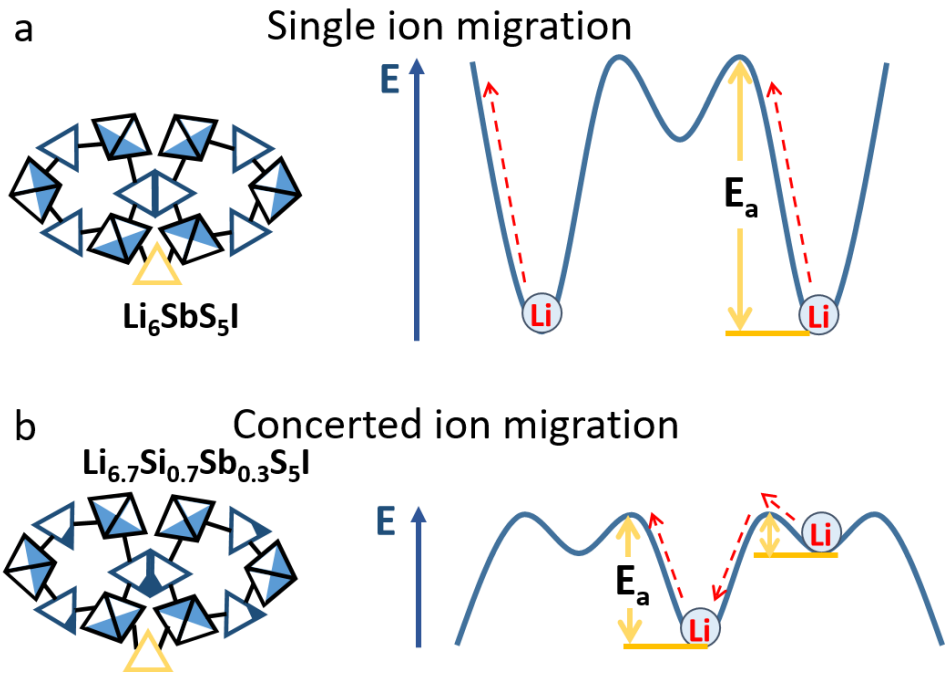

Figure 4.18 Proposed mechanism of (a) traditional vacancy Li ion diffusion mechanism for Li_6SbS_5I and (b) concerted Li ion migration with a flatter energy landscape induced by Li ion site disorder. The triangle indicates a tetrahedral site, and the filled ones indicate a partially occupied site. The empty sites are depicted by an open triangle. The energy landscape is shown for the intracage jump. Black triangles: Li1(48*h*); blue triangles: Li3(48*h*), unoccupied site for Li_6SbS_5I; yellow triangles: unoccupied sites on the pathway on the intercage jump pathway.

Li1(48*h*)-Li2(24*g*)-Li1(48*h*) equilibrium sites (within one bipyramid), as shown in **Figure 4.19a** (we do not speculate on the role of the Li4(4*d*) site due to its very low occupancy, **Table 4.8**). The redistribution of Li ions from Li1-2 onto the Li3 sites and hence the creation of vacancies on those sites helps eliminate the defect formation step for Li ion diffusion. The increased Li ion concentration in $Li_{6+x}Si_xSb_{1-x}S_5I$ pushes the additional Li ions into these high-energy interstitial sites. These positions are very close (~ 1.6 Å) to the low energy sites with higher occupancy and increase the Li^+-Li^+ interactions. Thus, the site energies of Li1 and Li3 become closer with increasing Li ion content, as both increase due to Coulombic repulsion (**Figure 4.19b**). The resultant repulsion will activate concerted ion migration[85] with a significantly lower activation energy for Li ion diffusion, as described schematically in **Figure 4.18b**. The new inter-cage jump (**Figure 4.11c**) - directly through the face-shared Li3(48*h*) tetrahedra with a presumed low activation energy barrier[86] - connects the Li cages in the unit cell and should also favor macroscopic long-range Li ion diffusion (superionic conductivity). These high-energy interstitial sites for diffusion indicate the existence of local minima with no strongly preferred positions which leads to an overall lowering of the activation energy.[131, 132, 148, 149] A similar principle was identified in Li-stuffed garnets. The garnet-type compounds $Li_5La_3M_2O_{12}$ (M = Nb, Ta) initially were reported to exhibit a Li-ion conductivity of $\sim 10^{-6}$ $S.cm^{-1}$ at 25 °C, but substitution on the La and M sites by lower-valent metal ions led to Li-rich garnet-type materials, where conductivities of 1 $mS.cm^{-1}$ are achieved.[45]

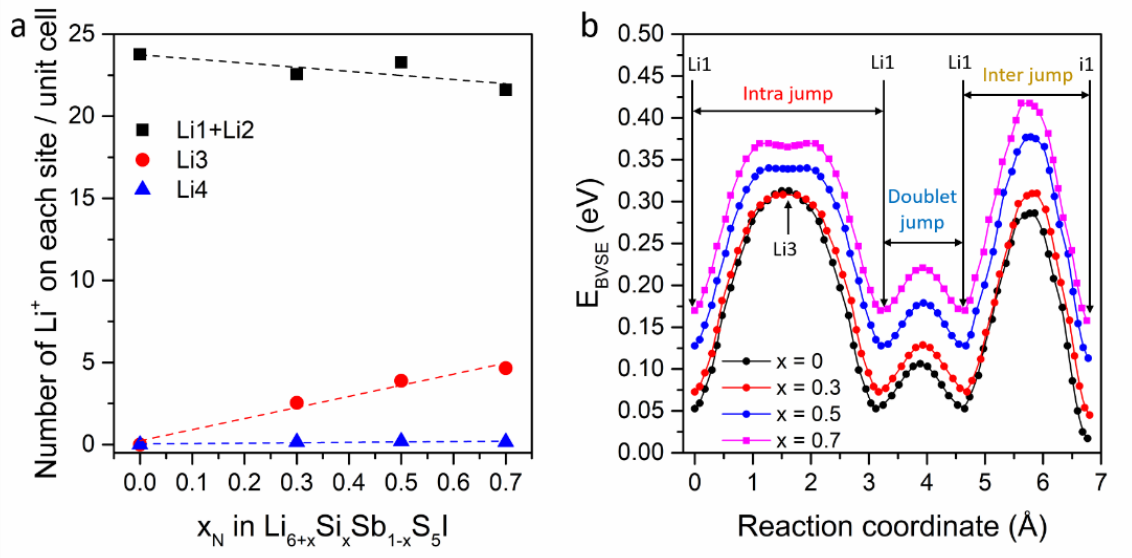

Figure 4.19 (a) Li^+ content of each site per unit cell vs x_N of $Li_{6+x}Si_xSb_{1-x}S_5I$ from neutron diffraction results; (b) BVSE models of migration barriers with $Li_{6+x}Si_xSb_{1-x}S_5I$ (x = 0, 0.3, 0.5, 0.7).

4.9 Conclusion

Exploration of the series $Li_{6+x}M_xSb_{1-x}S_5I$ (M=Si, Sn, Ge) reveals a highly promising sulfide SE, $Li_{6.6}Si_{0.6}Sb_{0.4}S_5I$ that exhibits superionic conductivity owing to a unique framework with minor S^{2-}/I^- anion disorder and a distinctly disordered Li ion distribution. Using a combination of single crystal and powder synchrotron and neutron diffraction and impedance spectroscopy, changes in the Li^+ occupancies and S^{2-}/I^- anion disorder across the series were monitored for the Si members of the series. With the increasing substitution of Si^{4+} onto the Sb^{5+} site and Li ions into the lattice, a significant lowering of the activation energy barrier for Li ion mobility is related to the slightly increased S^{2-}/I^- site disorder but mostly to the disordered Li ion distribution. The additional Li ions populate high-energy interstitial sites, thus activating concerted ion migration. This process further leads to a very low activation energy barrier and superionic conductivity of 14.8 $mS.cm^{-1}$ for cold pressed $Li_{6.6}Si_{0.6}Sb_{0.4}S_5I$

which can be utilized in ASSBs. The ionic conductivity can be further increased by decreasing the grain boundary contributions, and thus sintered pellets exhibit a higher ionic conductivity of 24 $mS.cm^{-1}$. Furthermore, the new superionic conductors exhibit good stability with Li metal, where no apparent microshorts were evident even at high current density stripping/plating experiments conducted at 0.6 $mA.cm^{-2}$ at a capacity 0.6 $mAh.cm^{-2}$. Excellent electrochemical performance is observed for a prototype TiS_2/LiIn ASSBs, which augers well for the future development of advanced all-solid-state Li metal batteries. Most importantly, our work shows that structural changes leading to Li site disorder can induce alterations to the potential energy landscape for the mobile Li ions in fast-ion conductors; namely (as predicted theoretically),[150] pushing Li ions into high energy sites will induce concerted ion migration with a reduced migration energy barrier in Li-rich phases. This strategy should prove invaluable for further optimizing solid electrolyte materials towards high ionic conductivity, new material discovery, and allow the commercialization and practical use of ASSBs.

Chapter 5. A New Halospinel Fast Ion Conductor $Li_2Sc_{2/3}Cl_4$ for High Voltage All Solid-State Li Batteries

5.1 Introduction

Among a range of SE materials which have been studied,[17, 18] sulfide materials generally exhibit high ionic conductivity approaching or even surpassing those of organic liquid electrolytes (>10 $mS.cm^{-1}$), and ductile nature. The latter makes it easy to process and realize intimate contact between the SE - SE and SE - active material, and thus sulfides have been a particular focus of research.[47, 65, 67, 137, 151-153] However, these materials feature a low upper voltage stability window (< 2.5 V vs Li/Li^+) which is not compatible with the typical cathode active materials (CAMs) ($LiCoO_2$, $LiNi_{1-x-y}Mn_xCo_yO_2$ (NMC)) that do not utilize an insulating coating.[92, 154-156] Incorporation of these sulfide SEs in ASSBs with bare $LiCoO_2$ or NMC leads to oxidation of the SE to form a passivating, blocking interphase.[156] The increase in internal resistance results in a dramatic capacity fade.[157] Coating of the CAM particles with an electronically insulating/ionically conductive, chemically compatible material is required to address this problem, which brings a myriad of additional issues. These include the difficulty of finding and processing suitable materials to achieve a homogeneous, functional coating.[158-160] Some oxide SEs, such as garnets, exhibit high ionic conductivity, good chemical stability with Li metal and a wide electrochemical stability window.[45, 161] However, generally oxides are brittle, very difficult to process into SE/active material composites and can lead to high interfacial and grain boundary resistance. They also require high synthesis temperatures which are prohibitively costly and are not amenable to cold (or elevated temperature) sintering. Thus,

it is still challenging to find SEs that can simultaneously meet all the requirements of fast ion conductivity, a wide electrochemical window and good mechanical properties.

Recently, several lithium transition metal halide materials, including Li_3ErCl_6, Li_3YCl_6, Li_3InCl_6, and $Li_{3-x}M_{1-x}Zr_xCl_6$ (M = Er, Y) were reported with relatively high ionic conductivities of 0.31 - 1.49 $mS.cm^{-1}$ and a wide electrochemical window.[80-83] In poorly crystalline Li_3MCl_6 derived from mechanochemical milling, the increase in ionic conductivity (from ~10^{-5} to 0.3 $mS.cm^{-1}$) was ascribed to cation site disorder.[81] Substitution of Y (or Er) by Zr in crystalline Li_3MCl_6 induces a trigonal-to-orthorhombic phase transition and leads to much higher ionic conductivity (up to 1.4 $mS.cm^{-1}$) than in the parent phases, accruing from distinctly different and more favorable Li-ion diffusion pathways.[83] The reason for the significantly increased ionic conductivity of Li_3InCl_6 compared to the value reported in 1992 (~ 0.01 $mS.cm^{-1}$) is still unclear.[162] Although such materials are not stable with lithium metal because the transition metal cation in the halide can be easily reduced, Li_3YCl_6, Li_3InCl_6, and $Li_{3-x}M_{1-x}Zr_xCl_6$ (M = Er, Y) show very good compatibility with high voltage cathodes such as $LiCoO_2$.[80, 82, 83] In this regard, halides (specifically chlorides, which possesses higher anodic stability than bromides and iodides) are attractive for applications in high voltage ASSBs. Until now, very limited materials have been reported with ionic conductivity > 1 $mS.cm^{-1}$. Thus, it is essential to search for other halides that could exhibit such promising properties. Materials with a spinel structure, including Li_2MgCl_4 and Li_2ZnCl_4, were studied in the 1970s-1980s.[163-166] However, these spinel chlorides exhibit extremely low ionic conductivity (< 10^{-3} $mS.cm^{-1}$ at room temperature), and thus cannot be used as SEs in ASSBs.

Herein, we report on a new disordered-spinel chloride fast ion conductor, $Li_2Sc_{2/3}Cl_4$, which exhibits a high ionic conductivity of 1.5 $mS.cm^{-1}$ and is based on the relatively more abundant element scandium compared to indium or erbium. The spinel is prepared via a simple synthetic procedure, unlike Li_3YCl_6 and Li_3ErCl_6 which require long duration high energy ball-milling to reach a conductivity of 0.3 $mS.cm^{-1}$. $Li_2Sc_{2/3}Cl_4$ represents the first spinel-type fast ion conductor, due to significant Li-site disorder in the lattice as determined by neutron diffraction studies. Delocalized Li-ion density serves as interstitial sites that provide critical Li ion diffusion pathways, similar to other fast ion conductors.[45, 65, 161] Importantly, $Li_2Sc_{2/3}Cl_4$ exhibits excellent electrochemical performance combined with typical high voltage CAMs with a bare surface ($LiCoO_2$, NMC622, and NMC85; no coatings applied) due to their stable interface formed with this halide SE and its mechanically pliable and high oxidative stable nature. Cells cycled at room temperature with a high upper cutoff voltage between 4.3 and 4.6 V exhibit stable behavior for over 70 - 110 cycles and capacity up to 215 $mAh.g^{-1}$ at a C/5 rate.

Dr. Qiang Zhang performed powder the neutron diffraction measurement. Chun Yuen Kwok performed the SEM measurements.

5.2 Experimental Approaches

5.2.1 Materials Synthesis

A simple approach based on mixing and heating of the precursors was used. Stoichiometric amounts of LiCl (Sigma-Aldrich, 99.9%) and $ScCl_3$ (Strem Chemical, 99.99%) were mixed together at the targeted ratio. The mixtures were pelletized and placed in a sealed quartz tube under vacuum. $Li_{4-3x}Sc_xCl_4$ ($0.64 \leq x \leq 0.8$) was heated to 650 ^oC for 48 hours with a ramp rate of 5 $°C.min^{-1}$.

5.2.2 Electrochemical measurements

For linear sweep voltammetry (LSV) measurements, 90 mg of $Li_2Sc_{2/3}Cl_4$ was filled into a polyether ether ketone (PEEK) cylinder and pressed at 2 tons for 1 min (10 mm diameter). To prepare the $Li_2Sc_{2/3}Cl_4$-Super P carbon composite, $Li_2Sc_{2/3}Cl_4$ and carbon were mixed in a weight ratio of 7:3 and hand-ground in an agate mortar for 15 min. A mass of 5 mg of the composite was put into one side of the SE pellet to serve as a working electrode and pressed at 2 tons for another 1 min. On the other side of the pellet, a thin indium foil (10 mm diameter, Alfa Aesar, 99.99%, 0.125 mm thickness) was attached and ~0.3 mg Li powder (FMC Lithium) was spread over the indium foil. The cell was then placed into a stainless-steel casing with a constant applied pressure of ~1.5 tons. The LSV measurement was performed with a scan rate of 0.1 $mV.s^{-1}$.

For the fabrication of Li | $Li_2Sc_{2/3}Cl_4$ | Li symmetric cells, ~100 mg of $Li_2Sc_{2/3}Cl_4$ powder was placed into a PEEK cylinder and cold-pressed at 3 tons for 1 min (10 mm diameter). On both sides of the SE pellet, Li foil (99.9%, Sigma-Aldrich, 0.38 mm thickness) with a diameter of 10 mm was attached. The cell was subjected to constant uniaxial pressure using the screw of a stainless-steel framework with 4 Nm torque. Galvanostatic cycling of the symmetric cell was carried out at a current density and capacity of 0.1 $mA.cm^{-2}$ and 0.1 $mAh.cm^{-2}$.

All-solid-state batteries employing the $Li_2Sc_{2/3}Cl_4$ SE in combination with a $LiCoO_2$ (LCO, Wellcos corporation) or NMC622 (BASF) or NMC85 (BASF) cathode and a Li-In alloy anode were assembled in an argon filled glovebox. $LiCoO_2$, NMC622, and NMC85 powders were dried in a Buchi oven under vacuum at 200 ^oC for 20 h before use. $Li_{6.7}Si_{0.7}Sb_{0.3}S_5I$ was

synthesized following our previously reported procedure.[65] First, ~ 60 mg of $Li_{6.7}Si_{0.7}Sb_{0.3}S_5I$ powder was placed into a PEEK cylinder and pressed at 2 tons for 1 min (10 mm diameter), and then ~ 40 mg of $Li_2Sc_{2/3}Cl_4$ was spread over one side of the SE pellet and pressed at 2 tons for another 1 min. The composite cathode mixtures were prepared by mixing LCO or NMC622 or NMC85 and $Li_2Sc_{2/3}Cl_4$ in an agate mortar in a weight ratio of 8:2. On the $Li_2Sc_{2/3}Cl_4$ side of the SE pellet, ~ 6-9 mg of the composite cathode mixture (corresponding to a capacity of ~1-1.25 $mAh.cm^{-2}$) was spread and pressed at 3 tons for 3 min. On the other side of the pellet, a thin indium foil (10 mm diameter, Alfa Aesar, 99.99%, 0.125 mm thickness) was attached and ~1 mg Li powder (FMC Lithium) was spread over the indium foil. The cell was placed into a stainless-steel casing with a constant applied pressure of ~1.5 tons. Galvanostatic cycling of the cell was carried out in the voltage range of 3 - 4.3 V vs Li^+/Li for the LCO cell (1C = 137 $mAh.g^{-1}$) and 2.8 - 4.3 V or 2.8 - 4.6 V vs Li^+/Li for the NMC622 (1C = 180 $mAh.g^{-1}$) cell.

5.3 Structural Evolution of Disordered Spinel $Li_2Sc_{2/3}Cl_4$

X-ray diffraction (**Figure 5.1a**, red pattern) shows that the targeted synthesis of spinel $Li_2Sc_{2/3}Cl_4$ provides almost phase-pure polycrystalline powder with only a trace amount of unknown impurities. Preparing the material for XRD analysis clearly revealed its soft and ductile nature. The pattern was indexed in the same cubic space group, $Fd\bar{3}m$ which is adopted by other spinel materials. A lower Sc^{3+} content leads to increasing amounts of LiCl impurity, as shown in **Figure 5.1a**, black pattern. A slightly higher Sc^{3+} content leads to lower ionic conductivity (see below) and even higher Sc^{3+} content leads to a $ScCl_3$ impurity (**Figure 5.2**). The title composition is therefore optimal. The structure of spinel $Li_2Sc_{2/3}Cl_4$ was determined

from Rietveld refinement of the ToF PND pattern, as shown in **Figure 5.1b** and the crystallographic details are summarized in **Table 5.1**. The framework is somewhat similar to the previously reported spinel Li_2MgCl_4.[164] The important difference is that the disordered spinel $Li_2Sc_{2/3}Cl_4$ exhibits four Li sites: Li2 and Li3 are new while Li1 and Li4 are also present in spinel Li_2MgCl_4, as shown in **Figure 5.3a,c,d**. Li_2MgCl_4 is constructed from edge-sharing $(Mg1/Li2)Cl_6$ octahedra (**Figure 5.3b**) and Li1 fills the corner-sharing tetrahedral site (**Figure 5.3d**). In contrast, while $Li_2Sc_{2/3}Cl_4$ also contains edge-sharing $(Sc1/Li4)Cl_6$ octahedra, Li1,2,3 fill the face-sharing octahedral and tetrahedral sites, as shown in **Figure 5.3c-e**.

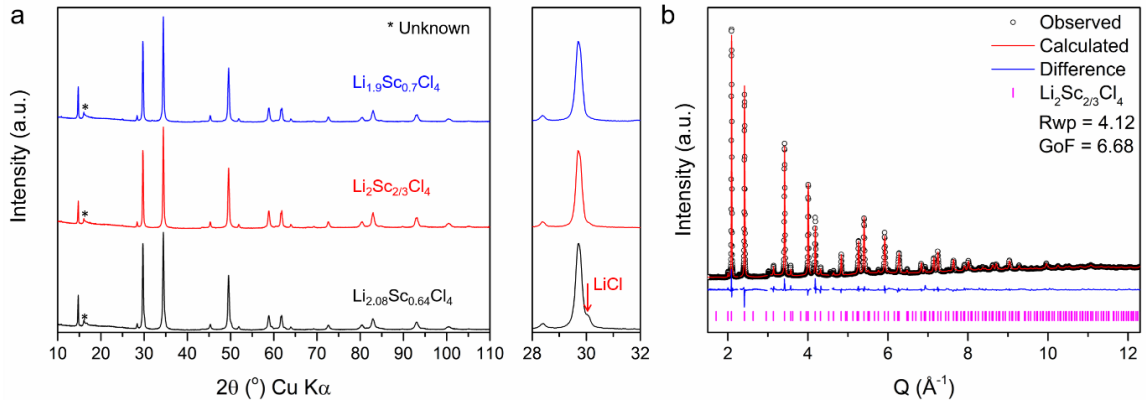

Figure 5.1 (a) Powder X-ray diffraction patterns of $Li_{2.08}Sc_{0.64}Cl_4$ (black), $Li_2Sc_{2/3}Cl_4$ (red) and $Li_{1.9}Sc_{0.7}Cl_4$ (blue). All reflections correspond to the respective spinel phase except for the unknown impurity as marked; red arrows indicate LiCl impurity. (b) Time-of-flight neutron diffraction and the corresponding Rietveld refinement fit of $Li_2Sc_{2/3}Cl_4$, excluded regions (Q = 2.28, 3.01, 4.11 and 4.56 $Å^{-1}$) correspond to trace unknown impurity phase. Experimental data are shown in black circles; the red line denotes the calculated pattern; the difference profile is shown in blue and calculated positions of the Bragg reflections are shown as vertical ticks. Rwp and GoF are the weighted profile R-factor and goodness of fit respectively.

Table 5.1 Atomic coordinates, occupation factors, and isotropic displacement parameter of $Li_2Sc_{2/3}Cl_4$ obtained from time-of-flight powder neutron diffraction at 300 K.

a = 10.4037 (5) Å, Space group: $Fd\bar{3}m$						
Atom	Wyck. Site	x	y	z	Occ.	U_{iso} (Å^2)
Li1 tet	8*a*	0.125	0.125	0.125	0.141(27)	0.025(20)
Li2 oct	16*c*	0	0	0	0.218(13)	0.038(5)
Li3 tet	48*f*	0.125	0.125	0.886(16)	0.0282(63)	0.025
Li4 oct	16*d*	0.5	0.5	0.5	0.689(2)	0.0029(6)
Sc1	16*d*	0.5	0.5	0.5	0.311(2)	0.0029(6)
Cl1	32*e*	0.25435(6)	0.25435(6)	0.25435(6)	1	0.0208(2)

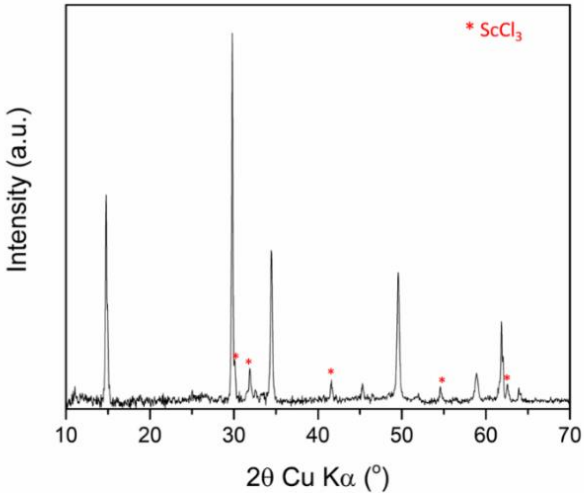

Figure 5.2 Powder X-ray diffraction of $Li_{1.6}Sc_{0.8}Cl_4$. All reflections correspond to the respective spinel phase except for the $ScCl_3$ impurity as marked.

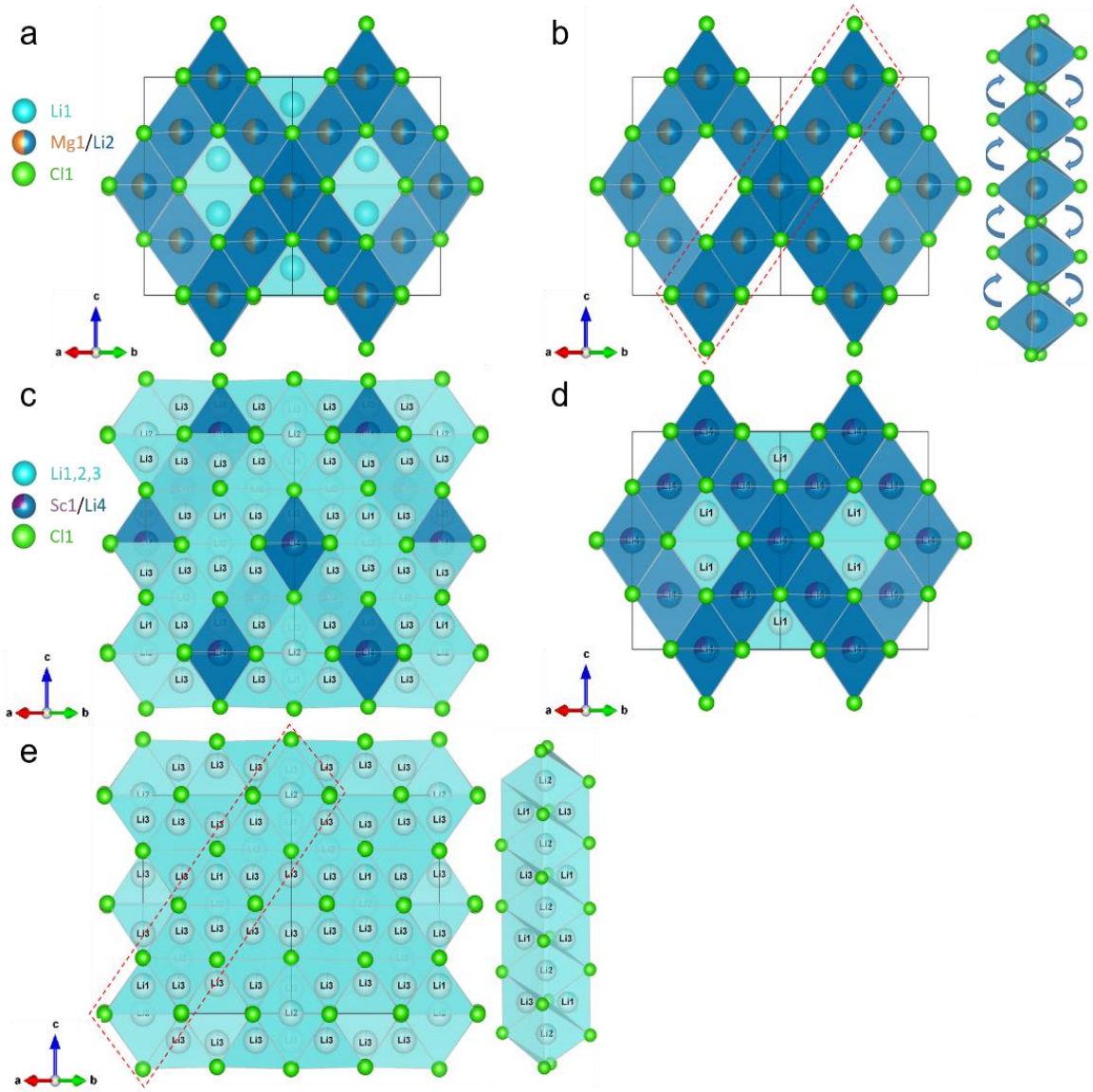

Figure 5.3 (a) Structure of spinel Li_2MgCl_4 from single crystal X-ray diffraction reported in Ref. 145 and (b) structure of spinel Li_2MgCl_4 (corner-sharing $Li(1)Cl_4$ tetrahedra are not shown) depicting a possible Li^+ ion diffusion pathway formed by edge-shared $(Mg1/Li2)Cl_6$ octahedra whose faces border empty tetrahedral sites (enlarged); $Li(1)Cl_4$ - (light blue) tetrahedra and $(Mg1/Li2)Cl_6$ - (dark blue) octahedra. (c) structure of disordered spinel $Li_2Sc_{2/3}Cl_4$ from ToF powder neutron diffraction and (d) structure without illustrating $Li(2)Cl_6$ octahedra and $Li(3)Cl_4$ tetrahedra, demonstrating that it is related to spinel Li_2MgCl_4 but with different site occupancies. $(Sc1/Li4)Cl_6$ octahedra are in dark blue and $Li(1)Cl_4$ tetrahedra in light blue; (e) structure of disordered spinel $Li_2Sc_{2/3}Cl_4$ only showing face-sharing $Li(1,3)Cl_4$ tetrahedra and $Li(2)Cl_6$ octahedra that represent a 3D Li ion diffusion pathway; expansion shows potential ion diffusion through $Li(2)Cl_6$ octahedra passing by $Li(1,3)Cl_4$ tetrahedra.

5.4 Ionic Conductivity and Li ion diffusion Pathways

Temperature-dependent impedance spectroscopy measurements were performed to determine the ionic conductivity of cold-pressed $Li_2Sc_{2/3}Cl_4$ and the activation energy for Li ion transport (**Figure 5.4**). The corresponding impedance responses (illustrated as Nyquist plots) are shown in **Figure 5.4a, b**. $Li_2Sc_{2/3}Cl_4$ exhibits fast ion conductivity of 1.5 $mS.cm^{-1}$ at room temperature. The Nyquist plots at different temperatures were fit to derive ionic

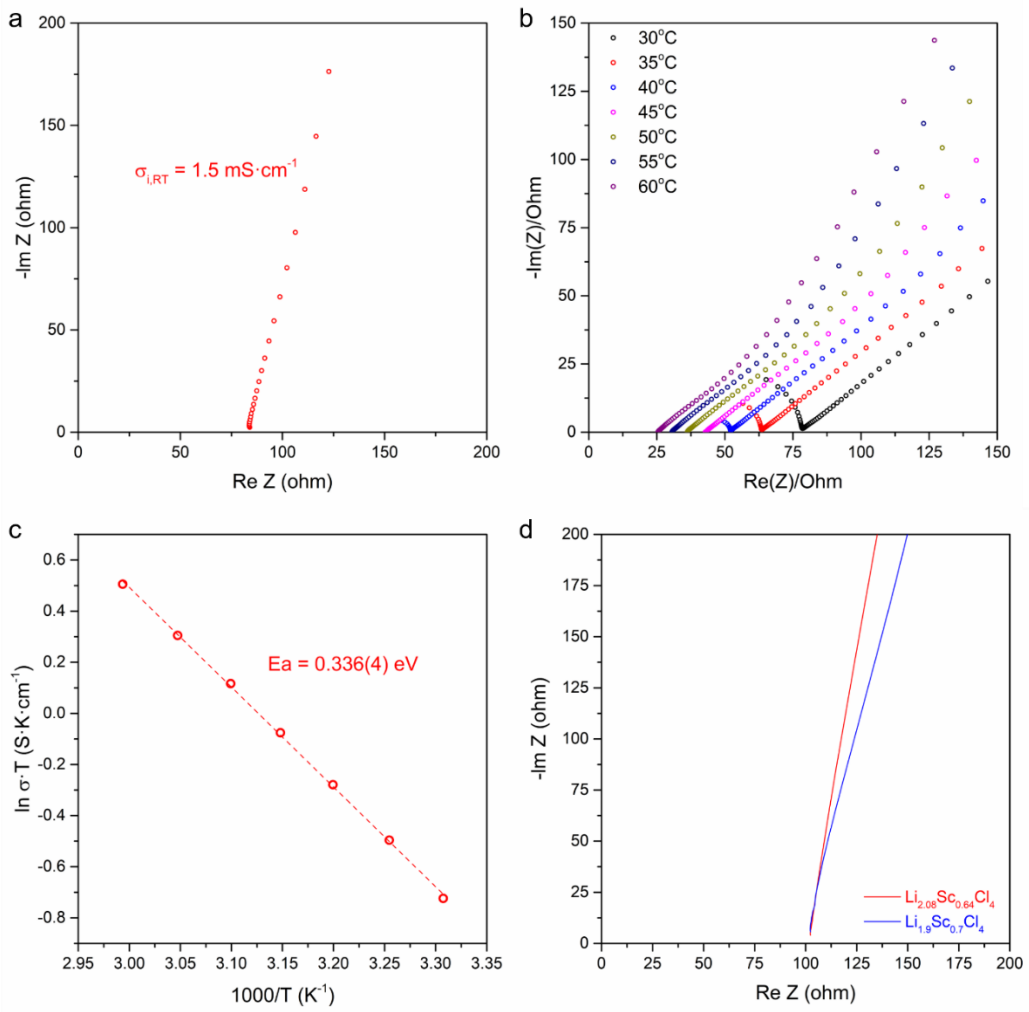

Figure 5.4 Nyquist plots of $Li_2Sc_{2/3}Cl_4$ (a) at room temperature and (b) at each temperature used to determine activation energy; (c) Arrhenius plots of the conductivity values for $Li_2Sc_{2/3}Cl_4$ in the temperature range from 30 to 60 °C. (d) Nyquist plots of $Li_{2.08}Sc_{0.64}Cl_4$ (red) and $Li_{1.9}Sc_{0.7}Cl_4$ (blue) at room temperature.

conductivity values that were used for the corresponding Arrhenius plot that yielded a low activation energy, E_a = 0.34 eV (**Figure 5.4c**). $Li_{2.08}Sc_{0.64}Cl_4$ exhibits slightly lower ionic conductivity of 1.22 $mS.cm^{-1}$ due to minor LiCl impurities and $Li_{1.9}Sc_{0.7}Cl_4$ also exhibits a lower ionic conductivity of 1.09 $mS.cm^{-1}$ due to a lower carrier concentration (**Figure 5.4d**).

The ionic conductivity of the new disordered spinel, $Li_2Sc_{2/3}Cl_4$, is more than three orders of magnitude higher than previously reported chlorospinels including Li_2MCl_4 (M= Mg, V, Cr, Mn, Fe, Co, Zn, Cd) which exhibit very low ionic transport, ionic conductivity < 10^{-3} $mS.cm^{-1}$. The difference is that $Li_2Sc_{2/3}Cl_4$ exhibits multiple Li sites in the spinel lattice (and two new Li sites) compared to the other materials. Taking Li_2MgCl_4 as an example, Li ions would likely diffuse through the faces of edge-shared $Li(2)Cl_6$ octahedra that border an empty tetrahedral site (**Figure 5.3b**). While the Li2 site is also a shared site with Mg^{2+} (half occupied by both Mg^{2+} and Li^+), both Li1 and Li2 sites are fully occupied. Hence a defect formation step is necessary to sustain macroscopic Li ion diffusion. Furthermore, divalent Mg^{2+} is present within the main diffusion pathway, which will hinder Li ion diffusion due to its presumed low mobility.[168] The sum of these factors results in the high activation energy and low ionic conductivity previously reported.[166] For the disordered spinel $Li_2Sc_{2/3}Cl_4$, the same possible $(Sc1/Li4)Cl_6$ octahedral pathway (via empty face-shared sites described in **Figure 5.3b** for Li_2MgCl_4) also exists, shown in **Figure 5.3a**. However, trivalent Sc^{3+} ions also sit within the pathway and are anticipated to block Li ion diffusion; thus Li ions in this site will have very low mobility, as supported by their very low atomic displacement parameter (**Table 5.1**). This Li/Sc shared site forms a rigid framework that allows the diffusion of Li ions resident on the other sites. The additional Li ions are spread over the other face-sharing octahedral and

tetrahedral Li1,2,3 sites, which form a proposed, infinite 3D Li ion diffusion pathway shown in **Figure 5.3e**. The relatively low occupancy of the Li1,2,3 sites results in vacancies which help eliminate the defect formation step for Li ion diffusion. The re-distribution of Li ion density over available tetrahedral and octahedral sites within the lattice suggests the Li site energies are relatively similar which would lead to a relatively flat energy landscape for Li ion diffusion.[45, 65, 161] Overall, the relatively low activation energy is supported by the new probable diffusion pathway and considerable vacancies that promote Li ion mobility.

5.5 Electrochemical Performance

Bulk-type ASSBs with $Li_2Sc_{2/3}Cl_4$ as a SE using uncoated high voltage CAMs (bare-$LiCoO_2$ and bare-NMC622 or NMC85) and Li-In alloy as the negative electrode were constructed to demonstrate the electrochemical performance of this new chlorospinel SE. Li-In alloy was chosen as the anode because Sc^{3+} can be reduced by Li (in **Figure 5.5**). A highly-superionic conductive sulfide solid electrolyte layer ($Li_{6.7}Si_{0.7}Sb_{0.3}S_5I$, 12.6 $mS.cm^{-1}$)[65] was added between Li-In alloy and $Li_2Sc_{2/3}Cl_4$ layer to further prevent the reduction of $Li_2Sc_{2/3}Cl_4$ and decrease the total cell resistance. Bulk-type ASSBs show very good performance in terms of Coulombic efficiency and cycling performance (**Figure 5.6**). In large part, this owes to the high oxidative stability of $Li_2Sc_{2/3}Cl_4$ as indicated by linear sweep voltammetry (LSV) performed on chlorospinel electrodes mixed with 30 wt% Super P carbon (**Figure 5.7a**). The ultra-slow sweep (0.1 $mV.s^{-1}$), which effectively probes the equilibrium potential limit, suggests that $Li_2Sc_{2/3}Cl_4$ is thermodynamically stable up to ~ 4.3 V vs Li^+/Li (and kinetically beyond, see below), *i.e*, very much higher than sulfide materials (~2.5 V).[92]

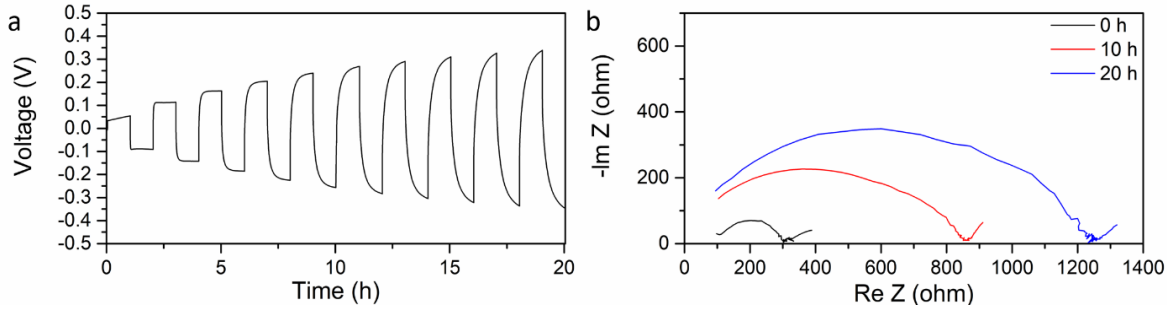

Figure 5.5 (a) Voltage profile of Li stripping/plating in a Li/$Li_2Sc_{2/3}Cl_4$/Li symmetric cell, cycled at 0.1mA.cm^{-2} and 0.1 mAh.cm^{-2} for 20 h; (b) corresponding Nyquist plots of the symmetric cell: before cycling (black), cycling for 10 h (red) and 20 h(blue). This figure shows the instability between $Li_2Sc_{2/3}Cl_4$ and Li metal, as Sc^{3+} can be reduced by Li to form an insulating interphase.

The initial charge/discharge curves of LCO and NMC622 cells cycled in different voltage ranges, up to 4.5 V vs Li^+/Li are shown in **Figure 5.7b, c**. All cells exhibit high initial Coulombic efficiency > 93.7%, which indicates the $Li_2Sc_{2/3}Cl_4$ chlorospinel is stable with these high voltage cathode materials. **Figure 5.8** shows the cross-section of ASSBs after cycling (fully discharged state) which reveals that the NMC622 and $LiCoO_2$ particles are well embedded in the $Li_2Sc_{2/3}Cl_4$ matrix with excellent contact. The LCO cell exhibits excellent rate capacity (**Figure 5.6a, b**). With an upper cutoff voltage of 4.3 V vs Li^+/Li, the cell exhibits a high initial discharge capacity of 135 mAh.g^{-1} at a 0.5C rate (**Figure 5.6b**) and good capacity retention. Even at 1C, the cell still retains a reversible capacity over 120 mAh.g^{-1} (**Figure 5.6a** and **5.9a**), which is significantly better than those of state-of-art $LiCoO_2$ ASSBs.[141, 169, 170] **Figure 5.10** shows the initial and final EIS data of the corresponding LCO cells in **Figure 5.6a**. The total impedance of cells cycled at fast rates is almost the same as the initial state, which further demonstrates the excellent high voltage stability of $Li_2Sc_{2/3}Cl_4$.

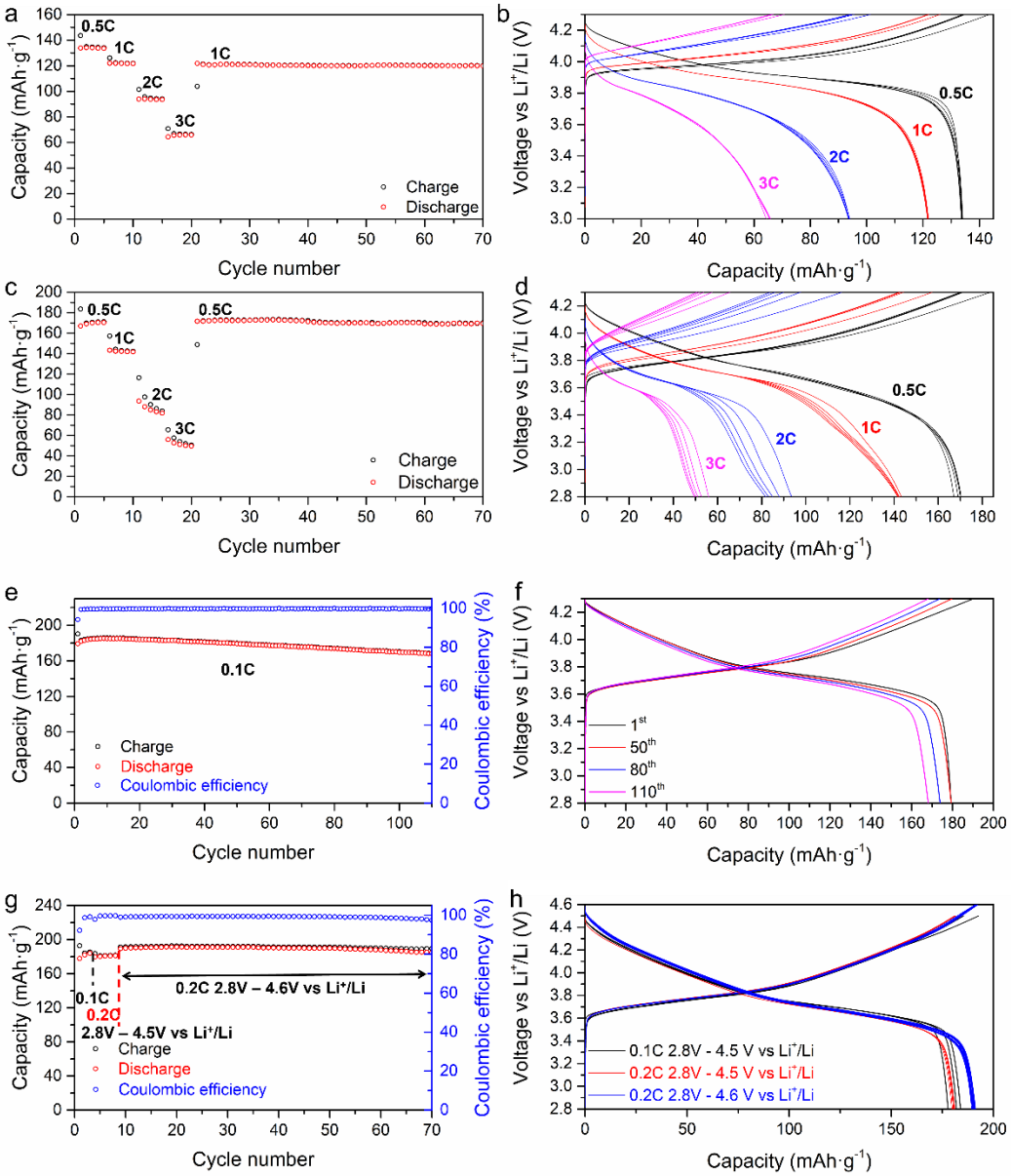

Figure 5.6 Electrochemical performance of $LiCoO_2$ and NMC622 ASSBs using $Li_2Sc_{2/3}Cl_4$ as the solid electrolyte at room temperature. Charge-discharge capacity as a function of cycle number at different C-rates for (a) $LCoO_2$ ASSB and (c) NMC622 ASSB and corresponding charge-discharge curves at different C-rates for (b) $LiCoO_2$ ASSB and (d) NMC622 ASSB. (e) Charge-discharge capacity and the Coulombic efficiency (CE) as a function of cycle number for NMC 622 ASSB cycled at 0.1C between 2.8 V and 4.3V vs Li^+/Li and (f) corresponding charge-discharge curves. (g) Charge-discharge capacity and the Coulombic efficiency (CE) as a function of cycle number for NMC622 ASSB cycled at 0.1C, 0.2C between 2.8V and 4.5V and 4.6V vs Li^+/Li and (h) corresponding charge-discharge curves.

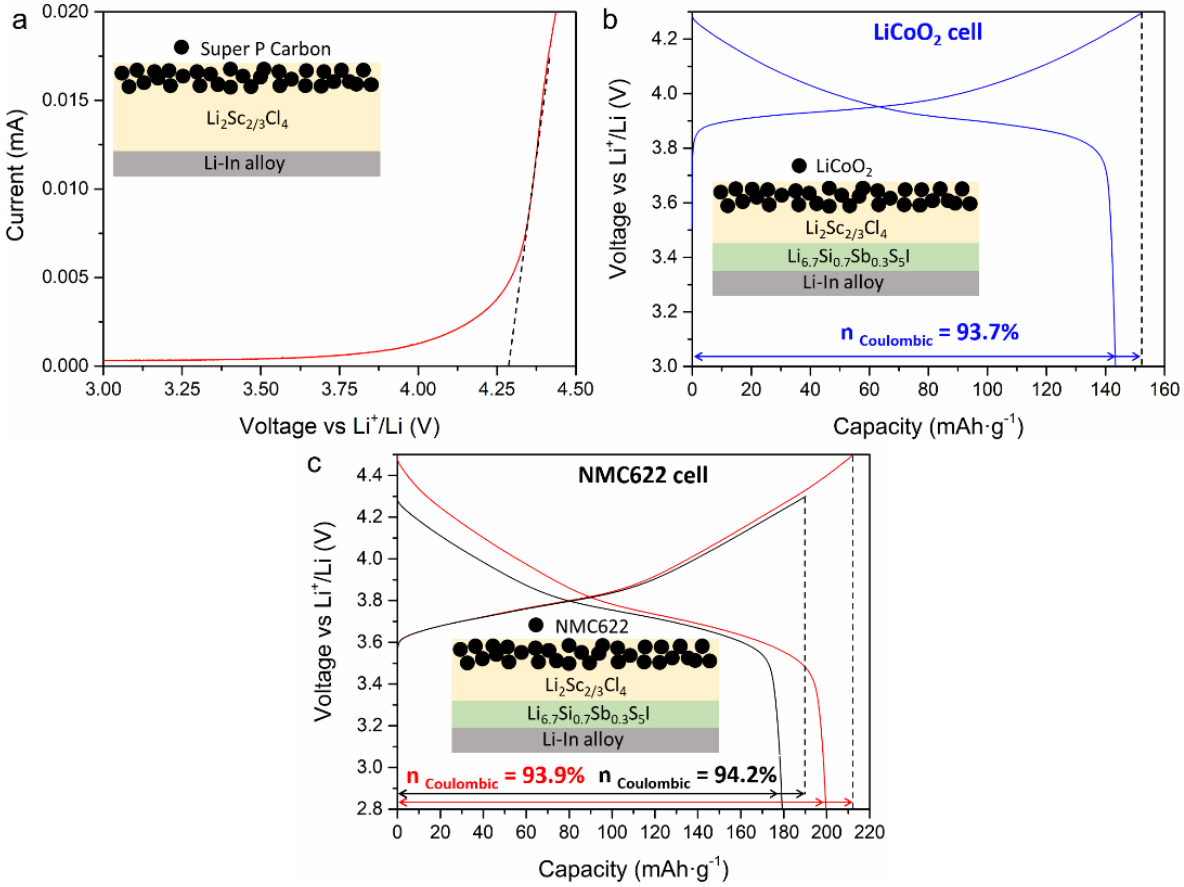

Figure 5.7 (a) Linear sweep voltammograms at a scan rate of 0.1 mV·s^{-1} with Li-In alloy as the reference; $Li_2Sc_{2/3}Cl_4$/Super P carbon mixture (70:30wt%) as the counter electrode and $Li_2Sc_{2/3}Cl_4$ as the solid electrolyte layer. Initial charge/discharge curves of bulk-type ASSLBs of (b) $LiCoO_2$ cell cycled between 3V - 4.3V vs Li^+/Li and (c) NMC622 cell cycled between 2.8V- 4.3V and 2.8V- 4.5V vs Li^+/Li at room temperature at a rate of 0.1 C. Insets show cell configurations.

The NMC622 cell also exhibits good rate capability (**Figure 5.6c,d** and **5.9b**), although a little lower than the LCO cell described above, possibly due to the microstructure of NMC622 particles that contains randomly oriented grains (*i.e.*, small primary particles aggregated into large secondary particles).[171] In comparison, LCO is comprised of large single $LiCoO_2$ crystallites (**Figure 5.11**). Tuning cathode particle size and microstructure will potentially further improve the electrochemical performance of ASSBs.[171-174] **Figure 5.6e, f** shows the

long-term cycling of the NMC622 cell at 0.1 C between 2.8 V and 4.3 V vs Li^+/Li. It exhibits very stable capacity retention with very little capacity fade, maintaining a capacity of ~170 $mAh \cdot g^{-1}$ after 110 cycles with high Coulombic efficiency: ~ 99.8% on average. The NMC622

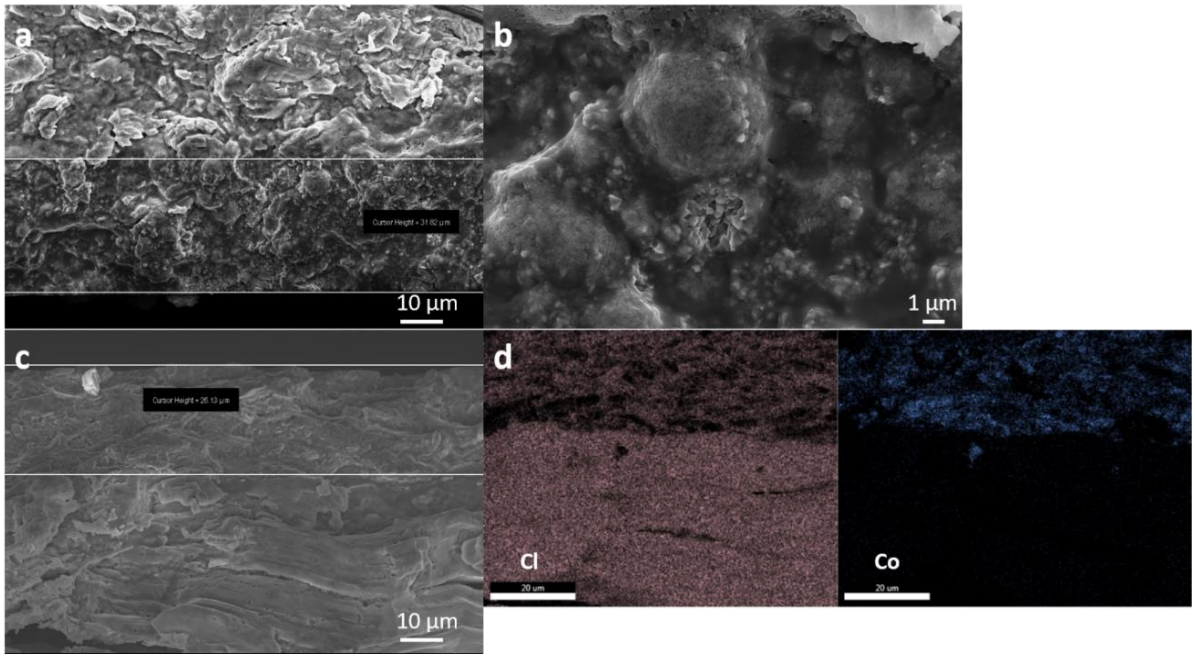

Figure 5.8 Cross-sectional SEM images of (a) the NMC622 cathode composite and $Li_2Sc_{2/3}Cl_4$ electrolyte section and (b) enlarged cathode composite section shows the NMC622 particles (spheres) are well embedded in the $Li_2Sc_{2/3}Cl_4$ matrix. (c) SEM cross-sectional images and (d) EDX mapping of the $LiCoO_2$ cathode composite and $Li_2Sc_{2/3}Cl_4$ electrolyte section, illustrating that the $LiCoO_2$ cannot be distinguished from the solid electrolyte; EDX mapping (Cl and Co) shows the $LiCoO_2$ particles and $Li_2Sc_{2/3}Cl_4$ are well mixed.

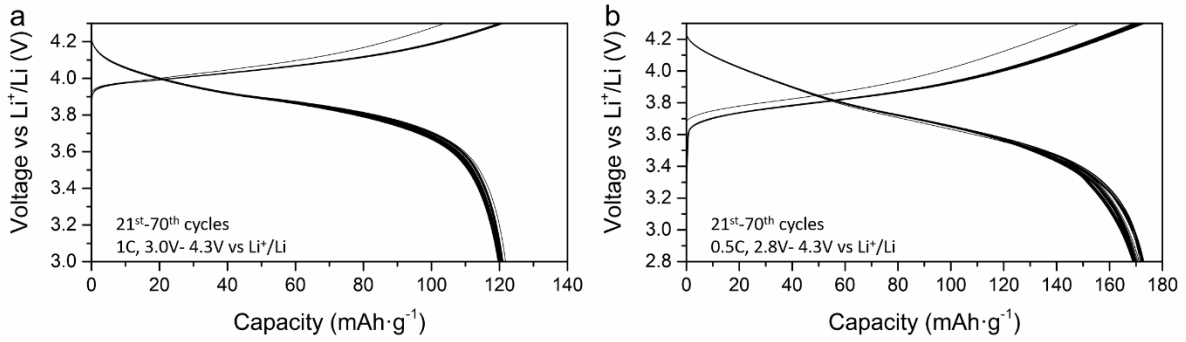

Figure 5.9 Charge-discharge curves corresponding to the 21^{st}-70^{th} cycles of ASSBs for a: (a) $LiCoO_2$ cell cycled at 1C and (b) NMC622 cell cycled at 0.5C.

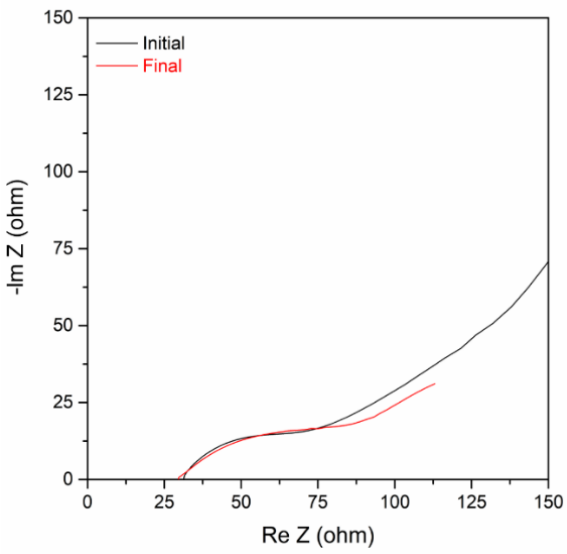

Figure 5.10 Nyquist plots of a $LiCoO_2$ ASSB at the initial state and after 70 cycles, showing no increase of internal resistance upon cycling.

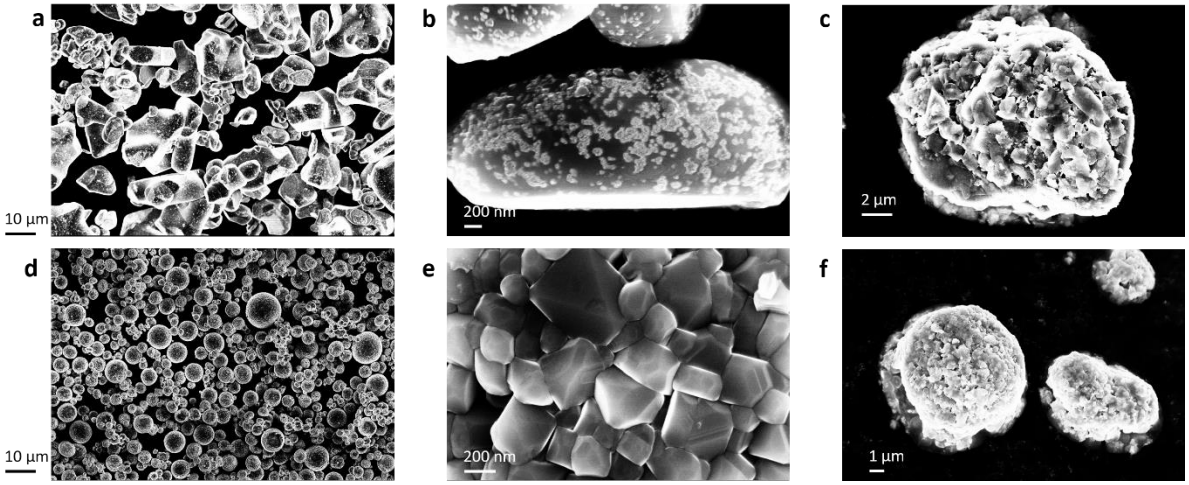

Figure 5.11 SEM images of pristine (a,b) $LiCoO_2$ particles and (d,e) NMC622 particles showing the particle size distribution and microstructure. SEM images of the particle morphology after hand-grinding with 20 wt% $Li_2Sc_{2/3}Cl_4$ shows (c) $LiCoO_2$ and (f) NMC622 particle surfaces are covered with the $Li_2Sc_{2/3}Cl_4$ solid electrolyte.

cell also exhibits excellent cycling performance with a cutoff voltage of 4.6 V vs Li^+/Li with very low-capacity fade, maintaining a capacity of ~190 $mAh.g^{-1}$ with high Coulombic efficiency of ~ 99.6% on average at 0.2 C over 70 cycles (**Figure 5.6g**); typical voltage profiles

are shown in **Figure 5.6h**. This performance is significantly better than previously reported ASSBs with typical coated NMC cathodes married with a sulfide SE.[175] This data suggests that while the thermodynamic stability of $Li_2Sc_{2/3}Cl_4$ is ~ 4.3 V vs Li^+/Li, in fact, a kinetically quasi-stable interface forms between NMC622 and $Li_2Sc_{2/3}Cl_4$ up to 4.6 V. The exact nature of this interface will be explored in future studies.

High-Ni NMC85 cathode materials provide even higher capacity, which can further improve the energy density of ASSBs. With an upper cutoff voltage of 4.3 V vs Li^+/Li, cells exhibit a stable discharge capacity >190 $mAh.g^{-1}$ at a rate of 0.2C and good capacity retention for 90 cycles (**Figure 5.12a, b**). NMC85 cells cycled with a high upper cutoff voltage of 4.5 V also exhibit stable cycling with high discharge capacity up to 214 $mAh.g^{-1}$ at 0.2C and good capacity retention for 70 cycles (**Figure 5.12c, d**). These findings represent the first 4.5 V NMC85 ASSBs with stable performance. Typically, NMC85 cells with liquid electrolytes show capacity fade when charged to high potential.[176-178] This is due to the surface of NMC85 particles being converted to spinel and rock-salt types phases, and the formation of a cathode-electrolyte interface (CEI) due to the oxidation of liquid electrolyte by the strongly oxidizing $Ni^{3+/4+}$ sites, which impede Li ion diffusion.[179-181] The excellent cycling of NMC85 ASSBs is likely due to the good oxidative stability of $Li_2Sc_{2/3}Cl_4$, as no Li ion blocking interface is built up between the contact of the NMC and $Li_2Sc_{2/3}Cl_4$. Nonetheless, the intrinsic nature of high-Ni NMC materials and their aggregate microstructure ((**Figure 5.13**) undoubtedly leads to the very slow capacity fading in NMC ASSBs, shown in **Figure 5.12.** This can be due to Ni migration/phase transformation at high potential, and micro-cracks formed in cycled NMC

particles due to the volume change during cycling that can create loss of contact within the electrode.

In addition to being employed as a SE in ASSBs, $Li_2Sc_{2/3}Cl_4$ can be also utilized as a high voltage cathode coating material, where the coated cathode materials can be used with lower-cost sulfide solid electrolytes. Overall, the excellent electrochemical performance of ASSBs employing this novel $Li_2Sc_{2/3}Cl_4$ solid electrolyte and a > 4 V voltage uncoated NMC/LCO cathode highlights its high room temperature Li ion conductivity and oxidative stability window, which bodes well for practical applications of ASSBs.

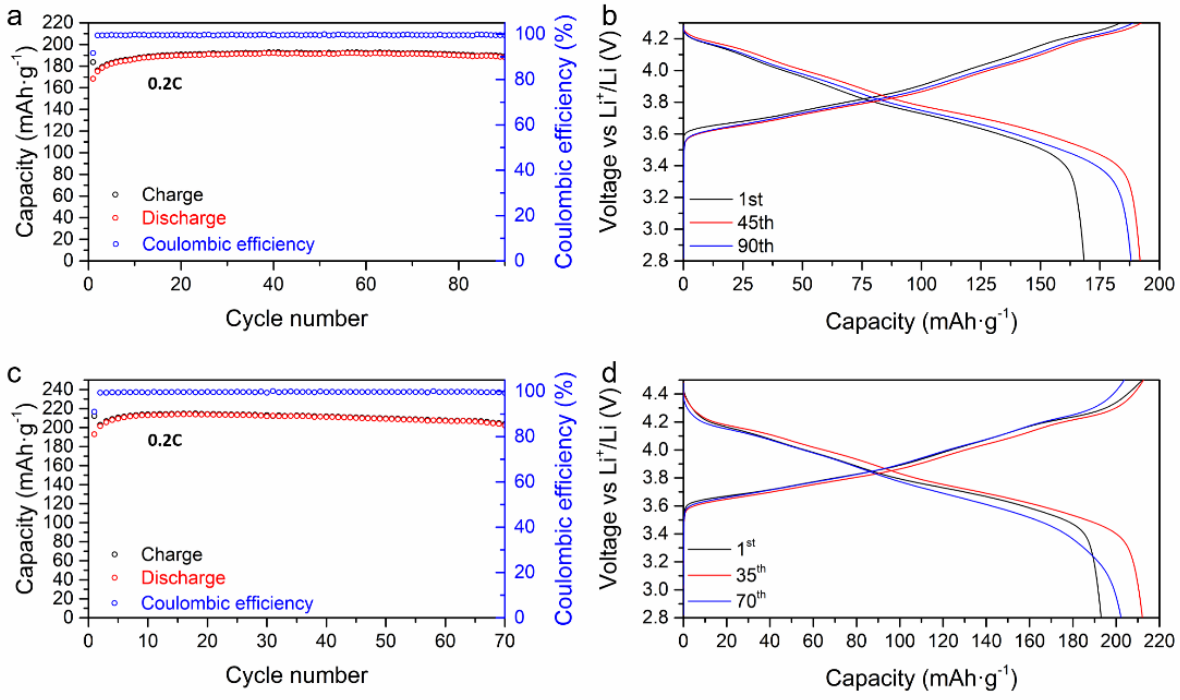

Figure 5.12 Electrochemical performance of NMC85 ASSBs using $Li_2Sc_{2/3}Cl_4$ as the solid electrolyte at room temperature. Charge-discharge capacity and the Coulombic efficiency (CE) as a function of cycle number for NMC85 ASSBs cycled at 0.2C (a) between 2.8 V and 4.3 V and (c) between 2.8 V and 4.5 V vs Li^+/Li and (b,d) corresponding charge-discharge curves.

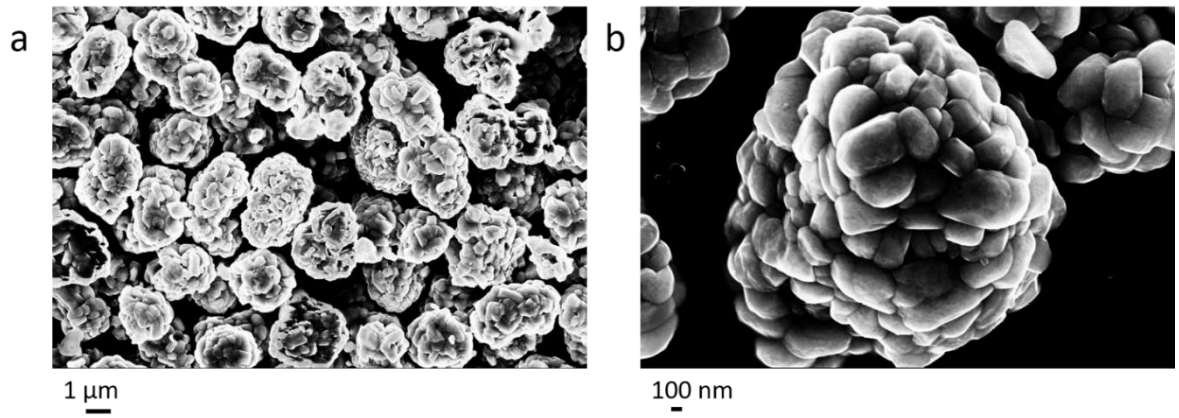

Figure 5.13 SEM images of NMC85 particles showing the (a) particle size distribution and (b) microstructure. NMC85 exhibits a small particle size compared to LCO and NMC622.

5.6 Conclusions

In summary, we have synthesized a new chloride fast ion conductor, $Li_2Sc_{2/3}Cl_4$, with a disordered spinel structure and high Li ion conductivity of 1.5 $mS.cm^{-1}$, representing the first spinel structure fast ion conductor. Excellent electrochemical performance is observed for bulk-type ASSBs with bare $LiCoO_2$ or NMC cathode materials (no external coating) at potentials up to 4.6 V, which augers well for the future development of advanced high energy density and stable cycling life ASSBs. Most importantly, while we report the first spinel fast ion conductors, multiple elemental doping can be conducted to further increase the ionic conductivity. The same concept can be applied to other Li-spinel structured materials including sulfides and oxides, which opens a new avenue in developing new SEs for ASSBs.

Chapter 6. High-Areal Capacity Long Cycle-Life 4.8 V Ceramic All Solid-State Li batteries with Chloride Solid Electrolytes

6.1 Introduction

As above-mentioned, sulfide SEs exhibit high ionic conductivity comparable to traditional liquid electrolytes and form a quasi-stable SEI with Li metal, thus are suitable for separator layer in ASSBs. Chloride SEs are suitable for high voltage ASSBs, due to their intrinsic high voltage stability and good ductility. However, to date, a very limited number of chloride SEs have been reported with high ionic conductivity > 1 $mS.cm^{-1}$, driving an essential search for new materials.

Another major challenge for ASSBs is the moderate CAM loadings that are typically utilized (< 1.25 $mAh.cm^{-2}$). To improve energy density, high loading cathode composites (*i.e.*, with areal capacities of > 3 $mAh.cm^{-2}$) must be developed to make ASSBs practically competitive with conventional LIBs.[115] However, as the active material loading increases in an ASSB, the ionic and electronic conduction percolation within the catholyte declines significantly, leading to poor CAM utilization.[114] Thus catholyte engineering along with a highly conductive SE are needed.

Herein, we report a family of chloride fast Li-ion conductors, $Li_2In_xSc_{0.666-x}Cl_4$ ($0 < x \leq 0.666$), which exhibit ionic conductivity up to 2.0 $mS.cm^{-1}$. Incorporation of as little as 10 wt% $Li_2In_{1/3}Sc_{1/3}Cl_4$ with bare CAMs forms a cathode composite with excellent electrochemical ASSB performance, owing to a low-impedance SE/CAM interface. ASSBs utilizing un-coated $LiCoO_2$ (LCO), $LiNi_{0.6}Co_{0.2}Mn_{0.2}O_2$ (NCM622), and high-Ni $LiNi_{0.85}Co_{0.1}Mn_{0.05}O_2$ (NCM85) at typical cell loading levels of ~1.25 $mAh.cm^{-2}$ exhibit

superior rate capability and significantly more stable long-term cycling up to 4.8 V vs Li^+/Li, compared to state-of-the-art ASSBs. Furthermore, NCM85 ASSBs show an exceptionally long life at room temperature: up to 3000 cycles with > 80 % capacity retention. LCO ASSBs with CAM loadings up to 52.5 $mg.cm^{-2}$ (7 $mAh.cm^{-2}$) also exhibit very steady long-term cycling with high specific capacity at both room temperature and high temperature (50 °C). High-Ni NCM85 ASSB with a high loading of 21.6 $mg.cm^{-2}$ exhibit a capacity of > 4 $mAh.cm^{-2}$ (> 190 $mAh.g^{-1}$) with no fading. These ultra-stable high voltage and high loading ASSBs provide valuable insight into the design and development of ASSBs and may serve as an important point of reference.

Dr. Tongtong Zuo performed the Tof-SIMS measurements and analyzed the data with Dr. Juergen Janek. Dr. Abdeljalil Assoud performed single crystal X-ray diffraction and structural resolution. Dr. Qiang Zhang performed powder neutron diffraction measurements. Chun Yuen Kwok performed SEM measurements. Dr. Se Young Kim assembled liquid cells.

6.2 Experimental Approaches

6.2.1 Materials Synthesis

A simple approach based on mixing and heating of the precursors was used. Stoichiometric amounts of LiCl (Sigma-Aldrich, 99.9%), $InCl_3$ (Alfa Aesar, 99.99%), and $ScCl_3$ (Strem Chemical, 99.99%) were combined at the targeted ratio, pelletized, and placed in a sealed quartz tube under vacuum. The pellet was heated to 650 ^oC at a heating rate of 5 $°C.min^{-1}$ and sintered at 650 ^oC for 48 hours, then slowly cooled to room temperature at 10 $°C.h^{-1}$. $Li_2Sc_{2/3}Cl_4$ was synthesized as described in our previous paper.[182]

6.2.2 Neutron Powder Diffraction

ToF-PND data was collected on POWGEN at the Spallation Neutron Source (SNS) at the Oak Ridge National Laboratory. The sample (~1 g) was loaded into a vanadium can under an argon atmosphere and sealed with a copper gasket and aluminum lid. The sample was measured at 300 K, and a single bank wave with a center wavelength of 1.5 Å was used.

6.2.3 Electrochemical Measurement

ASSBs employing the $Li_2In_{1/3}Sc_{1/3}Cl_4$ SE in combination with a $LiCoO_2$ (LCO, Wellcos corporation, D50 = 16.2 μm), $LiNi_{0.6}Co_{0.2}Mn_{0.2}O_2$ (NCM622, BASF, D50 = 5 μm) or $LiNi_{0.85}Co_{0.1}Mn_{0.05}O_2$ (NCM85, BASF, D50 = 5 μm) cathode active material and a In/InLi anode were assembled in an argon filled glovebox. All CAMs were stored in Ar-glovebox and used as received without any treatment. $Li_{6.7}Si_{0.7}Sb_{0.3}S_5I$ was synthesized following our previously reported procedure.[65] First, ~ 100 mg of $Li_{6.7}Si_{0.7}Sb_{0.3}S_5I$ powder was placed into a PEEK cylinder and pressed at 2 tons for 1 min (10 mm diameter), and then ~ 40 mg of $Li_2In_{1/3}Sc_{1/3}Cl_4$ was spread over one side of the $Li_{6.7}Si_{0.7}Sb_{0.3}S_5I$ pellet and pressed at 2 tons for another 1 min. The composite cathode mixtures were prepared by mixing LCO or NCM622 or NCM85 and $Li_2In_{1/3}Sc_{1/3}Cl_4$ at a weight ratio of 8:2 or 9:1. On the $Li_2In_{1/3}Sc_{1/3}Cl_4$ side of the SE pellet, ~ 6-9 mg of the composite cathode mixture (corresponding to an areal capacity of ~1.1 - 1.25 $mAh.cm^{-2}$) was spread and pressed at 3 tons for 3 min. For high loading cells, ~ 20 - 53 mg cathode composite was used, and the corresponding areal capacities are labeled in the figures. On the other side of the pellet, a thin indium foil (10 mm diameter, 99.99%, 0.1 mm thickness) was attached and ~1 mg Li foil (Sigma-Aldrich) was rolled into a thin foil

(around 5 mm diameter) and placed over the indium foil. The cell was placed into a custom-made stainless-steel casing with a constant applied pressure of ~250 MPa during cycling.

NCM liquid cells were assembled following standard procedures. For electrode fabrication, NCM622 or NCM85 powder was mixed with Super P carbon (Timcal) and polyvinylidene fluoride (PVDF) (Sigma-Aldrich, average $M_w \approx$ 534,000 GPC) to achieve a final weight ratio of 8:1:1 (active material: carbon: binder). The powdered mixture was then suspended in N-methyl-2-pyrrolidinone (Sigma-Aldrich, 99.5%) to obtain a viscous slurry, which was cast on Al foil with a typical loading of ~ 3.6 $mg.cm^{-2}$. The electrodes were punched to a 1 cm^2 geometric area and dried in a vacuum oven at 120 °C overnight. Electrochemical studies were carried out in 2325 coin-type half cells with a Li-metal anode, Celgard 3501 separator, and LP57 electrolyte (Gotion Inc., 1M $LiPF_6$ in ethylene carbonate: ethyl methyl carbonate = 3:7).

Galvanostatic cycling of the cell was carried out in different voltage ranges at different rates (as labeled) using a VMP3 (Bio-Logic) cycler. Rate current density calculations used conventional values for LCO (1C = 137 $mA.g^{-1}$) and NCM622/NCM85 (1C = 180 $mA.g^{-1}$).

ASSBs with LCO, NCM622, and NCM85 CAMs were constructed for impedance measurements following the same procedure as above and cycled at a C/5 or C/2 rate as indicated. Measurements were conducted after every 1 hour of charge/discharge, before and after which the cells were placed at rest for 30 min, respectively. For the impedance measurements after full discharge, the same procedure was followed except the cells were placed at rest for 1 h before and after the measurement.

ASSBs with NCM85 for aging experiments were constructed following the same procedure. Cells were first charged to 4.3 V, 4.6 V, and 4.8 V vs Li^+/Li respectively, and followed by constant potential aging at 4.3 V, 4.6 V, and 4.8 V for 30 h. EIS was conducted every 20 min aging with constant applied potential 4.3 V, 4.6 V, and 4.8 V and no rest. After aging, the cells were continuously cycled for several cycles. Then, the final EIS was measured at discharged state with no applied potential and 0.5 h rest after discharge.

6.2.4 Time-of-flight secondary-ion mass spectrometry

Cycled cathode composites NCM85- $Li_2In_{1/3}Sc_{1/3}Cl_4$ (cut-off 4.3 V for 160 cycles, cut-off 4.6 V for 20 cycles, and cut-off 4.8 V for 10 cycles) are compared to pristine SE, uncycled cathode composite and all measurements were conducted at discharged state. The chemical characterization was performed on a Hybrid ToF-SIMS M6 machine (IONTOF GmbH). To transfer the samples from the glovebox into the measurement chamber, the transfer module Leica EM VCT500 (Leica Microsystems GmbH) was applied to guarantee an argon atmosphere. The measurements were conducted on the top surface of the cathode composite pellets.

In order to avoid the topographic interference and ensure the reproducibility, we measured 12 mass spectra in different areas on each sample. The measurement was carried out in spectrometry mode (bunched mode), which enables a high mass resolution (FWHM $m/\Delta m$ > 7000 at m/z 34.97 (Cl^-)). All spectra were collected in negative ion mode using 60 keV Bi_3^{++}cluster primary ion gun. The cycle time was set to 100 µs. The measurement area was set to 150×150 μm^2 and rasterized with 256×256 pixels. For each patch, 1 frame and 1 shot per

pixel and frame were chosen. The primary ion current was about 0.43 pA. To enable the semi-quantitative analysis, the stop condition was set with the primary ion dose of 10^{12} ions/cm^2.

The data evaluation was conducted with software Surfacelab 7.2 (IONTOF GmbH). The secondary ion signals were normalized to the total ion signals, and all signal intensities were collected from the corresponding normalized secondary ion images.

6.3 Synthesis and characterization of lithium mixed-metal chloride SEs

New chloride fast Li ion conductors with composition $Li_2In_xSc_{0.666-x}Cl_4$ ($0 \leq x \leq 0.666$) were synthesized by the simple solid-state reaction to explore the structural changes and influences of increasing In^{3+} content on the ionic conductivity. X-ray diffraction patterns (**Figure 6.1a**) show that the targeted synthesis of $Li_2In_xSc_{0.666-x}Cl_4$ provides an almost phase-pure cubic spinel phase within the solid solution range of $0 \leq x < 0.444$. At higher In^{3+} content ($x \geq 0.555$) monoclinic Li_3InCl_6 and LiCl impurities start to increase (**Figure 6.1a**). Temperature-dependent impedance spectroscopy measurements were performed to determine the ionic conductivity and activation energy for Li-ion transport. The Nyquist plots at room temperature are shown in **Figure 6.1b**, and the data at different temperatures were fit to derive ionic conductivity values that were used to generate the Arrhenius plots (**Figure 6.2**). The corresponding room temperature ionic conductivities and activation energies are summarized in **Figure 6.1c** and **Table 6.1**. All compositions $Li_2In_xSc_{0.666-x}Cl_4$ ($0 < x < 0.666$) exhibit high ionic conductivity between 1.83 - 2.03 mS.cm^{-1} and a low activation energy of ~ 0.33 eV (**Figure 6.1c**). The electronic conductivity measured by the Hebb-Wagner DC polarization method (**Figure 6.3**) was 4.7 x 10^{-10} S·cm^{-1} for $Li_2In_{1/3}Sc_{1/3}Cl_4$ which is almost one order of

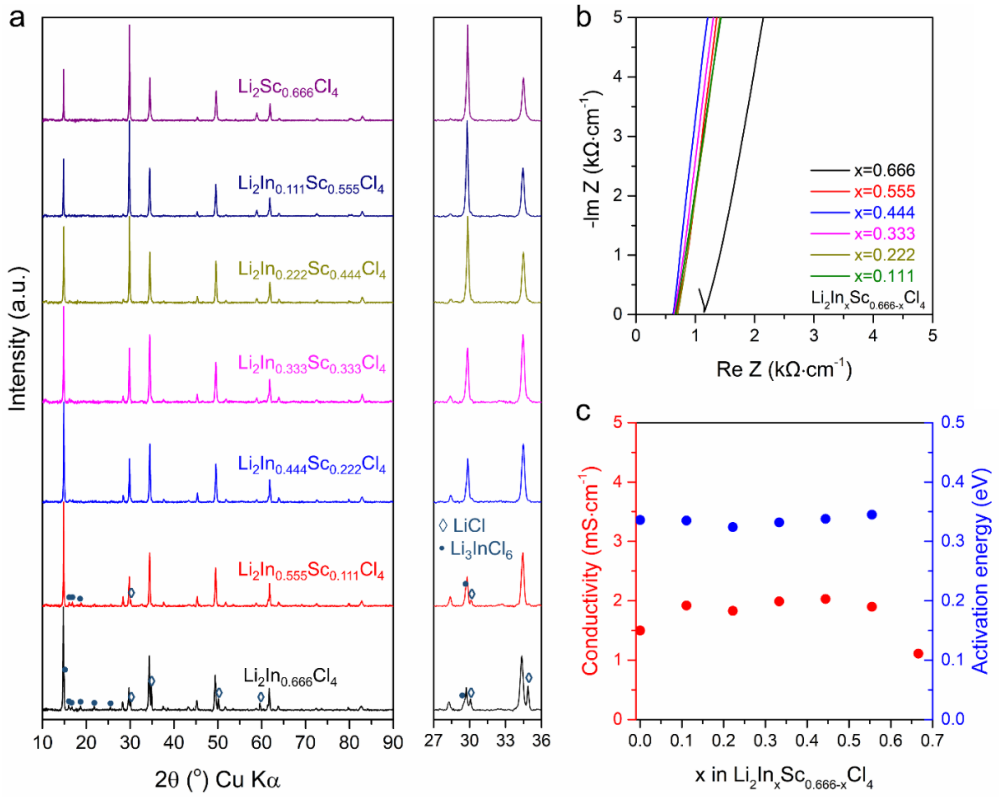

Figure 6.1(a) X-ray diffraction patterns of $Li_2In_xSc_{0.666-x}Cl_4$ ($0 \leq x \leq 0.666$); (b) Nyquist plots of $Li_2In_xSc_{0.666-x}Cl_4$ ($0.111 \leq x \leq 0.666$) at room temperature; (c) Ionic conductivity and activation energy of $Li_2In_xSc_{0.666-x}Cl_4$ ($0 \leq x \leq 0.666$) as a function of nominal In^{3+} content. The ionic conductivity and activation energy values for x = 0 were previously reported in Ref. [182].

magnitude lower than the $Li_2Sc_{2/3}Cl_4$ (4.2 x 10^{-9} S·cm^{-1}) and indicating that $Li_2In_{1/3}Sc_{1/3}Cl_4$ is essentially a pure ionic conductor.

The structure of $Li_2In_{1/3}Sc_{1/3}Cl_4$ was determined from Rietveld refinement of the ToF PND pattern (**Figure 6.4a**; crystallographic details are summarized in **Table 6.2**). The framework is same as that of our previously reported halospinel $Li_2Sc_{2/3}Cl_4$, and also contains four Li sites, albeit with somewhat different occupations. Four Li sites in a spinel structure were also recently reported for lithiated spinel $Li_4Ti_5O_{12}$ that exhibits facile Li-ion mobility ($Li_8Ti_5O_{12}$).[183] The metastable intermediate Li sites in $Li_{4+x}Ti_5O_{12}$ ($0 \leq x \leq 3$) lead to excellent

Li-ion mobility which allow fast rate capability.[184, 185] The edge-sharing (Li4/Sc1/In1) octahedra form a rigid framework whereas the additional Li ions are spread over other available octahedral and tetrahedral sites within the lattice (**Figure 6.4b**). The face-sharing Li2 octahedra and Li1 or Li3 tetrahedra with low occupancies (~ 0.2 - 0.3) form a 3D Li ion diffusion pathway (**Figure 6.4c, d).** Owing to the relatively low activation energy (0.33 eV from EIS measurement) for Li-ion diffusion and 3D Li ion diffusion pathways with considerable vacancies that promote Li ion mobility, a high ionic conductivity of 2.0 $mS.cm^{-1}$ is obtained.

Table 6.1 Ionic conductivity at room temperature and corresponding activation energy for the materials described in the main text.

Compositions	Ionic conductivity ($mS.cm^{-1}$)	Activation energy (eV)
$Li_2In_{0.111}Sc_{0.555}Cl_4$	1.92	0.34
$Li_2In_{0.222}Sc_{0.444}Cl_4$	1.83	0.32
$Li_2In_{0.333}Sc_{0.333}Cl_4$	1.99	0.33
$Li_2In_{0.444}Sc_{0.222}Cl_4$	2.03	0.34
$Li_2In_{0.555}Sc_{0.111}Cl_4$	1.90	0.35
$Li_2In_{0.666}Cl_4$	1.11	

Table 6.2 Atomic coordinates, occupation factors, and isotropic displacement parameters of $Li_2In_{0.333}Sc_{0.333}Cl_4$ obtained from time-of-flight powder neutron diffraction at 300 K.

a = 10.42138(8) Å, space group: $Fd\bar{3}m$						
Atom	Wyck. Site	x	y	z	Occupancy	U_{iso} (Å^2)
Li1	8*a*	0.125	0.125	0.125	0.28(5)	0.025(12)
Li2	16*c*	0	0	0	0.19(2)	0.034(8)
Li3	48*f*	0.125	0.125	0.89(2)	0.008(7)	0.025
Li4	16*d*	0.5	0.5	0.5	0.675(2)	0.0038(7)
Sc1	16*d*	0.5	0.5	0.5	0.164(1)	0.0038(7)
In1	16*d*	0.5	0.5	0.5	0.161(2)	0.0038(7)
Cl1	32*e*	0.25424(6)	0.25424(6)	0.25424(6)	1	0.0203(2)

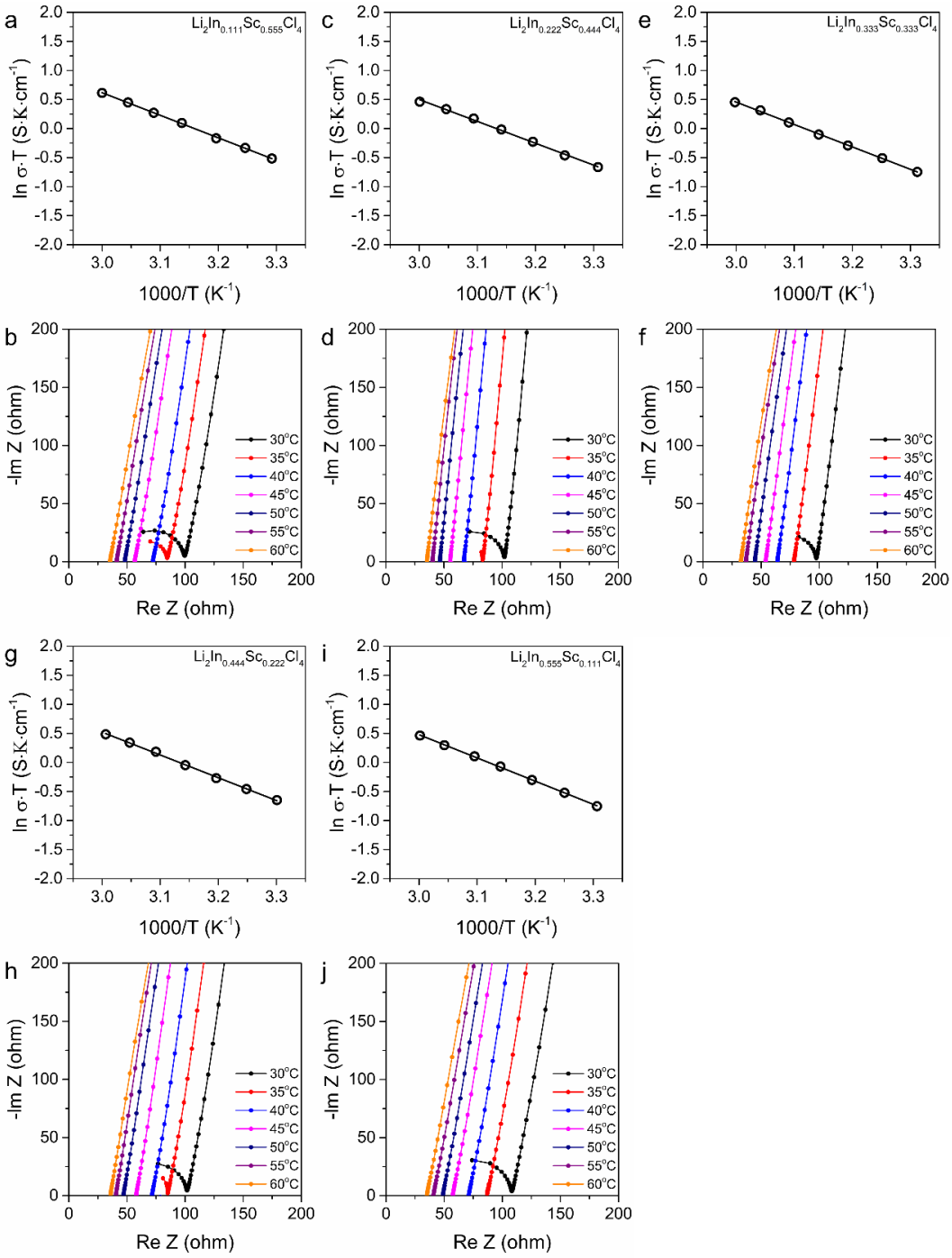

Figure 6.2 Arrhenius plots for (a) $Li_2In_{0.111}Sc_{0.555}Cl_4$; (c) $Li_2In_{0.222}Sc_{0.444}Cl_4$; (e) $Li_2In_{0.333}Sc_{0.333}Cl_4$; (g) $Li_2In_{0.444}Sc_{0.222}Cl_4$ and (i) $Li_2In_{0.555}Sc_{0.111}Cl_4$ in the temperature range from 30 to 60 °C. Corresponding Nyquist plots of (b) $Li_2In_{0.111}Sc_{0.555}Cl_4$; (d) $Li_2In_{0.222}Sc_{0.444}Cl_4$; (f) $Li_2In_{0.333}Sc_{0.333}Cl_4$; (h) $Li_2In_{0.444}Sc_{0.222}Cl_4$ and (j) $Li_2In_{0.555}Sc_{0.111}Cl_4$ at each temperature used in the Arrhenius plots.

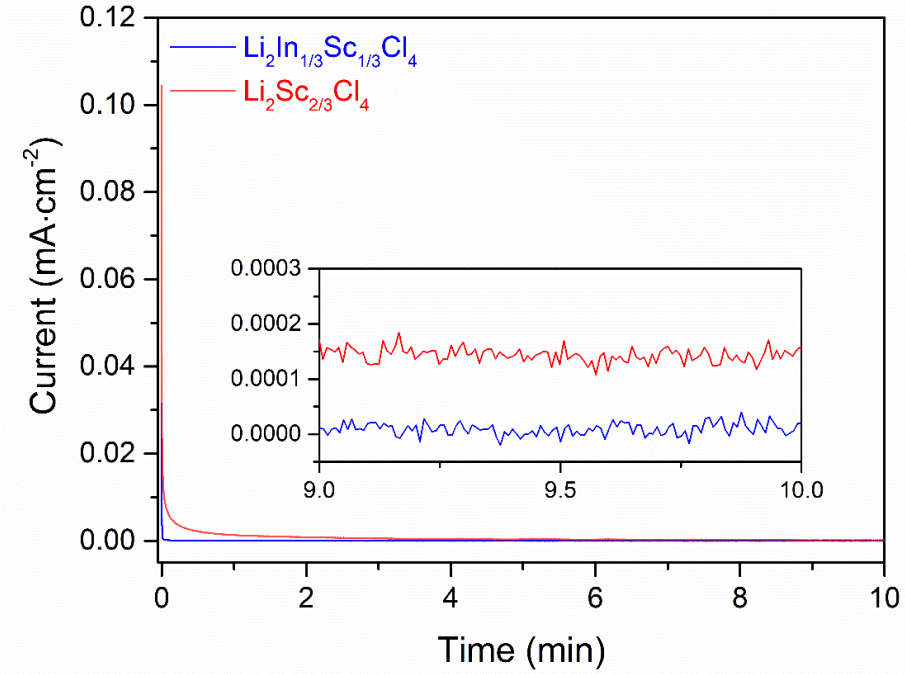

Figure 6.3 Chronoamperometry result for the Stainless steel | SE | stainless steel cells with a constant voltage of 1 V, and the corresponding electronic conductivity of $Li_2In_{1/3}Sc_{1/3}Cl_4$ (blue curve) is 4.7 x 10 $^{-10}$ S·cm^{-1} and $Li_2Sc_{2/3}Cl_4$ (red curve) is 4.2 x 10 $^{-9}$ S·cm^{-1}.

The higher-indium composition, $Li_2In_{0.444}Sc_{0.222}Cl_4$, shows additional reflections (Q = 1.1 - 1.9 Å^{-1}) in the neutron diffraction pattern that correspond to a non-spinel monoclinic phase, (**Figure 6.5a**). Its high-resolution powder X-ray diffraction pattern (**Figure 6.5b**) also reveals reflections at 2θ: 15º-25º due to this monoclinic material identified as $Li_3In_{2/3}Sc_{1/3}Cl_6$ (note that the main peaks overlap with spinel reflections), which are almost completely invisible in $Li_2In_{1/3}Sc_{1/3}Cl_4$. A crystal of $Li_3In_{2/3}Sc_{1/3}Cl_6$ was picked from the two-phase mixture, and its structure was confirmed by single-crystal diffraction measurement (crystallographic details are summarized in **Tables 6.3-4**). The refinement yields a lower-than-expected Li content ($Li_{2.18}In_{0.664}Sc_{0.336}Cl_6$) due to poor sensitivity of X-rays for light lithium atoms, but the In/Sc ratio is as targeted (2:1). The framework of $Li_3In_{2/3}Sc_{1/3}Cl_6$ is identical to monoclinic Li_3ScCl_6.[186] One difference between the cubic spinel and monoclinic structures is

the fact that the Li/metal site (Li4/Sc1/In1) is shared in the spinel, whereas all of the Li and metal sites are crystallographically distinct in the latter (*i.e.*, ordered), as shown in **Figure 6.6**. The ordering is possibly due to the relatively larger ionic radius difference between Li^+ (0.76 Å, C.N.=6) and In^{3+} (0.8 Å, C.N.=6), compared to Sc^{3+} (0.745 Å, C.N.=6), which triggers the

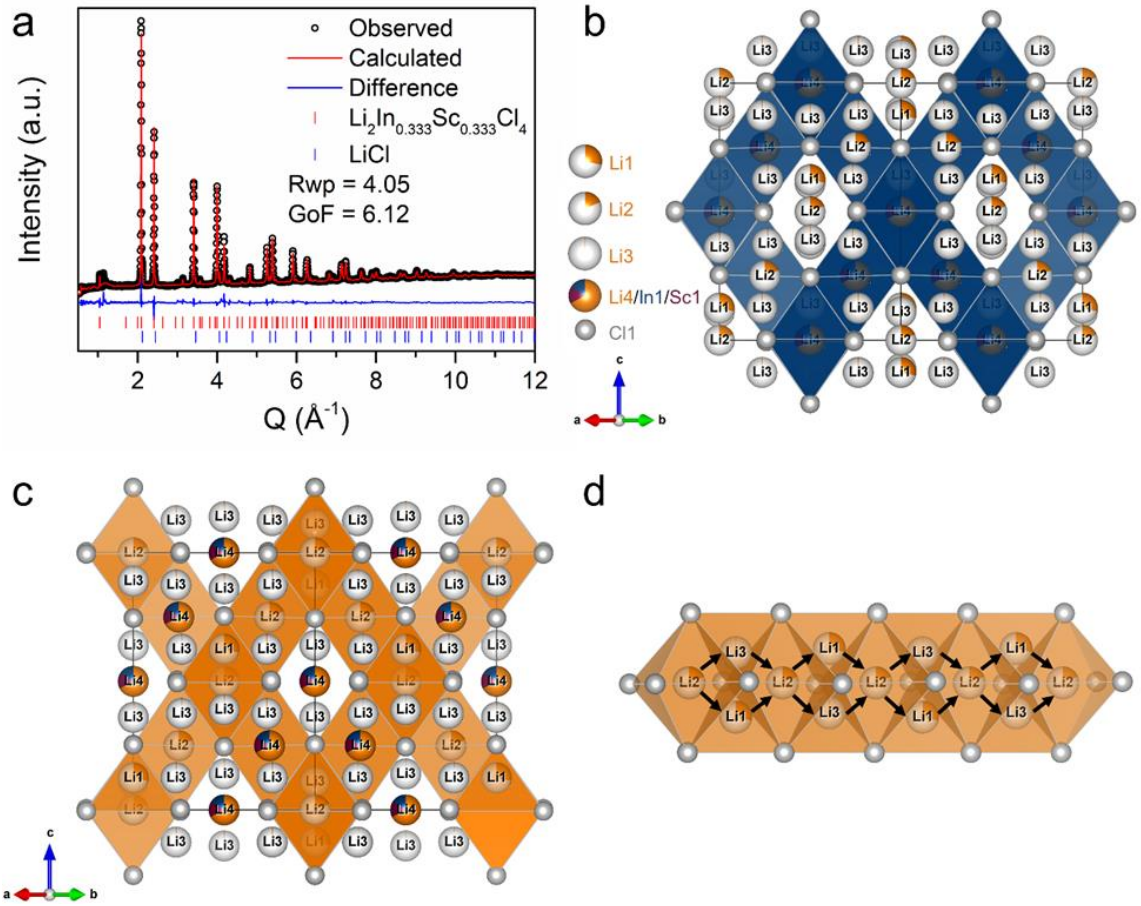

Figure 6.4 (a) Time-of-flight neutron diffraction pattern and the corresponding Rietveld refinement of $Li_2In_{1/3}Sc_{1/3}Cl_4$; experimental data are shown in black circles; the red line denotes the calculated pattern; the difference profile is shown in blue and calculated positions of the Bragg reflections are shown as red ($Li_2In_{1/3}Sc_{1/3}Cl_4$, 97.424 wt %) and blue (LiCl, 2.576 wt %) vertical ticks. R_{wp} and GoF are the weighted profile R-factor and goodness of fit, respectively. (b) structure of $Li_2In_{1/3}Sc_{1/3}Cl_4$ from the refinement, showing only the blue Li4/In1/Sc1 octahedral framework; (c) structure depicting the face-sharing Li1 tetrahedra and Li2 octahedra that represent the main 3D Li ion diffusion pathway; Li1 tetrahedra and Li2 octahedra in light orange; (d) enlarged Li^+ diffusion pathway through Li2 octahedra passing through Li1 or Li3 tetrahedra.

formation of about 40 wt% $Li_3In_{2/3}Sc_{1/3}Cl_6$ in the high-indium content material upon slow cooling (see neutron diffraction refinement results, **Figure 6.4a** and **Table 6.5**). As both spinel[182] and monoclinic phases[82, 187] reported previously display good ionic conductivities, the two phase composition with x = 0.444 also exhibits high ionic conductivity (**Figure 6.1c**). A detailed study of different synthesis conditions' effects (different sintering temperature and time, ramping rate) will be reported elsewhere.

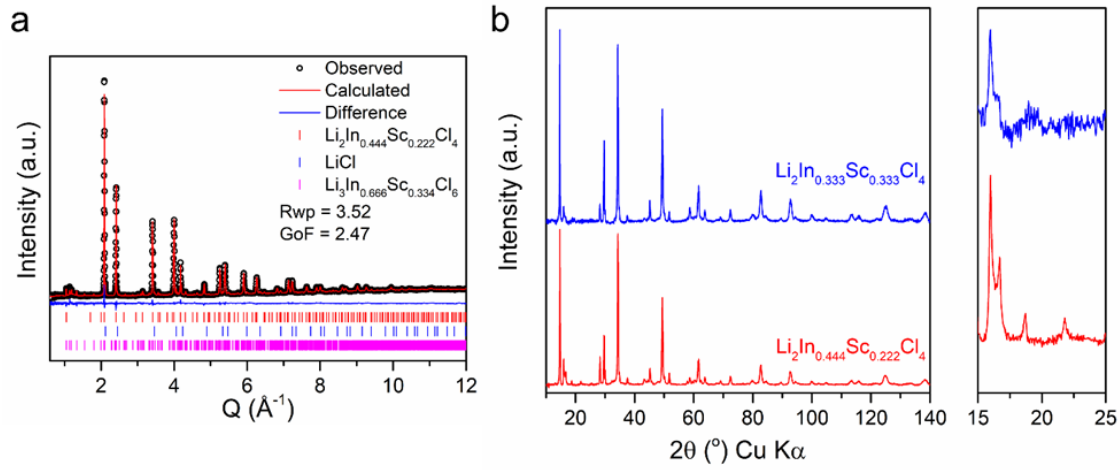

Figure 6.5 (a) Time-of-flight neutron diffraction pattern and the corresponding Rietveld refinement of $Li_2In_{0.444}Sc_{0.222}Cl_4$, Experimental data are shown in black circles; the red line denotes the calculated pattern; the difference profile is shown in blue and calculated positions of the Bragg reflections are shown as red ($Li_2In_{0.444}Sc_{0.222}Cl_4$, 58.784%), blue (LiCl, 1.817%) and pink ($Li_3In_{0.666}Sc_{0.334}Cl_6$, 39.400%) vertical ticks. R_{wp} and GoF are the weighted profile R-factor and goodness of fit respectively. Due to the peak overlap between cubic spinel and monoclinic phases, the refinement was initially conducted with only the cubic spinel phase and LiCl, and then all the structural parameters were fixed. Finally, the monoclinic phase was added to the refinement, with the single crystal diffraction framework used as a starting point. The Sc and In occupancies were fixed from single crystal results during the refinement. (b) powder X-ray diffraction patterns collected in Debye-Scherrer geometry, of $Li_2In_{0.444}Sc_{0.222}Cl_4$ (red), and $Li_2In_{0.333}Sc_{0.333}Cl_4$ (blue) at high-resolution with long scan times to identify trace impurities. Samples were sealed in 0.3 mm (diameter) glass capillaries under argon. The enlarged area shows reflections corresponding to the monoclinic phase, which is almost invisible for $Li_2In_{0.333}Sc_{0.333}Cl_4$.

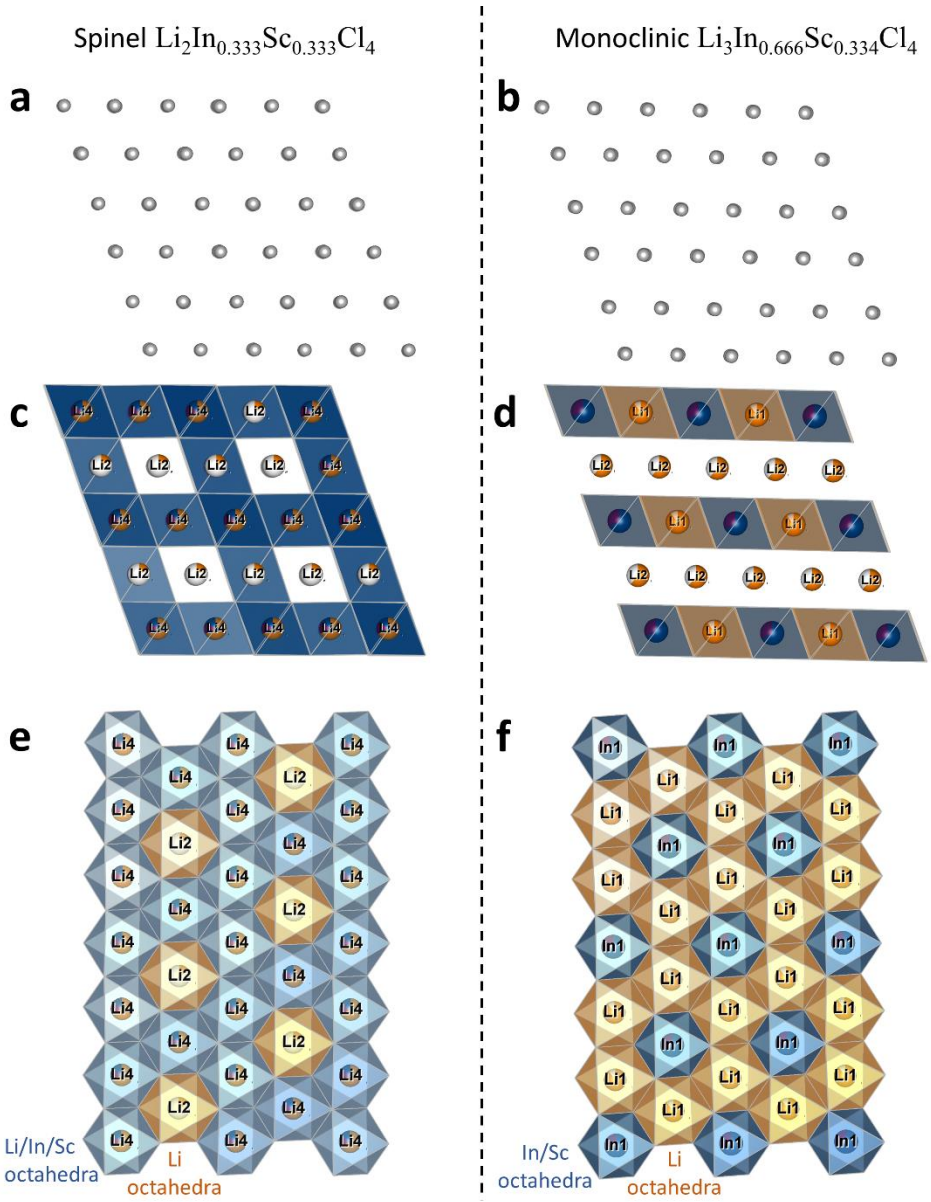

Figure 6.6 Structure comparison between spinel $Li_2In_{0.333}Sc_{0.333}Cl_4$ and monoclinic $Li_3In_{0.666}Sc_{0.334}Cl_6$. (a, b) a cubic close-packed (ccp)-like Cl anion arrangement in both structures; (c) spinel structure with Sc/In occupy Li layer, and (d) monoclinic structure with no Sc/In in Li layer; (e) spinel structure with Sc/In/Li shared site, and (f) monoclinic structure with distinct In/Sc and Li site (no shared occupancy).

Table 6.3 Atomic coordinates, occupation factors, and equivalent isotropic displacement parameters of $Li_3In_{0.666}Sc_{0.334}Cl_6$ obtained from single crystal X-ray diffraction at 270 K.

Monoclinic $Li_{2.18(4)}In_{0.664(7)}Sc_{0.336(7)}Cl_6$ (refined composition), space group: *C*2/*m* *a*= 6.404(1) Å, *b* = 11.066(2) Å, *c* = 6.383(1) Å, *b* = 109.790(5) º						
Atom	Wyck. Site	*x*	*y*	*z*	Occupancy	U_{eq} (Å^2)
Li1	4*g*	0.5	-0.1660(7)	0	1	0.030(2)
Li2	4*h*	0	0.170(12)	0.5	0.09(7)	0.05(6) (U_{iso})
In1	2*a*	0	0	0	0.664(7)	0.0143(2)
Sc1	2*a*	0	0	0	0.336(7)	0.0143(2)
Cl1	4*i*	0.7561(2)	0	0.2336(2)	1	0.0202(3)
Cl2	8*j*	0.2410(2)	0.83788(6)	0.2383(2)	1	0.0202(3)

Table 6.4 Anisotropic displacement parameters of $Li_3In_{0.666}Sc_{0.334}Cl_6$ obtained from single crystal X-ray diffraction at 270 K.

Atom	U_{11} (Å^2)	U_{22} (Å^2)	U_{33} (Å^2)	U_{23} (Å^2)	U_{13} (Å^2)	U_{12} (Å^2)
Li1	0.023(4)	0.015(4)	0.056(6)	0.000	0.020(4)	0.000
In1	0.0117(2)	0.0112(3)	0.0213(3)	0.000	0.00711(18)	0.000
Sc1	0.0117(2)	0.0112(3)	0.0213(3)	0.000	0.00711(18)	0.000
Cl1	0.0180(5)	0.0230(5)	0.0225(5)	0.000	0.0108(4)	0.000
Cl2	0.0200(4)	0.0172(4)	0.0219(4)	0.0032(2)	0.0051(3)	0.0040(2)

Table 6.5 Atomic coordinates, occupation factors, and isotropic displacement parameters of $Li_2In_{0.444}Sc_{0.222}Cl_4$ and $Li_3In_{0.666}Sc_{0.334}Cl_6$ obtained from time-of-flight powder neutron diffraction at 300 K. U_{iso} values for the Li1 and Li2 sites in $Li_3In_{0.666}Sc_{0.334}Cl_6$ were refined to be equal and the Sc1 and In1 site occupancies were fixed from the single crystal results.

Spinel $Li_2In_{0.444}Sc_{0.222}Cl_4$, a = 10.42562(8) Å, space group: $Fd\bar{3}m$						
Atom	Wyck. Site	*x*	*y*	*z*	Occupancy	U_{iso} (Å^2)
Li1	8*a*	0.125	0.125	0.125	0.28(5)	0.025(13)
Li2	16*c*	0	0	0	0.20(2)	0.040(9)
Li3	48*f*	0.125	0.125	0.89(4)	0.008(7)	0.025
Li4	16*d*	0.5	0.5	0.5	0.673(3)	0.0025(10)
Sc1	16*d*	0.5	0.5	0.5	0.109(1)	0.0025(10)
In1	16*d*	0.5	0.5	0.5	0.218(3)	0.0025(10)
Cl1	32*e*	0.25414(6)	0.25414(6)	0.25414(6)	1	0.0208(2)

Monoclinic $Li_3In_{0.666}Sc_{0.334}Cl_6$, space group: *C*2/*m* *a*= 6.4017(3) Å, *b* = 11.0596(3) Å, *c* = 6.3756(2) Å, *b* = 109.781(4) ^{o}						
Atom	Wyck. Site	*x*	*y*	*z*	Occupancy	U_{iso} (Å^2)
Li1	4*g*	0.5	-0.170(3)	0	0.89(4)	0.040(3)
Li2	4*h*	0	0.19(2)	0.5	0.61(4)	0.040(3)
In1	2*a*	0	0	0	0.664	0.0104(8)
Sc1	2*a*	0	0	0	0.336	0.0104(8)
Cl1	4*i*	0.7541(8)	0	0.2321(7)	1	0.0139(8)
Cl2	8*j*	0.2390(6)	0.8382(4)	0.2352(4)	1	0.0197(5)

6.4 Electrochemical performance of ASSBs with typical cell loading 1.25 mAh.cm^{-2}

ASSBs using $Li_2In_{1/3}Sc_{1/3}Cl_4$ as the catholyte with uncoated high voltage CAMs (bare-LCO, bare-NCM622 or NCM85), and Li-In alloy as the negative electrode (see cell design in **Figure 6.7**) were fabricated to examine the electrochemical performance of $Li_2In_{1/3}Sc_{1/3}Cl_4$. A thin layer of highly conductive argyrodite SE ($Li_{6.7}Si_{0.7}Sb_{0.3}S_5I$)[65] was added on top of the Li-In alloy to reduce the total cell resistance and prevent reduction of the chloride SE. A layer of $Li_2In_{1/3}Sc_{1/3}Cl_4$ between the negative electrode and the cathode composite served as the separator. The cathode composite typically consisted of 80 wt% CAM and 20 wt% $Li_2In_{1/3}Sc_{1/3}Cl_4$. **Figure 6.8** shows the excellent rate capability of both LCO (**Figure 6.8a, b**) and NMC85 (**Figure 6.8c, d)** ASSBs. With an upper cutoff voltage of 4.3 V vs Li^+/Li, the LCO cell retained a reversible capacity of 137 mAh.g^{-1} for LCO (*i.e.*, theoretical capacity) at a C/2 rate. Even at a 3C rate, the LCO cell still exhibits a capacity of 86 mAh.g^{-1}. Similarly, the NMC85 cell exhibits a high capacity of 195 mAh.g^{-1} at C/5; 180 mAh.g^{-1} at a C/2 rate, and 89 mAh.g^{-1} at a 3C rate at room temperature. The excellent rate capability of both cells represents the best ASSB performance for chloride SEs.[80, 82, 83, 182]

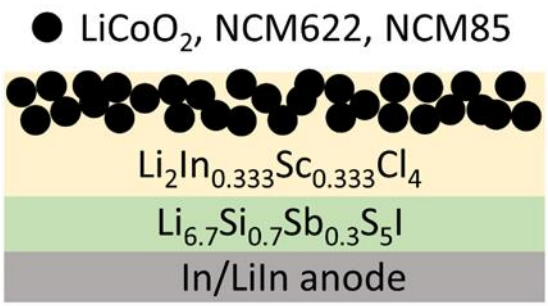

Figure 6.7 Schematic illustration of the ASSB configuration, with Li-In alloy as the negative electrode, $Li_{6.7}Si_{0.7}Sb_{0.3}S_5I$ as the separator and $Li_2In_{0.333}Sc_{0.333}Cl_4$ as the solid electrolyte for the catholyte and separator.

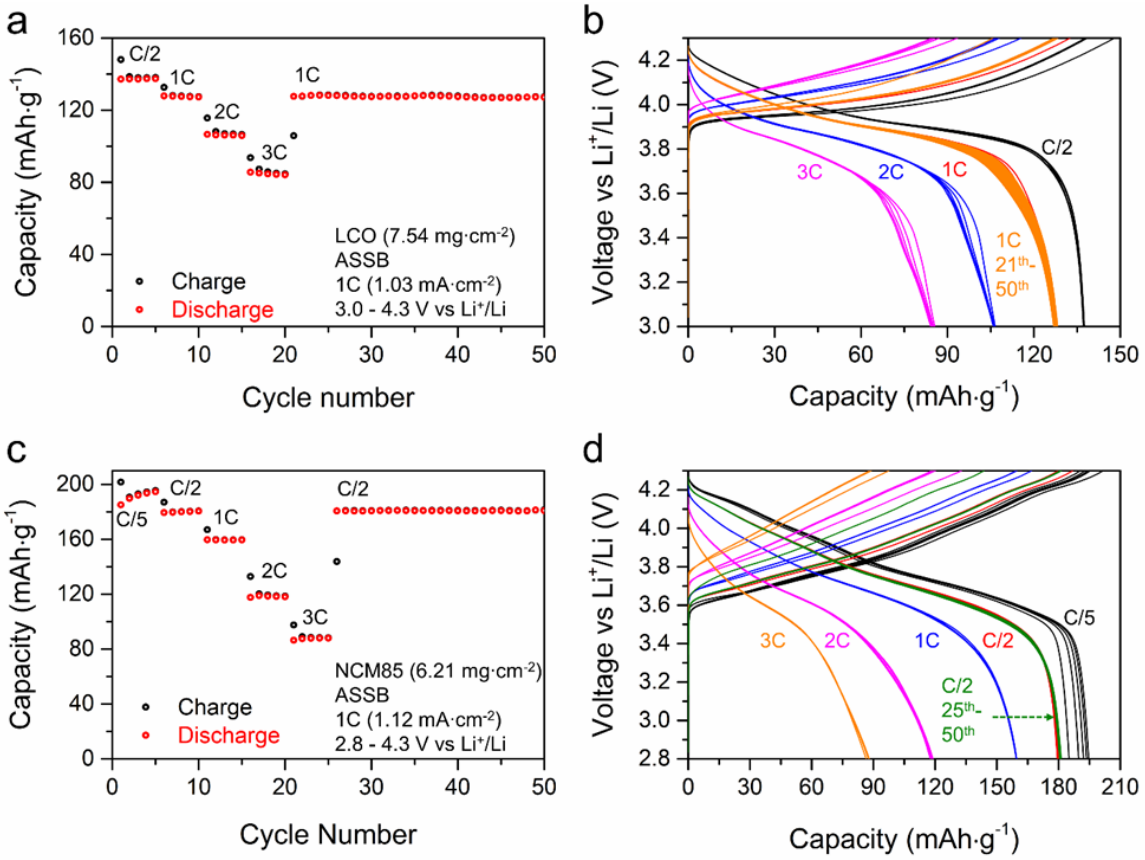

Figure 6.8 Charge-discharge capacity as a function of cycle number at different C-rates for ASSBs comprised of cathode active materials and 20 wt% $Li_2In_{1/3}Sc_{1/3}Cl_4$: (a) LCO and (c) NMC85; and corresponding charge-discharge curves at different C-rates for (b) LCO and (d) NMC85.

Long-term cycling at a C/5 rate was performed for NCM85 cycled between 2.8 V - 4.3 V vs Li^+/Li (**Figure 6.9a** and **6.10a**) and NCM622 cycled between 2.8 V - 4.6 V vs Li^+/Li (**Figure 6.9b** and **6.10b**). Liquid cells with NCM85 or NCM622 cathodes and an LP57 liquid electrolyte were constructed and cycled under the same conditions as the ASSBs for comparison. The NCM85 ASSB exhibits only minor capacity fade, maintaining 90% capacity retention over > 600 cycles. In contrast, the NCM85 liquid cell shows fast capacity fade with 80% capacity retention over only 100 cycles (**Figure 6.10c, d**). **Figure 6.9b** and **6.10b** show the capacity retention and charge-discharge voltage profile of NCM622 cell cycled up to 4.6

V vs Li^+/Li at a C/5 rate which achieves up to 194 $mAh \cdot g^{-1}$ and sustains > 180 $mAh \cdot g^{-1}$ over 320 cycles. Conversely, the NCM622 liquid cell fades very quickly, and the cell retains a mere 62 $mAh \cdot g^{-1}$ capacity over 150 cycles (**Figure 6.10e, f**), owing to the combination of interphase impedance growth on the cathode and Li metal anode, respectively.

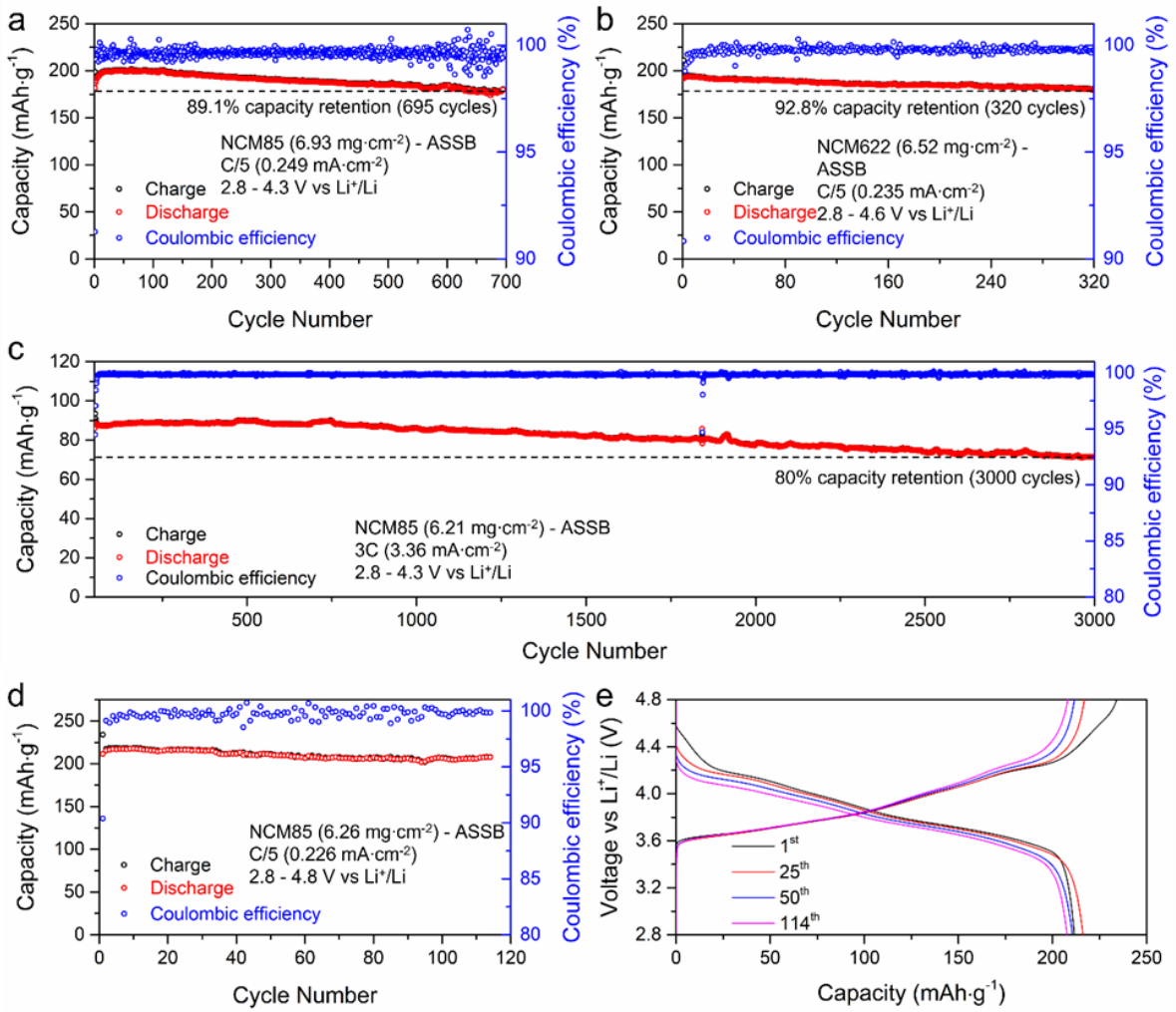

Figure 6.9 Charge-discharge capacity and the coulombic efficiency (CE) as a function of cycle number for (a) NCM85 ASSB; (b) NCM622 ASSB; (c) long term cycling of the NCM85 ASSB (performed after rate cycling) at a 3C rate and (d) ultra-high voltage NCM85 ASSB cycled between 2.8 - 4.8 V vs Li^+/Li and corresponding charge-discharge voltage profile (e).

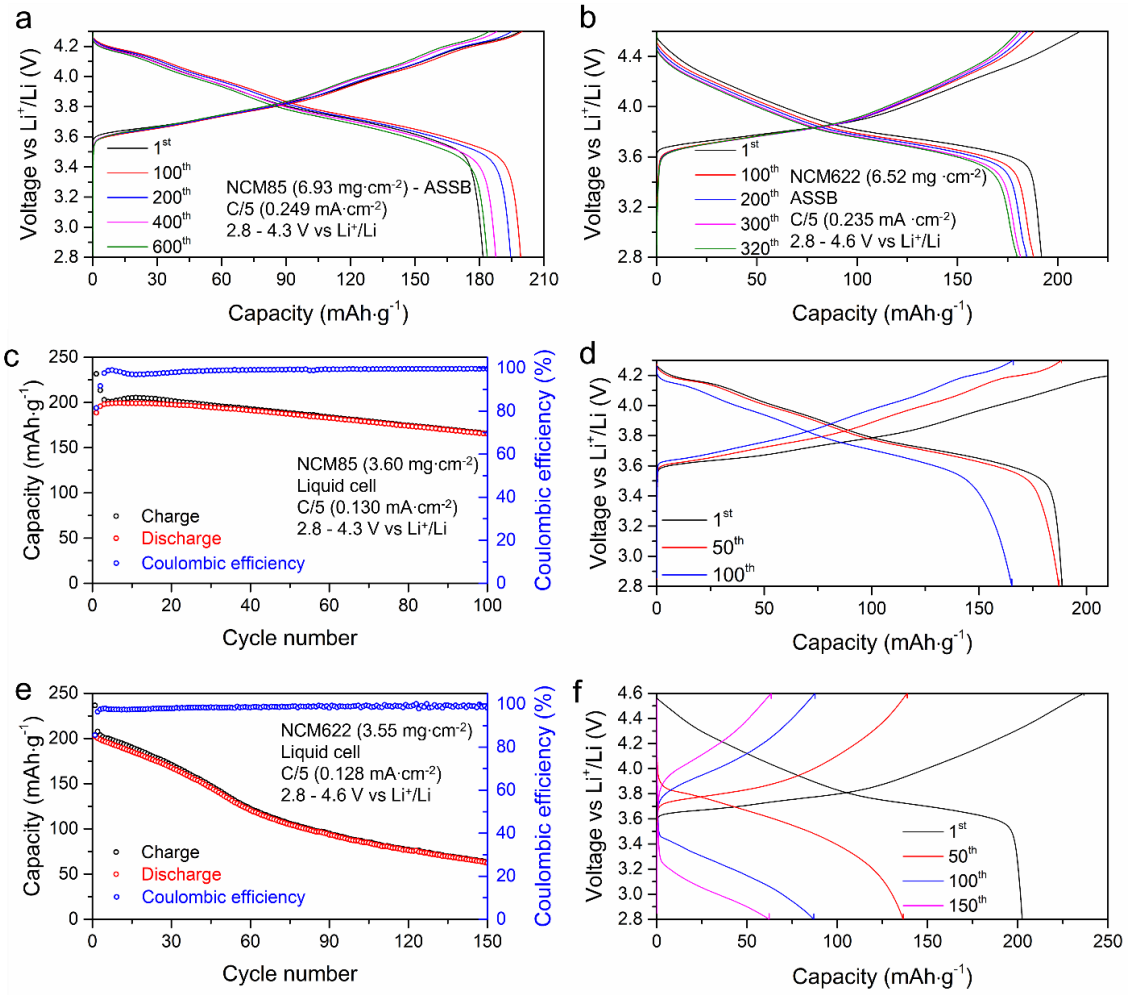

Figure 6.10 Charge-discharge voltage profile of an NCM85 (a) ASSB cycled at a C/5 rate between 2.8 - 4.3 V vs Li^+/Li; and an NCM622 (b) ASSB cycled at C/5 rate between 2.8 - 4.6 V vs Li^+/Li. Charge-discharge capacity and the coulombic efficiency (CE) as a function of cycle number and corresponding charge-discharge voltage profile for an NCM85 (c, d) liquid cell cycled at C/5 rate between 2.8 - 4.3 V vs Li^+/Li; and an NCM622 liquid cell cycled at C/5 rate between 2.8 - 4.6 V vs Li^+/Li. This demonstrates the superior stable cycling of the ASSB compared to the conventional liquid cell.

NCM85 ASSBs also exhibit stable cycling and very slow capacity fading at high voltage, even at 4.8 V vs Li^+/Li over > 110 cycles as shown in **Figure 6.9d, e**. The slow capacity fading is not due to SE decomposition (see next section), but is likely related to the known structural transformation of high-Ni NCM at high voltage (H2-H3 transition) and O_2

release. The cell maintains 95% capacity retention over 110 cycles, which is better than recently reported $LiNi_{0.8}Co_{0.1}Mn_{0.1}O_2$ liquid cell performance (up to 4.7 V, 88.1% capacity retention over 100 cycles) in a highly engineered sulfonamide-based electrolyte.[188]

Since a typical commercial LIB contains more than 90 wt% CAM, for comparison we also fabricated a NMC85 ASSB with 10 wt% chloride SE and 90 wt% CAM (**Figure 6.11)**. The cell exhibits very good cycling behavior, but slightly lower discharge capacity (180 $mAh.g^{-1}$) compared to the ASSB with 80 wt% NMC85 (**Figure 6.9a**). We ascribe this to poorer ionic conduction percolation within the cathode composite due to the lower content of solid electrolyte, which would likely be improved by further nanostructuring the catholyte and optimizing cathode crystallize size and morphology.[172-174]

In order to demonstrate the long-term cycle life of the ASSBs, after the rate cycling studies in **Figure 6.8d** were conducted, cycling of the NMC85 ASSB weas continued at a super-high rate corresponding to charge-discharge in 20 minutes (*i.e.*, 3C). Over more than 1000 cycles **(Figure 6.9c** and **6.12**) the NMC85 ASSB exhibits virtually no fading and maintains a capacity > 86 $mAh.g^{-1}$. Moreover, the cell sustains >80% capacity over 3000 cycles.

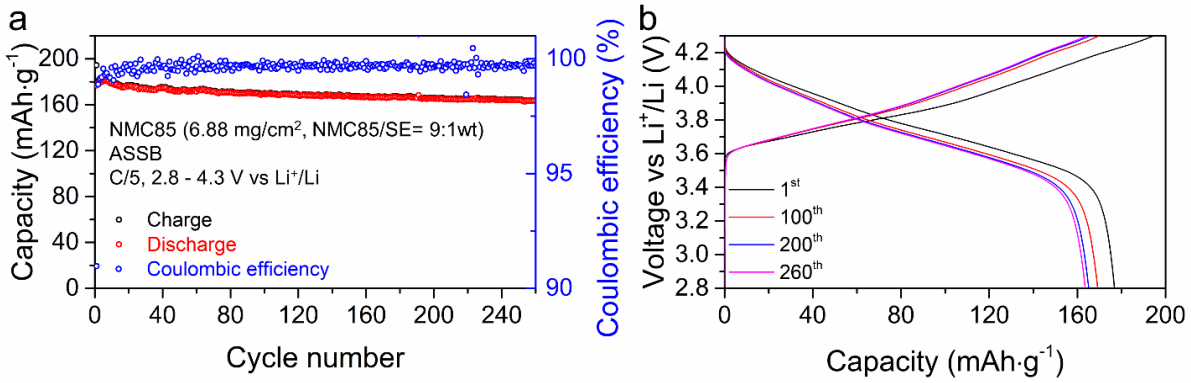

Figure 6.11 Charge–discharge capacity and the coulombic efficiency as a function of cycle number for (a) NMC85 ASSB with a cathode composite weight ratio of NMC85 and $Li_2In_{0.333}Sc_{0.333}Cl_4$ solid electrolyte of 90:10, (b) corresponding charge-discharge curves.

A second cell was also constructed and exhibited the same excellent long term cycling stability (see **Figure 6.13**). At a 2C rate, the cell maintains a high discharge capacity ~ 155 mAh·g^{-1} and sustains > 94% capacity over 1000 cycles (see **Figure 6.14**). The overall performance is amongst the best compared to that reported for all-ceramic ASSBs.[80, 82, 83, 137, 182, 189, 190]

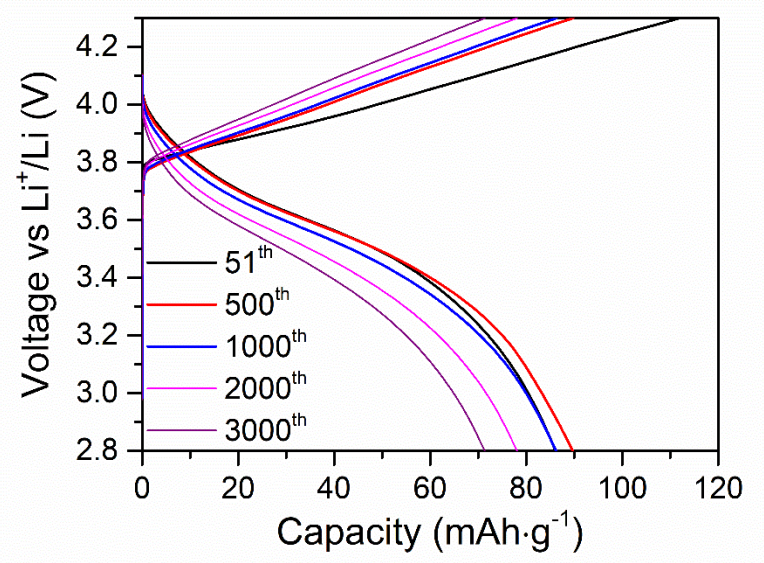

Figure 6.12 Charge-discharge curves of long-term cycling of the NMC85 ASSB (after rate cycling) at 3C, demonstrating excellent cycling stability over more than 3000 cycles.

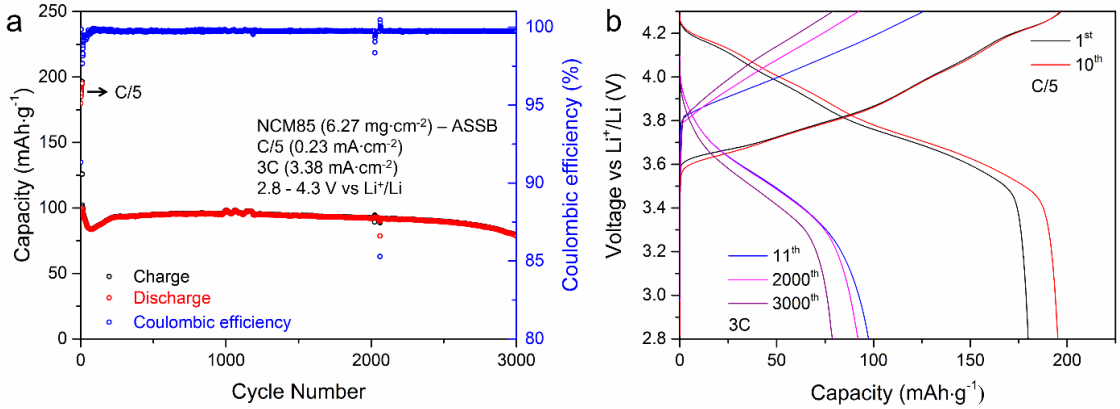

Figure 6.13 (a) Charge-discharge capacity and coulombic efficiency as a function of cycle number and (b) Charge-discharge voltage profiles for NCM85 ASSB cycled at 3C rate between 2.8 - 4.3 V vs Li$^+$/Li, with initial 10 cycles cycled at C/5.

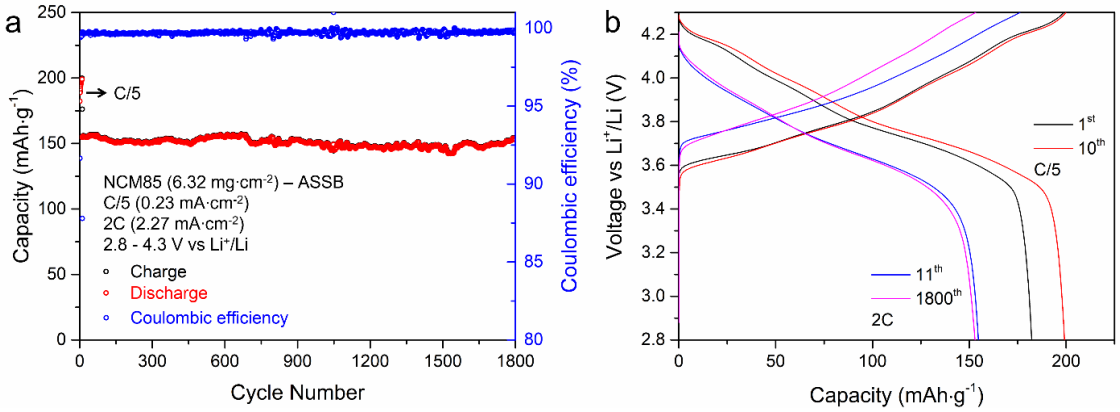

Figure 6.14 (a) Charge-discharge capacity and the coulombic efficiency as a function of cycle number and (b) Charge-discharge voltage profiles for NCM85 ASSB cycled at a 2C rate between 2.8 - 4.3 V vs Li^+/Li, with the initial 10 cycles cycled at C/5. Small fluctuations in capacity and CE in (a) are due to temperature variation during cycling.

6.5 Electrochemical performance of high-loading ASSBs

While the above-mentioned ASSBs exhibit superior electrochemical performance (*vis a vis* previously reported results) at typical cathode loadings of 6 - 8 mg.cm^{-2}, it is desirable to increase the loading to provide comparable areal capacities to commercial LIBs (typically > 3 mAh.cm^{-2}).[115] We note the paucity of data on such cells in the literature.[115, 189, 191] **Figures 6.15a** and **6.16a** show the results for high loading ASSBs (27 mg.cm^{-2} LCO; corresponding to a theoretical value of 3.7 mAh.cm^{-2}) cycled at a high current density of 1.24 mA.cm^{-2} (C/3 rate) at room temperature. They deliver stable capacity retention and high specific capacity (> 3 mAh.cm^{-2} and > 110 mAh.g^{-1} over 180 cycles), albeit with moderately high overpotential under these aggressive conditions. LCO ASSBs with similar CAM-loading cycled at 50 ^{o}C, at an even higher current density of 1.79 mA.cm^{-2} (C/2) deliver excellent reversible capacity and high specific capacity with much lower overpotential (**Figure 6.15b** and **6.16b**). Furthermore, owing to the high electronic conductivity of LCO, ultra-high loading LCO ASSBs (52.46 mg.cm^{-2}, a theoretical value of 7.2 mAh.cm^{-2}) deliver stable areal capacity of 3 mAh.cm^{-2} at

room temperature and 4.5 mAh.cm^{-2} at 50 ºC at a high current density of 1.20 mA.cm^{-2} with no capacity fade for over 500 cycles (**Figure 6.15c** and **6.16c**).

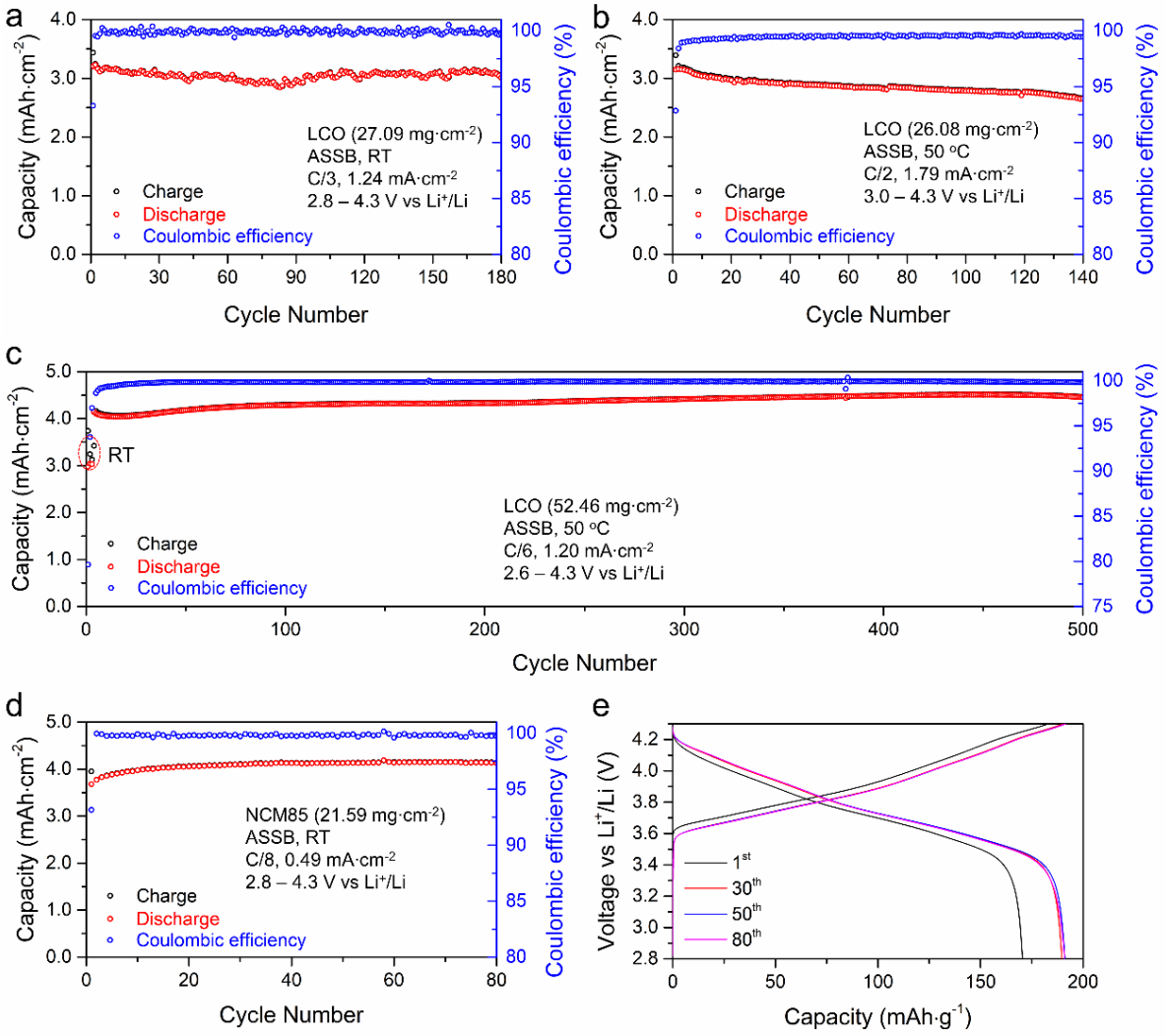

Figure 6.15 High loading ASSB electrochemical performance. Charge-discharge capacity and the coulombic efficiency (CE) as a function of cycle number for LCO ASSBs with areal capacity > 3.5 mAh.cm^{-2} cycled at (a) room temperature between 2.8 - 4.3 V vs Li$^+$/Li at C/3 (1.24 mA.cm^{-2}) and (b) at 50 ºC between 3.0 - 4.3 V vs Li$^+$/Li at C/2 (1.79 mA.cm^{-2}); (c) ultra-high loading LCO ASSB with 52.46 mg.cm^{-2} loading, cycled at room temperature between 2.6 - 4.4 V vs Li$^+$/Li and at 50 ºC between 2.6 - 4.3 V vs Li$^+$/Li at C/6 (1.20 mA.cm^{-2}) and (d) high loading NMC85 ASSB with 21.59 mg.cm^{-2} loading cycled at room temperature between 2.8 - 4.3 V vs Li$^+$/Li at C/8 (0.49 mA.cm^{-2}) and the corresponding charge-discharge curves.

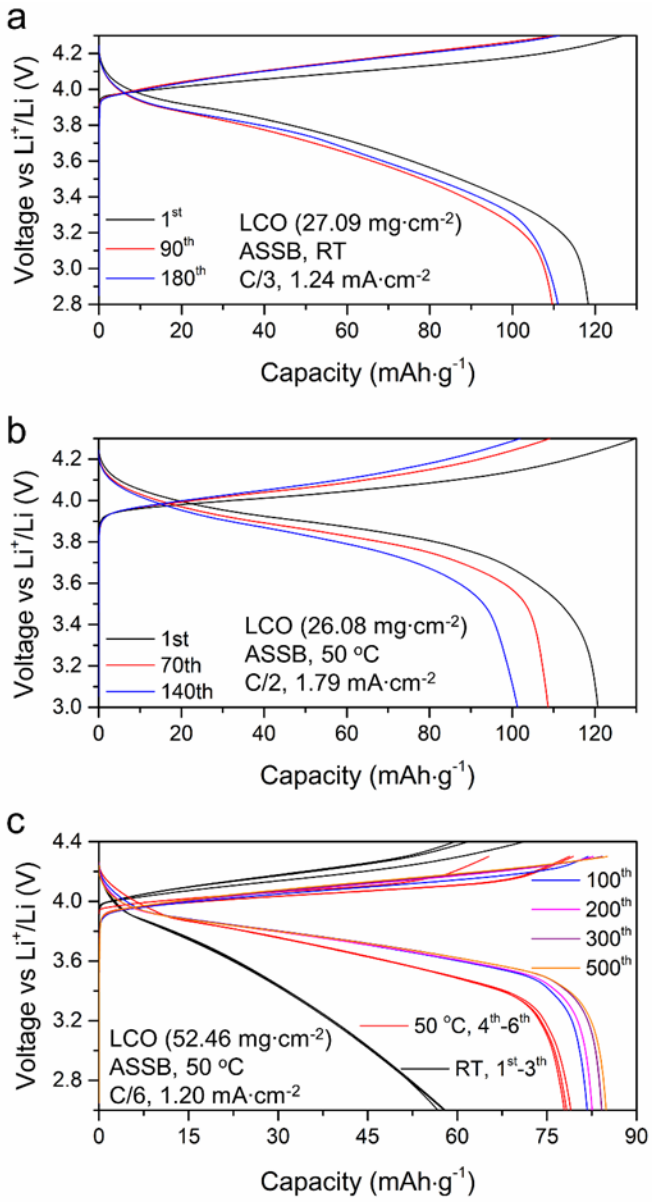

Figure 6.16 Charge-discharge curves of high-loading long-term cycling of LCO ASSBs at (a) room temperature, cycled at C/3 between 2.8 V - 4.3 V vs Li^+/Li and (b) 50 ºC, cycled at C/2 between 3.0 V - 4.3 V vs Li^+/Li and of (c) ultra high-loading LCO ASSB cycled at a C/6 rate and room temperature between 2.6 V - 4.4 V vs Li^+/Li and 50 ºC between 2.6 V - 4.3 V vs Li^+/Li. At high cathode active material loadings, the kinetics of Li ion/electron diffusion within the thick cathode composite are more limited than at low loadings. At high current densities, that results in a high overpotential. The ionic conductivity of the solid electrolyte and both ionic/electronic conductivity of cathode active materials increases with increasing temperature, thus giving better Li ion/electron diffusion kinetics and lower overpotentials. In short, a wider cut-off potential window was used for high-loading ASSB cycled at RT.

As the battery market is focused on high-Ni NMC type CAMs,[7] we also benchmarked high loading NMC85 ASSB (21.59 mg.cm^{-2}). Cells cycled at room temperature between 2.8 - 4.3 V vs Li^{+}/Li at a current density of 0.49 mA.cm^{-2} (**Figure 6.15d, e**) deliver an areal capacity of 4.14 mAh.cm^{-2} (specific capacity of 192 mAh.g^{-1}; very close to the typical value of 200 mAh.g^{-1} observed in liquid LIBs), representing one of the best high-loading ASSBs reported to date. The high loading NMC85 ASSBs were repeated twice (22.31 and 22.00 mg.cm^{-2} loading, respectively, **Figure 6.17**), essentially providing the same results and demonstrating reproducibility. Since using a In/InLi anode will significantly lower the cell energy density, pre-lithiated Si can be used as an alternative negative electrode due to its high electronic

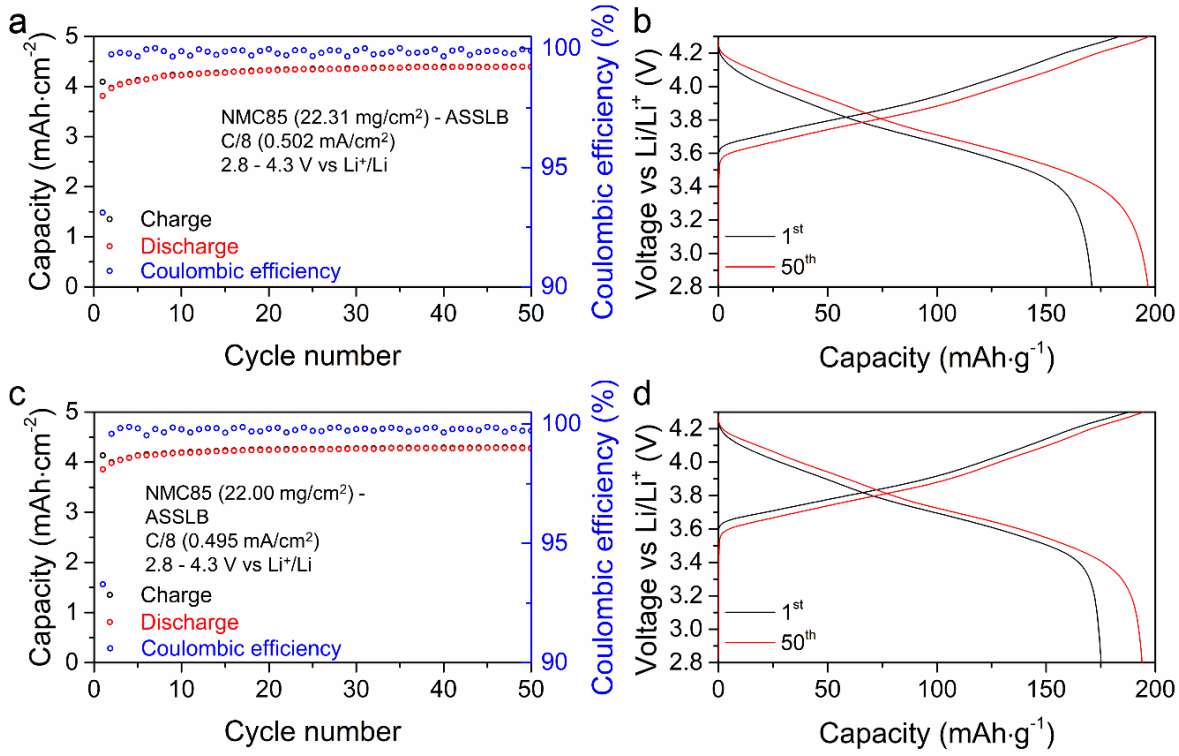

Figure 6.17 High loading NMC85 ASSBs with 22.31 and 22.00 mg/cm^2 CAM-loading cycled at room temperature between 2.8 - 4.3 V vs Li^{+}/Li at a C/8 rate and the corresponding charge-discharge curves. The data, which are essentially the same as shown in Figure 6.15d,e, demonstrate the reproducibility of the electrochemical performance.

conductivity and good mechanical properties. $Li_{12}Si_7$ was synthesized by gently mixing ball-milled Silicon powder (99%, Sigma-Aldrich, 325 mesh, 400 rpm for 10 hours) with stoichiometric amounts of Li powder (FMC) and then grounding in an agate mortar until a homogeneous black colored powder was obtained. The NCM85 ASSB was fabricated using the same procedure as for the cell with In/InLi, using 21.6 mg cathode composite loading and 3.5 mg $Li_{12}Si_7$ powder as the anode. **Figure 6.18** illustrates the fabrication of such an NCM85 cell that exhibits stable cycling and high discharge capacity.

6.6 Origin of superior electrochemical performance

The underlying origin of the exceptional electrochemical performance of $Li_2In_{1/3}Sc_{1/3}Cl_4$ lies in the intrinsically high oxidation stability of lithium metal chlorides and their high ductility.[83] We previously showed that such chlorides are thermodynamically stable up to 4.3 V vs Li^+/Li with a kinetically driven higher oxidation limit up to 4.6 V vs Li^+/Li. [182] All lithium metal chlorides should exhibit similar thermodynamic oxidation potentials in the range of 4.21 - 4.25 V vs Li^+/Li based on theory;[192] and in principle, ASSBs utilizing chloride SEs with similar ionic conductivity should also exhibit comparable electrochemical properties. However, previously reported ASSBs with chloride SEs[80, 82, 83, 187] exhibit poorer performance than we described above, suggesting that other factors including the active material/solid electrolyte ratio, catholyte fabrication, and cell pressure play a factor.

Figure 6.19a shows the electrochemical impedance spectra (EIS) that monitor the internal resistance evolution of an NCM622 ASSB cycled between 2.8 - 4.6 V during the 1st cycle. The points on the voltage profile where the spectra were collected are indicated. The semicircles in the Nyquist plot represent the overlapping charge transfer contributions from

the SE-cathode (and anode) interfaces. On charging (**Figure 6.19a**, top), the cell resistance decreases slightly to reach a minimum at 50% SOC (point 4) and then maximizes at 100%

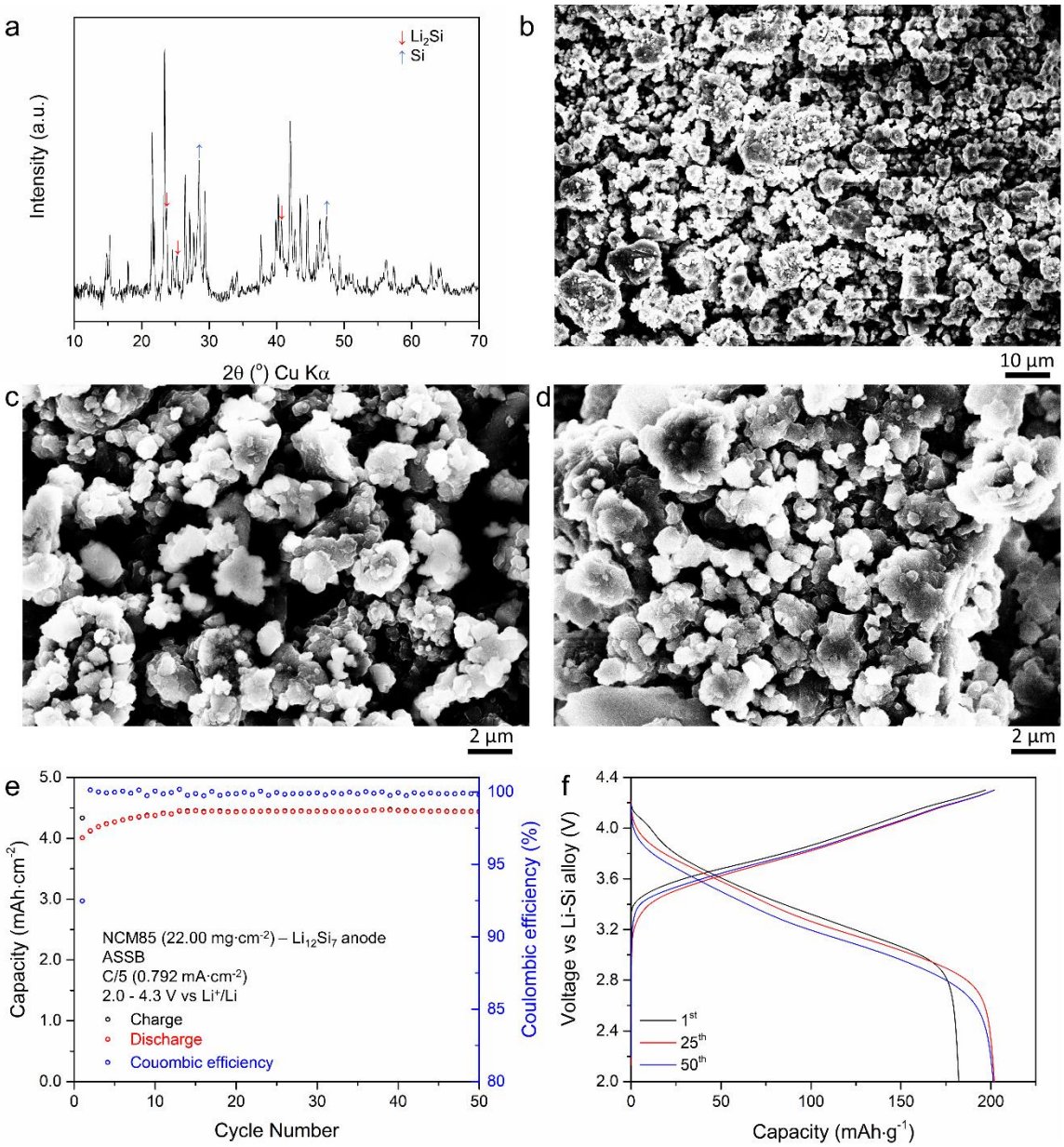

Figure 6.18(a) XRD pattern of a Li-Si alloy synthesized by mixing Li and Si powder; the main reflections are assigned to $Li_{12}Si_7$ and residual Si and Li_2Si are indicated. (b-d) SEM images of the as-synthesized Li-Si alloy showing micron-sized particles. (e) Charge-discharge capacity and the coulombic efficiency as a function of cycle number and (f) Charge-discharge voltage profiles for NCM85 ASSB with the Li-Si alloy anode cycled at a C/5 rate between 2.0 - 4.3 V.

SOC (point 7). While the changes are small, they can be ascribed to changes in the electronic[193] and ionic conductivity[194] of $Li_{1-x}Ni_{0.6}Co_{0.2}Mn_{0.2}O_2$ during de-lithiation. On discharge (**Figure 6.19a**, bottom), the process reverses (points 7-11). The much higher impedance at the lowest frequency (100 mHz) for the fully discharged cell (point 12) and in point 1 (**Figure 6.20**) is

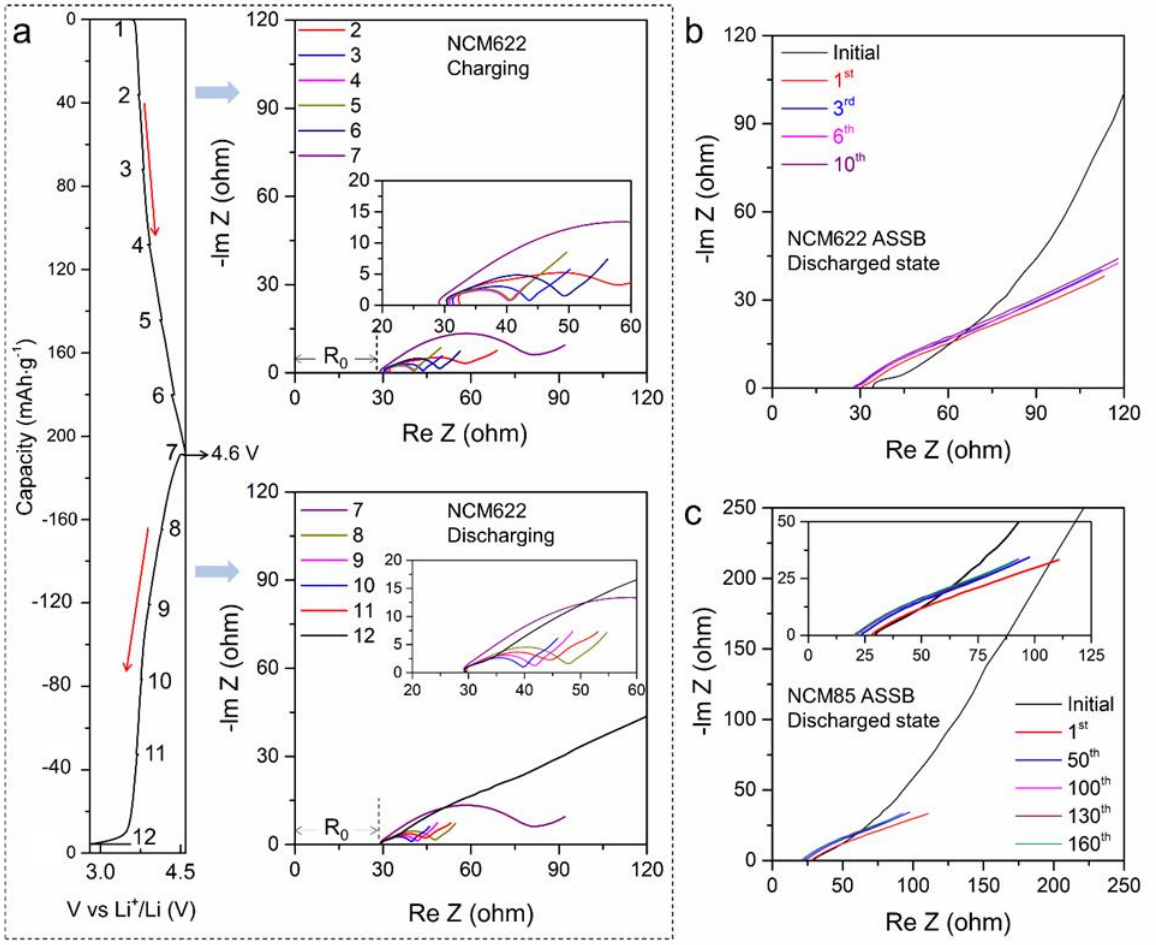

Figure 6.19 (a) Impedance evolution during the first cycle of an NMC622 ASSB cycled between 2.8 - 4.6 V vs Li^+/Li. The corresponding voltage profile (left) and impedance spectra (right) collected during charging (top) and discharging (bottom) are shown. The numbers on the voltage profile correspond to the points where the EIS spectra were collected at every hour after a 30 min rest (before and after). Nyquist plots of (b) an NMC622 ASSB cycled between 2.8 - 4.6 V vs Li^+/Li for 10 cycles at full discharge, cells were equilibrated for 1 h before and after (c) an NMC85 ASSB cycled between 2.8 - 4.3 V vs Li^+/Li for 90 cycles and equilibrated at full discharge for 1 h. All studies were conducted at a C/5 rate.

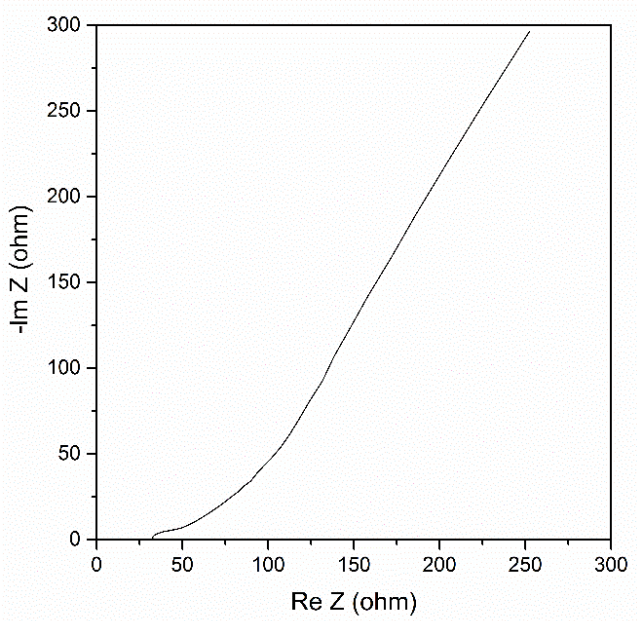

Figure 6.20 Initial Nyquist plot of the NMC622 ASSB and the corresponding impedance evolution during the first cycle that is shown in Figure 6.19a.

attributed to diffusion limitation in the bulk NCM particles in their reduced state.[194] The same processes were observed for NCM85 and LCO, as shown in **Figure 6.20,21**. Overall, the total cell resistance is very low during cycling (< 80 Ω). Nyquist plots for NCM622 (**Figure 6.19b;** 2.8 - 4.6 V vs Li^+/Li) and LCO (**Figure 6.23;** 2.8 - 4.3 V vs Li^+/Li) ASSBs collected at the fully discharged state for cells cycled at C/5 or C/2 show negligible internal resistance increase over 10 cycles. Long term EIS measurements were conducted for NCM85 ASSBs upon charge to 4.3 V and the corresponding Nyquist plots in **Figure 6.19c** show no internal resistance increase over 160 cycles. Such remarkably stable impedance confirms the high oxidation stability of chloride SE (up to 4.6 V vs Li^+/Li) that allows the use of bare CAMs.

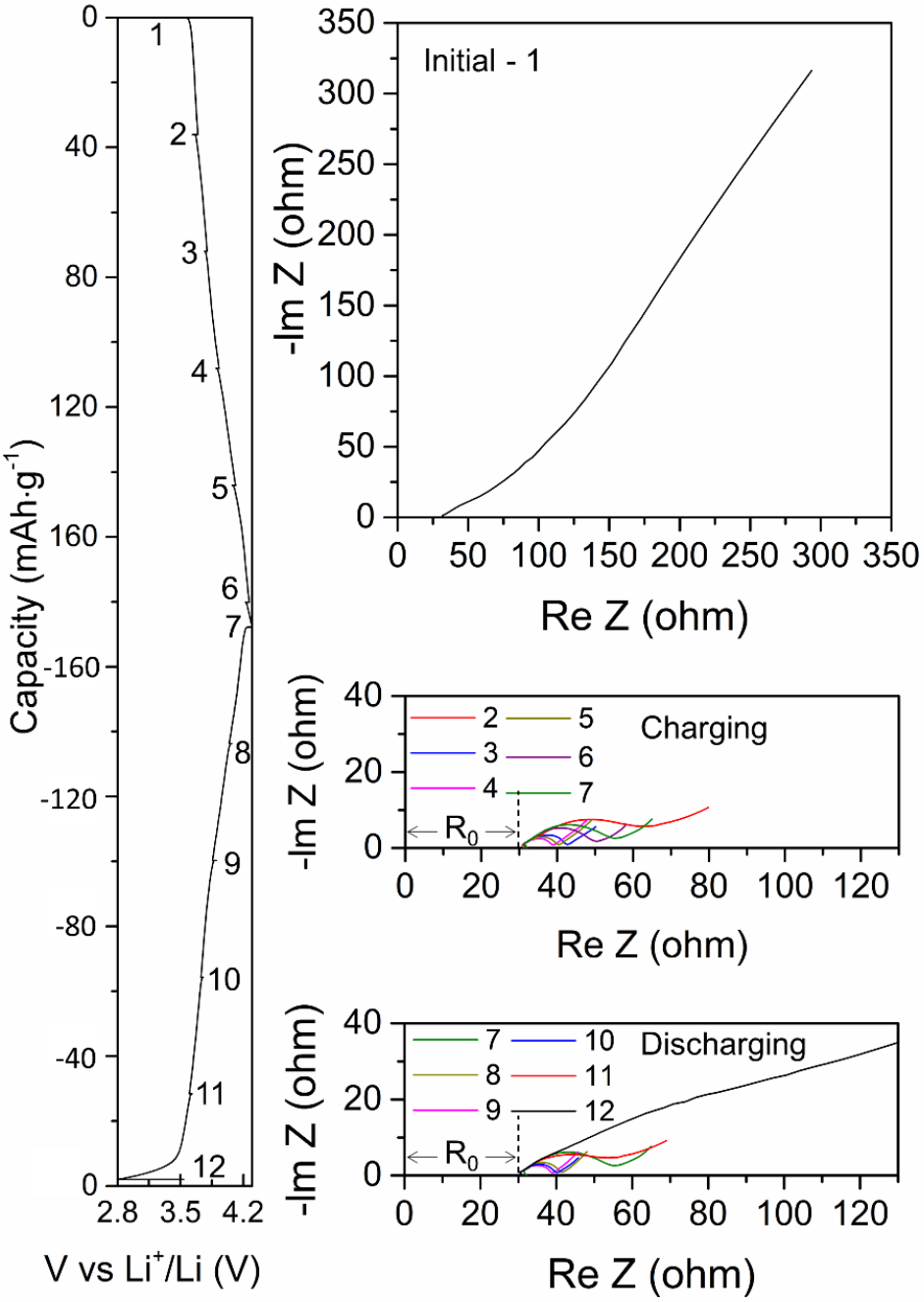

Figure 6.21 Impedance evolution during the first cycle of an NMC85 ASSB cycled between 2.8 - 4.3 V vs Li^+/Li. The corresponding voltage profile (left) and impedance spectra (right) collected on the first cycle (top); during charging (middle) and discharging (bottom) are shown. The numbers on the voltage profile correspond to the points where the EIS spectra were collected at every hour after a 30 min rest (before and after). All studies were conducted at a C/5 rate.

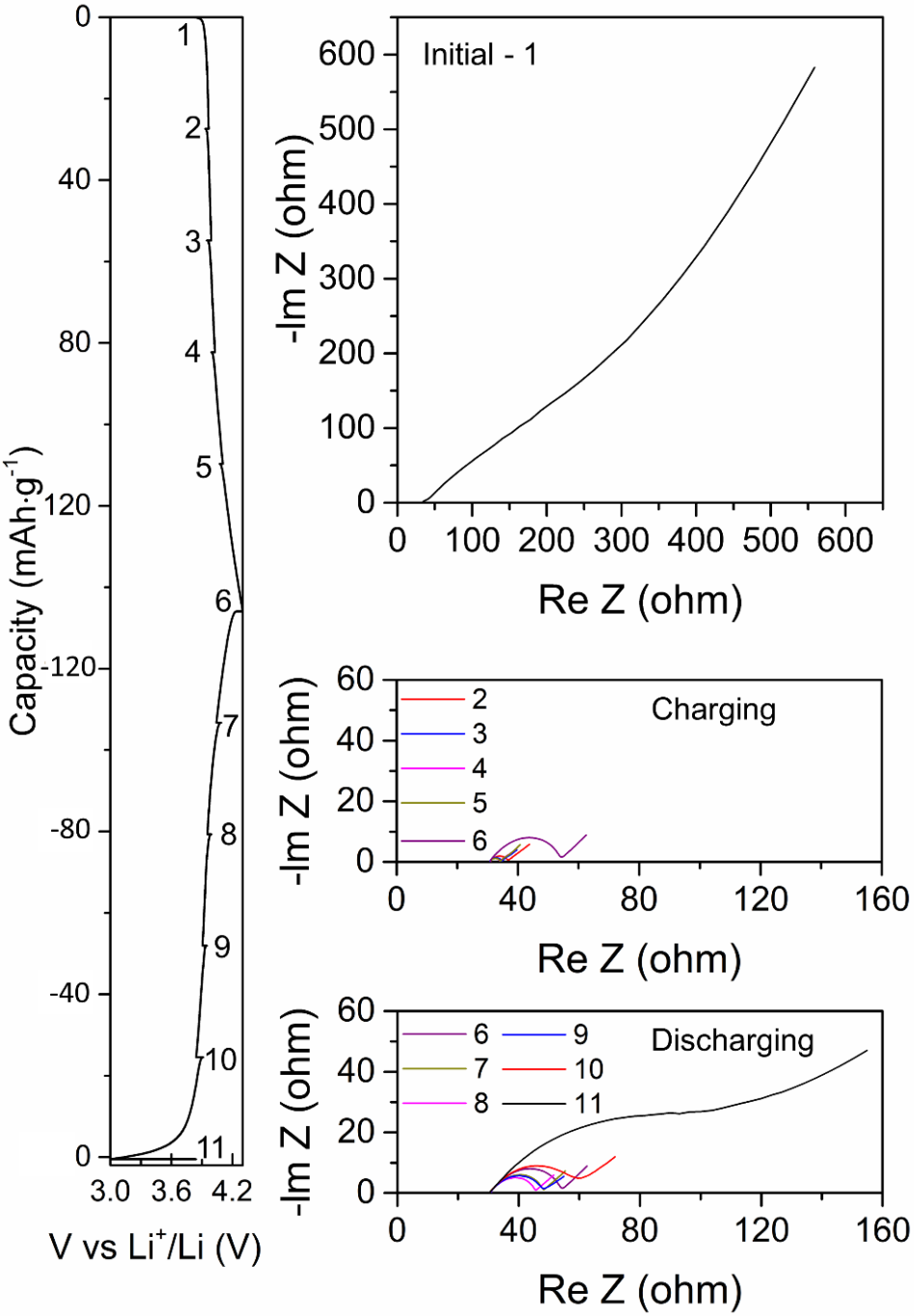

Figure 6.22 Impedance evolution during the first cycle of an LCO ASSB cycled between 3.0 - 4.3 V vs Li^+/Li. The corresponding voltage profile (left) and impedance spectra (right) collected on the first cycle (top); during charging (middle) and discharging (bottom) are shown. The numbers on the voltage profile correspond to the points where the EIS spectra were collected at every hour after a 30 min rest (before and after). All studies were conducted at a C/5 rate.

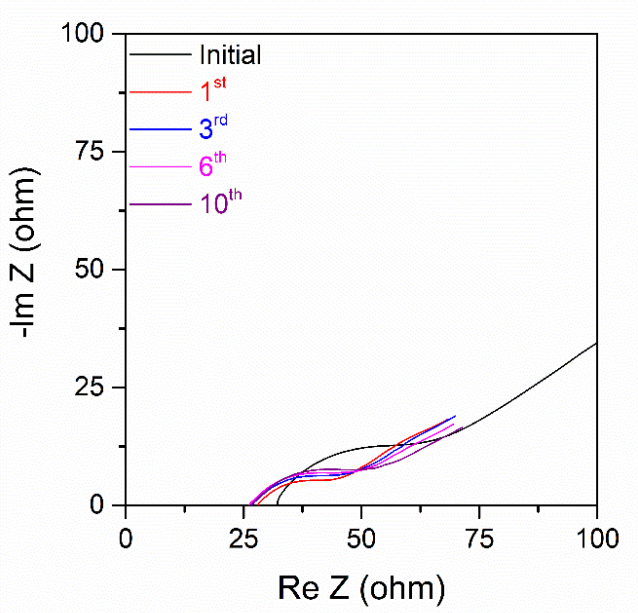

Figure 6.23 Nyquist plots of fully discharged LCO ASSB cycled at a C/2 rate between 2.8 - 4.3 V vs Li^+/Li, shown over the first 10 cycles.

To evaluate interphase growth between NCM85 and the SE at a higher potential of 4.8 V vs Li^+/Li, the impedance was also monitored at numerous points during the first charge-discharge cycle, and showed excellent reversibility (**Figure 6.24**) as observed for NCM622 (see above). An accelerated degradation test was conducted by charging the cell to 4.8 V vs Li^+/Li and holding for an extended period. The 4.8 V aging-test leakage current (**Figure 6.25a**) quickly decreased to reach a minimum value of < 1 μA at the end of a 30 h hold, which suggests the presence of a stable interphase is formed between NCM85 and $Li_2In_{1/3}Sc_{1/3}Cl_4$. The EIS data (**Figure 6.26a**) shows a continuous increase of cell impedance during this process and a final charge transfer resistance of 31 kΩ (**Figure 6.26b**), caused by the very large drop in Li-ion mobility[194] and electronic conductivity in highly de-lithiated NCM85 (estimated here to be $Li_{0.07}Ni_{0.85}Co_{0.1}Mn_{0.05}O_2$). We note that if this impedance originated from the decomposition of chloride SE at high voltage, the cell would show significantly increased overpotential and

decreased capacity in the following cycles. That is not observed, however. Stable cycling (**Figure 6.25b**) after aging and low impedance (**Figure 6.25c**) after final discharge confirms the existence of a stable interface between NCM85 and $Li_2In_{1/3}Sc_{1/3}Cl_4$ even at 4.8 V vs Li^+/Li. A similar stable interface was observed for cells aged at 4.3 V and 4.6 V vs Li^+/Li (see **Figure 6.27,28**).

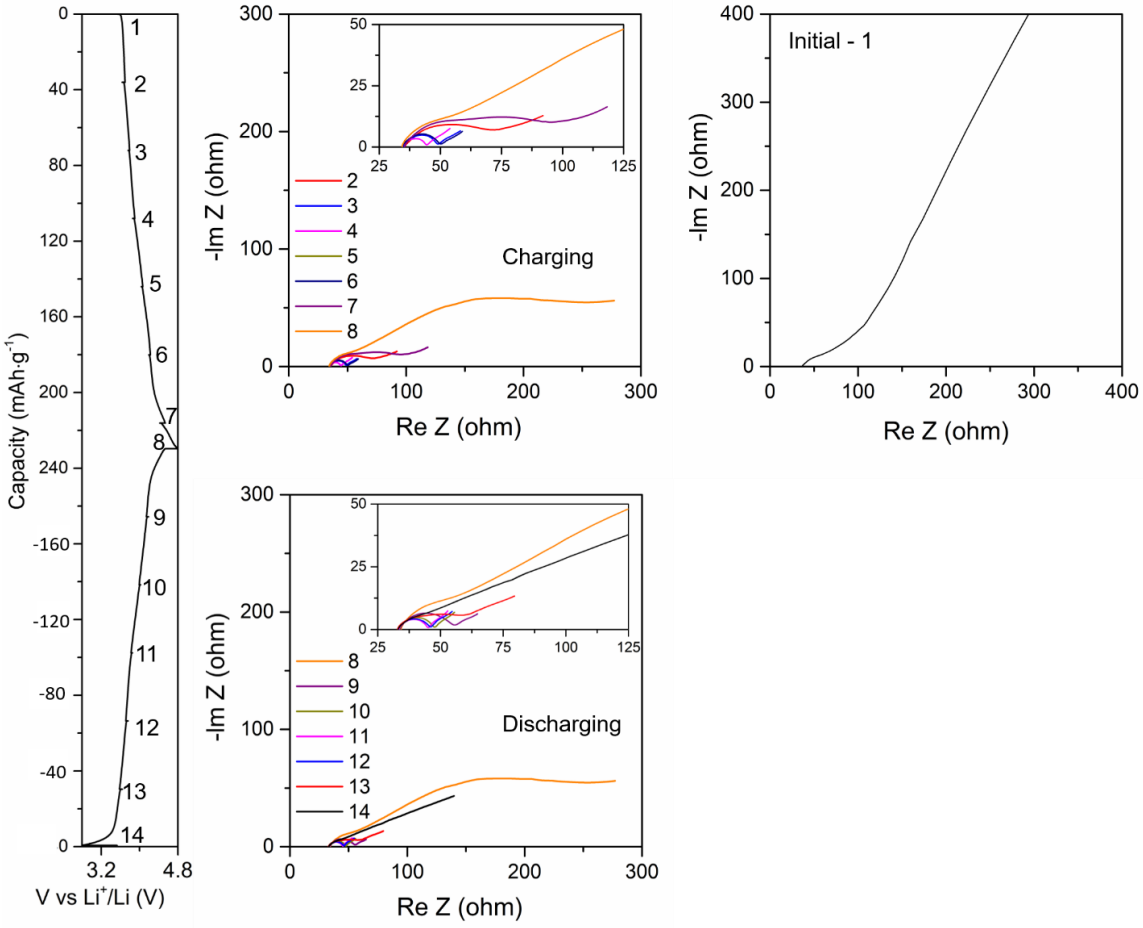

Figure 6.24 Impedance evolution during the first cycle of an NCM85 ASSB cycled between 2.8 - 4.8 V vs Li^+/Li. The corresponding voltage profile (left) and impedance spectra (right) collected in the first cycle; during charging (middle top), discharging (middle bottom), and initial (right) are shown. The numbers on the voltage profile correspond to the points where the EIS spectra were collected at every hour after a 30 min rest (before and after). All studies were conducted at a C/5 rate.

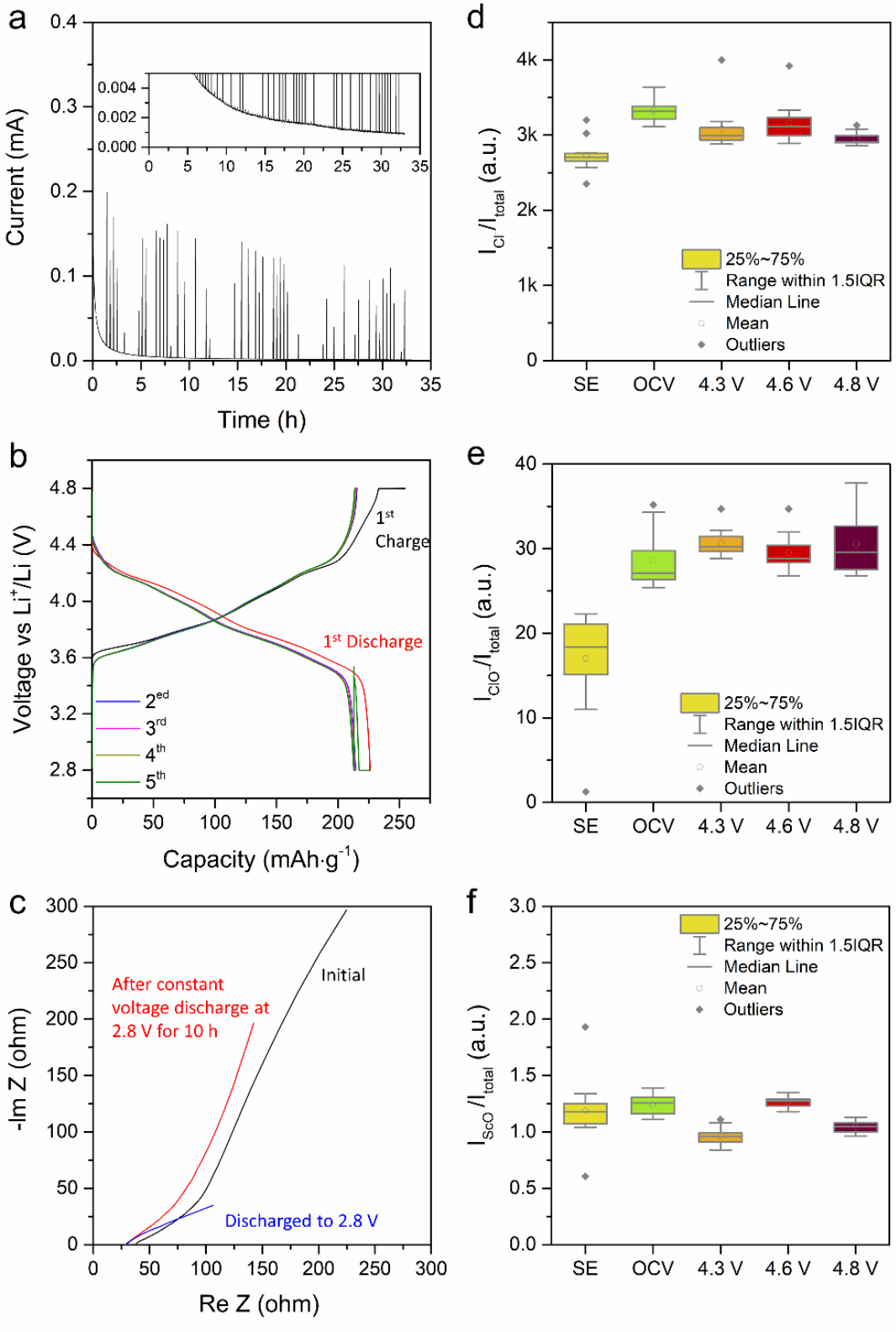
a
Current (mA)
Time (h)
b
Voltage vs Li+/Li (V)
Capacity (mAh·g-1)
1st Charge
1st Discharge
2ed
3rd
4th
5th
c
-Im Z (ohm)
Re Z (ohm)
After constant voltage discharge at 2.8 V for 10 h
Initial
Discharged to 2.8 V
d
ICl/Itotal (a.u.)
e
IClO/Itotal (a.u.)
f
IScO/Itotal (a.u.)
25%~75%
Range within 1.5IQR
Median Line
Mean
Outliers
SE
OCV
4.3 V
4.6 V
4.8 V

Figure 6.25 (a) Leakage current during a hold of NCM85 ASSB at a constant voltage of 4.8 V vs Li^+/Li after 1st charge (aging test). (b) Charge-discharge voltage profile of NCM85 ASSB. After the initial charge, the cell was aged at 4.8 V vs Li^+/Li for 30 hours, followed by continuous cycling after aging. (c) Nyquist plots of NCM85 ASSB at the initial state, after 5th discharge, and after cell discharge held at 2.8 V vs Li^+/Li for 10h. ToF-SIMS surface analysis results of (d) Cl^-, (e) ClO^-, and (f) ScO^- fragments of bare SE, uncycled cathode composite and cycled composites with cut-off potential of 4.3 V (160 cycles), 4.6 V (20 cycles), and 4.8 V (10 cycles) vs Li^+/Li, at a discharged state. The box plots were obtained based on the corresponding normalized signal tensities of 12 spectra on each sample. Box plot center line represents the median (of median F1-scores); lower and upper box limits represent the 25% and 75% quantiles, respectively; whisker extend to box limit ± 1.5 × IQR; outlying points plotted individually.

Interphase stability is further confirmed by time-of-flight secondary-ion mass spectrometry (ToF-SIMS) surface analysis (**Figure 6.25d-f** and **Figure 6.29**). ToF-SIMS is highly sensitive even to small fractions of components, and it has recently been shown that SE degradation at the SE/CAM and thin coatings can be well analyzed.[94, 195] Cathode composites cycled to different cut-off potentials (4.3 V, 4.6 V, and 4.8 V vs Li^+/Li) were compared to an uncycled cathode composite and the pristine SE. The ClO^- and ScO^- fragments could be the sign of the decomposition of $Li_2In_{1/3}Sc_{1/3}Cl_4$ and reaction with lattice oxygen from the NCM at high voltage. However, both signals in **Figure 6.25e,f** exhibit no significant increase after cycling compared to the uncycled composite (indicated as OCV), which indicates the minimal reaction of chloride SE occurs with NCM even up to 4.8 V vs Li^+/Li as a result of a kinetic overpotential due to the extremely low electronic conductivity of the SE. The presence of ClO^- and ScO^- signals in the pristine SE and the uncycled composite may well originate from impurities in the synthesis of chloride SE, as residual H_2O could be present in the precursors and quartz tube. The slightly increased signal in the uncycled composite compared to pristine SE could originate either from the residual H_2O or Li_2CO_3 contamination on the surface of NCM85

particles as well as from a slightly higher formation rate of secondary ions in presence of electronically conducting NCM. We point to the much higher and also unchanged signal of Cl^- ions, which also supports the stability of the SE at the interface with NCM.

Sulfide SEs, on the other hand, require a CAM coating layer with low electronic and high ionic conductivity to prevent electrolyte oxidation. $LiNbO_3$ is the most commonly used material.[95] It is electronically insulating (10^{-11} $S.cm^{-1}$) but exhibits low Li^+ conductivity (~ 10^{-6} $S.cm^{-1}$).[196] While thin coatings inhibit detrimental side reactions for the most part, the niobate also significantly limits Li ion and electron transport. Electronic conduction between cathode particles is hindered since no continuous electronic conduction pathway exists; furthermore, the low ionic conductivity limits Li ions transfer at the CAM - SE interface (**Figure 6.30a**). Not only it is difficult for the thin coating to homogeneously cover the CAM particles, but the layer can rupture during the fabrication of the catholyte composite. Partial electronic

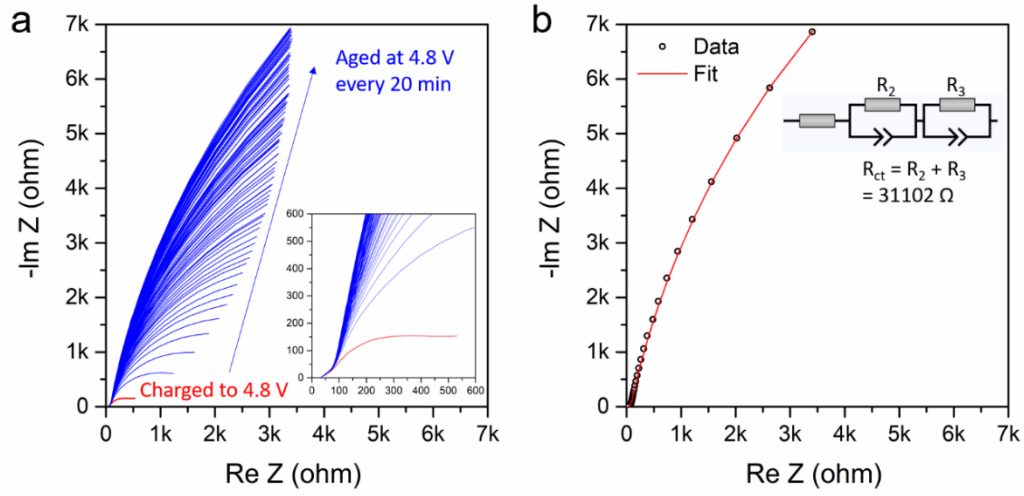

Figure 6.26 (a) Impedance evolution at high-voltage, where the EIS spectra were collected every 20 min of "aging" at a constant applied potential of 4.8 V vs Li^+/Li. (b) Equivalent circuit fit of the final Nyquist plot of NCM85 ASSB after 30 h aging at 4.8 V vs Li^+/Li, which shows increased charge transfer resistance between NCM85 and $Li_2In_{1/3}Sc_{1/3}Cl_4$ due to significantly decreased Li-ion mobility and electronic conductivity in highly de-lithiated NCM85.

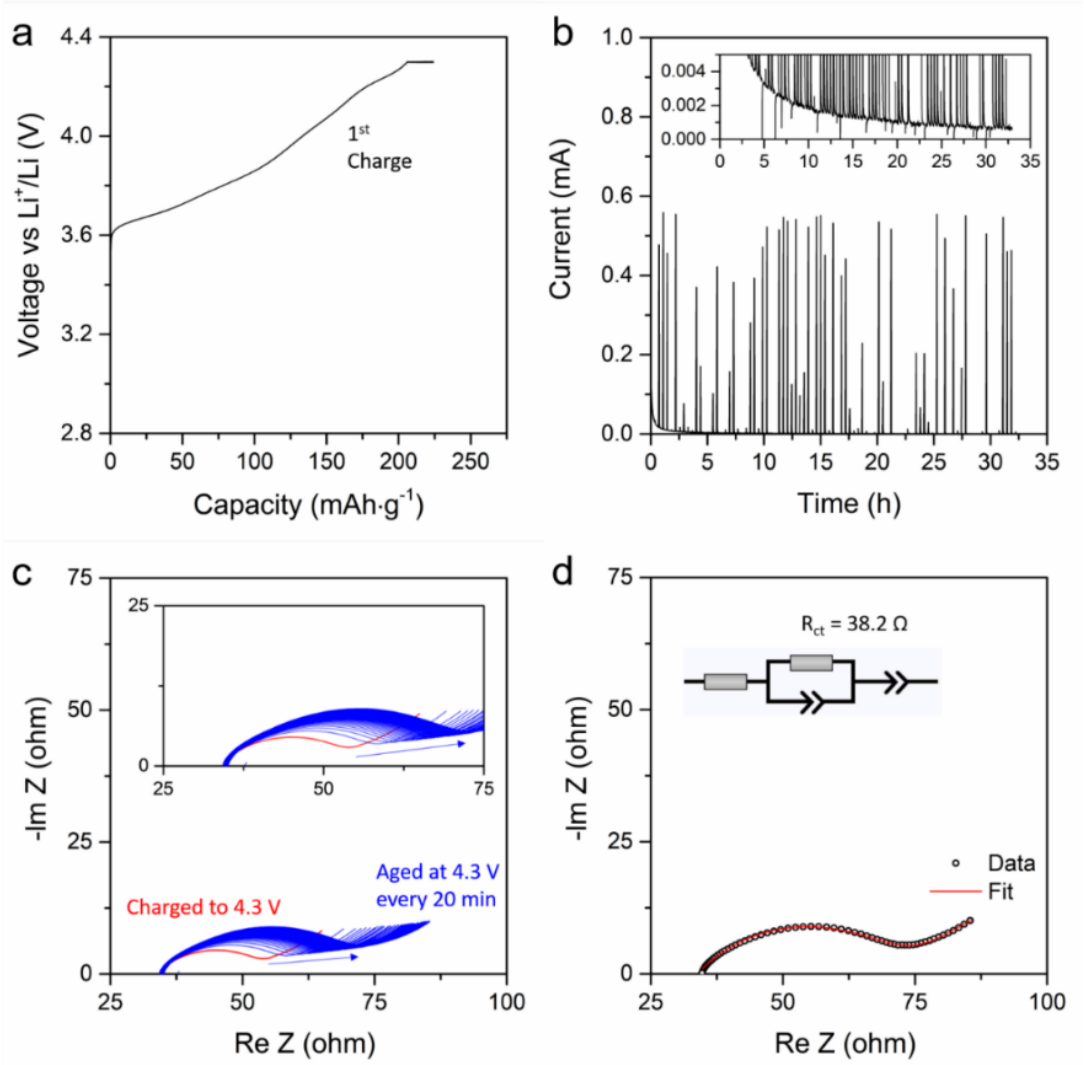

Figure 6.27 (a) Charge voltage profile of NCM85 ASSB. After charging to 4.3 V vs Li^+/Li, the cell was held at that constant potential for 30 h; (b) the corresponding leakage current during the 4.3 V vs Li^+/Li constant voltage hold ("aging"). (c) Impedance evolution during the voltage hold at constant applied potential of 4.3 V vs Li^+/Li, where EIS spectra were collected every 20 min. The lack of significant change in the spectra indicates the formation of a stable interface between NCM85 and the chloride SE at this potential. (d) Equivalent circuit fit of the final Nyquist plot of NCM85 ASSB after 30 h "aging" at 4.3 V vs Li^+/Li, which shows very low charge transfer resistance.

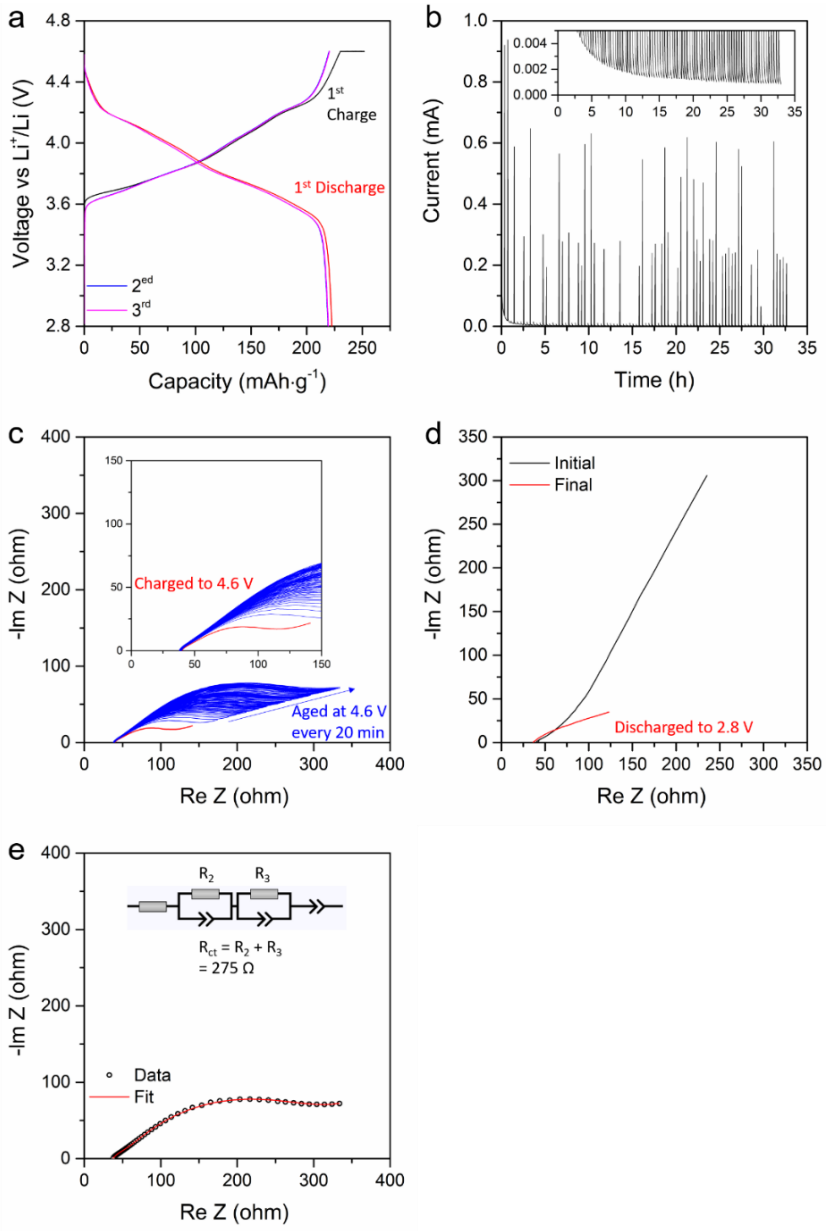

Figure 6.28 (a) Charge-discharge voltage profile of NCM85 ASSB, initial and after two subsequent cycles. After the initial charge to 4.6 V vs Li^+/Li, the cell was held at that potential for 30 h. (b) the corresponding leakage current during the 4.6 V constant hold ("aging") period. (c) Impedance evolution during the voltage hold at 4.6 V vs Li^+/Li, where the EIS spectra were collected every 20 min. (d) Nyquist plots of NCM85 ASSB at initial state, and at 3rd discharge. Upon re-lithiation on discharge, the cell impedance returns to its low value suggesting the formation of a stable interface between NCM85 and the chloride SE. (e) Equivalent circuit fit of the final Nyquist plot of NCM85 ASSB at 4.6 V vs Li^+/Li after the 30 h hold at that potential, showing low charge transfer resistance.

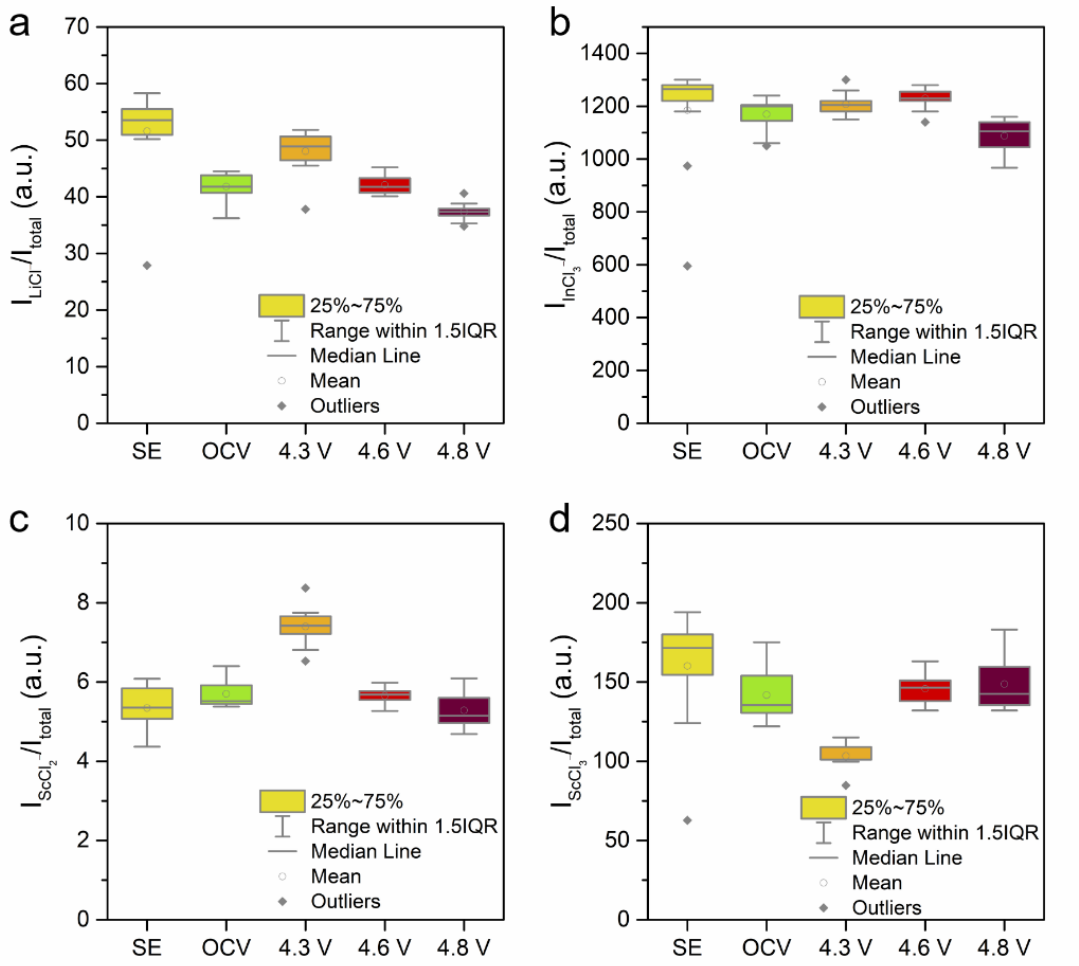

Figure 6.29 ToF-SIMS surface analysis results of (a) $LiCl^-$, (b) $InCl^{3-}$, (c) $ScCl^{2-}$ and (d) $ScCl^{3-}$ fragments of bare SE, uncycled cathode composite and cycled composite with cut-of potential of 4.3 V (160 cycles), 4.6 V (20 cycles) and 4.8 V (10 cycles) vs Li^+/Li. These fragments' signals originate from the chloride SE and show no clear change after cycling, which demonstrate the stable interface at high voltage up to 4.8 V vs Li^+/Li.

conduction through cathode particles can thus occur, and trigger SE oxidation.[98, 157, 197] The high potential limit of chloride SEs means that bare CAMs can be used, which takes advantage of their inherently high electronic and ionic conductivity.[198] Catholytes with a high-volume ratio of CAM/SE provide direct electronic and Li ion percolation pathways between CAM particles (**Figure 6.30a**). Due to the high deformability of the chloride SE, simply grinding it

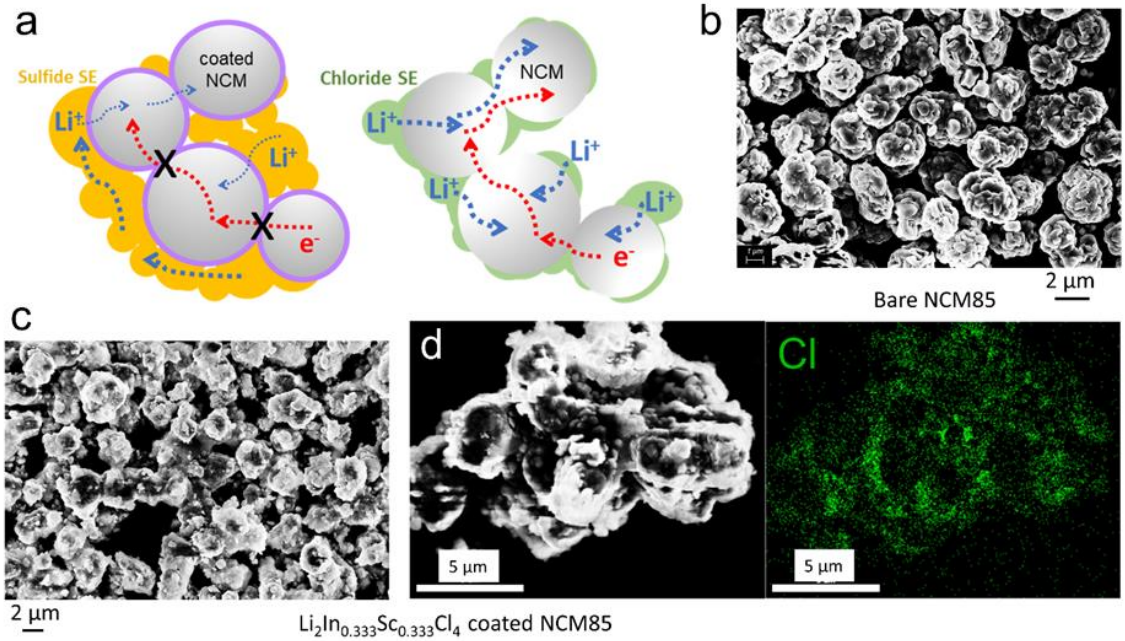

Figure 6.30 (a) Schematic illustration of ionic and electronic conduction percolation within a cathode composite of $LiNbO_3$-coated NMC with a sulfide solid electrolyte, and bare NMC with a chloride solid electrolyte. With the poorly conductive (e^-/Li^+) $LiNbO_3$ coating, both electronic and ionic conductivity between NMC particles is significantly blocked. However, for uncoated-NMC and the chloride solid electrolyte, direct contact between NMC particles provides sufficient electronic percolation; combined with Li ion diffusion through the solid electrolyte and within NMC particles, conduction within cathode composite is significantly enhanced. Red arrows show e^- conduction between NMC particles and black crosses indicate blockage of conduction. Blue arrows show Li^+ conduction between NMC particles and between NMC particle and SE and within SE (thinner line arrow indicates suppressed Li^+ conduction by the low ionic conductivity coating). SEM images of (b) bare NMC85 and (c) $Li_2In_{1/3}Sc_{1/3}Cl_4$ - coated NMC85 after grinding. (d) Expanded SEM image of $Li_2In_{1/3}Sc_{1/3}Cl_4$-coated NMC85 with EDX mapping of Cl demonstrates the presence of the chloride solid electrolyte on the surface of NMC85 particles.

with the CAM results in a thin coating on the cathode surface as revealed by SEM images (**Figure 6.30b, c**), and EDX maps (**Figure 6.30d**) of $Li_2In_{1/3}Sc_{1/3}Cl_4$-coated NMC85. The same highly effective coating approach is shown in **Figure 6.31-32** for other cathode active materials (LCO and NMC622). By controlling the volume ratio between CAM and chloride SE, a semi-uniform thin coating on the CAM is obtained and the residual bare surface provides an

electronic conduit between particles. Together with the SE in the catholyte, a 3D interconnected mixed ionic/electronic network is thus realized which is essential for ASSB performance. Operation of the cell under external pressure is necessary to maintain the network on cycling (**Figure 6.33-34**), since volume expansion/contraction of the CAM particles will otherwise lead to loss of contact of CAM and SE and increasing internal resistance.[11] However, high Ni-content CAMs such as NMC85 still inevitably form cracks and voids on extended cycling that slowly degrade the contact, although over 80% capacity retention can still be maintained over 3000+ cycles (**Figure 6.9c**). While recognizing that a high applied pressure is not practical in commercial cells, the pressure required partly depends on the nature of the CAM. Hence future research would benefit from exploration of (new) CAMs that exhibit minimal volume change during Li extraction/insertion and ideally high ionic and electronic conductivity.

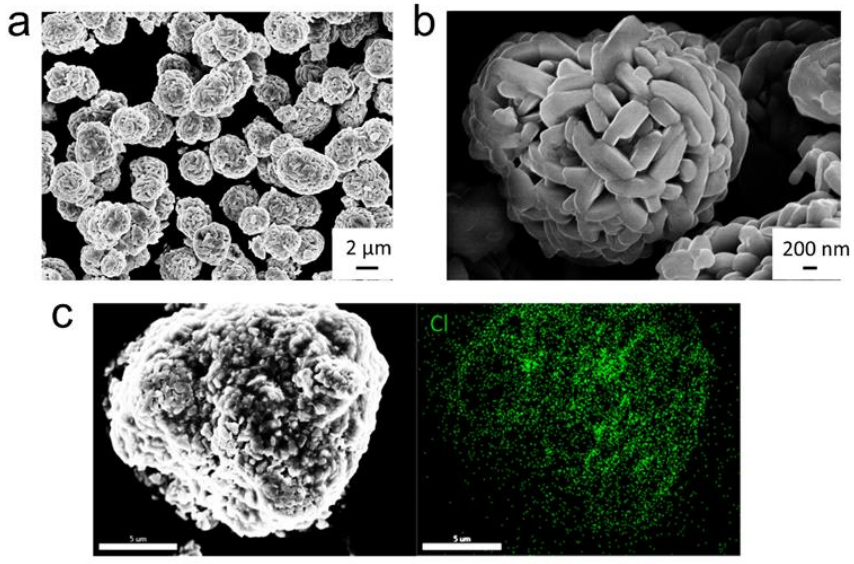

Figure 6.31 SEM images of (a) bare NMC622 and (b) enlarged image of a bare NMC622 particle. (c) Enlarged SEM image of one $Li_2In_{0.333}Sc_{0.333}Cl_4$ coated NMC622 particle. The EDX map (Cl, for simplicity) shows the slightly patchy coating of the chloride solid electrolyte on the surface of the NMC622 particles.

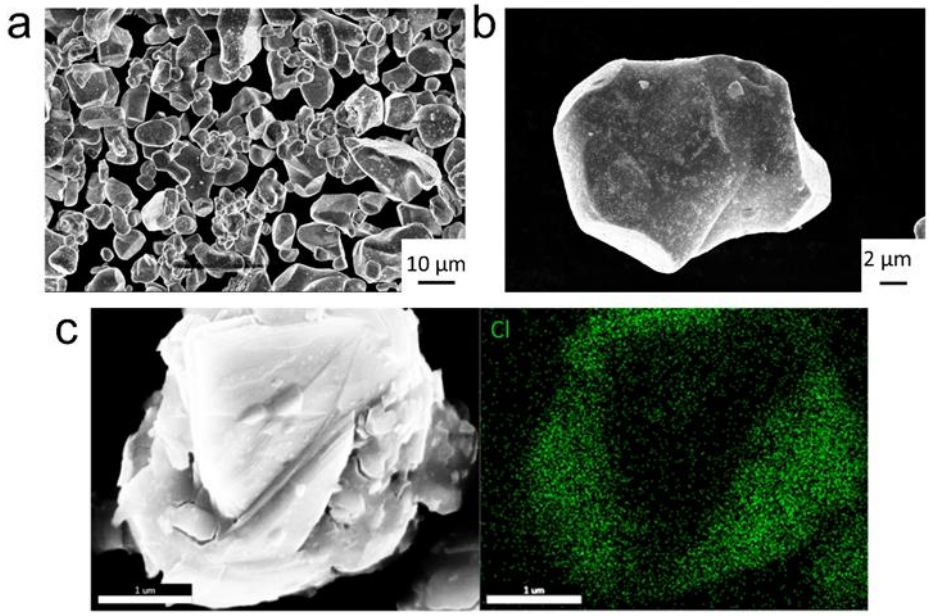

Figure 6.32 SEM images of (a) bare LCO and (b) enlarged image of a bare LCO particle. (c) Enlarged SEM image of one $Li_2In_{0.333}Sc_{0.333}Cl_4$ coated LCO particle. The EDX map (Cl, for simplicity) shows the patchy coating of the chloride solid electrolyte on the surface of the LCO particles.

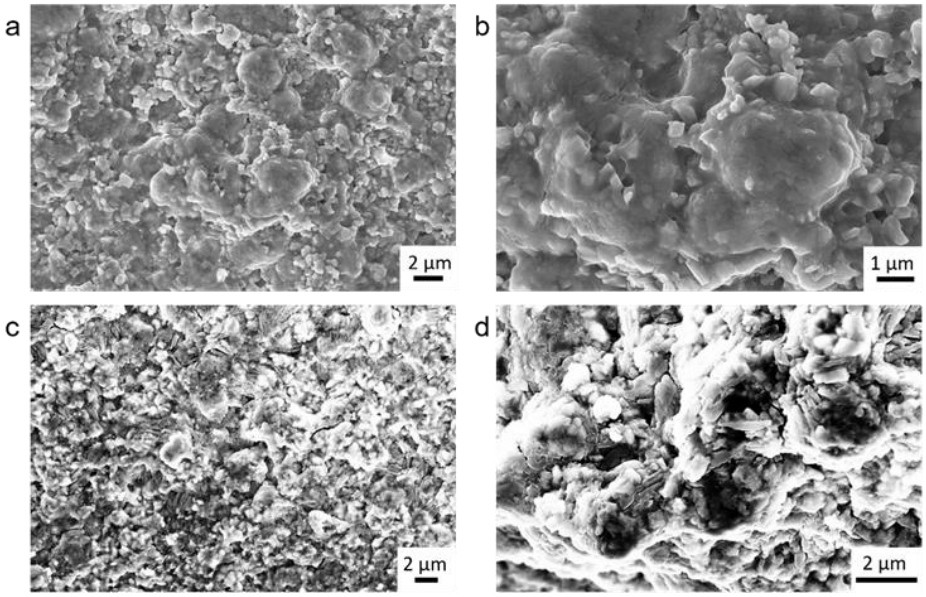

Figure 6.33 Cross-sectional SEM image of the cathode composite of NCM85 ASSBs cycled between 2.8 - 4.3 V vs Li^+/Li at the (a) 3rd charged state and (b) enlarged cross-sectional SEM image, showing no clear void formation between NCM85 particles and SE; and (c) 80th discharged state and (d) enlarged cross-sectional SEM image, showing some crack formation within the cathode composite, but nonetheless good contact between NCM85 and the SE.

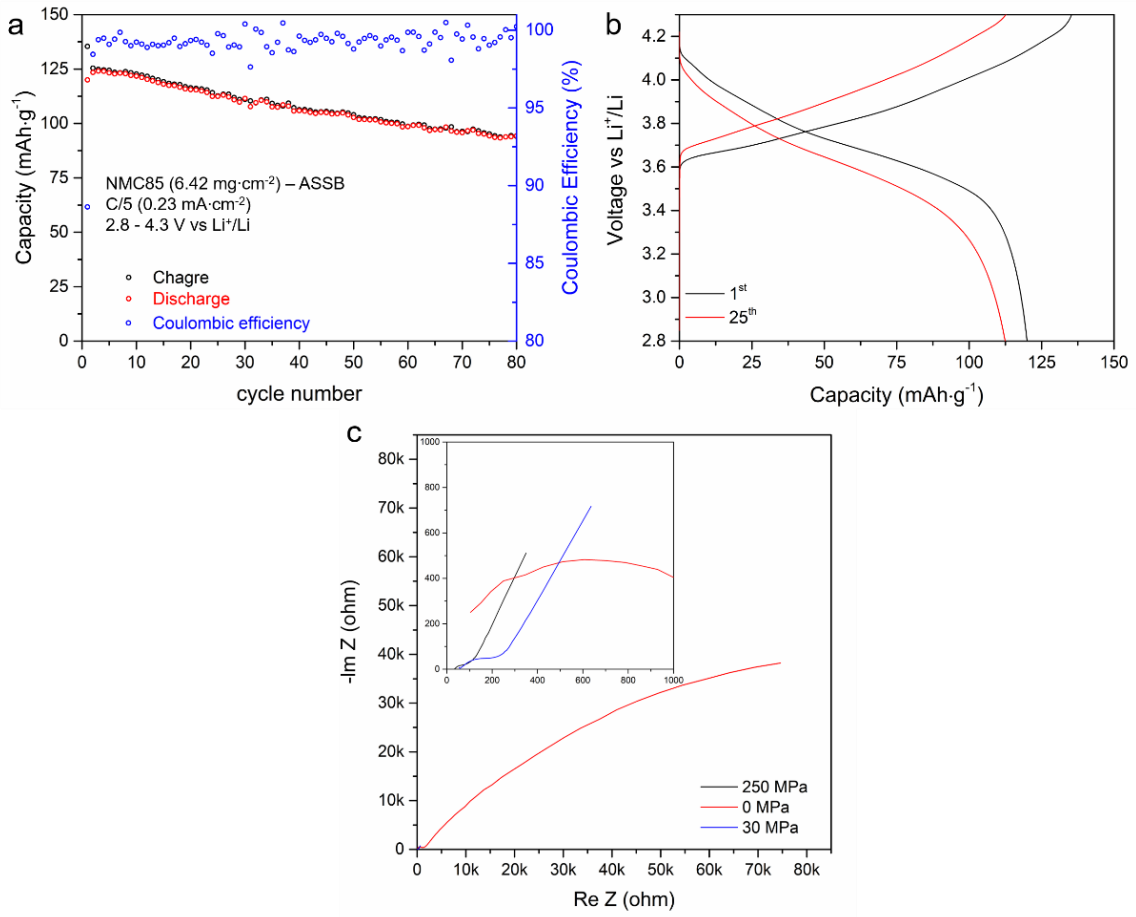

Figure 6.34 (a) Charge-discharge capacity and the coulombic efficiency as a function of cycle number and (b) Charge-discharge voltage profiles for NCM85 ASSB cycled at a C/5 rate between 2.8 - 4.3 V vs Li^+/Li with a much lower applied pressure of 30 MPa during cycling, compared to other cells (cycled at 250 MPa). (c) EIS of the cell before cycling with 250 MPa, 0 MPa, and 30 MPa applied pressure, showing the significantly increased cell resistance with lower applied pressure due to poor contact, which explains the lower discharge capacity. The fast capacity fading of cell cycled at 30 MPa compared to the stable cycling of cells cycled at 250 MPa (Figure 4a) clearly demonstrates the importance of high applied pressure to maintain the contact between the CAM and SE to withstand the CAM volume change.

6.7 Conclusions

A new lithium mixed-metal chloride family of SEs, $Li_2In_xSc_{0.666-x}Cl_4$, exhibits high ionic conductivity up to 2.0 $mS.cm^{-1}$ over a wide compositional range. Excellent electrochemical performance is demonstrated for bulk-type ASSBs with $Li_2In_{1/3}Sc_{1/3}Cl_4$ in

combination with bare-LCO, NCM622, and NCM85 functioning as cathode composites at potentials up to 4.8 V vs Li^+/Li. EIS and ToF-SIMS results indicate a stable interface exists between CAMs and chloride SE, confirming the high oxidation stability and chemical compatibility of $Li_2In_{1/3}Sc_{1/3}Cl_4$ in contact with uncoated oxide CAMs. These cells show long cycle life, maintaining 80% capacity retention at high current densities (3.36 $mA.cm^{-2}$; 3C rate) over more than 3000 cycles. These promising properties are in part due to the high plasticity of the chloride SE that allows a semi-uniform thin coating on the CAM to be obtained by gentle grinding. The residual bare surface facilitates electron transport between cathode particles. Incorporation of the SE in the cathode composite (between 10 - 20 wt%) thus provides a 3D interconnected mixed ionic/electronic network. The applied pressure ensures good CAM-SE contact during long-term cycling, which is essential for ASSB performance. Thus, ASSBs with high CAM loading (up to 52.5 $mg.cm^{-2}$ of LCO) deliver stable capacity retention. NCM85 cells are also realized with high areal capacity (> 4 $mAh.cm^{-2}$), high specific capacity (> 190 $mAh.g^{-1}$), and good cycling behavior, even at a high cut-off of potential 4.8 V vs Li^+/Li. Further developments that will translate the concepts to more earth-abundant and cost-effective lithium metal chloride SEs - and fluoride SEs for next-generation 5 V cells - are anticipated, along with advances in cell design and architecture. These can potentially meet the growing demand for next-generation energy storage systems for applications such as electric mobility.

Chapter 7. Summary and Future Perspectives

This thesis presents the investigation on the synthesis, characterization, and electrochemical performance of novel sulfide and chloride Li fast ion conductors and developing high energy density, long-lasting all solid-state batteries. That also includes the understanding of fundamental structure-property relationships in inorganic ionic conductors, and the critical requirements for the operations of all solid-state batteries.

Two families of sulfide solid electrolytes, $Li_{3+x}Si_xP_{1-x}S_4$ and $Li_{6+x}M_xSb_{1-x}S_5I$ (M = Si, Ge, Sn), are developed with high ionic conductivity up to 24 $mS.cm^{-1}$. For $Li_{3+x}Si_xP_{1-x}S_4$, aliovalent substitution induces structural splitting of the localized Li sites, effectively stabilizing bulk β-Li_3PS_4 structure at room temperature and delocalizing Li ion density, which leads to a frustrated energy landscape for Li ion diffusion and a high ionic conductivity up to 1.22 $mS.cm^{-1}$. For $Li_{6+x}M_xSb_{1-x}S_5I$ (M = Si, Ge, Sn), aliovalent substitution induces minor S^{2-} /I^- anion site disorder, but more importantly drives Li^+ cation site disorder. The additional delocalized Li ion density, located in new high energy lattice sites, provides intermediate interstitial positions for Li ion diffusion and activates concerted ion migration, leading to a low activation energy and excellent room temperature ionic conductivity up to 24 $mS.cm^{-1}$. These two examples prove aliovalent 'tuning' can increase Li site disorder which significantly enhances Li ion conduction and lowers the activation energy barrier for Li ion diffusion. This represents an important strategy toward the development of new superionic conductors.

Sulfide solid electrolytes, especially argyrodites, represent one of the most promising solid electrolytes for all solid-state battery fabrication. To achieve high energy density, ultra-

high ionic conductivity is needed to allow for thick cathode configurations. Conductivities in the range of 10 $mS.cm^{-1}$ are necessary. Further exploration is needed to determine the ionic conductivity limits of these materials, and the ideal substituents, for example reaching 100 $mS.cm^{-1}$. For large-scale manufacturing, it is important to develop more suitable synthesis approaches and understand the influence on ionic transport. Whereas solution synthesis has been developed for many argyrodites,[78] direct coating is still problematic due to the high crystallization temperatures that are still required. Although solution synthesis is promising and scalable, the superionic conductors $Li_{6+x}M_x(P/Sb)_{1-x}S_5I$ (M = Si, Ge, Sn) have not yet been synthesized by this approach. Finding more facile, low-temperature synthesis routes for these promising argyrodite solid electrolytes remains challenging. Although most argyrodites are relatively stable with Li metal, they cannot sustain high current density and high areal capacity Li stripping/plating due to dendrite formation. Exploration other high specific capacity anode materials like Si, which may form better and more stable interface with sulfide solid electrolytes, also offers great promise.[199] In order to reach higher energy density compared to conventional liquid cells, a thin solid electrolyte separator layer is needed, and large-scale thin film processing and how such thin film can suppress Li dendrite growth at high current density and capacity remains challenging and unclear. Finding suitable cathode active material coatings and a homogeneous coating method is necessary for utilizing sulfide solid electrolytes in cathode composite with high voltage cathode active materials, due to their low oxidative stability. As low electronic conductivity can lead to kinetically-driven higher oxidation stability limit, future research should also focus on lowering the defect concentration of these highly conductive sulfide solid electrolytes to lower their electronic conductivity to make it

kinetically compatible with high voltage cathode materials. The intrinsic instability of sulfide materials towards moisture which generates toxic and flammable H_2S gas also requires proper process and storage of sulfide solid electrolytes and a special design of cell packing to prevent H_2S leakage. Thus, improving the moisture stability of sulfide solid electrolytes with oxygen substitution and so on is needed too.

Two chloride spinel fast ion conductors, $Li_2Sc_{2/3}Cl_4$ and $Li_2In_xSc_{0.666-x}Cl_4$ ($0 \leq x \leq 0.666$), are also developed with high ionic conductivity 1.5 - 2.0 $mS.cm^{-1}$. As proven by neutron diffraction studies, significant Li site disorder in the lattice creates delocalized Li ion density and provides facile pathways for Li ion diffusion. Most importantly, owing to its high oxidative stability of the chloride solid electrolytes, all solid-state batteries with these two chloride solid electrolytes exhibit excellent electrochemical performance in a potential window up to 4.8 V vs Li^+/Li, combined with typical high voltage cathode materials (LCO, NMC622, NMC85), with no coatings.

Chloride solid electrolytes which gain more attention in recent years, duo to its intrinsic high oxidative stability, which is compatible with typical 4 V high voltage cathode active materials. However, to date, only a limit number of chloride solid electrolytes have been developed with ionic conductivity > 1 $mS.cm^{-1}$. Furthermore, the use of rare earth metal significantly increases the cost of chloride solid electrolytes, and the limited resource of those rare earth elements limits the practical use of these materials for large scale production. Exploration of other earth-abundant compositions with higher ionic conductivity *i.e.*, 10 $mS.cm^{-1}$, are necessary. Although, chloride solid electrolytes are compatible with typical cathode material and show promising cell performance. To pair with ultra-high voltage 5 V

cathode active materials, exploration of fluoride and oxyfluoride solid electrolytes is necessary. Since fluorides exhibit > 6 V vs Li^+/Li thermodynamic stability window, increasing their electronic conductivity to have mix ionic and electronic conductive fluorides will be beneficial for Li ion/electron percolation within cathode composites. The mechanical failure due to volume expansion and construction of active material during Li extraction and insertion remains as a major challenging facing all solid-state batteries. Although I have shown applying high pressure during cell cycling can effectively suppress the mechanical failure, which is not practical for commercialized cells at present. Thus, exploration of possible cathode active materials with minor volume change during Li extraction/insertion is also future research directions.

Further exploration of other solid electrolytes which are stable with Li metal and high voltage stable is final target for the development of solid electrolytes. One promising candidate is the hydro-borate, hydro-carbaborate systems.[200] As they are yet a underexplored solid electrolyte class and exhibit attractive properties, including stable with Li/Na metal anode, good mechanical properties, high thermal and chemical stability, solution processability. However, limit materials have been developed with high ionic conductivity and a better understanding its interfacial stability with high voltage cathode active materials is needed. A much cheaper and safer synthesis and processing method will be essential for commercialization.

Taken together, the last years in research focusing on the discovery of new solid electrolytes have provided a tremendous understanding of ionic transport, led to the discovery of new sulfide superionic conductors with ionic conductivities > 10 $mS.cm^{-1}$, and high voltage

compatible and good ductility chloride solid electrolytes, and on the interface study in all solid-state battery has helped to get well-performing solid-state batteries. Some companies have claimed extremely well-performing all solid-state batteries with long term stable cycling, excellent low temperature and high temperature performance. And they have even claimed solving the long-lasting Li dendrite issue, with no information given on the battery set-up and materials used. However, this does highlight the great promise of all solid-state batteries and promote more research on this topic. The future surely holds more options for optimization of the exciting solid electrolyte materials and gaining a better understanding of ion transport-structure relationship to guide future developments of new solid electrolyte materials and design of all solid-state batteries. Furthermore, an easy and cost-effective solid electrolyte thin film processing method and a better understanding of interface formation in all solid-state batteries which can guide the interface design to prevent solid electrolyte oxidation or reduction and prevent Li dendrite growth are needed, especially for thin-film solid electrolytes. Future studies on all solid-state batteries should also focus on the compatibility of processing all solid-state batteries with current state-of-art conventional liquid lithium-ion batteries set-up to promote the commercialization of all solid-state batteries without requiring other expensive equipment. In the forthcoming years, the commercialization of ceramic all solid-state batteries will remain challenging, but other types quasi all solid-state batteries with small amounts of liquid electrolytes or gel/polymer electrolytes are promising and start to appear on the market, which act as a middle transition from convention liquid cell to actual all solid-state batteries.

References

1. Larcher, D.; Tarascon, J. M., Towards greener and more sustainable batteries for electrical energy storage. *Nature Chemistry* **2015,** *7* (1), 19-29.

2. Trahey, L.; Brushett, F. R.; Balsara, N. P.; Ceder, G.; Cheng, L.; Chiang, Y.-M.; Hahn, N. T.; Ingram, B. J.; Minteer, S. D.; Moore, J. S.; Mueller, K. T.; Nazar, L. F.; Persson, K. A.; Siegel, D. J.; Xu, K.; Zavadil, K. R.; Srinivasan, V.; Crabtree, G. W., Energy storage emerging: A perspective from the Joint Center for Energy Storage Research. *Proceedings of the National Academy of Sciences* **2020,** *117* (23), 12550-12557.

3. Ellis, B. L.; Lee, K. T.; Nazar, L. F., Positive Electrode Materials for Li-Ion and Li-Batteries. *Chemistry of Materials* **2010,** *22* (3), 691-714.

4. Goodenough, J. B.; Park, K.-S., The Li-Ion Rechargeable Battery: A Perspective. *Journal of the American Chemical Society* **2013,** *135* (4), 1167-1176.

5. Whittingham, M. S., Electrical Energy Storage and Intercalation Chemistry. *Science* **1976,** *192* (4244), 1126-1127.

6. Manthiram, A., A reflection on lithium-ion battery cathode chemistry. *Nature Communications* **2020,** *11* (1), 1550.

7. Choi, J. U.; Voronina, N.; Sun, Y.-K.; Myung, S.-T., Recent Progress and Perspective of Advanced High-Energy Co-Less Ni-Rich Cathodes for Li-Ion Batteries: Yesterday, Today, and Tomorrow. *Advanced Energy Materials* **2020,** *10* (42), 2002027.

8. Xu, W.; Wang, J.; Ding, F.; Chen, X.; Nasybulin, E.; Zhang, Y.; Zhang, J.-G., Lithium metal anodes for rechargeable batteries. *Energy & Environmental Science* **2014,** *7* (2), 513-537.

9. Pang, Q.; Liang, X.; Shyamsunder, A.; Nazar, L. F., An In Vivo Formed Solid Electrolyte Surface Layer Enables Stable Plating of Li Metal. *Joule* **2017,** *1* (4), 871-886.

10. Nishida, T.; Nishikawa, K.; Rosso, M.; Fukunaka, Y., Optical observation of Li dendrite growth in ionic liquid. *Electrochimica Acta* **2013,** *100*, 333-341.

11. Koerver, R.; Zhang, W.; de Biasi, L.; Schweidler, S.; Kondrakov, A. O.; Kolling, S.; Brezesinski, T.; Hartmann, P.; Zeier, W. G.; Janek, J., Chemo-mechanical expansion of lithium electrode materials - on the route to mechanically optimized all-solid-state batteries. *Energy & Environmental Science* **2018,** *11* (8), 2142-2158.

12. Janek, J.; Zeier, W. G., A solid future for battery development. *Nature Energy* **2016,** *1* (9), 16141.

13. Manthiram, A.; Yu, X.; Wang, S., Lithium battery chemistries enabled by solid-state electrolytes. *Nature Reviews Materials* **2017,** *2* (4), 16103.

14. Randau, S.; Weber, D. A.; Kötz, O.; Koerver, R.; Braun, P.; Weber, A.; Ivers-Tiffée, E.; Adermann, T.; Kulisch, J.; Zeier, W. G.; Richter, F. H.; Janek, J., Benchmarking the performance of all-solid-state lithium batteries. *Nature Energy* **2020,** *5* (3), 259-270.

15. Jung, K.-N.; Shin, H.-S.; Park, M.-S.; Lee, J.-W., Solid-State Lithium Batteries: Bipolar Design, Fabrication, and Electrochemistry. *ChemElectroChem* **2019,** *6* (15), 3842-3859.

16. Xu, K., Electrolytes and Interphases in Li-Ion Batteries and Beyond. *Chemical Reviews* **2014,** *114* (23), 11503-11618.

17. Zhang, Z.; Shao, Y.; Lotsch, B.; Hu, Y.-S.; Li, H.; Janek, J.; Nazar, L. F.; Nan, C.-W.; Maier, J.; Armand, M.; Chen, L., New horizons for inorganic solid state ion conductors. *Energy & Environmental Science* **2018,** *11* (8), 1945-1976.

18. Bachman, J. C.; Muy, S.; Grimaud, A.; Chang, H.-H.; Pour, N.; Lux, S. F.; Paschos, O.; Maglia, F.; Lupart, S.; Lamp, P.; Giordano, L.; Shao-Horn, Y., Inorganic Solid-State Electrolytes for Lithium Batteries: Mechanisms and Properties Governing Ion Conduction. *Chemical Reviews* **2016,** *116* (1), 140-162.

19. Chen, R.; Li, Q.; Yu, X.; Chen, L.; Li, H., Approaching Practically Accessible Solid-State Batteries: Stability Issues Related to Solid Electrolytes and Interfaces. *Chemical Reviews* **2020,** *120* (14), 6820-6877.

20. Hong, H.-P., Crystal structure and ionic conductivity of $Li_{14}Zn(GeO_4)_4$ and other new Li^+ superionic conductors. *Materials Research Bulletin* **1978,** *13* (2), 117-124.

21. Thangadurai, V.; Weppner, W., Recent progress in solid oxide and lithium ion conducting electrolytes research. *Ionics* **2006,** *12* (1), 81-92.

22. Brous, J.; Fankuchen, I.; Banks, E., Rare earth titanates with a perovskite structure. *Acta Crystallographica* **1953,** *6* (1), 67-70.

23. Inaguma, Y.; Liquan, C.; Itoh, M.; Nakamura, T.; Uchida, T.; Ikuta, H.; Wakihara, M., High ionic conductivity in lithium lanthanum titanate. *Solid State Communications* **1993,** *86* (10), 689-693.

24. Stramare, S.; Thangadurai, V.; Weppner, W., Lithium Lanthanum Titanates: A Review. *Chemistry of Materials* **2003,** *15* (21), 3974-3990.

25. Takada, K., Progress and prospective of solid-state lithium batteries. *Acta Materialia* **2013,** *61* (3), 759-770.

26. Lu, J.; Li, Y., Perovskite-type Li-ion solid electrolytes: a review. *Journal of Materials Science: Materials in Electronics* **2021**.

27. Stramare, S.; Thangadurai, V.; Weppner, W., Lithium lanthanum titanates: a review. *Chemistry of materials* **2003,** *15* (21), 3974-3990.

28. Fu, J., Superionic conductivity of glass-ceramics in the system Li_2O-Al_2O_3-TiO_2-P_2O_5. *Solid State Ionics* **1997,** *96* (3), 195-200.

29. Fu, J., Fast Li^+ ion conducting glass-ceramics in the system Li_2O-Al_2O_3-GeO_2-P_2O_5. *Solid State Ionics* **1997,** *104* (3), 191-194.

30. Choi, J.-w.; Lee, J.-w., Improved electrochemical properties of $Li(Ni_{0.6}Mn_{0.2}Co_{0.2})O_2$ by surface coating with $Li_{1.3}Al_{0.3}Ti_{1.7}(PO_4)_3$. *Journal of Power Sources* **2016,** *307*, 63-68.

31. Kobylianska, S.; Demchuk, D.; Khomenko, V.; Barsukov, V.; Belous, A., Surface Modification of the $LiNi_{0.5}Co_{0.2}Mn_{0.3}O_2$ Cathode by a Protective Interface Layer of $Li_{1.3}Ti_{1.7}Al_{0.3}(PO_4)_3$. *Journal of The Electrochemical Society* **2019,** *166* (10), A1920-A1925.

32. Song, G.; Zhong, H.; Wang, Z.; Dai, Y.; Zhou, X.; Yang, J., Interfacial Film $Li_{1.3}Al_{0.3}Ti_{1.7}PO_4$-Coated $LiNi_{0.6}Co_{0.2}Mn_{0.2}O_2$ for the Long Cycle Stability of Lithium-Ion Batteries. *ACS Applied Energy Materials* **2019,** *2* (11), 7923-7932.

33. Li, L.; Zhao, R.; Xu, T.; Wang, D.; Pan, D.; Zhang, K.; Yu, C.; Lu, X.; He, G.; Bai, Y., Stabilizing a high-voltage $LiNi_{0.5}Mn_{1.5}O_4$ cathode towards all solid state batteries: a Li-Al-Ti-P-O solid electrolyte nano-shell with a host material. *Nanoscale* **2019,** *11* (18), 8967-8977.

34. Wang, Y.; Zhang, Q.; Xue, Z.-C.; Yang, L.; Wang, J.; Meng, F.; Li, Q.; Pan, H.; Zhang, J.-N.; Jiang, Z.; Yang, W.; Yu, X.; Gu, L.; Li, H., An In Situ Formed Surface Coating Layer Enabling $LiCoO_2$ with Stable 4.6 V High-Voltage Cycle Performances. *Advanced Energy Materials* **2020,** *10* (28), 2001413.

35. Wang, C.; Fu, K.; Kammampata, S. P.; McOwen, D. W.; Samson, A. J.; Zhang, L.; Hitz, G. T.; Nolan, A. M.; Wachsman, E. D.; Mo, Y.; Thangadurai, V.; Hu, L., Garnet-Type Solid-State Electrolytes: Materials, Interfaces, and Batteries. *Chemical Reviews* **2020,** *120* (10), 4257-4300.

36. Connell, J. G.; Fuchs, T.; Hartmann, H.; Krauskopf, T.; Zhu, Y.; Sann, J.; Garcia-Mendez, R.; Sakamoto, J.; Tepavcevic, S.; Janek, J., Kinetic versus Thermodynamic Stability of LLZO in Contact with Lithium Metal. *Chemistry of Materials* **2020,** *32* (23), 10207-10215.

37. Murugan, R.; Thangadurai, V.; Weppner, W., Fast Lithium Ion Conduction in Garnet-Type $Li_7La_3Zr_2O_{12}$. *Angewandte Chemie International Edition* **2007,** *46* (41), 7778-7781.

38. O'Callaghan, M. P.; Lynham, D. R.; Cussen, E. J.; Chen, G. Z., Structure and ionic-transport properties of lithium-containing garnets $Li_3Ln_3Te_2O_{12}$ (Ln= Y, Pr, Nd, Sm-Lu). *Chemistry of materials* **2006,** *18* (19), 4681-4689.

39. Gao, Y.; Wang, X.; Wang, W.; Fang, Q., Sol-gel synthesis and electrical properties of $Li_5La_3Ta_2O_{12}$ lithium ionic conductors. *Solid State Ionics* **2010,** *181* (1-2), 33-36.

40. Peng, H.; Wu, Q.; Xiao, L., Low temperature synthesis of $Li_5La_3Nb_2O_{12}$ with cubic garnet-type structure by sol–gel process. *Journal of sol-gel science and technology* **2013,** *66* (1), 175-179.

41. Thangadurai, V.; Weppner, W., $Li_6ALa_2Ta_2O_{12}$ (A= Sr, Ba): novel garnet‐like oxides for fast lithium ion conduction. *Advanced Functional Materials* **2005,** *15* (1), 107-112.

42. Reddy, M. V.; Julien, C. M.; Mauger, A.; Zaghib, K., Sulfide and Oxide Inorganic Solid Electrolytes for All-Solid-State Li Batteries: A Review. *Nanomaterials* **2020,** *10* (8), 1606.

43. Wang, Y.; Lai, W., High Ionic Conductivity Lithium Garnet Oxides of $Li_{7-x}La_3Zr_{2-x}Ta_xO_{12}$ Compositions. *Electrochemical and Solid-State Letters* **2012,** *15* (5), A68.

44. Li, Y.; Han, J.-T.; Wang, C.-A.; Xie, H.; Goodenough, J. B., Optimizing Li^+ conductivity in a garnet framework. *Journal of Materials Chemistry* **2012,** *22* (30), 15357-15361.

45. Samson, A. J.; Hofstetter, K.; Bag, S.; Thangadurai, V., A bird's-eye view of Li-stuffed garnet-type $Li_7La_3Zr_2O_{12}$ ceramic electrolytes for advanced all-solid-state Li batteries. *Energy & Environmental Science* **2019,** *12* (10), 2957-2975.

46. Thangadurai, V.; Narayanan, S.; Pinzaru, D., Garnet-type solid-state fast Li ion conductors for Li batteries: critical review. *Chemical Society Reviews* **2014,** *43* (13), 4714-4727.

47. Kamaya, N.; Homma, K.; Yamakawa, Y.; Hirayama, M.; Kanno, R.; Yonemura, M.; Kamiyama, T.; Kato, Y.; Hama, S.; Kawamoto, K.; Mitsui, A., A lithium superionic conductor. *Nature Materials* **2011,** *10* (9), 682-686.

48. McGrogan, F. P.; Swamy, T.; Bishop, S. R.; Eggleton, E.; Porz, L.; Chen, X.; Chiang, Y.-M.; Van Vliet, K. J., Compliant Yet Brittle Mechanical Behavior of Li_2S-P_2S_5 Lithium-Ion-Conducting Solid Electrolyte. *Advanced Energy Materials* **2017,** *7* (12), 1602011.

49. Mercier, R.; Malugani, J.-P.; Fahys, B.; Robert, G., Superionic conduction in Li_2S-P_2S_5-LiI - glasses. *Solid State Ionics* **1981,** *5*, 663-666.

50. Pradel, A.; Ribes, M., Electrical properties of lithium conductive silicon sulfide glasses prepared by twin roller quenching. *Solid State Ionics* **1986,** *18-19*, 351-355.

51. Pradel, A.; Ribes, M., Lithium chalcogenide conductive glasses. *Materials Chemistry and Physics* **1989,** *23* (1), 121-142.

52. Sakamoto, R.; Tatsumisago, M.; Minami, T., Preparation of Fast Lithium Ion Conducting Glasses in the System Li_2S-SiS_2-Li_3N. *The Journal of Physical Chemistry B* **1999,** *103* (20), 4029-4031.

53. Kennedy, J. H.; Zhang, Z., Further Characterization of SiS_2 - Li_2S Glasses Doped with Lithium Halide. *Journal of The Electrochemical Society* **1988,** *135* (4), 859-862.

54. Wada, H.; Menetrier, M.; Levasseur, A.; Hagenmuller, P., Preparation and ionic conductivity of new B_2S_3-Li_2S-LiI glasses. *Materials Research Bulletin* **1983,** *18* (2), 189-193.

55. Kanno, R.; Murayama, M., Lithium Ionic Conductor Thio-LISICON: The Li_2S-GeS_2-P_2S_5 System. *Journal of The Electrochemical Society* **2001,** *148* (7), A742.

56. Tachez, M.; Malugani, J.-P.; Mercier, R.; Robert, G., Ionic conductivity of and phase transition in lithium thiophosphate Li_3PS_4. *Solid State Ionics* **1984,** *14* (3), 181-185.

57. Liu, Z.; Fu, W.; Payzant, E. A.; Yu, X.; Wu, Z.; Dudney, N. J.; Kiggans, J.; Hong, K.; Rondinone, A. J.; Liang, C., Anomalous High Ionic Conductivity of Nanoporous β-Li_3PS_4. *Journal of the American Chemical Society* **2013,** *135* (3), 975-978.

58. Murayama, M.; Kanno, R.; Irie, M.; Ito, S.; Hata, T.; Sonoyama, N.; Kawamoto, Y., Synthesis of New Lithium Ionic Conductor Thio-LISICON-Lithium Silicon Sulfides System. *Journal of Solid State Chemistry* **2002,** *168* (1), 140-148.

59. Wenzel, S.; Randau, S.; Leichtweiß, T.; Weber, D. A.; Sann, J.; Zeier, W. G.; Janek, J., Direct Observation of the Interfacial Instability of the Fast Ionic Conductor $Li_{10}GeP_2S_{12}$ at the Lithium Metal Anode. *Chemistry of Materials* **2016,** *28* (7), 2400-2407.

60. Kuhn, A.; Gerbig, O.; Zhu, C.; Falkenberg, F.; Maier, J.; Lotsch, B. V., A new ultrafast superionic Li-conductor: ion dynamics in $Li_{11}Si2PS_{12}$ and comparison with other tetragonal LGPS-type electrolytes. *Physical Chemistry Chemical Physics* **2014,** *16* (28), 14669-14674.

61. Kuhn, A.; Duppel, V.; Lotsch, B. V., Tetragonal $Li_{10}GeP_2S_{12}$ and Li_7GePS_8 – exploring the Li ion dynamics in LGPS Li electrolytes. *Energy & Environmental Science* **2013,** *6* (12), 3548-3552.

62. Bron, P.; Johansson, S.; Zick, K.; Schmedt auf der Günne, J.; Dehnen, S.; Roling, B., $Li_{10}SnP_2S_{12}$: An Affordable Lithium Superionic Conductor. *Journal of the American Chemical Society* **2013,** *135* (42), 15694-15697.

63. Kato, Y.; Hori, S.; Kanno, R., $Li_{10}GeP_2S_{12}$-Type Superionic Conductors: Synthesis, Structure, and Ionic Transportation. *Advanced Energy Materials* **2020,** *10* (42), 2002153.

64. Zhou, L.; Minafra, N.; Zeier, W. G.; Nazar, L. F., Innovative Approaches to Li-Argyrodite Solid Electrolytes for All-Solid-State Lithium Batteries. *Accounts of Chemical Research* **2021,** *54* (12), 2717-2728.

65. Zhou, L.; Assoud, A.; Zhang, Q.; Wu, X.; Nazar, L. F., New Family of Argyrodite Thioantimonate Lithium Superionic Conductors. *Journal of the American Chemical Society* **2019,** *141* (48), 19002-19013.

66. Kraft, M. A.; Culver, S. P.; Calderon, M.; Böcher, F.; Krauskopf, T.; Senyshyn, A.; Dietrich, C.; Zevalkink, A.; Janek, J.; Zeier, W. G., Influence of Lattice Polarizability on the Ionic Conductivity in the Lithium Superionic Argyrodites Li_6PS_5X (X = Cl, Br, I). *Journal of the American Chemical Society* **2017,** *139* (31), 10909-10918.

67. Kraft, M. A.; Ohno, S.; Zinkevich, T.; Koerver, R.; Culver, S. P.; Fuchs, T.; Senyshyn, A.; Indris, S.; Morgan, B. J.; Zeier, W. G., Inducing High Ionic Conductivity in the Lithium Superionic Argyrodites $Li_{6+x}P_{1-x}Ge_xS_5I$ for All-Solid-State Batteries. *Journal of the American Chemical Society* **2018,** *140* (47), 16330-16339.

68. Deiseroth, H.-J.; Kong, S.-T.; Eckert, H.; Vannahme, J.; Reiner, C.; Zaiß, T.; Schlosser, M., Li_6PS_5X: A Class of Crystalline Li-Rich Solids With an Unusually High Li^+ Mobility. *Angewandte Chemie International Edition* **2008,** *47* (4), 755-758.

69. Adeli, P.; Bazak, J. D.; Park, K. H.; Kochetkov, I.; Huq, A.; Goward, G. R.; Nazar, L. F., Boosting Solid-State Diffusivity and Conductivity in Lithium Superionic Argyrodites by Halide Substitution. *Angewandte Chemie International Edition* **2019,** *58* (26), 8681-8686.

70. Sakuda, A.; Yamauchi, A.; Yubuchi, S.; Kitamura, N.; Idemoto, Y.; Hayashi, A.; Tatsumisago, M., Mechanochemically Prepared Li_2S-P_2S_5-$LiBH_4$ Solid Electrolytes with an Argyrodite Structure. *ACS Omega* **2018,** *3* (5), 5453-5458.

71. Kong, S.-T.; Deiseroth, H.-J.; Reiner, C.; Gün, Ö.; Neumann, E.; Ritter, C.; Zahn, D., Lithium Argyrodites with Phosphorus and Arsenic: Order and Disorder of Lithium Atoms, Crystal Chemistry, and Phase Transitions. *Chemistry – A European Journal* **2010,** *16* (7), 2198-2206.

72. Ohno, S.; Helm, B.; Fuchs, T.; Dewald, G.; Kraft, M. A.; Culver, S. P.; Senyshyn, A.; Zeier, W. G., Further Evidence for Energy Landscape Flattening in the Superionic Argyrodites $Li_{6+x}P_{1-x}M_xS_5I$ (M = Si, Ge, Sn). *Chemistry of Materials* **2019,** *31* (13), 4936-4944.

73. Schneider, H.; Du, H.; Kelley, T.; Leitner, K.; ter Maat, J.; Scordilis-Kelley, C.; Sanchez-Carrera, R.; Kovalev, I.; Mudalige, A.; Kulisch, J.; Safont-Sempere, M. M.; Hartmann, P.; Weiβ, T.; Schneider, L.; Hinrichsen, B., A novel class of halogen-free, super-conductive lithium argyrodites: Synthesis and characterization. *Journal of Power Sources* **2017,** *366*, 151-160.

74. Wang, P.; Liu, H.; Patel, S.; Feng, X.; Chien, P.-H.; Wang, Y.; Hu, Y.-Y., Fast Ion Conduction and Its Origin in $Li_{6-x}PS_{5-x}Br_{1+x}$. *Chemistry of Materials* **2020,** *32* (9), 3833-3840.

75. Huang, W.; Yoshino, K.; Hori, S.; Suzuki, K.; Yonemura, M.; Hirayama, M.; Kanno, R., Superionic lithium conductor with a cubic argyrodite-type structure in the Li-Al-Si-S system. *Journal of Solid State Chemistry* **2019,** *270*, 487-492.

76. Inoue, Y.; Suzuki, K.; Matsui, N.; Hirayama, M.; Kanno, R., Synthesis and structure of novel lithium-ion conductor $Li_7Ge_3PS_{12}$. *Journal of Solid State Chemistry* **2017,** *246*, 334-340.

77. Kong, S.-T.; Deiseroth, H.-J.; Maier, J.; Nickel, V.; Weichert, K.; Reiner, C., Li_6PO_5Br and Li_6PO_5Cl: The first Lithium-Oxide-Argyrodites *Zeitschrift für anorganische und allgemeine Chemie* **2010,** *636* (11), 1920-1924.

78. Zhou, L.; Park, K.-H.; Sun, X.; Lalère, F.; Adermann, T.; Hartmann, P.; Nazar, L. F., Solvent-Engineered Design of Argyrodite Li_6PS_5X (X = Cl, Br, I) Solid Electrolytes with High Ionic Conductivity. *ACS Energy Letters* **2019,** *4* (1), 265-270.

79. Kong, S.-T.; Deiseroth, H.-J.; Reiner, C.; Gün, Ö.; Neumann, E.; Ritter, C.; Zahn, D., Lithium Argyrodites with Phosphorus and Arsenic: Order and Disorder of Lithium Atoms, Crystal Chemistry, and Phase Transitions. *Chemistry - A European Journal* **2010,** *16* (7), 2198-2206.

80. Asano, T.; Sakai, A.; Ouchi, S.; Sakaida, M.; Miyazaki, A.; Hasegawa, S., Solid Halide Electrolytes with High Lithium-Ion Conductivity for Application in 4 V Class Bulk-Type All-Solid-State Batteries. *Advanced Materials* **2018,** *30* (44), 1803075.

81. Schlem, R.; Muy, S.; Prinz, N.; Banik, A.; Shao-Horn, Y.; Zobel, M.; Zeier, W. G., Mechanochemical Synthesis: A Tool to Tune Cation Site Disorder and Ionic Transport Properties of Li_3MCl_6 (M = Y, Er) Superionic Conductors. *Advanced Energy Materials* **2020,** *10* (6), 1903719.

82. Li, X.; Liang, J.; Luo, J.; Norouzi Banis, M.; Wang, C.; Li, W.; Deng, S.; Yu, C.; Zhao, F.; Hu, Y.; Sham, T.-K.; Zhang, L.; Zhao, S.; Lu, S.; Huang, H.; Li, R.; Adair, K. R.; Sun, X., Air-stable Li_3InCl_6 electrolyte with high voltage compatibility for all-solid-state batteries. *Energy & Environmental Science* **2019,** *12* (9), 2665-2671.

83. Park, K.-H.; Kaup, K.; Assoud, A.; Zhang, Q.; Wu, X.; Nazar, L. F., High-Voltage Superionic Halide Solid Electrolytes for All-Solid-State Li-Ion Batteries. *ACS Energy Letters* **2020,** *5* (2), 533-539.

84. Riegger, L. M.; Schlem, R.; Sann, J.; Zeier, W. G.; Janek, J., Lithium-Metal Anode Instability of the Superionic Halide Solid Electrolytes and the Implications for Solid-State Batteries. *Angewandte Chemie International Edition* **2021,** *60* (12), 6718-6723.

85. He, X.; Zhu, Y.; Mo, Y., Origin of fast ion diffusion in super-ionic conductors. *Nature Communications* **2017,** *8* (1), 15893.

86. Wang, Y.; Richards, W. D.; Ong, S. P.; Miara, L. J.; Kim, J. C.; Mo, Y.; Ceder, G., Design principles for solid-state lithium superionic conductors. *Nature Materials* **2015,** *14* (10), 1026-1031.

87. Krauskopf, T.; Pompe, C.; Kraft, M. A.; Zeier, W. G., Influence of Lattice Dynamics on Na+ Transport in the Solid Electrolyte Na3PS4 − xSex. *Chemistry of Materials* **2017,** *29* (20), 8859-8869.

88. Wenzel, S.; Sedlmaier, S. J.; Dietrich, C.; Zeier, W. G.; Janek, J., Interfacial reactivity and interphase growth of argyrodite solid electrolytes at lithium metal electrodes. *Solid State Ionics* **2018,** *318*, 102-112.

89. Kasemchainan, J.; Zekoll, S.; Spencer Jolly, D.; Ning, Z.; Hartley, G. O.; Marrow, J.; Bruce, P. G., Critical stripping current leads to dendrite formation on plating in lithium anode solid electrolyte cells. *Nature Materials* **2019,** *18* (10), 1105-1111.

90. Dewald, G. F.; Ohno, S.; Kraft, M. A.; Koerver, R.; Till, P.; Vargas-Barbosa, N. M.; Janek, J.; Zeier, W. G., Experimental Assessment of the Practical Oxidative Stability of Lithium Thiophosphate Solid Electrolytes. *Chemistry of Materials* **2019,** *31* (20), 8328-8337.

91. Zhu, Y.; He, X.; Mo, Y., Origin of Outstanding Stability in the Lithium Solid Electrolyte Materials: Insights from Thermodynamic Analyses Based on First-Principles Calculations. *ACS Applied Materials & Interfaces* **2015,** *7* (42), 23685-23693.

92. Richards, W. D.; Miara, L. J.; Wang, Y.; Kim, J. C.; Ceder, G., Interface Stability in Solid-State Batteries. *Chemistry of Materials* **2016,** *28* (1), 266-273.

93. Auvergniot, J.; Cassel, A.; Ledeuil, J.-B.; Viallet, V.; Seznec, V.; Dedryvère, R., Interface Stability of Argyrodite Li_6PS_5Cl toward $LiCoO_2$, $LiNi_{1/3}Co_{1/3}Mn_{1/3}O_2$, and $LiMn_2O_4$ in Bulk All-Solid-State Batteries. *Chemistry of Materials* **2017,** *29* (9), 3883-3890.

94. Walther, F.; Koerver, R.; Fuchs, T.; Ohno, S.; Sann, J.; Rohnke, M.; Zeier, W. G.; Janek, J., Visualization of the Interfacial Decomposition of Composite Cathodes in Argyrodite-Based All-Solid-State Batteries Using Time-of-Flight Secondary-Ion Mass Spectrometry. *Chemistry of Materials* **2019,** *31* (10), 3745-3755.

95. Ohta, N.; Takada, K.; Sakaguchi, I.; Zhang, L.; Ma, R.; Fukuda, K.; Osada, M.; Sasaki, T., $LiNbO_3$-coated $LiCoO_2$ as cathode material for all solid-state lithium secondary batteries. *Electrochemistry Communications* **2007,** *9* (7), 1486-1490.

96. Seino, Y.; Ota, T.; Takada, K., High rate capabilities of all-solid-state lithium secondary batteries using $Li_4Ti_5O_{12}$-coated $LiNi_{0.8}Co_{0.15}Al_{0.05}O_2$ and a sulfide-based solid electrolyte. *Journal of Power Sources* **2011,** *196* (15), 6488-6492.

97. Takada, K.; Ohta, N.; Zhang, L.; Fukuda, K.; Sakaguchi, I.; Ma, R.; Osada, M.; Sasaki, T., Interfacial modification for high-power solid-state lithium batteries. *Solid State Ionics* **2008,** *179* (27), 1333-1337.

98. Strauss, F.; Teo, J. H.; Maibach, J.; Kim, A. Y.; Mazilkin, A.; Janek, J.; Brezesinski, T., Li_2ZrO_3-Coated NCM622 for Application in Inorganic Solid-State Batteries: Role of Surface Carbonates in the Cycling Performance. *ACS Applied Materials & Interfaces* **2020,** *12* (51), 57146-57154.

99. Fu, K.; Gong, Y.; Liu, B.; Zhu, Y.; Xu, S.; Yao, Y.; Luo, W.; Wang, C.; Lacey, S. D.; Dai, J.; Chen, Y.; Mo, Y.; Wachsman, E.; Hu, L., Toward garnet electrolyte-based Li metal batteries: An ultrathin, highly effective, artificial solid-state electrolyte/metallic Li interface. *Science Advances* **2017,** *3* (4), e1601659.

100. Aguesse, F.; Manalastas, W.; Buannic, L.; Lopez del Amo, J. M.; Singh, G.; Llordés, A.; Kilner, J., Investigating the Dendritic Growth during Full Cell Cycling of Garnet Electrolyte in Direct Contact with Li Metal. *ACS Applied Materials & Interfaces* **2017,** *9* (4), 3808-3816.

101. Porz, L.; Swamy, T.; Sheldon, B. W.; Rettenwander, D.; Frömling, T.; Thaman, H. L.; Berendts, S.; Uecker, R.; Carter, W. C.; Chiang, Y.-M., Mechanism of Lithium Metal Penetration through Inorganic Solid Electrolytes. *Advanced Energy Materials* **2017,** *7* (20), 1701003.

102. Manalastas, W.; Rikarte, J.; Chater, R. J.; Brugge, R.; Aguadero, A.; Buannic, L.; Llordés, A.; Aguesse, F.; Kilner, J., Mechanical failure of garnet electrolytes during Li electrodeposition observed by in-operando microscopy. *Journal of Power Sources* **2019,** *412*, 287-293.

103. Swamy, T.; Park, R.; Sheldon, B. W.; Rettenwander, D.; Porz, L.; Berendts, S.; Uecker, R.; Carter, W. C.; Chiang, Y.-M., Lithium metal penetration induced by electrodeposition through solid electrolytes: example in single-crystal $Li_6La_3ZrTaO_{12}$ garnet. *Journal of the Electrochemical Society* **2018,** *165* (16), A3648.

104. Ning, Z.; Jolly, D. S.; Li, G.; De Meyere, R.; Pu, S. D.; Chen, Y.; Kasemchainan, J.; Ihli, J.; Gong, C.; Liu, B.; Melvin, D. L. R.; Bonnin, A.; Magdysyuk, O.; Adamson, P.; Hartley, G. O.; Monroe, C. W.; Marrow, T. J.; Bruce, P. G., Visualizing plating-induced cracking in lithium-anode solid-electrolyte cells. *Nature Materials* **2021,** *20* (8), 1121-1129.

105. Hänsel, C.; Kundu, D., The Stack Pressure Dilemma in Sulfide Electrolyte Based Li Metal Solid-State Batteries: A Case Study with Li_6PS_5Cl Solid Electrolyte. *Advanced Materials Interfaces* **2021,** *8* (10), 2100206.

106. Albertus, P.; Anandan, V.; Ban, C.; Balsara, N.; Belharouak, I.; Buettner-Garrett, J.; Chen, Z.; Daniel, C.; Doeff, M.; Dudney, N. J.; Dunn, B.; Harris, S. J.; Herle, S.; Herbert, E.; Kalnaus, S.; Libera, J. A.; Lu, D.; Martin, S.; McCloskey, B. D.; McDowell, M. T.; Meng, Y. S.; Nanda, J.; Sakamoto, J.; Self, E. C.; Tepavcevic, S.; Wachsman, E.; Wang, C.; Westover, A. S.; Xiao, J.; Yersak, T., Challenges for and Pathways toward Li-Metal-Based All-Solid-State Batteries. *ACS Energy Letters* **2021,** *6* (4), 1399-1404.

107. Balaish, M.; Gonzalez-Rosillo, J. C.; Kim, K. J.; Zhu, Y.; Hood, Z. D.; Rupp, J. L. M., Processing thin but robust electrolytes for solid-state batteries. *Nature Energy* **2021,** *6* (3), 227-239.

108. Zhu, Y.; Gonzalez-Rosillo, J. C.; Balaish, M.; Hood, Z. D.; Kim, K. J.; Rupp, J. L. M., Lithium-film ceramics for solid-state lithionic devices. *Nature Reviews Materials* **2021,** *6* (4), 313-331.

109. Chen, Y.-T.; Duquesnoy, M.; Tan, D. H. S.; Doux, J.-M.; Yang, H.; Deysher, G.; Ridley, P.; Franco, A. A.; Meng, Y. S.; Chen, Z., Fabrication of High-Quality Thin Solid-State Electrolyte Films Assisted by Machine Learning. *ACS Energy Letters* **2021,** *6* (4), 1639-1648.

110. Self, E. C.; Hood, Z. D.; Brahmbhatt, T.; Delnick, F. M.; Meyer, H. M.; Yang, G.; Rupp, J. L. M.; Nanda, J., Solvent-Mediated Synthesis of Amorphous Li_3PS_4/Polyethylene Oxide Composite Solid Electrolytes with High Li^+ Conductivity. *Chemistry of Materials* **2020,** *32* (20), 8789-8797.

111. Li, Y.; Wang, X.; Zhou, H.; Xing, X.; Banerjee, A.; Holoubek, J.; Liu, H.; Meng, Y. S.; Liu, P., Thin Solid Electrolyte Layers Enabled by Nanoscopic Polymer Binding. *ACS Energy Letters* **2020,** *5* (3), 955-961.

112. Kim, K. T.; Oh, D. Y.; Jun, S.; Song, Y. B.; Kwon, T. Y.; Han, Y.; Jung, Y. S., Tailoring Slurries Using Cosolvents and Li Salt Targeting Practical All-Solid-State Batteries Employing Sulfide Solid Electrolytes. *Advanced Energy Materials 11* (17), 2003766.

113. Oh, D. Y.; Nam, Y. J.; Park, K. H.; Jung, S. H.; Kim, K. T.; Ha, A. R.; Jung, Y. S., Slurry-Fabricable Li^+-Conductive Polymeric Binders for Practical All-Solid-State Lithium-Ion Batteries Enabled by Solvate Ionic Liquids. *Advanced Energy Materials* **2019,** *9* (16), 1802927.

114. Bielefeld, A.; Weber, D. A.; Janek, J., Modeling Effective Ionic Conductivity and Binder Influence in Composite Cathodes for All-Solid-State Batteries. *ACS Applied Materials & Interfaces* **2020,** *12* (11), 12821-12833.

115. Kato, Y.; Shiotani, S.; Morita, K.; Suzuki, K.; Hirayama, M.; Kanno, R., All-Solid-State Batteries with Thick Electrode Configurations. *The Journal of Physical Chemistry Letters* **2018,** *9* (3), 607-613.

116. www.xtal.iqfr.csic.es/Cristalografia/parte_05_5-en.html. **retrieved on April 12, 2021.**

117. Toby, B. H.; Von Dreele, R. B., GSAS-II: the genesis of a modern open-source all purpose crystallography software package. *Journal of Applied Crystallography* **2013,** *46* (2), 544-549.

118. http://en.wikipedia.org/wiki/Scanning_electron_microsc. **retrieved on April 12, 2021.**

119. Rost, C. M.; Sachet, E.; Borman, T.; Moballegh, A.; Dickey, E. C.; Hou, D.; Jones, J. L.; Curtarolo, S.; Maria, J.-P., Entropy-stabilized oxides. *Nature Communications* **2015,** *6* (1), 8485.

120. Momma, K.; Ikeda, T.; Belik, A. A.; Izumi, F., Dysnomia, a computer program for maximum-entropy method (MEM) analysis and its performance in the MEM-based pattern fitting. *Powder Diffraction* **2013,** *28* (3), 184-193.

121. Chen, H.; Wong, L. L.; Adams, S., SoftBV - a software tool for screening the materials genome of inorganic fast ion conductors. *Acta Crystallographica Section B* **2019,** *75* (1), 18-33.

122. Chen, H.; Adams, S., Bond softness sensitive bond-valence parameters for crystal structure plausibility tests. *IUCrJ* **2017,** *4* (5), 614-625.

123. Chen, Y.; Cai, L.; Liu, Z.; Cruz, C. R. d.; Liang, C.; An, K., Correlation of anisotropy and directional conduction in β-Li_3PS_4 fast Li^+ conductor. *Applied Physics Letters* **2015,** *107* (1), 013904.

124. Mercier, R.; Malugani, J.-P.; Fahys, B.; Robert, G.; Douglade, J., Structure du tetrathiophosphate de lithium. *Acta Crystallographica Section B* **1982,** *38* (7), 1887-1890.

125. Abrahams, I.; Bruce, P. G., Defect clustering in the superionic conductor lithium germanium vanadate. *Acta Crystallographica Section B* **1991,** *47* (5), 696-701.

126. Bruce, P. G.; Abrahams, I.; West, A. R., Defect clustering in lisicon solid electrolytes. *Solid State Ionics* **1990,** *40-41*, 293-299.

127. Stöffler, H.; Zinkevich, T.; Yavuz, M.; Senyshyn, A.; Kulisch, J.; Hartmann, P.; Adermann, T.; Randau, S.; Richter, F. H.; Janek, J.; Indris, S.; Ehrenberg, H., Li^+-Ion Dynamics in β-Li_3PS_4 Observed by NMR: Local Hopping and Long-Range Transport. *The Journal of Physical Chemistry C* **2018,** *122* (28), 15954-15965.

128. Hori, S.; Suzuki, K.; Hirayama, M.; Kato, Y.; Saito, T.; Yonemura, M.; Kanno, R., Synthesis, structure, and ionic conductivity of solid solution, $Li_{10+\delta}M_{1+\delta}P_{2-\delta}S_{12}$ (M = Si, Sn). *Faraday Discussions* **2014,** *176* (0), 83-94.

129. Eckert, H.; Zhang, Z.; Kennedy, J. H., Glass formation in non-oxide chalcogenide systems. Structural elucidation of $Li_2S \cdot SiS_2 \cdot LiI$ solid electrolytes by quantitative ^{29}Si, ^{6}Li and ^{7}Li high resolution solid state NMR methods. *Journal of Non-Crystalline Solids* **1989,** *107* (2), 271-282.

130. Gobet, M.; Greenbaum, S.; Sahu, G.; Liang, C., Structural Evolution and Li Dynamics in Nanophase Li_3PS_4 by Solid-State and Pulsed-Field Gradient NMR. *Chemistry of Materials* **2014,** *26* (11), 3558-3564.

131. Kweon, K. E.; Varley, J. B.; Shea, P.; Adelstein, N.; Mehta, P.; Heo, T. W.; Udovic, T. J.; Stavila, V.; Wood, B. C., Structural, Chemical, and Dynamical Frustration: Origins of Superionic Conductivity in closo-Borate Solid Electrolytes. *Chemistry of Materials* **2017,** *29* (21), 9142-9153.

132. Düvel, A.; Heitjans, P.; Fedorov, P.; Scholz, G.; Cibin, G.; Chadwick, A. V.; Pickup, D. M.; Ramos, S.; Sayle, L. W. L.; Sayle, E. K. L.; Sayle, T. X. T.; Sayle, D. C., Is Geometric Frustration-Induced Disorder a Recipe for High Ionic Conductivity? *Journal of the American Chemical Society* **2017,** *139* (16), 5842-5848.

133. Keen, D. A.; Goodwin, A. L., The crystallography of correlated disorder. *Nature* **2015,** *521* (7552), 303-309.

134. Phani Dathar, G. K.; Balachandran, J.; Kent, P. R. C.; Rondinone, A. J.; Ganesh, P., Li-ion site disorder driven superionic conductivity in solid electrolytes: a first-principles investigation of β-Li_3PS_4. *Journal of Materials Chemistry A* **2017,** *5* (3), 1153-1159.

135. Seino, Y.; Ota, T.; Takada, K.; Hayashi, A.; Tatsumisago, M., A sulphide lithium super ion conductor is superior to liquid ion conductors for use in rechargeable batteries. *Energy & Environmental Science* **2014,** *7* (2), 627-631.

136. Sun, Y.; Suzuki, K.; Hori, S.; Hirayama, M.; Kanno, R., Superionic Conductors: $Li_{10+\delta}[Sn_ySi_{1-y}]_{1+\delta}P_{2-\delta}S_{12}$ with a $Li_{10}GeP_2S_{12}$-type Structure in the Li_3PS_4-Li_4SnS_4-Li_4SiS_4 Quasi-ternary System. *Chemistry of Materials* **2017,** *29* (14), 5858-5864.

137. Kato, Y.; Hori, S.; Saito, T.; Suzuki, K.; Hirayama, M.; Mitsui, A.; Yonemura, M.; Iba, H.; Kanno, R., High-power all-solid-state batteries using sulfide superionic conductors. *Nature Energy* **2016,** *1* (4), 16030.

138. Rayavarapu, P. R.; Sharma, N.; Peterson, V. K.; Adams, S., Variation in structure and Li^+-ion migration in argyrodite-type Li_6PS_5X (X = Cl, Br, I) solid electrolytes. *Journal of Solid State Electrochemistry* **2012,** *16* (5), 1807-1813.

139. Yu, C.; Ganapathy, S.; Hageman, J.; van Eijck, L.; van Eck, E. R. H.; Zhang, L.; Schwietert, T.; Basak, S.; Kelder, E. M.; Wagemaker, M., Facile Synthesis toward the Optimal Structure-Conductivity Characteristics of the Argyrodite Li_6PS_5Cl Solid-State Electrolyte. *ACS Applied Materials & Interfaces* **2018,** *10* (39), 33296-33306.

140. de Klerk, N. J. J.; Rosłoń, I.; Wagemaker, M., Diffusion Mechanism of Li Argyrodite Solid Electrolytes for Li-Ion Batteries and Prediction of Optimized Halogen Doping: The Effect of Li Vacancies, Halogens, and Halogen Disorder. *Chemistry of Materials* **2016,** *28* (21), 7955-7963.

141. Zhang, W.; Weber, D. A.; Weigand, H.; Arlt, T.; Manke, I.; Schröder, D.; Koerver, R.; Leichtweiss, T.; Hartmann, P.; Zeier, W. G.; Janek, J., Interfacial Processes and Influence of Composite Cathode Microstructure Controlling the Performance of All-Solid-State Lithium Batteries. *ACS Applied Materials & Interfaces* **2017,** *9* (21), 17835-17845.

142. Wu, F.; Fitzhugh, W.; Ye, L.; Ning, J.; Li, X., Advanced sulfide solid electrolyte by core-shell structural design. *Nature Communications* **2018,** *9* (1), 4037.

143. Xu, R.; Wu, Z.; Zhang, S.; Wang, X.; Xia, Y.; Xia, X.; Huang, X.; Tu, J., Construction of All-Solid-State Batteries based on a Sulfur-Graphene Composite and $Li_{9.54}Si_{1.74}P_{1.44}S_{11.7}Cl_{0.3}$ Solid Electrolyte. *Chemistry – A European Journal* **2017,** *23* (56), 13950-13956.

144. Dawson, J. A.; Canepa, P.; Famprikis, T.; Masquelier, C.; Islam, M. S., Atomic-Scale Influence of Grain Boundaries on Li-Ion Conduction in Solid Electrolytes for All-Solid-State Batteries. *Journal of the American Chemical Society* **2018,** *140* (1), 362-368.

145. Zhang, Z.; Chen, S.; Yang, J.; Wang, J.; Yao, L.; Yao, X.; Cui, P.; Xu, X., Interface Re-Engineering of $Li_{10}GeP_2S_{12}$ Electrolyte and Lithium anode for All-Solid-State Lithium Batteries with Ultralong Cycle Life. *ACS Applied Materials & Interfaces* **2018,** *10* (3), 2556-2565.

146. Gao, Y.; Wang, D.; Li, Y. C.; Yu, Z.; Mallouk, T. E.; Wang, D., Salt-Based Organic–Inorganic Nanocomposites: Towards A Stable Lithium Metal/$Li_{10}GeP_2S_{12}$ Solid Electrolyte Interface. *Angewandte Chemie International Edition* **2018,** *57* (41), 13608-13612.

147. Krauskopf, T.; Dippel, R.; Hartmann, H.; Peppler, K.; Mogwitz, B.; Richter, F. H.; Zeier, W. G.; Janek, J., Lithium-Metal Growth Kinetics on LLZO Garnet-Type Solid Electrolytes. *Joule* **2019,** *3* (8), 2030-2049.

148. Zhou, L.; Assoud, A.; Shyamsunder, A.; Huq, A.; Zhang, Q.; Hartmann, P.; Kulisch, J.; Nazar, L. F., An Entropically Stabilized Fast-Ion Conductor: $Li_{3.25}[Si_{0.25}P_{0.75}]S_4$. *Chemistry of Materials* **2019,** *31* (19), 7801-7811.

149. Deng, Y.; Eames, C.; Chotard, J.-N.; Lalère, F.; Seznec, V.; Emge, S.; Pecher, O.; Grey, C. P.; Masquelier, C.; Islam, M. S., Structural and Mechanistic Insights into Fast Lithium-Ion Conduction in Li_4SiO_4–Li_3PO_4 Solid Electrolytes. *Journal of the American Chemical Society* **2015,** *137* (28), 9136-9145.

150. He, X.; Bai, Q.; Liu, Y.; Nolan, A. M.; Ling, C.; Mo, Y., Crystal Structural Framework of Lithium Super-Ionic Conductors. *Advanced Energy Materials* **2019,** *9* (43), 1902078.

151. Doux, J.-M.; Yang, Y.; Tan, D. H. S.; Nguyen, H.; Wu, E. A.; Wang, X.; Banerjee, A.; Meng, Y. S., Pressure effects on sulfide electrolytes for all solid-state batteries. *Journal of Materials Chemistry A* **2020,** *8* (10), 5049-5055.

152. Chu, I.-H.; Nguyen, H.; Hy, S.; Lin, Y.-C.; Wang, Z.; Xu, Z.; Deng, Z.; Meng, Y. S.; Ong, S. P., Insights into the Performance Limits of the $Li_7P_3S_{11}$ Superionic Conductor: A Combined First-Principles and Experimental Study. *ACS Applied Materials & Interfaces* **2016,** *8* (12), 7843-7853.

153. Muy, S.; Bachman, J. C.; Giordano, L.; Chang, H.-H.; Abernathy, D. L.; Bansal, D.; Delaire, O.; Hori, S.; Kanno, R.; Maglia, F.; Lupart, S.; Lamp, P.; Shao-Horn, Y., Tuning mobility and stability of lithium ion conductors based on lattice dynamics. *Energy & Environmental Science* **2018,** *11* (4), 850-859.

154. Xiao, Y.; Wang, Y.; Bo, S.-H.; Kim, J. C.; Miara, L. J.; Ceder, G., Understanding interface stability in solid-state batteries. *Nature Reviews Materials* **2020,** *5* (2), 105-126.

155. Tan, D. H. S.; Wu, E. A.; Nguyen, H.; Chen, Z.; Marple, M. A. T.; Doux, J.-M.; Wang, X.; Yang, H.; Banerjee, A.; Meng, Y. S., Elucidating Reversible Electrochemical Redox of Li_6PS_5Cl Solid Electrolyte. *ACS Energy Letters* **2019,** *4* (10), 2418-2427.

156. Doux, J.-M.; Nguyen, H.; Tan, D. H. S.; Banerjee, A.; Wang, X.; Wu, E. A.; Jo, C.; Yang, H.; Meng, Y. S., Stack Pressure Considerations for Room-Temperature All-Solid-State Lithium Metal Batteries. *Advanced Energy Materials* **2020,** *10* (1), 1903253.

157. Banerjee, A.; Tang, H.; Wang, X.; Cheng, J.-H.; Nguyen, H.; Zhang, M.; Tan, D. H. S.; Wynn, T. A.; Wu, E. A.; Doux, J.-M.; Wu, T.; Ma, L.; Sterbinsky, G. E.; D'Souza, M. S.; Ong, S. P.; Meng, Y. S., Revealing Nanoscale Solid–Solid Interfacial Phenomena for Long-Life and High-Energy All-Solid-State Batteries. *ACS Applied Materials & Interfaces* **2019,** *11* (46), 43138-43145.

158. Banerjee, A.; Wang, X.; Fang, C.; Wu, E. A.; Meng, Y. S., Interfaces and Interphases in All-Solid-State Batteries with Inorganic Solid Electrolytes. *Chemical Reviews* **2020,** *120* (14), 6878-6933.

159. Xiao, Y.; Miara, L. J.; Wang, Y.; Ceder, G., Computational Screening of Cathode Coatings for Solid-State Batteries. *Joule* **2019,** *3* (5), 1252-1275.

160. Nolan, A. M.; Liu, Y.; Mo, Y., Solid-State Chemistries Stable with High-Energy Cathodes for Lithium-Ion Batteries. *ACS Energy Letters* **2019,** *4* (10), 2444-2451.

161. Buschmann, H.; Dölle, J.; Berendts, S.; Kuhn, A.; Bottke, P.; Wilkening, M.; Heitjans, P.; Senyshyn, A.; Ehrenberg, H.; Lotnyk, A.; Duppel, V.; Kienle, L.; Janek, J., Structure and dynamics of the fast lithium ion conductor "$Li_7La_3Zr_2O_{12}$". *Physical Chemistry Chemical Physics* **2011,** *13* (43), 19378-19392.

162. Steiner, H.-J.; Lutz, H. D., Neue schnelle Ionenleiter vom Typ $M^IM^{III}Cl_6$ (M^I = Li, Na, Ag; M^{III} = In, Y). *Zeitschrift für anorganische und allgemeine Chemie* **1992,** *613* (7), 26-30.

163. Lutz, H. D.; Schmidt, W.; Haeuseler, H., Chloride spinels: A new group of solid lithium electrolytes. *Journal of Physics and Chemistry of Solids* **1981,** *42* (4), 287-289.

164. van Loon, C. J. J.; de Jong, J., Some chlorides with the inverse spinel structure. *Acta Crystallographica Section B* **1975,** *31* (10), 2549-2550.

165. Partik, M.; Schneider, M.; Lutz, H. D., Kristallstrukturen von $MgCr_2O_4$-Typ Li_2VCl_4 und Spinell-Typ Li_2MgCl_4 und Li_2CdCl_4. *Zeitschrift für anorganische und allgemeine Chemie* **1994,** *620* (5), 791-795.

166. Kanno, R.; Takeda, Y.; Yamamoto, O., Structure, ionic conductivity and phase transformation of double chloride spinels. *Solid State Ionics* **1988,** *28-30*, 1276-1281.

167. Cros, C.; Hanebali, L.; Latie´, L.; Villeneuve, G. r.; Gang, W., Structure, ionic motion and conductivity in some solid-solutions of the LiCl-MCl_2 systems (M=Mg,V,Mn). *Solid State Ionics* **1983,** *9-10*, 139-147.

168. Canepa, P.; Bo, S.-H.; Sai Gautam, G.; Key, B.; Richards, W. D.; Shi, T.; Tian, Y.; Wang, Y.; Li, J.; Ceder, G., High magnesium mobility in ternary spinel chalcogenides. *Nature Communications* **2017,** *8* (1), 1759.

169. Park, K. H.; Oh, D. Y.; Choi, Y. E.; Nam, Y. J.; Han, L.; Kim, J.-Y.; Xin, H.; Lin, F.; Oh, S. M.; Jung, Y. S., Solution-Processable Glass LiI-Li_4SnS_4 Superionic Conductors for All-Solid-State Li-Ion Batteries. *Advanced Materials* **2016,** *28* (9), 1874-1883.

170. Jung, S. H.; Oh, K.; Nam, Y. J.; Oh, D. Y.; Brüner, P.; Kang, K.; Jung, Y. S., Li_3BO_3-Li_2CO_3: Rationally Designed Buffering Phase for Sulfide All-Solid-State Li-Ion Batteries. *Chemistry of Materials* **2018,** *30* (22), 8190-8200.

171. Jung, S. H.; Kim, U.-H.; Kim, J.-H.; Jun, S.; Yoon, C. S.; Jung, Y. S.; Sun, Y.-K., Ni-Rich Layered Cathode Materials with Electrochemo-Mechanically Compliant Microstructures for All-Solid-State Li Batteries. *Advanced Energy Materials* **2020,** *10* (6), 1903360.

172. Shi, T.; Tu, Q.; Tian, Y.; Xiao, Y.; Miara, L. J.; Kononova, O.; Ceder, G., High Active Material Loading in All-Solid-State Battery Electrode via Particle Size Optimization. *Advanced Energy Materials* **2020,** *10* (1), 1902881.

173. Strauss, F.; Bartsch, T.; de Biasi, L.; Kim, A. Y.; Janek, J.; Hartmann, P.; Brezesinski, T., Impact of Cathode Material Particle Size on the Capacity of Bulk-Type All-Solid-State Batteries. *ACS Energy Letters* **2018,** *3* (4), 992-996.

174. Bielefeld, A.; Weber, D. A.; Janek, J., Microstructural Modeling of Composite Cathodes for All-Solid-State Batteries. *The Journal of Physical Chemistry C* **2019,** *123* (3), 1626-1634.

175. Kim, A. Y.; Strauss, F.; Bartsch, T.; Teo, J. H.; Hatsukade, T.; Mazilkin, A.; Janek, J.; Hartmann, P.; Brezesinski, T., Stabilizing Effect of a Hybrid Surface Coating on a Ni-Rich NCM Cathode Material in All-Solid-State Batteries. *Chemistry of Materials* **2019,** *31* (23), 9664-9672.

176. Susai, F. A.; Sclar, H.; Maiti, S.; Burstein, L.; Perkal, O.; Grinblat, J.; Talianker, M.; Ruthstein, S.; Erk, C.; Hartmann, P.; Markovsky, B.; Aurbach, D., Stabilized Behavior of $LiNi_{0.85}Co_{0.10}Mn_{0.05}O_2$ Cathode Materials Induced by Their Treatment with SO_2. *ACS Applied Energy Materials* **2020,** *3* (4), 3609-3618.

177. Schweidler, S.; de Biasi, L.; Garcia, G.; Mazilkin, A.; Hartmann, P.; Brezesinski, T.; Janek, J., Investigation into Mechanical Degradation and Fatigue of High-Ni NCM Cathode Material: A Long-Term Cycling Study of Full Cells. *ACS Applied Energy Materials* **2019,** *2* (10), 7375-7384.

178. Schweidler, S.; de Biasi, L.; Hartmann, P.; Brezesinski, T.; Janek, J., Kinetic Limitations in Cycled Nickel-Rich NCM Cathodes and Their Effect on the Phase Transformation Behavior. *ACS Applied Energy Materials* **2020,** *3* (3), 2821-2827.

179. Sun, H. H.; Ryu, H.-H.; Kim, U.-H.; Weeks, J. A.; Heller, A.; Sun, Y.-K.; Mullins, C. B., Beyond Doping and Coating: Prospective Strategies for Stable High-Capacity Layered Ni-Rich Cathodes. *ACS Energy Letters* **2020,** *5* (4), 1136-1146.

180. Tatara, R.; Yu, Y.; Karayaylali, P.; Chan, A. K.; Zhang, Y.; Jung, R.; Maglia, F.; Giordano, L.; Shao-Horn, Y., Enhanced Cycling Performance of Ni-Rich Positive Electrodes (NMC) in Li-Ion Batteries by Reducing Electrolyte Free-Solvent Activity. *ACS Applied Materials & Interfaces* **2019,** *11* (38), 34973-34988.

181. Yin, L.; Li, Z.; Mattei, G. S.; Zheng, J.; Zhao, W.; Omenya, F.; Fang, C.; Li, W.; Li, J.; Xie, Q.; Erickson, E. M.; Zhang, J.-G.; Whittingham, M. S.; Meng, Y. S.; Manthiram, A.; Khalifah, P. G., Thermodynamics of Antisite Defects in Layered NMC Cathodes: Systematic Insights from High-Precision Powder Diffraction Analyses. *Chemistry of Materials* **2020,** *32* (3), 1002-1010.

182. Zhou, L.; Kwok, C. Y.; Shyamsunder, A.; Zhang, Q.; Wu, X.; Nazar, L. F., A new halospinel superionic conductor for high-voltage all solid state lithium batteries. *Energy & Environmental Science* **2020,** *13* (7), 2056-2063.

183. Liu, H.; Zhu, Z.; Huang, J.; He, X.; Chen, Y.; Zhang, R.; Lin, R.; Li, Y.; Yu, S.; Xing, X.; Yan, Q.; Li, X.; Frost, M. J.; An, K.; Feng, J.; Kostecki, R.; Xin, H.; Ong, S. P.; Liu, P., Elucidating the Limit of Li Insertion into the Spinel $Li_4Ti_5O_{12}$. *ACS Materials Letters* **2019,** *1* (1), 96-102.

184. Ganapathy, S.; Wagemaker, M., Fast interfaces. *Nature Energy* **2020,** *5* (6), 424-425.

185. Zhang, W.; Seo, D.-H.; Chen, T.; Wu, L.; Topsakal, M.; Zhu, Y.; Lu, D.; Ceder, G.; Wang, F., Kinetic pathways of ionic transport in fast-charging lithium titanate. *Science* **2020,** *367* (6481), 1030-1034.

186. BOHNSACK, A.; STENZEL, F.; ZAJONC, A.; BALZER, G.; WICKLEDER, M. S.; MEYER, G., ChemInform Abstract: Ternary Halides of the A_3MX_6 Type. Part 6. Ternary Chlorides of the Rare-Earth Elements with Lithium, Li_3LnCl_6 (Ln: Tb-Lu, Y, Sc): Synthesis, Crystal Structures, and Ionic Motion. *ChemInform* **1997,** *28* (39).

187. Liang, J.; Li, X.; Wang, S.; Adair, K. R.; Li, W.; Zhao, Y.; Wang, C.; Hu, Y.; Zhang, L.; Zhao, S.; Lu, S.; Huang, H.; Li, R.; Mo, Y.; Sun, X., Site-Occupation-Tuned Superionic Li_xScCl_{3+x} Halide Solid Electrolytes for All-Solid-State Batteries. *Journal of the American Chemical Society* **2020,** *142* (15), 7012-7022.

188. Xue, W.; Huang, M.; Li, Y.; Zhu, Y. G.; Gao, R.; Xiao, X.; Zhang, W.; Li, S.; Xu, G.; Yu, Y.; Li, P.; Lopez, J.; Yu, D.; Dong, Y.; Fan, W.; Shi, Z.; Xiong, R.; Sun, C.-J.; Hwang, I.;

Lee, W.-K.; Shao-Horn, Y.; Johnson, J. A.; Li, J., Ultra-high-voltage Ni-rich layered cathodes in practical Li metal batteries enabled by a sulfonamide-based electrolyte. *Nature Energy* **2021,** *6* (5), 495-505.

189. Lee, Y.-G.; Fujiki, S.; Jung, C.; Suzuki, N.; Yashiro, N.; Omoda, R.; Ko, D.-S.; Shiratsuchi, T.; Sugimoto, T.; Ryu, S.; Ku, J. H.; Watanabe, T.; Park, Y.; Aihara, Y.; Im, D.; Han, I. T., High-energy long-cycling all-solid-state lithium metal batteries enabled by silver–carbon composite anodes. *Nature Energy* **2020,** *5* (4), 299-308.

190. Han, F.; Yue, J.; Chen, C.; Zhao, N.; Fan, X.; Ma, Z.; Gao, T.; Wang, F.; Guo, X.; Wang, C., Interphase Engineering Enabled All-Ceramic Lithium Battery. *Joule* **2018,** *2* (3), 497-508.

191. Xu, L.; Lu, Y.; Zhao, C.-Z.; Yuan, H.; Zhu, G.-L.; Hou, L.-P.; Zhang, Q.; Huang, J.-Q., Toward the Scale-Up of Solid-State Lithium Metal Batteries: The Gaps between Lab-Level Cells and Practical Large-Format Batteries. *Advanced Energy Materials* **2021,** *11* (4), 2002360.

192. Wang, S.; Bai, Q.; Nolan, A. M.; Liu, Y.; Gong, S.; Sun, Q.; Mo, Y., Lithium Chlorides and Bromides as Promising Solid-State Chemistries for Fast Ion Conductors with Good Electrochemical Stability. *Angewandte Chemie International Edition* **2019,** *58* (24), 8039-8043.

193. Amin, R.; Chiang, Y.-M., Characterization of Electronic and Ionic Transport in $Li_{1-x}Ni_{0.33}Mn_{0.33}Co_{0.33}O_2$(NMC333) and $Li_{1-x}Ni_{0.50}Mn_{0.20}Co_{0.30}O_2$(NMC523) as a Function of Li Content. *Journal of The Electrochemical Society* **2016,** *163* (8), A1512-A1517.

194. Märker, K.; Reeves, P. J.; Xu, C.; Griffith, K. J.; Grey, C. P., Evolution of Structure and Lithium Dynamics in $LiNi_{0.8}Mn_{0.1}Co_{0.1}O_2$ (NMC811) Cathodes during Electrochemical Cycling. *Chemistry of Materials* **2019,** *31* (7), 2545-2554.

195. Walther, F.; Strauss, F.; Wu, X.; Mogwitz, B.; Hertle, J.; Sann, J.; Rohnke, M.; Brezesinski, T.; Janek, J., The Working Principle of a $Li_2CO_3/LiNbO_3$ Coating on NCM for Thiophosphate-Based All-Solid-State Batteries. *Chemistry of Materials* **2021,** *33* (6), 2110-2125.

196. Glass, A. M.; Nassau, K.; Negran, T. J., Ionic conductivity of quenched alkali niobate and tantalate glasses. *Journal of Applied Physics* **1978,** *49* (9), 4808-4811.

197. Zhang, Y.-Q.; Tian, Y.; Xiao, Y.; Miara, L. J.; Aihara, Y.; Tsujimura, T.; Shi, T.; Scott, M. C.; Ceder, G., Direct Visualization of the Interfacial Degradation of Cathode Coatings in Solid State Batteries: A Combined Experimental and Computational Study. *Advanced Energy Materials* **2020,** *10* (27), 1903778.

198. Wang, S.; Yan, M.; Li, Y.; Vinado, C.; Yang, J., Separating electronic and ionic conductivity in mix-conducting layered lithium transition-metal oxides. *Journal of Power Sources* **2018,** *393*, 75-82.

199. Tan, D. H. S.; Chen, Y.-T.; Yang, H.; Bao, W.; Sreenarayanan, B.; Doux, J.-M.; Li, W.; Lu, B.; Ham, S.-Y.; Sayahpour, B.; Scharf, J.; Wu, E. A.; Deysher, G.; Han, H. E.; Hah, H. J.; Jeong, H.; Lee, J. B.; Chen, Z.; Meng, Y. S., Carbon-free high-loading silicon anodes enabled by sulfide solid electrolytes. *Science* **2021,** *373* (6562), 1494-1499.

200. Asakura, R.; Reber, D.; Duchêne, L.; Payandeh, S.; Remhof, A.; Hagemann, H.; Battaglia, C., 4 V room-temperature all-solid-state sodium battery enabled by a passivating cathode/hydroborate solid electrolyte interface. *Energy & Environmental Science* **2020,** *13* (12), 5048-5058.

Appendix A Supporting information for Chapter 3

Table A1 Atomic coordinates, occupation factors and equivalent isotropic displacement parameters of $Li_{3.15}Si_{0.15}P_{0.85}S_4$ obtained from single crystal X-ray diffraction at 280 K.

S. G. : *Pnma*, *a* = 13.0469(18) Å, *b* = 8.0707(12) Å, *c* = 6.1395(9) Å						
Atom	**Wyck. site**	***x***	***y***	***z***	**Occ.**	**U_{eq} (Å^2)**
Li1	8*d*	0.3310(4)	0.0322(5)	0.3899 (9)	0.976(19)	0.0451(19)
Li2	8*d*	0.0056(8)	0.0477(11)	0.5580(14)	0.492(16)	0.048(4)
Li3	4*c*	-0.081(4)	0.25	-0.220(11)	0.28(5)	0.14(3)
P1	4*c*	0.08777(6)	0.25	0.15737(11)	0.85	0.01725(18)
Si1	4*c*	0.08777(6)	0.25	0.15737(11)	0.15	0.01725(18)
S1	8*d*	0.15251(4)	0.03757(7)	0.27752(9)	1	0.02667(16)
S2	4*c*	-0.06224(6)	0.25	0.26951(12)	1	0.02230(18)
S3	4*c*	0.10262(6)	0.25	-0.17381(12)	1	0.0265(2)

Table A2 Anisotropic displacement parameters of $Li_{3.15}Si_{0.15}P_{0.85}S_4$ obtained from single crystal X-ray diffraction at 280 K.

Atom	**U_{11} (Å^2)**	**U_{22} (Å^2)**	**U_{33} (Å^2)**	**U_{23} (Å^2)**	**U_{13} (Å^2)**	**U_{12} (Å^2)**
Li1	0.037(3)	0.041(3)	0.058(3)	0.018(2)	-0.007(2)	-0.0006(18)
Li2	0.040(5)	0.062(7)	0.042(7)	0.028(5)	0.007(5)	0.001(5)
Li3	0.10(4)	0.10(4)	0.22(8)	0	-0.03(3)	0
P1	0.0182(4)	0.0202(3)	0.0133(3)	0	0.0009(3)	0
Si1	0.0182(4)	0.0202(3)	0.0133(3)	0	0.0009(3)	0
S1	0.0246(3)	0.0279(3)	0.0275(3)	0.0060(2)	0.0006(2)	0.0045(2)
S2	0.0192(3)	0.0255(3)	0.0222(4)	0	0.0021(3)	0
S3	0.0369(5)	0.0279(4)	0.0148(3)	0	0.0030(3)	0

Table A3 Anisotropic displacement parameters of $Li_{3.25}Si_{0.25}P_{0.75}S_4$ obtained from single crystal X-ray diffraction at 280 K.

Atom	U_{11} (Å^2)	U_{22} (Å^2)	U_{33} (Å^2)	U_{23} (Å^2)	U_{13} (Å^2)	U_{12} (Å^2)
Li1A	0.0301(15)	0.0363(15)	0.054(2)	0.0166(14)	-0.0037(13)	0.0012(11)
Li1B	0.0301(15)	0.0363(15)	0.054(2)	0.0166(14)	-0.0037(13)	0.0012(11)
Li2	0.040(4)	0.056(5)	0.041(4)	0.022(3)	0.001(3)	-0.012(3)
Li3A	0.07(2)	0.046(16)	0.10(6)	0	-0.02(2)	0
Li3B	0.046(18)	0.045(16)	0.05(3)	0	-0.010(15)	0
P1	0.0162(2)	0.0159(2)	0.01357(19)	0	0.00137(15)	0
Si1	0.0162(2)	0.0159(2)	0.01357(19)	0	0.00137(15)	0
S1	0.02099(17)	0.02320(17)	0.02658(16)	0.00543(11)	0.00036(11)	0.00414(12)
S2	0.0174(2)	0.0201(2)	0.0222(2)	0	0.00197(15)	0
S3	0.0328(3)	0.0224(2)	0.01478(18)	0	0.00339(16)	0

Table A4 Atomic coordinates, occupation factors and isotropic displacement parameters of $Li_{3.25}Si_{0.25}P_{0.75}S_4$ obtained from single crystal X-ray diffraction at 180 K (Li3B site was refined isotropically).

S. G. : *Pnma*, *a* = 13.156(7) Å, *b* = 8.016(4) Å, *c* = 6.132(3) Å						
Atom	**Wyck. site**	***x***	***y***	***z***	**Occ.**	**U_{eq} (Å^2)**
Li1A	8*d*	0.3300(4)	0.0303(5)	0.3839(9)	0.918(10)	0.0326(13)
Li1B	8*d*	0.338(4)	0.015(7)	0.217(10)	0.082(10)	0.0326(13)
Li2	8*d*	0.0052(7)	0.0448(11)	0.5544(15)	0.442(17)	0.029(3)
Li3A	4*c*	-0.083(3)	0.25	-0.167(8)	0.20(4)	0.052(18)
Li3B	4*c*	-0.070(3)	0.25	-0.305(9)	0.14(4)	0.025(16)
P1	4*c*	0.08714(6)	0.25	0.15547(11)	0.75	0.01239(17)
Si1	4*c*	0.08714(6)	0.25	0.15547(11)	0.25	0.01239(17)
S1	8*d*	0.15276(4)	0.03467(6)	0.27540(8)	1	0.01825(15)
S2	4*c*	-0.06200(6)	0.25	0.26907(12)	1	0.01579(17)
S3	4*c*	0.10062(6)	0.25	-0.17941(11)	1	0.01811(18)

Table A5 Anisotropic displacement parameters of $Li_{3.25}Si_{0.25}P_{0.75}S_4$ obtained from single crystal X-ray diffraction at 180 K.

Atom	**U_{11} (Å^2)**	**U_{22} (Å^2)**	**U_{33} (Å^2)**	**U_{23} (Å^2)**	**U_{13} (Å^2)**	**U_{12} (Å^2)**
Li1A	0.027(2)	0.028(2)	0.043(3)	0.017(2)	-0.006(2)	-0.0008(18)
Li1B	0.027(2)	0.028(2)	0.043(3)	0.017(2)	-0.006(2)	-0.0008(18)
Li2	0.020(5)	0.033(6)	0.035(6)	0.015(4)	0.010(4)	-0.004(4)
Li3A	0.07(3)	0.05(2)	0.04(3)	0	-0.00(2)	0
P1	0.0156(4)	0.0127(3)	0.0088(3)	0	0.0015(3)	0
Si1	0.0156(4)	0.0127(3)	0.0088(3)	0	0.0015(3)	0
S1	0.0189(3)	0.0182(3)	0.0176(2)	0.00329(19)	0.00030(18)	0.0027(2)
S2	0.0169(4)	0.0160(3)	0.0145(3)	0	0.0010(2)	0
S3	0.0273(4)	0.0172(3)	0.0098(3)	0	0.0026(3)	0

Table A6 Atomic coordinates, occupation factors and isotropic displacement parameters of $Li_{3.25}Si_{0.25}P_{0.75}S_4$ obtained from neutron powder diffraction at 300 K.

S. G.: *Pnma*, *a* = 13.1259(9) Å, *b* = 8.0439(5) Å, *c* = 6.1290(4) Å						
Atom	**Wyck. site**	***x***	***y***	***z***	**Occ.**	**U_{iso} (Å^2)**
Li1A	8*d*	0.3349(7)	0.030(1)	0.387(2)	0.896(8)	0.039(2)
Li1B	8*d*	0.365(4)	0.021(9)	0.225(12)	0.104(8)	0.03(2)
Li2	8*d*	0.0075(15)	0.036(2)	0.557(3)	0.465(8)	0.048(5)
Li3A	4*c*	-0.067(4)	0.25	-0.191(9)	0.19(2)	0.04(1)
Li3B	4*c*	-0.103(5)	0.25	-0.317(15)	0.17(2)	0.06(2)
P1	4*c*	0.0866(3)	0.25	0.1540(6)	0.75	0.010(2)
Si1	4*c*	0.0866(3)	0.25	0.1540(6)	0.25	0.010(2)
S1	8*d*	0.1548(4)	0.0368(5)	0.2749(9)	1	0.027(2)
S2	4*c*	-0.0648(5)	0.25	0.265(2)	1	0.026(2)
S3	4*c*	0.1044(4)	0.25	-0.1747(9)	1	0.010(2)

Table A7 Atomic coordinates, occupation factor and isotropic displacement parameters of $Li_{3.25}Si_{0.25}P_{0.75}S_4$ obtained from neutron powder diffraction at 180 K.

S. G.: *Pnma*, *a* = 13.1444(6) Å, *b* = 8.0238(4) Å, *c* = 6.1273(3) Å						
Atom	**Wyck. site**	***x***	***y***	***z***	**Occ.**	**U_{iso} (Å^2)**
Li1A	8*d*	0.3302(6)	0.0329(9)	0.385(1)	0.905(9)	0.027(3)
Li1B	8*d*	0.368(4)	0.002(8)	0.255(12)	0.095(9)	0.033(25)
Li2	8*d*	0.0055(13)	0.040(2)	0.560(2)	0.453 (9)	0.027(5)
Li3A	4*c*	-0.067(3)	0.25	-0.200(7)	0.22(2)	0.01(1)
Li3B	4*c*	-0.113(5)	0.25	-0.354(14)	0.15(2)	0.044(22)
P1	4*c*	0.0864(3)	0.25	0.1533(5)	0.75	0.010(2)
Si1	4*c*	0.0864(3)	0.25	0.1533(5)	0.25	0.010(2)
S1	8*d*	0.1528(3)	0.0345(5)	0.2737(8)	1	0.023(2)
S2	4*c*	-0.0624(4)	0.25	0.272(1)	1	0.013(3)
S3	4*c*	0.1021(4)	0.25	-0.1749(9)	1	0.011(3)

Table A8 Atomic coordinates, occupation factors and equivalent isotropic displacement parameters of $Li_{3.33}Si_{0.33}P_{0.67}S_4$ obtained from single crystal X-ray diffraction at 280 K.

S. G.: *Pnma*, a = 13.2489(4) Å, b = 8.0094(2) Å, c = 6.1311(2) Å						
Atom	**Wyck. site**	***x***	***y***	***z***	**Occ.**	**U_{eq} (Å^2)**
Li1A	8*d*	0.32949(17)	0.0296(3)	0.3815(5)	0.863(8)	0.0404(7)
Li1B	8*d*	0.3338(9)	0.0071(16)	0.208(3)	0.137(8)	0.039(5)
Li2	8*d*	0.0065(4)	0.0430(7)	0.5551(7)	0.437(8)	0.0465(16)
Li3A	4*c*	-0.0833(13)	0.25	-0.160(5)	0.24(2)	0.060(9)
Li3B	4*c*	-0.0693(12)	0.25	-0.309(4)	0.21(2)	0.044(6)
P1	4*c*	0.08727(2)	0.25	0.15573(5)	0.67	0.01609(7)
Si1	4*c*	0.08727(2)	0.25	0.15573(5)	0.33	0.01609(7)
S1	8*d*	0.15328(2)	0.03433(3)	0.27543(4)	1	0.02442(7)
S2	4*c*	-0.06159(2)	0.25	0.26835(5)	1	0.02055(7)
S3	4*c*	0.09947(2)	0.25	-0.17975(5)	1	0.02408(8)

Table A9 Anisotropic displacement parameters of $Li_{3.33}Si_{0.33}P_{0.67}S_4$ obtained from single crystal X-ray diffraction at 280 K.

Atom	**U_{11} (Å^2)**	**U_{22} (Å^2)**	**U_{33} (Å^2)**	**U_{23} (Å^2)**	**U_{13} (Å^2)**	**U_{12} (Å^2)**
Li1A	0.0325(10)	0.0378(12)	0.0511(17)	0.0148(10)	-0.003(1)	0.0004(8)
Li1B	0.017(5)	0.018(5)	0.083(14)	0.006(6)	-0.004(6)	0.000(4)
Li2	0.039(2)	0.055(3)	0.046(3)	0.024(2)	0.003(2)	-0.010(2)
Li3A	0.049(9)	0.044(8)	0.09(2)	0	-0.027(10)	0
Li3B	0.048(9)	0.036(7)	0.048(13)	0	-0.007(7)	0
P1	0.01696(13)	0.01652(13)	0.01480(13)	0	0.00148(9)	0
Si1	0.01696(13)	0.01652(13)	0.01480(13)	0	0.00148(9)	0
S1	0.02191(11)	0.02404(11)	0.02730(11)	0.00523(7)	0.00030(7)	0.00407(7)
S2	0.01844(14)	0.02230(13)	0.02299(13)	0	0.00172(9)	0
S3	0.03357(16)	0.02254(14)	0.01614(13)	0	0.00356(10)	0

Table A10 Atomic coordinates, occupation factors and equivalent isotropic displacement parameters of $Li_{3.5}Si_{0.5}P_{0.5}S_4$ obtained from single crystal X-ray diffraction at 280 K.

S. G.: *Pnma*, *a* = 13.4165(19) Å, *b* = 7.9107(11) Å, *c* = 6.1283(8) Å						
Atom	**Wyck. site**	***x***	***y***	***z***	**Occ.**	**U_{eq} (Å^2)**
Li1A	8*d*	0.3289(6)	0.0263(11)	0.3740(17)	0.73(2)	0.049(3)
Li1B	8*d*	0.3298(14)	0.005(3)	0.186(3)	0.27(2)	0.032(6)
Li2	8*d*	0.0099(13)	0.031(3)	0.547(2)	0.38(2)	0.043(6)
Li3A	4*c*	-0.087(2)	0.25	-0.132(5)	0.35(7)	0.039(10)
Li3B	4*c*	-0.068(5)	0.25	-0.282(17)	0.46(9)	0.14(4)
P1	4*c*	0.08749(7)	0.25	0.15490(15)	0.5	0.0163(2)
Si1	4*c*	0.08749(7)	0.25	0.15490(15)	0.5	0.0163(2)
S1	8*d*	0.15498(5)	0.03079(9)	0.27334(11)	1	0.0235(2)
S2	4*c*	-0.06011(7)	0.25	0.26838(15)	1	0.0201(2)
S3	4*c*	0.09530(8)	0.25	-0.18368(15)	1	0.0241(2)

Table A11 Anisotropic displacement parameters of $Li_{3.5}Si_{0.5}P_{0.5}S_4$ obtained from single crystal X-ray diffraction at 280 K.

Atom	**U_{11} (Å^2)**	**U_{22} (Å^2)**	**U_{33} (Å^2)**	**U_{23} (Å^2)**	**U_{13} (Å^2)**	**U_{12} (Å^2)**
Li1A	0.040(5)	0.040(5)	0.067(7)	0.015(4)	-0.006(4)	0.003(4)
Li1B	0.029(10)	0.030(11)	0.038(12)	0.002(8)	-0.008(8)	0.005(8)
Li2	0.033(9)	0.064(15)	0.032(11)	0.022(9)	-0.004(8)	-0.007(8)
Li3A	0.044(17)	0.050(17)	0.021(16)	0	-0.008(10)	0
Li3B	0.18(5)	0.028(16)	0.21(9)	0	-0.12(5)	0
P1	0.0184(5)	0.0146(5)	0.0160(4)	0	0.0013(3)	0
Si1	0.0184(5)	0.0146(5)	0.0160(4)	0	0.0013(3)	0
S1	0.0226(3)	0.0212(4)	0.0266(3)	0.0044(3)	-0.0005(2)	0.0034(2)
S2	0.0195(4)	0.0181(5)	0.0228(4)	0	0.0015(3)	0
S3	0.0336(5)	0.0211(5)	0.0176(4)	0	0.0045(3)	0

Table A12 Atomic coordinates, occupation factors and equivalent isotropic displacement parameters of $Li_{3.67}Si_{0.67}P_{0.33}S_4$ obtained from single crystal X-ray diffraction at 280 K.

S. G.: *Pnma*, a = 13.6750(18) Å, b = 7.7946(10) Å, c = 6.1411(9) Å						
Atom	**Wyck. site**	***x***	***y***	***z***	**Occ.**	**U_{eq} (Å^2)**
Li1A	8*d*	0.3263(8)	0.0210(15)	0.351(3)	0.44(3)	0.032(5)
Li1B	8*d*	0.3280(9)	0.0024(15)	0.187(2)	0.46(3)	0.029(4)
Li2	4*b*	0	0	0.5	0.85(4)	0.079(7)
Li3A	4*c*	-0.0877(9)	0.25	-0.139(3)	0.64(5)	0.030(5)
Li3B	4*c*	-0.070(4)	0.25	-0.304(11)	0.36(6)	0.08(2)
P1	4*c*	0.08733(6)	0.25	0.15211(15)	0.3333	0.0129(2)
Si1	4*c*	0.08733(6)	0.25	0.15211(15)	0.6667	0.0129(2)
S1	8*d*	0.15533(4)	0.02628(8)	0.26971(10)	1	0.0172(2)
S2	4*c*	-0.05954(6)	0.25	0.26589(13)	1	0.0140(1)
S3	4*c*	0.09092(7)	0.25	-0.19126(15)	1	0.0186(2)

Table A13 Anisotropic displacement parameters of $Li_{3.67}Si_{0.67}P_{0.33}S_4$ obtained from single crystal X-ray diffraction at 280 K.

Atom	**U_{11} (Å^2)**	**U_{22} (Å^2)**	**U_{33} (Å^2)**	**U_{23} (Å^2)**	**U_{13} (Å^2)**	**U_{12} (Å^2)**
Li1A	0.015(5)	0.021(6)	0.059(11)	0.016(6)	0.003(5)	0.008(4)
Li1B	0.028(6)	0.027(6)	0.032(8)	0.012(5)	-0.007(5)	0.001(5)
Li2	0.065(9)	0.077(10)	0.095(12)	0.060(9)	0.046(8)	0.039(7)
Li3A	0.027(7)	0.024(6)	0.04(1)	0	-0.010(5)	0
Li3B	0.10(4)	0.05(2)	0.09(4)	0	-0.05(3)	0
P1	0.0130(4)	0.0132(4)	0.0125(4)	0	0.0005(3)	0
Si1	0.0130(4)	0.0132(4)	0.0125(4)	0	0.0005(3)	0
S1	0.0144(3)	0.0149(4)	0.0221(3)	0.0028(2)	-0.0010(2)	0.0030(2)
S2	0.0119(4)	0.0127(4)	0.0174(4)	0	0.0015(3)	0
S3	0.0242(5)	0.0167(4)	0.0151(4)	0	0.0022(3)	0

Table A14 Atomic coordinates, occupation factors and equivalent isotropic displacement parameters of $Li_{3.8}Si_{0.8}P_{0.2}S_4$ obtained from single crystal X-ray diffraction at 280 K.

S. G.: $P2_1/m$, a = 6.112(2) Å, b = 7.781(3) Å, c = 6.880(3) Å, β= 91.147(9)°						
Atom	**Wyck. site**	***x***	***y***	***z***	**Occ.**	**U_{eq} (Å^2)**
Li1	2*e*	0.647(2)	0.25	0.3296(15)	0.94(5)	0.038(5)
Li2	2*c*	0	0	0.5	0.90(6)	0.060(7)
Li3	4*f*	0.662(3)	-0.0157(19)	0.8512(19)	0.51(4)	0.030(6)
Li4	4*f*	0.818(4)	-0.009(2)	0.846(2)	0.48(4)	0.035(7)
P1	2*e*	0.3557(2)	0.25	0.67385(17)	0.2	0.0120(3)
Si1	2*e*	0.3557(2)	0.25	0.67385(17)	0.8	0.0120(3)
S1	4*f*	0.23904(14)	0.47431(12)	0.80985(12)	1	0.0172(2)
S2	2*e*	0.23235(19)	0.25	0.38059(16)	1	0.0141(3)
S3	2*e*	0.70126(19)	0.25	0.67884(17)	1	0.0171(3)

Table A15 Anisotropic displacement parameters of $Li_{3.8}Si_{0.8}P_{0.2}S_4$ obtained from single crystal X-ray diffraction at 280 K.

Atom	**U_{11} (Å^2)**	**U_{22} (Å^2)**	**U_{33} (Å^2)**	**U_{23} (Å^2)**	**U_{13} (Å^2)**	**U_{12} (Å^2)**
Li1	0.063(9)	0.028(7)	0.025(6)	0	0.020(5)	0
Li12	0.058(10)	0.068(12)	0.051(10)	0.030(8)	-0.036(7)	-0.043(8)
Li3	0.036(13)	0.030(9)	0.024(7)	0.003(6)	0.000(6)	0.010(7)
Li4	0.043(15)	0.041(11)	0.022(8)	0.007(6)	0.008(7)	-0.004(8)
P1	0.0126(6)	0.0122(6)	0.0112(6)	0	-0.0010(4)	0
Si1	0.0126(6)	0.0122(6)	0.0112(6)	0	-0.0010(4)	0
S1	0.0213(4)	0.0149(5)	0.0153(4)	-0.0032(3)	0.0009(3)	0.0013(3)
S2	0.0160(6)	0.0137(6)	0.0125(5)	0	-0.0020(4)	0
S3	0.0131(5)	0.0162(6)	0.0219(6)	0	-0.0025(4)	0

Appendix B Supporting information for Chapter 4

Table B1 Atomic coordinates, occupation factors and isotropic displacement parameter of representative $Li_{6.7}Si_{0.7}Sb_{0.3}S_5I$ obtained from powder neutron diffraction at 195 K.

S. G.: $F\bar{4}3m$, a = 10.30464(4) Å, 4.06 wt% Li_2S, 6.45 wt% LiI						
Atom	**Wyck. Site**	***x***	***y***	***z***	**Occ.**	**U_{iso} (Å^2)**
Li1	48*h*	0.2895(8)	0.5181(7)	0.7895(9)	0.34(2)	0.035(2)
Li2	24*g*	0.0207(9)	0.25	0.25	0.30(3)	0.020(4)
Li3	48*h*	0.728(3)	0.070(2)	0.570(2)	0.062(7)	0.04(1)
Li4	4*d*	0.75	0.25	0.25	0.02(1)	0.013(38)
Si1	4*b*	0.5	0.5	0.5	0.655	0.0110(3)
Sb1	4*b*	0.5	0.5	0.5	0.345	0.0110(3)
S1	4*c*	0.25	0.25	0.25	0.983	0.0142(4)
S2	16*e*	0.3771(2)	0.3771(2)	0.6229(2)	1	0.0201(3)
S3	4*a*	0.5	0.5	0	0.026	0.0342(4)
I1	4*a*	0.5	0.5	0	0.974	0.0342(4)
I2	4*c*	0.25	0.25	0.25	0.017	0.0142(4)

Table B2 Atomic coordinates, occupation factors and isotropic displacement parameter of representative Li_6SbS_5I obtained from powder neutron diffraction at 300 K.

S. G.: $F\bar{4}3m$, a = 10.41912(5) Å, 0.91 wt% Li_2S, 1.65 wt% LiI						
Atom	**Wyck. Site**	***x***	***y***	***z***	**Occ.**	**U_{iso} (Å^2)**
Li1	48*h*	0.2950(5)	0.5236(4)	0.7950(5)	0.36(2)	0.033(2)
Li2	24g	0.016(1)	0.25	0.25	0.27(2)	0.035(4)
Sb1	4*b*	0.5	0.5	0.5	1	0.0129(4)
S1	4*c*	0.25	0.25	0.25	1	0.0172(4)
S2	16*e*	0.3720(2)	0.3720(2)	0.6280(2)	1	0.0176(2)
I1	4*a*	0.5	0.5	0	1	0.0366(4)

Table B3 Atomic coordinates, occupation factors and isotropic displacement parameter of representative $Li_{6.3}Si_{0.3}Sb_{0.7}S_5I$ obtained from powder neutron diffraction at 300 K.

S. G.: $F\bar{4}3m$, *a* = 10.38800(4) Å, 2.58 wt% Li_2S, 2.55 wt% LiI						
Atom	**Wyck. Site**	***x***	***y***	***z***	**Occ.**	**U_{iso} (Å^2)**
Li1	48*h*	0.2891(7)	0.5206(6)	0.7891(7)	0.37(2)	0.024(2)
Li2	24*g*	0.026(1)	0.25	0.25	0.20(3)	0.031(7)
Li3	48*h*	0.723(4)	0.058(3)	0.5558(3)	0.053(7)	0.05(1)
Li4	4*d*	0.75	0.25	0.25	0.06(1)	0.021(15)
Si1	4*b*	0.5	0.5	0.5	0.263	0.0119(2)
Sb1	4*b*	0.5	0.5	0.5	0.737	0.0119(2)
S1	4*c*	0.25	0.25	0.25	0.989	0.0168(4)
S2	16*e*	0.3731(2)	0.3731(2)	0.6269(2)	1	0.0237(3)
S3	4*a*	0.5	0.5	0	0.022	0.0358(4)
I1	4*a*	0.5	0.5	0	0.978	0.0358(4)
I2	4*c*	0.25	0.25	0.25	0.011	0.0168(4)

Table B4 Atomic coordinates, occupation factors and isotropic displacement parameter of representative $Li_{6.5}Si_{0.5}Sb_{0.5}S_5I$ obtained from powder neutron diffraction at 300 K.

S. G.: $F\bar{4}3m$, *a* = 10.35594(4) Å, 2.83 wt% Li_2S, 2.96 wt% LiI						
Atom	**Wyck. Site**	***x***	***y***	***z***	**Occ.**	**U_{iso} (Å^2)**
Li1	48*h*	0.2890(8)	0.5188(7)	0.7890(8)	0.35(2)	0.038(2)
Li2	24*g*	0.022(1)	0.25	0.25	0.27(3)	0.032(5)
Li3	48*h*	0.735(4)	0.071(3)	0.571(3)	0.081(8)	0.10(2)
Li4	4*d*	0.75	0.25	0.25	0.05(1)	0.019(17)
Si1	4*b*	0.5	0.5	0.5	0.465	0.0114(2)
Sb1	4*b*	0.5	0.5	0.5	0.535	0.0123(3)
S1	4*c*	0.25	0.25	0.25	0.991	0.0162(4)
S2	16*e*	0.3752(1)	0.3752(1)	0.6248(1)	1	0.0237(3)
I1	4*a*	0.5	0.5	0	1	0.0377(4)
I2	4*c*	0.25	0.25	0.25	0.009	0.0162(4)

Table B5 Atomic coordinates, occupation factors and isotropic displacement parameters of $Li_{6.1}Si_{0.1}Sb_{0.9}S_5I$ obtained from synchrotron powder diffraction at room temperature.

S. G.: $F\bar{4}3m$, *a* = 10.42024(5) Å; R_w = 7.321; GoF = 2.33; 1.09(6) wt% Li_2S						
Atom	**Wyck. Site**	***x***	***y***	***z***	**Occ.**	U_{iso} **(Å^2)**
Sb1	4*b*	0.5	0.5	0.5	0.935(6)	0.0094(3)
Si1	4*b*	0.5	0.5	0.5	0.065(6)	0.0094(3)
S1	4*c*	0.25	0.25	0.25	0.989(3)	0.0176(9)
S2	16*e*	0.3708(2)	0.3708(2)	0.6292(2)	1	0.0190(6)
S3	4*a*	0.5	0.5	0	0.033(5)	0.0344(4)
I1	4*a*	0.5	0.5	0	0.967(5)	0.0344(4)
I2	4*c*	0.25	0.25	0.25	0.011(3)	0.0176(9)

Table B6 Atomic coordinates, occupation factors and isotropic displacement parameters of $Li_{6.2}Si_{0.2}Sb_{0.8}S_5I$ obtained from synchrotron powder diffraction at room temperature.

S. G.: $F\bar{4}3m$, *a* = 10.41101(4) Å; R_w = 5.110; GoF = 1.65; 3.61(6) wt% Li_2S						
Atom	**Wyck. Site**	***x***	***y***	***z***	**Occ.**	U_{iso} **(Å^2)**
Sb1	4*b*	0.5	0.5	0.5	0.830(3)	0.0100(2)
Si1	4*b*	0.5	0.5	0.5	0.170(3)	0.0100(2)
S1	4*c*	0.25	0.25	0.25	1	0.0191(5)
S2	16*e*	0.3714 (1)	0.3714(1)	0.6286(1)	1	0.0211(4)
S3	4*a*	0.5	0.5	0	0.026(3)	0.0363(3)
I1	4*a*	0.5	0.5	0	0.974(3)	0.0363(3)

Table B7 Atomic coordinates, occupation factors and isotropic displacement parameters of $Li_{6.3}Si_{0.3}Sb_{0.7}S_5I$ obtained from synchrotron powder diffraction at room temperature.

S. G.: $F\bar{4}3m$, a = 10.3972(2) Å; R_w = 6.118; GoF = 2.03; 3.2(1) wt% Li_2S						
Atom	**Wyck. Site**	***x***	***y***	***z***	**Occ.**	U_{iso} **(Å^2)**
Sb1	4*b*	0.5	0.5	0.5	0.737(4)	0.0104(3)
Si1	4*b*	0.5	0.5	0.5	0.263(4)	0.0104(3)
S1	4*c*	0.25	0.25	0.25	0.989(3)	0.0203(9)
S2	16*e*	0.3722(1)	0.3722(1)	0.6278(1)	1	0.0212(5)
S3	4*a*	0.5	0.5	0	0.022(4)	0.0367(4)
I1	4*a*	0.5	0.5	0	0.978(4)	0.0367(4)
I2	4*c*	0.25	0.25	0.25	0.011(3)	0.0203(9)

Table B8 Atomic coordinates, occupation factors and isotropic displacement parameters of $Li_{6.4}Si_{0.4}Sb_{0.6}S_5I$ obtained from synchrotron powder diffraction at room temperature.

S. G.: $F\bar{4}3m$, a = 10.38134(3) Å; R_w = 4.162; GoF = 1.39; 0.111(9) wt% LiI, 2.61(4) wt% Li_2S						
Atom	**Wyck. Site**	***x***	***y***	***z***	**Occ.**	U_{iso} **(Å^2)**
Sb1	4*b*	0.5	0.5	0.5	0.643(2)	0.0109(2)
Si1	4*b*	0.5	0.5	0.5	0.357(2)	0.0109(2)
S1	4*c*	0.25	0.25	0.25	0.997(2)	0.0191(6)
S2	16*e*	0.37341(8)	0.37341(8)	0.62659(8)	1	0.0225(3)
S3	4*a*	0.5	0.5	0	0.015(3)	0.0387(2)
I1	4*a*	0.5	0.5	0	0.985(3)	0.0387(2)
I2	4*c*	0.25	0.25	0.25	0.003(2)	0.0203(9)

Table B9 Atomic coordinates, occupation factors and isotropic displacement parameters of $Li_{6.5}Si_{0.5}Sb_{0.5}S_5I$ obtained from synchrotron powder diffraction at room temperature.

S. G.: $F\bar{4}3m$, a = 10.36445(4) Å; R_w = 4.06; GoF = 1.36; 2.36(2) wt% LiI, 2.93(4) wt% Li_2S

Atom	**Wyck. Site**	***x***	***y***	***z***	**Occ.**	U_{iso} **(Å^2)**
Sb1	4*b*	0.5	0.5	0.5	0.535(2)	0.0117(3)
Si1	4*b*	0.5	0.5	0.5	0.465(2)	0.0117(3)
S1	4*c*	0.25	0.25	0.25	0.991(2)	0.0185(6)
S2	16*e*	0.37492(8)	0.37492(8)	0.62508(8)	1	0.0231(3)
I1	4*a*	0.5	0.5	0	1	0.0390(3)
I2	4*c*	0.25	0.25	0.25	0.009(2)	0.0185(6)

Table B10 Atomic coordinates, occupation factors and isotropic displacement parameters of $Li_{6.6}Si_{0.6}Sb_{0.4}S_5I$ obtained from synchrotron powder diffraction at room temperature.

S. G.: $F\bar{4}3m$, a = 10.3472(2) Å; R_w = 3.18; GoF = 1.23; 2.65(3) wt% LiI, 3.92(7) wt% Li_2S

Atom	**Wyck. Site**	***x***	***y***	***z***	**Occ.**	U_{iso} **(Å^2)**
Sb1	4*b*	0.5	0.5	0.5	0.439(2)	0.0072(4)
Si1	4*b*	0.5	0.5	0.5	0.561(2)	0.0072(4)
S1	4*c*	0.25	0.25	0.25	0.976(2)	0.0134(6)
S2	16*e*	0.3762(1)	0.3762(1)	0.6238(1)	1	0.0188(4)
S3	4*a*	0.5	0.5	0	0.014(7)	0.337(4)
I1	4*a*	0.5	0.5	0	0.986(7)	0.0337(4)
I2	4*c*	0.25	0.25	0.25	0.024(2)	0.0134(6)

Table B11 Atomic coordinates, occupation factors and isotropic displacement parameters of $Li_{6.7}Si_{0.7}Sb_{0.3}S_5I$ obtained from synchrotron powder diffraction at room temperature.

S. G.: $F\bar{4}3m$, a = 10.32893(5) Å; R_w = 4.672; GoF = 1.42; 4.46(2) wt% LiI, 6.24(6) wt% Li_2S

Atom	**Wyck. Site**	***x***	***y***	***z***	**Occ.**	U_{iso} **(Å^2)**
Sb1	4*b*	0.5	0.5	0.5	0.345(2)	0.0125(5)
Si1	4*b*	0.5	0.5	0.5	0.655(2)	0.0125(5)
S1	4*c*	0.25	0.25	0.25	0.983(2)	0.0185(7)
S2	16*e*	0.37776(9)	0.37776(9)	0.62224(9)	1	0.0220(5)
S3	4*a*	0.5	0.5	0	0.026(6)	0.0389(4)
I1	4*a*	0.5	0.5	0	0.974(6)	0.0389(4)
I2	4*c*	0.25	0.25	0.25	0.017(2)	0.0185(7)

Table B12 Atomic coordinates, occupation factors and isotropic displacement parameters of Li_6SbS_5I obtained from synchrotron powder diffraction at room temperature.

S. G.: $F\bar{4}3m$, a = 10.4161(2) Å; R_w = 6.408; GoF = 1.84; 0.93(3) wt% LiI

Atom	**Wyck. Site**	***x***	***y***	***z***	**Occ.**	U_{iso} **(Å^2)**
Sb1	4*b*	0.5	0.5	0.5	1	0.0076(2)
S1	4*c*	0.25	0.25	0.25	1	0.0099(6)
S2	16*e*	0.3708(1)	0.3708(1)	0.6292(1)	1	0.0107(4)
I1	4*a*	0.5	0.5	0	1	0.0307(3)

Table B13 Atomic coordinates, occupation factors and equivalent isotropic displacement parameters of $Li_{6.1}Si_{0.1}Sb_{0.9}S_5I$ obtained from single crystal X-ray diffraction at 280 K.

S. G.: $F\bar{4}3m$, a = 10.4104(4) Å						
Atom	**Wyck. Site**	***x***	***y***	***z***	**Occ.**	**U_{eq} (Å^2)**
Li1	48*h*	0.2845(10)	0.5232(11)	0.7845(10)	0.48(2)	0.042(5)
Sb1	4*b*	0.5	0.5	0.5	0.924(9)	0.013(1)
Si1	4*b*	0.5	0.5	0.5	0.076(9)	0.013(1)
S1	4*c*	0.25	0.25	0.25	0.984(6)	0.019(1)
S2	16*e*	0.3719(1)	0.3719(1)	0.6281(1)	1	0.020(1)
S3	4*a*	0.5	0.5	0	0.009(6)	0.035(1)
I1	4*a*	0.5	0.5	0	0.991(6)	0.035(1)
I2	4*c*	0.25	0.25	0.25	0.016(6)	0.019(1)

Table B14 Anisotropic displacement parameters of $Li_{6.1}Si_{0.1}Sb_{0.9}S_5I$ obtained from single crystal X-ray diffraction at 280 K.

Atom	**U_{11} (Å^2)**	**U_{22} (Å^2)**	**U_{33} (Å^2)**	**U_{23} (Å^2)**	**U_{13} (Å^2)**	**U_{12} (Å^2)**
Li1	0.051(6)	0.024(7)	0.051(6)	0.002(3)	0.026(5)	0.002(3)
Sb1	0.013(1)	0.013(1)	0.013(1)	0	0	0
Si1	0.013(1)	0.013(1)	0.013(1)	0	0	0
S1	0.019(1)	0.019(1)	0.019(1)	0	0	0
S2	0.020(1)	0.020(1)	0.020(1)	0.003(1)	0.003(1)	-0.003(1)
S3	0.035(1)	0.035(1)	0.035(1)	0	0	0
I1	0.035(1)	0.035 (1)	0.035(1)	0	0	0
I2	0.019(1)	0.019(1)	0.019(1)	0	0	0

Table B15 Atomic coordinates, occupation factors and equivalent isotropic displacement parameters of $Li_{6.4}Si_{0.4}Sb_{0.6}S_5I$ obtained from single crystal X-ray diffraction at 280 K.

S. G.: $F\bar{4}3m$, a = 10.3782(3) Å						
Atom	**Wyck. Site**	***x***	***y***	***z***	**Occ.**	**U_{eq} (Å^2)**
Li1	48*h*	0.2831(8)	0.5219(7)	0.7831(8)	0.48(2)	0.059(4)
Sb1	4*b*	0.5	0.5	0.5	0.658(5)	0.013(1)
Si1	4*b*	0.5	0.5	0.5	0.342(5)	0.013(1)
S1	4*c*	0.25	0.25	0.25	1	0.018(1)
S2	16*e*	0.3744(1)	0.3744(1)	0.6256(1)	1	0.023(1)
S3	4*a*	0.5	0.5	0	0.012(5)	0.039(1)
I1	4*a*	0.5	0.5	0	0.988(5)	0.039(1)

Table B16 Anisotropic displacement parameters of $Li_{6.4}Si_{0.4}Sb_{0.6}S_5I$ obtained from single crystal X-ray diffraction at 280 K.

Atom	**U_{11} (Å^2)**	**U_{22} (Å^2)**	**U_{33} (Å^2)**	**U_{23} (Å^2)**	**U_{13} (Å^2)**	**U_{12} (Å^2)**
Li1	0.074(5)	0.028(4)	0.074(5)	0.000(3)	0.041(5)	0.000(3)
Sb1	0.013(1)	0.013(1)	0.013(1)	0	0	0
Si1	0.013(1)	0.013(1)	0.013(1)	0	0	0
S1	0.018(1)	0.018(1)	0.018(1)	0	0	0
S2	0.023(1)	0.023(1)	0.023(1)	0.000(1)	0.000(1)	0.000(1)
S3	0.039(1)	0.039(1)	0.039(1)	0	0	0
I1	0.039(1)	0.039(1)	0.039(1)	0	0	0

Table B17 Atomic coordinates, occupation factors and equivalent isotropic displacement parameters of $Li_{6.5}Si_{0.5}Sb_{0.5}S_5I$ obtained from single crystal X-ray diffraction at 280 K.

S. G.: $F\bar{4}3m$, a = 10.3354(4) Å						
Atom	**Wyck. Site**	***x***	***y***	***z***	**Occ.**	**U_{eq} (Å^2)**
Li1	48*h*	0.2815(9)	0.5216(10)	0.7815(9)	0.52(2)	0.061(6)
Sb1	4*b*	0.5	0.5	0.5	0.549(5)	0.013(1)
Si1	4*b*	0.5	0.5	0.5	0.451(5)	0.013(1)
S1	4*c*	0.25	0.25	0.25	1	0.019(1)
S2	16*e*	0.3754(1)	0.3754(1)	0.6246(1)	1	0.024(1)
S3	4*a*	0.5	0.5	0	0.037(6)	0.040(1)
I1	4*a*	0.5	0.5	0	0.963(6)	0.040(1)

Table B18 Anisotropic displacement parameters of $Li_{6.5}Si_{0.5}Sb_{0.5}S_5I$ obtained from single crystal X-ray diffraction at 280 K.

Atom	**U_{11} (Å^2)**	**U_{22} (Å^2)**	**U_{33} (Å^2)**	**U_{23} (Å^2)**	**U_{13} (Å^2)**	**U_{12} (Å^2)**
Li1	0.074(9)	0.034(7)	0.074(9)	0.002(4)	0.039(8)	0.002(4)
Sb1	0.013(1)	0.013(1)	0.013(1)	0	0	0
Si1	0.013(1)	0.013(1)	0.013(1)	0	0	0
S1	0.019(1)	0.019(1)	0.019(1)	0	0	0
S2	0.024(1)	0.024(1)	0.024(1)	0.000(1)	0.000(1)	0.000(1)
S3	0.040(1)	0.040(1)	0.040(1)	0	0	0
I1	0.040(1)	0.040(1)	0.040(1)	0	0	0

Table B19 Atomic coordinates, occupation factors and equivalent isotropic displacement parameters of $Li_{6.7}Si_{0.7}Sb_{0.3}S_5I$ obtained from single crystal X-ray diffraction at 280 K.

S. G.: $F\bar{4}3m$, a = 10.330(2) Å						
Atom	**Wyck. Site**	***x***	***y***	***z***	**Occ.**	**U_{eq} (Å^2)**
Li1	48*h*	0.276(3)	0.519(2)	0.776(3)	0.51(4)	0.08(2)
Sb1	4*b*	0.5	0.5	0.5	0.378(8)	0.014(1)
Si1	4*b*	0.5	0.5	0.5	0.622(8)	0.014(1)
S1	4*c*	0.25	0.25	0.25	1	0.019(1)
S2	16*e*	0.3771(1)	0.3771(1)	0.6229(1)	1	0.025(1)
S3	4*a*	0.5	0.5	0	0.073(11)	0.040(1)
I1	4*a*	0.5	0.5	0	0.927(11)	0.040(1)

Table B20 Anisotropic displacement parameters of $Li_{6.7}Si_{0.7}Sb_{0.3}S_5I$ obtained from single crystal X-ray diffraction at 280 K.

Atom	**U_{11} (Å^2)**	**U_{22} (Å^2)**	**U_{33} (Å^2)**	**U_{23} (Å^2)**	**U_{13} (Å^2)**	**U_{12} (Å^2)**
Li1	0.11(3)	0.026(7)	0.11(3)	-0.011(8)	-0.07(3)	-0.011(8)
Sb1	0.014(1)	0.014(1)	0.014(1)	0	0	0
Si1	0.014(1)	0.014(1)	0.014(1)	0	0	0
S1	0.019(1)	0.019(1)	0.019(1)	0	0	0
S2	0.025(1)	0.025(1)	0.025(1)	0.000(1)	0.000(1)	0.000(1)
S3	0.040(1)	0.040(1)	0.040(1)	0	0	0
I1	0.040(1)	0.040(1)	0.040(1)	0	0	0

Table B21 Atomic coordinates, occupation factors and equivalent isotropic displacement parameters of $Li_{6.2}Ge_{0.2}Sb_{0.8}S_5I$ obtained from single crystal X-ray diffraction at 280 K.

S. G.: $F\bar{4}3m$, a = 10.413 (2) Å

Atom	**Wyck. Site**	***x***	***y***	***z***	**Occ.**	U_{eq} **(Å^2)**
Li1	48*h*	0.2843(11)	0.5220(11)	0.7843(11)	0.50(3)	0.050(5)
Sb1	4*b*	0.5	0.5	0.5	0.78(2)	0.013(1)
Ge1	4*b*	0.5	0.5	0.5	0.22(2)	0.013(1)
S1	4*c*	0.25	0.25	0.25	0.988(7)	0.019(1)
S2	16*e*	0.3725(1)	0.3725(1)	0.6275(1)	1	0.020(1)
S3	4*a*	0.5	0.5	0	0.024(6)	0.039(1)
I1	4*a*	0.5	0.5	0	0.976(8)	0.039(1)
I2	4*c*	0.25	0.25	0.25	0.012(7)	0.019(1)

Table B22 Anisotropic displacement parameters of $Li_{6.2}Ge_{0.2}Sb_{0.8}S_5I$ obtained from single crystal X-ray diffraction at 280 K.

Atom	U_{11} **(Å^2)**	U_{22} **(Å^2)**	U_{33} **(Å^2)**	U_{23} **(Å^2)**	U_{13} **(Å^2)**	U_{12} **(Å^2)**
Li1	0.059(6)	0.032(5)	0.059(6)	0.000(3)	0.030(6)	0.000(3)
Sb1	0.013(1)	0.013(1)	0.013(1)	0	0	0
Ge1	0.013(1)	0.013(1)	0.013(1)	0	0	0
S1	0.019(1)	0.019(1)	0.019(1)	0	0	0
S2	0.020(1)	0.020(1)	0.020(1)	0.002(1)	0.002(1)	-0.002(1)
S3	0.039 (1)	0.039(1)	0.039(1)	0	0	0
I1	0.039(1)	0.039(1)	0.030(1)	0	0	0
I2	0.019(1)	0.019(1)	0.019(1)	0	0	0

Table B23 Atomic coordinates, occupation factors and equivalent isotropic displacement parameters of $Li_{6.4}Ge_{0.4}Sb_{0.6}S_5I$ obtained from single crystal X-ray diffraction at 280 K.

S. G.: $F\bar{4}3m$, a = 10.406(2) Å						
Atom	**Wyck. Site**	***x***	***y***	***z***	**Occ.**	**U_{eq} (Å^2)**
Li1	48*h*	0.2827(8)	0.5220(8)	0.7827(8)	0.52(2)	0.059(5)
Sb1	4*b*	0.5	0.5	0.5	0.574(14)	0.013(1)
Ge1	4*b*	0.5	0.5	0.5	0.426(14)	0.013(1)
S1	4*c*	0.25	0.25	0.25	0.978(5)	0.019(1)
S2	16*e*	0.3738(1)	0.3738(1)	0.6262(1)	1	0.021(1)
S3	4*a*	0.5	0.5	0	0.026(5)	0.042(1)
I1	4*a*	0.5	0.5	0	0.974(5)	0.042(1)
I2	4*c*	0.25	0.25	0.25	0.022(5)	0.019(1)

Table B24 Anisotropic displacement parameters of $Li_{6.4}Ge_{0.4}Sb_{0.6}S_5I$ obtained from single crystal X-ray diffraction at 280 K.

Atom	**U_{11} (Å^2)**	**U_{22} (Å^2)**	**U_{33} (Å^2)**	**U_{23} (Å^2)**	**U_{13} (Å^2)**	**U_{12} (Å^2)**
Li1	0.072(6)	0.031(5)	0.072(6)	-0.001(3)	0.042(6)	-0.001(3)
Sb1	0.013(1)	0.013(1)	0.013(1)	0	0	0
Ge1	0.013(1)	0.013(1)	0.013(1)	0	0	0
S1	0.019(1)	0.019(1)	0.019(1)	0	0	0
S2	0.021(1)	0.021(1)	0.021(1)	0.002(1)	0.002(1)	-0.002(1)
S3	0.042 (1)	0.042(1)	0.042(1)	0	0	0
I1	0.042(1)	0.042(1)	0.042(1)	0	0	0
I2	0.019(1)	0.019(1)	0.019(1)	0	0	0

Table B25 Atomic coordinates, occupation factors and equivalent isotropic displacement parameters of $Li_{6.2}Sn_{0.2}Sb_{0.8}S_5I$ obtained from single crystal X-ray diffraction at 280 K.

S. G.: $F\bar{4}3m$, a = 10.4419(6) Å

Atom	**Wyck. Site**	***x***	***y***	***z***	**Occ.**	U_{eq} **(Å²)**
Li1	48*h*	0.292(2)	0.5238(14)	0.792(2)	0.42(5)	0.039(7)
Li2	24*g*	0.25	0.521(5)	0.75	0.24(10)	0.042(16) (U_{iso})
Sb1	4*b*	0.5	0.5	0.5	0.8	0.014(1)
Sn1	4*b*	0.5	0.5	0.5	0.2	0.014(1)
S1	4*c*	0.25	0.25	0.25	0.957(5)	0.020(1)
S2	16*e*	0.3715(1)	0.3715(1)	0.6285(1)	1	0.021(1)
S3	4*a*	0.5	0.5	0	0.010(4)	0.039(1)
I1	4*a*	0.5	0.5	0	0.990(4)	0.039(1)
I2	4*c*	0.25	0.25	0.25	0.043(5)	0.020(1)

Table B26 Anisotropic displacement parameters of $Li_{6.2}Sn_{0.2}Sb_{0.8}S_5I$ obtained from single crystal X-ray diffraction at 280 K.

Atom	U_{11} **(Å²)**	U_{22} **(Å²)**	U_{33} **(Å²)**	U_{23} **(Å²)**	U_{13} **(Å²)**	U_{12} **(Å²)**
Li1	0.041(9)	0.036(7)	0.041(9)	-0.002(5)	0.008(9)	-0.002(5)
Sb1	0.014(1)	0.014(1)	0.014(1)	0	0	0
Sn1	0.014(1)	0.014(1)	0.014(1)	0	0	0
S1	0.020(1)	0.020 (1)	0.020(1)	0	0	0
S2	0.021(1)	0.021(1)	0.021(1)	0.003(1)	0.003(1)	-0.003(1)
S3	0.039(1)	0.039(1)	0.039(1)	0	0	0
I1	0.039(1)	0.039(1)	0.039(1)	0	0	0
I2	0.020(1)	0.020(1)	0.020(1)	0	0	0